Extension of the Reactor Dynamics Code MGT-3D for Pebblebed and Blocktype High-Temperature-Reactors

Dunfu Shi

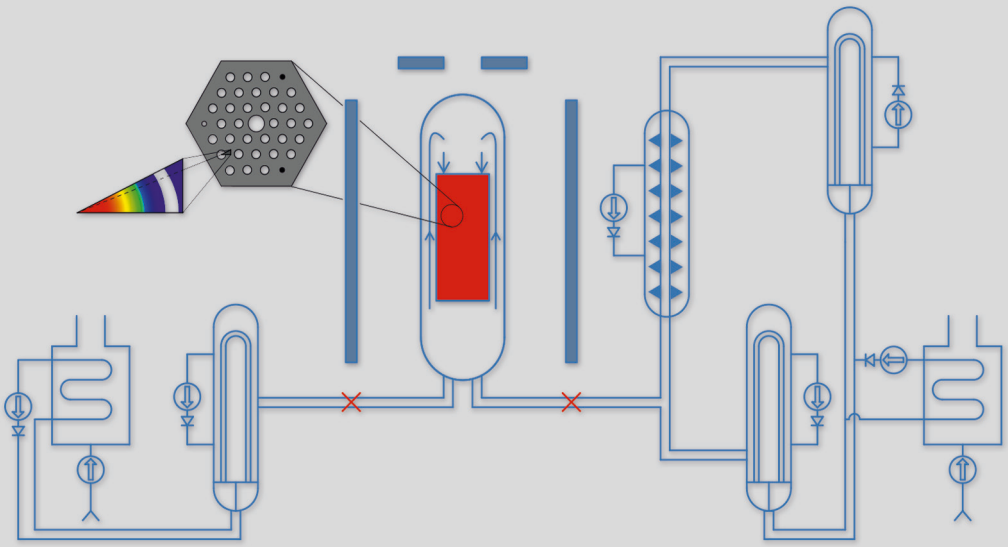

Energie & Umwelt / Energy & Environment
Band / Volume 257
ISBN 978-3-95806-045-6

JÜLICH
FORSCHUNGSZENTRUM

Schriften des Forschungszentrums Jülich
Reihe Energie & Umwelt / Energy & Environment Band / Volume 257

Forschungszentrum Jülich GmbH
Institut für Energie- und Klimaforschung
Nukleare Entsorgung und Reaktorsicherheit (IEK-6)

Extension of the Reactor Dynamics Code MGT-3D for Pebblebed and Blocktype High-Temperature-Reactors

Dunfu Shi

Schriften des Forschungszentrums Jülich
Reihe Energie & Umwelt / Energy & Environment Band / Volume 257

ISSN 1866-1793 ISBN 978-3-95806-045-6

Bibliographic information published by the Deutsche Nationalbibliothek.
The Deutsche Nationalbibliothek lists this publication in the Deutsche Nationalbibliografie; detailed bibliographic data are available in the Internet at http://dnb.d-nb.de.

Publisher and Distributor: Forschungszentrum Jülich GmbH
Zentralbibliothek
52425 Jülich
Tel: +49 2461 61-5368
Fax: +49 2461 61-6103
Email: zb-publikation@fz-juelich.de
www.fz-juelich.de/zb

Cover Design: Grafische Medien, Forschungszentrum Jülich GmbH

Printer: Grafische Medien, Forschungszentrum Jülich GmbH

Schriften des Forschungszentrums Jülich
Reihe Energie & Umwelt / Energy & Environment, Band / Volume 257

D 82 (Diss. RWTH Aachen University, 2014)

ISSN 1866-1793
ISBN 978-3-95806-045-6

The complete volume is freely available on the Internet on the Jülicher Open Access Server (JuSER) at www.fz-juelich.de/zb/openaccess.

Extension of the Reactor Dynamics Code MGT-3D for Pebblebed and Blocktype High-Temperature-Reactors

by

Dunfu Shi MSc

Abstract:

The High Temperature Gas cooled Reactor (HTGR) is an improved, gas cooled nuclear reactor. It was chosen as one of the candidates of generation IV nuclear plants [1]. The reactor can be shut down automatically because of the negative reactivity feedback due to the temperature's increasing in designed accidents. It is graphite moderated and Helium cooled. The residual heat can be transferred out of the reactor core by inactive ways as conduction, convection, and thermal radiation during the accident. In such a way, a fuel temperature does not go beyond a limit at which major fission product release begins.

In this thesis, the coupled neutronics and fluid mechanics code MGT-3D used for the steady state and time-dependent simulation of HTGRs, is enhanced and validated [2]. The fluid mechanics part is validated by SANA experiments in steady state cases as well as transient cases. The fuel temperature calculation is optimized by solving the heat conduction equation of the coated particles. It is applied in the steady state and transient simulation of PBMR, and the results are compared to the simulation with the old overheating model. New approaches to calculate the temperature profile of the fuel element of block-type HTGRs, and the calculation of the homogeneous conductivity of composite materials are introduced. With these new developments, MGT-3D is able to simulate block-type HTGRs as well. This extended MGT-3D is used to simulate a cuboid ceramic block heating experiment in the NACOK-II facility. The extended MGT-3D is also applied to LOFC and DLOFC simulation of GT-MHR. It is a fluid mechanics calculation with a given heat source. This calculation result of MGT-3D is verified with the calculation results of other codes. The design of the Japanese HTTR is introduced. The deterministic simulation of the LOFC experiment of HTTR is conducted with the Monte-Carlo code Serpent and MGT-3D, which is the LOFC Project organized by OECD/NEA [3]. With Serpent the burnup of the reactor core is calculated starting from the first loading. From this calculation the nuclide inventory is obtained and the result is interfaced to MGT-3D. The steady state and time dependent calculation is conducted with MGT-3D. The elapsed time and peak power level at the occurrence of the re-criticality of the LOFC experiment are compared to the simulation results. Up to now, these results meet the experimental values best compared with the other participants.

Erweiterung des gekoppelten Neutronik- und Fluidmechanikprogramm MGT-3D für Kugelhaufen-HTR und HTR mit prismatischen Blöcken

von

Dunfu Shi MSc

Kurzfassung:

Der mit Helium gekühlte, grafitmoderierte Hochtemperaturreaktor (HTGR) gehört zu den innovativen, gasgekühlten Reaktorkonzepten. Er ist einer von sechs ausgewählten Konzepten des Generation IV International Forums (GIF) [1]. Aufgrund seines stark negativen Temperaturkoeffizienten wird der Reaktor in Auslegungsstörfällen durch eine Erhöhung der Brennstofftemperatur automatisch abgeschaltet. Eines seiner herausragenden Sicherheitsmerkmale ist das Konzept der passiven Nachwärmeabfuhr. Die entstehende Wärme kann in einem Störfall selbsttätig durch Wärmeleitung, Konvektion und Wärmestrahlung aus dem Reaktorkern abgeführt werden. Während eines solchen Ereignisses bleiben die Temperaturen der Brennelemente unterhalb einer Temperatur, bei der eine signifikante Spaltproduktfreisetzung einsetzt.

In dieser Dissertation wird das gekoppelte Neutronik- und Fluidmechanikprogramm MGT-3D zur Simulation des stationären und zeitabhängigen Verhaltens von HTR erweitert und validiert [2]. Der Fluidmechanik-Teil wird u.a. anhand des SANA-Experiments für den stationären und zeitabhängigen Fall validiert. Die Berechnung der Brennelementtemperatur wird durch das Lösen der Wärmeleitungsgleichung der sogenannten "coated particles" optimiert. Diese wird im stationären und zeitabhängigen Fall zur Simulation des PBMR angewendet. Die Ergebnisse werden mit dem vorherigen, einfacheren Überhitzungsmodell verglichen. Neue Ansätze zur Berechnung des Temperaturprofils von prismatischen Brennelementen sowie die Berechnung der homogenen Leitfähigkeit des Verbundmaterials werden vorgestellt. Mit dieser neuen Entwicklung ist MGT-3D in der Lage auch prismatische Brennelemente fluidmechanisch abzubilden. Dieses so erweiterte MGT-3D wird zur Simulation eines NACOK-II-Experimentes genutzt. Des Weiteren wird MGT-3D für die Simulation eines LOFC- und eines DLOCF-Störfallszenarios im GT-MHR angewendet. Diese Berechnung wird mit Ergebnissen anderer Programme verifiziert. Die Simulation des LOFC-Experimentes am japanischen HTTR wird mit dem Monte-Carlo-Programm Serpent und mit MGT-3D ausgeführt. Das Experiment und die begleitenden Simulation gehören zum LOFC-Projekt der OECD/NEA [3]. Mit Serpent wird der Abbrand des Reaktorkerns ab der Erstbeladung berechnet. Aus dieser Rechnung wird das Nuklidinventar an MGT-3D übergeben. Die stationäre und zeitabhängige Berechnung wird mit MGT-3D durchgeführt. Der Zeitpunkt und die Höhe der Leistungsspitze des Eintritts der Rekritikalität im LOFC-Experiment werden mit den Simulationsergebnissen verglichen. MGT-3D beschreibt die experimentellen Werte, insbesondere im Vergleich mit den Ergebnissen der anderen Teilnehmer, sehr gut.

Contents

List of Figures

List of Tables

Abbreviations

AC Alternating Current

ACS Auxiliary Cooling System

AGC Auxiliary Gas Circulator

AGR Advanced Gas-cooled Reactor

AHX Auxiliary Heat Exchanger

AVR Arbeitsgemeinschaft Versuchsreaktor

BISO Bi-structural-Isotropic

CP-1 Chicago Pile-1

CREA Control Rod Ejection Accident

CRP Coordinated Research Projects

CRWA Control Rod Withdrawal Accident

CSNI Committee on the Safety of Nuclear Installations

DIN Deutsches Institut für Normung

DLOFC De-pressurized Loss of Forced Coolant

EFPD Effective Full Power Day

FSVR Fort St. Vrain Reactor

FWHM Full Width at Half Maximum

FZJ Forschungszentrum Jülich

GA General Atomics

GFR Gas-cooled Fast Reactor

GT-MHR Gas Turbine-Modular Helium Reactor

HTGR High Temperature Gas-cooled Reactor

HTR High Temperature Reactor

HTR-Modul Hochtemperaturreaktor-Modul

HTTR High Temperature Engineering Test Reactor

IAEA International Atomic Energy Agency

IHX Intermediate Heat Exchanger

INL Idaho National Laboratory

JAEA Japan Atomic Energy Agency

LFR Lead-cooled Fast Reactor

LOFC Loss of Forced Coolant

LWR Light Water Reactor

MCS Main Cooling System

MGT Multi-Group-TINTE

MHTGR Modular High-Temperature Gas-cooled Reactor

MINATOM Russian Federation Ministry for Atomic Energy

ML-1 Army's Mobile Low Power Reactor

MPI Message Passing Interface

MSR Molten Salt Reactor

NACOK Naturzug im Core mit Korrosion

NEA Nuclear Energy Agency

OECD Organisation for Economic Co-operation and Development

PBMR Pebble Bed Modular Reactor

PCRV Prestressed Concrete Reactor Vessel

PCS Power Conversion System

PGC Primary Gas Circulator

PHCS Primary Helium Cooling System

PIRT Phenomena Identification Ranking Tables

PIV Particle Image Velocimetry

PPWC Primary Pressurized Water Cooler

PRM Power Range Monitoring

PWCS Pressurized Water Cooling System

RCCS Reactor Cavity Cooling System

RHS Right Hand Side

RPV Reactor Pressure Vessel

SANA Selbststätige Abfuhr der Nachzerfallsleistung

SCS Shutdown Cooling System

SCWR Supercritical Water-cooled Reactor

SFR Sodium-cooled Fast Reactor

SHCS Secondary Helium/Helium Cooling System

SPWC Secondary Pressurized Water Cooler

TAREF Task Group on Advanced Reactor Experimental Facilities

THTR Thorium Hochtemperatur Reaktor

TINTE Time Dependent Neutronics and Temperatures

TRISO Tri-structural-Isotropic

USNRC United States Nuclear Regulatory Commission

VCS Vessel Cooling System

VHTR Very High Temperature Reactor

VSOP Very Superior Old Programs

VTT Valtion Teknillinen Tutkimuskeskus

WRM Wide Range Monitoring

Chapter 1

Introduction

Energy is the basic driving force of industry, and industrial development is always accompanied by energy-related innovations [5, 7, 8]. Today, fossil fuels that produce a large amount of CO_2 provide 80% of the global energy consumption. With the concern of global warming caused by greenhouse gas emissions into the atmosphere, the new energy alternatives that do not discharge CO_2 are proposed to be developed as priority in many countries. Additionally, the climate disasters have occurred more frequently in recent decades, which confirms mankind to promote the utilization of nuclear energy and green energies such as solar energy, wind energy, hydro-power, and geothermal energy.

By the end of 2012, 437 reactor units with a total power of 373 GW were operating worldwide. They supplied 11.3% of the global electricity production in 2012 [9]. The utilization of nuclear power avoids the emission of more than 2.4 billion tons of CO_2, which corresponds to 8% of the worldwide CO_2 emissions. The diversities of the energy supplies can guarantee the energy security of the country, which is an important issue for all of the governments. Nuclear energy is expected to play an important role in the mixed energy supplies of many countries. Since the Fukushima Daiichi nuclear disaster, people have paid even more attention to the safety aspects of nuclear reactors. More than 10 years ago, six nuclear reactor systems that offer significant advances in sustainability, safety, reliability and economics were selected by the Generation IV International Forum (GIF) as the most promising concepts for the next-fourth-generation of nuclear reactors [1]. They include the Gas-cooled Fast Reactor (GFR), the Lead-cooled Fast Reactor (LFR), the Molten Salt Reactor (MSR), the Supercritical Water-cooled Reactor (SCWR), the Sodium-cooled Fast Reactor (SFR) and the Very High Temperature Reactor (VHTR).

The VHTR, or High Temperature Gas-cooled Reactor (HTGR) system is characterized by its thermal neutron spectrum, graphite moderated core, helium coolant and high coolant outlet temperature of about 1000 $^{\circ}C$. It is the advanced type of gas-cooled nuclear reactor. It is assumed that the construction of small-sized, modular plants can reduce the capital cost of the plants, which makes the concept of HTGR attractive for industrial applications. HTGR has the following advantages:

- Safety aspects: the reactor has a large negative temperature coefficient of reactivity. Therefore, it can be shutdown without scram in the loss of forced coolant accident. The power density of the reactor is low, and it has a high heat capacity and thermal conductivity due to a large amount of graphite. The residual heat can be removed from the reactor and transferred to the outside structures by natural convection, heat conduction and thermal radiation. The reactor core can withstand temperature much higher than 1400 $^{\circ}C$ due to the ceramic coating on the fuel kernel. The helium coolant is an inert gas which does not react with the

components. The absorption cross section of helium is very low, and helium is difficult to activate, which makes the reactor easier to be maintained during normal operation.

- Flexible fuel cycle design: the reactor can be fueled with low enriched uranium, high enriched uranium and thorium. The reactor fuel can be deeply burned and has the flexibility to adopt U/Pu fuel cycles.
- High thermal efficiency: the gas outlet temperature of HTGR is higher than that of LWR. If the steam cycle is applied, the steam temperature can reach 500 $°C$ and the thermal efficiency of the reactor can be more than 40%. By using the high-efficiency direct Brayton cycle, the thermal efficiency can be further increased.
- Versatility: with the high outlet coolant temperature, HTGR can supply, besides electricity, high-quality process heat and steam needed in numerous industrial such as coal gasification, refining of crude oil, seawater desalination, metallurgical processes, or in hydrogen production, e.g. via the thermo-chemical sulfur-iodine cycle [10].

However, thought on a volume basis, the spend fuel output of HTGR is much larger than that of LWR. With the same power level, the vessel of HTGRs is much larger than the LWR. Therefore, the waste will be more compared with LWR when decommissioning the plants. Additionally, it is more difficult to reprocess the fuel materials than that of LWR due to the coating structures.

This chapter gives a short overview of the developmental history of the High Temperature Gas-cooled Reactors (HTGRs), a brief description of the design base of three representative HTGRs and the topics discussed in this thesis. In the first section, the past HTGR designs are introduced according to their developing sequence. In the second section, the basic design data of HTGRs which are referred to this thesis is presented. The third section introduces the objectives and the outline of this thesis.

1.1 History of HTGR

The development of the graphite-moderated, gas-cooled reactor has a long history. The first man-made critical assembly, Chicago pile-1 (CP-1), was a graphite-moderated thermal reactor. The Calder Hall power station was the first nuclear reactor to generate electricity in the world. Hence, it was a milestone in the utilization of nuclear energy on an industrial scale. The reactor started operating in 1956. It used graphite as moderator and CO_2 as coolant. The coolant outlet temperature was about 335 $°C$. The advanced gas-cooled reactor (AGR) adopted magnox alloy to clad the fuel rods. It can enhance the temperature of the steam to 538 $°C$. The gas outlet temperature of the AGR is limited, since the Boudouard reaction occurs at high temperature regimes causing corrosion of the graphite. AGRs were basically operated in France and England, the first starting in 1957 in Chimon, France.

The research of high-temperature, gas-cooled reactors started in the 1950s, representing a significant improvement compared to the AGRs. It uses helium as a coolant which is an inert gas and has better cooling performance than carbon dioxide. The fuel is coated by ceramics which can withstand very high temperatures. Thus, the outlet temperature of the coolant can be very high. The first HTGR demonstration test reactor "Dragon" was initiated in 1959 as an international project by the OECD countries and

was built in England. The reactor was designed for a power of 20 MW. First criticality was achieved in 1964 and the reactor operated at full power from 1966 [11]. The reactor used a prismatic core with an equivalent diameter of 1.08 m composed of 37 fuel element clusters. Each hexagonal fuel block consists of seven fuel rods. The inlet and outlet temperature of the helium were 350 $°C$ and 750 $°C$ respectively. It was the prototype of HTGRs and proved the concept of HTGRs. The researchers collected lots of information about the fuel performance of coated particles, the reactor materials and the system operation from the Dragon reactor.

Later, another two HTGR test reactors with different fuel element designs were constructed, which were the Peach Bottom 1 in the U.S. and the AVR in Germany. The Peach Bottom was a commercial power reactor with an electrical power of 40 MW. It achieved the first criticality in March 1966. Its fuel block also had a hexagonal shape, but the fuel rod and the coolant hole were distributed differently compared to the fuel design of Dragon. The BISO coated particles were embedded in the graphite matrix of the fuel rod. The reactor ran successfully with the ceramic coated particles, which proved that the coating layers are able to retain the fission products.

The AVR (Arbeitsgemeinschaft Versuchsreaktor) used an alternative concept of fuel element proposed by Schulten [12]. The BISO, later TRISO coated particles were embedded in the inner zone with the diameter of 5 cm of the graphite sphere with the diameter of 6 cm. The reactor core was composed of 100,000 spherical fuel elements, which were shuffled during operation and withdrawn once the final burnup was achieved. The electrical power and thermal power of the reactor were 15 MW and 46 MW. The first criticality was achieved in August 1966, and the reactor operation was terminated in 1989. The designed helium outlet temperature was 850 $°C$ which was raised to 950 $°C$ in 1974. Several kinds of fuel compositions such as U/Th, UC_2/UO_2 with BISO or TRISO coated particles were investigated in the reactor. Many experiments were conducted in the AVR, including the simulation of a LOFC accident scenario, which demonstrated the inherent safety characteristics of this reactor.

In Germany and the U.S., planning and designing of larger-size, follow-on HTGRs were starting eventually leading to the construction of commercial-scale prototype HTGRs, which were "Thorium Hochtemperatur Reaktor" (THTR-300) and "Fort St.Vrain Reactor" (FSVR). The THTR inherited the same fuel design feature of AVR using the pebble bed core and was fueled with a mixture of thorium and high-enriched uranium. The electrical power of the THTR was 300 MW. The power plant started to generate electricity in September 1985, and was permanently shut down in 1989 due to political and economical reasons. The FSVR used the same hexagonal fuel and reflector graphite block like Peach Bottom 1. The primary circuit was contained in an innovative prestressed concrete RPV similar to the THTR. Its electrical power was 330 MW. It was built by General Atomics and operated from 1977 until 1989.

Japan began the HTGR program in 1970s. Its High-Temperature Engineering Test Reactor (HTTR) achieved first criticality in 1998 and reached full thermal power of 30 MW in 1999 [13]. The prismatic core of the HTTR is composed of 150 fuel element blocks where the fuel rod and coolant gas are located in the same channel, which is different from the U.S. fuel block design. The HTTR achieves high gas outlet temperatures of upto 950 $°C$. It is the only operating HTGR with hexagonal fuel blocks today.

As a consequence of the operation experiences of HTGR test reactors, which were basically positive, and of the large, commercial HTGRs, which were comparatively poor, the modular HTGR concept has been proposed by Siemens/Interatom in the beginning

of the 1980s [14]. The basic feature of the modular HTGR was that, due to its slim core geometry, the residual heat can be transferred out of the reactor passively and with the maximum fuel temperature during serious accidents remaining below the limits that may impair the fuel. The simplified design of the system can reduce the construction investment. Its electrical power was between 100 MW and 300 MW. A larger power demand can be realized by building several modules on the same site. Various conceptional designs for a modular HTGR have been or are being developed in different countries. Away the most elaborated designs are the HTR-module by Siemens/Interatom, the Modular High-Temperature Gas-cooled Reactor (MHTGR) by General Atomics, the Pebble Bed Modular Reactor (PBMR) in South Africa, and the Gas Turbine High Temperature Reactor (GTHTR-300) by JAEA in Japan, while the HTR-Module and the PBMR have a pebble bed core, the MHTGR and the GTHTR-300 are equipped with a hexagonal fuel block core. They represent two different developing directions of HTGRs.

1.2 The Design Data of the PBMR, GT-MHR and HTTR

There are three kinds of HTGR designs that can be distinguished by their different fuel element concepts [15]. They are represented by the PBMR with spherical fuel elements, the GT-MHR with separated fuel and coolant channels and the HTTR with coaxial fuel and coolant channels. In this thesis, the extended model of MGT-3D is validated/verified against the benchmark data of these three designs. The basic features and design data are introduced in this section.

The Pebble Bed Modular Reactor

The Pebble Bed Modular Reactor (PBMR) has been developed by PBMR Ltd, South Africa [16]. The designed thermal power is 400 MW. The reactor uses the Brayton power conversion cycle and is expected to achieve an efficiency of more than 41%. The main design data are presented in Table 1.1. The spherical fuel elements according to the German reference design for the HTR-Module are located in the annular core between a fixed central reflector and the side reflector. The annular concept allows an increase of the reactor power, while still temperature peak in the center of the core. The reactor is fueled with low enrichment UO_2 located in the kernels of the coated particles. The reactor core contains about 452,000 fuel pebbles of which each one is fueled with about 9 g uranium. The reactor uses the on-line refueling and the fuel pebbles pass several times through the reactor core before discharged. The multi-pass fueling scheme can flatten the burnup profile.

The inner and outer radius of the annular core are 1 m and 1.85 m, respectively. The effective cylindrical core height is 11 m, and the thickness of the side reflector is about 0.9 m. 24 control rods are located in the side reflector to control the reactivity of the reactor and to guarantee the hot shutdown of the reactor. There are eight reserved shutdown holes for the falling of small absorber spheres in the central reflector which is used for cold shutdown. During the normal operation of the reactor, the absorber spheres fabricated from B_4C and graphite are placed in the storage tank of the top reflector. The valves of the tank will be opened, and the absorber spheres will fall into the reserved shutdown holes by gravity if the cold shutdown is triggered.

The coolant flow is blown into the inlet and distributed to the gas riser tubes which are arranged in the side reflector. The rising coolant meets in the top cavity of the reactor

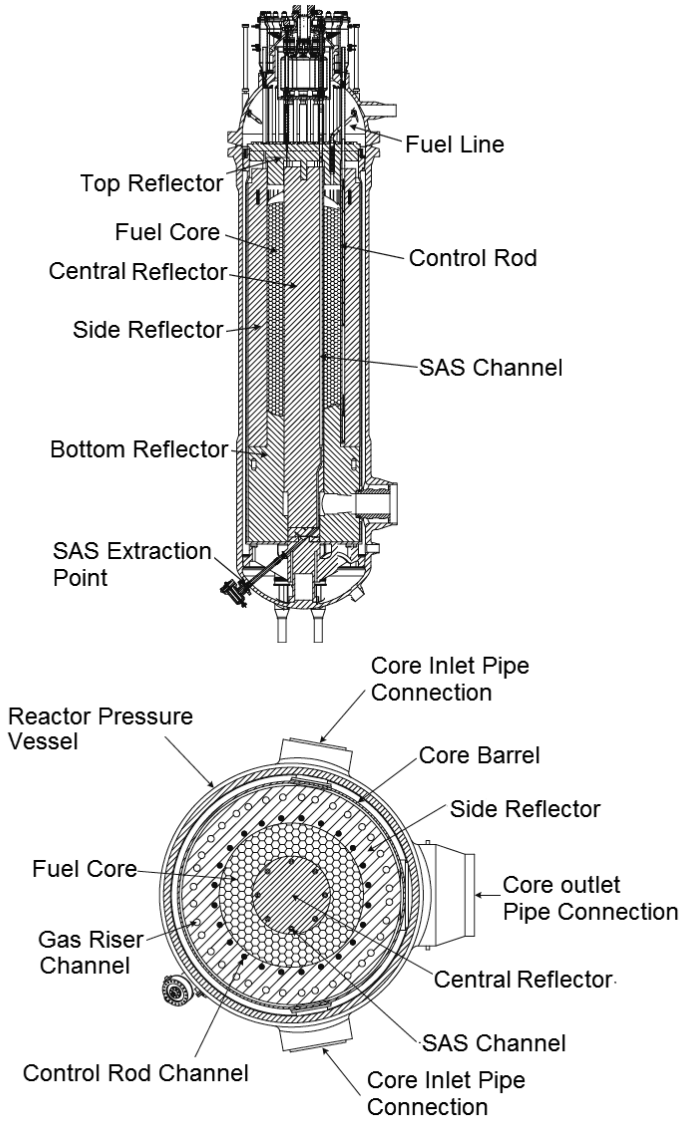

Figure 1.1: Schematic of the PBMR reactor [17]

Thermal power	400 MW
Electrical power	165 MW
Efficiency	>41%
Helium inlet temperature	500 $°C$
Helium outlet temperature	900 $°C$
Helium mass flow rate	192 kg/s
Pressure	9 MPa
Average power density	4.6 MW/m^3
Fuel element	Pebbles

Table 1.1: The main design data of PBMR [16]

pressure vessel (RPV). Then it passes through the reactor core from top to bottom, which can counter the rising movement of graphite pebble due to the blowing effect of the coolant flow. The heated helium flows from the outlet of the RPV to the power turbine, which drives the generator and the low and high pressure compressors. Finally, the helium is cooled and compressed before re-entering the reactor.

The RPV is cooled by the Reactor Cavity Cooling System (RCCS) during normal operation and accident scenarios. The RCCS is designed to maintain the RPV and concrete temperature. The heat is transferred from the surface of RPV to the water cooling pipes by conduction, thermal radiation and natural convection. Both active and passive system design models are applied. The RCCS can work for several days including the boil off time before water makeup is needed. Hence, it is important for protecting the investment. If the RCCS fails, the concrete provides an ultimate heat sink.

The Gas Turbine-Modular Helium Reactor

The Gas Turbine-Modular Helium Reactor (GT-MHR) has been developed from the MHTGR by using the gas turbine design, aiming to achieve higher efficiencies up to 50% [18]. The GT-MHR includes the reactor system and the power conversion system (PCS). They are located in separate steel vessels connected by a cross duct. The design data of the reactor operating at full power is presented in Table 1.2. These parameters were chosen to minimize the construction costs as well as the operation costs per power unit. The designed thermal power of the reactor is 600 MW and the power conversion efficiency can reach 48%.

Thermal power	600 MW
Electrical power	286 MW
Efficiency	48%-50%
Helium inlet temperature	490 $°C$
Helium outlet temperature	850 $°C$
Helium mass flow rate	320 kg/s
Pressure	6.9 MPa
Average power density	6.6 MW/m^3
Average burnup	642 MWd/kg
Fuel element	Hexagonal fuel block

Table 1.2: The main design data of GT-MHR [15]

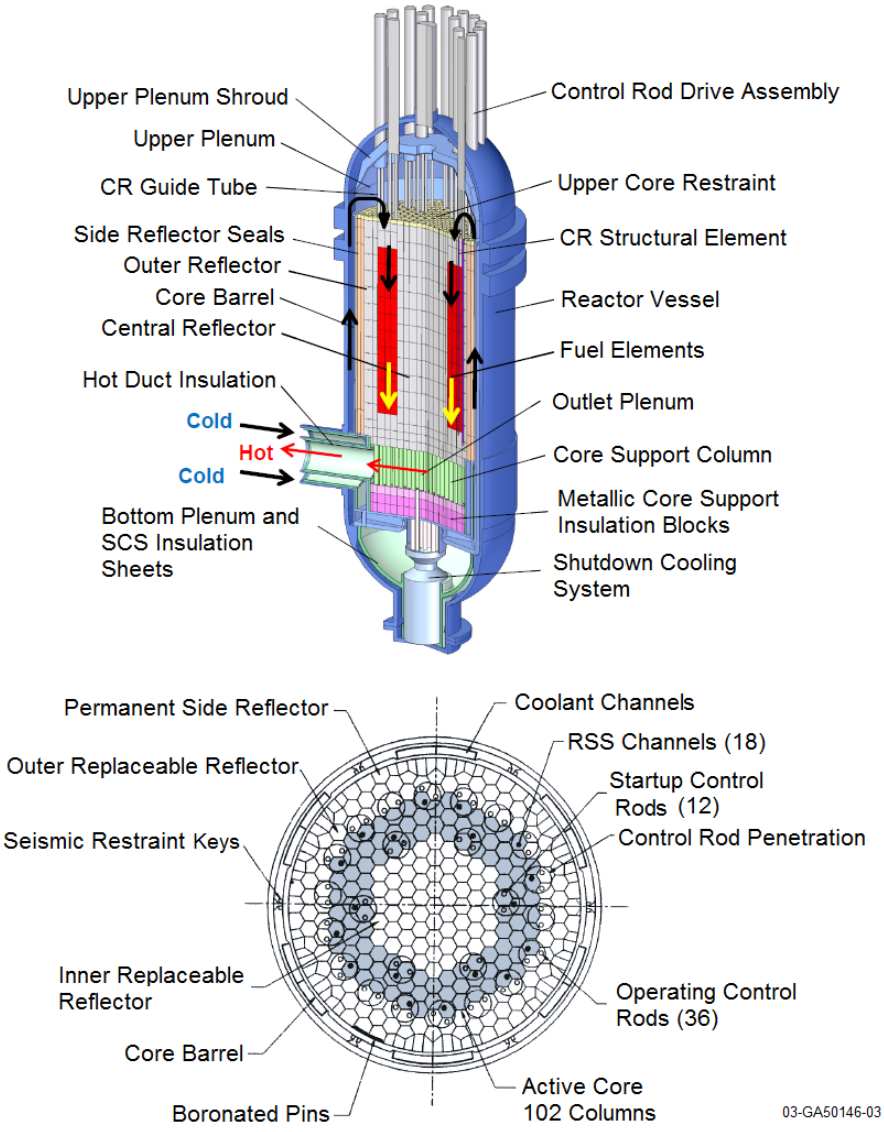

Figure 1.2: Schematic of the GT-MHR reactor [19]

In the GT-MHR, the hexagonal fuel blocks are assembled in the core in a annular ring. Graphite blocks are placed in the center of the reactor core as inner reflector. There are 102 fuel columns and 10 layers. 48 control rod guide holes and 18 reserved shutdown holes are located in the inner and outer circles close to the fuel assembly circle. Two types of fuel blocks are loaded, one with 108 coolant holes, 202 fuel rods, and 14 burnable poison sticks, and another with 89 coolant holes, 164 fuel rods and 10 burnable poison sticks. At the top and bottom of the fuel columns, there are graphite reflector blocks as well. The reactor core is refueled after 280 days. The power profile is flattened by the annular core and the re-arrangement of the fuel blocks during the refueling process. The reactor internals consisting of inner reflector, fuel blocks, outer reflector, permanent side reflector and core support structure are placed in the steel RPV.

The power conversion system is used to convert the thermal energy into electrical energy by the Brayton cycle, just like in the PBMR. The turbo-compressor, recuperator, precooler, intercooler and associated supports and ducts are integrated in a single vessel placed side-by-side with the RPV. The turbine is joined rigidly to a synchronous generator by a bearing. The high pressure, hot helium from the outlet of the primary circuit flows into the power conversion system and drives the turbine to generate electricity. Then the cooled, compressed helium flows into the primary circuit from the cold duct.

Two auxiliary cooling systems including the reactor shutdown cooling system (SCS) and RCCS are installed with different functions. The SCS is composed of a helium loop located at a bottom part of the RPV and driven by forced circulation, and a cooling water loop that exchanges heat with the helium loop in a helium/water heat exchanger. It cools down the RPV and PCS in fuel reloading or repair operations. The RCCS consists of two independent water cooling systems which include the surface cooler, pipelines, and water circulates. Each of the RCCS has a heat removal capacity of 4 MW. It ensures that the maximum fuel temperatures, RPV surface temperatures and concrete temperatures remain below 1600 $^{\circ}C$, 540 $^{\circ}C$ and 150 $^{\circ}C$, respectively, under normal operation as well as in accident scenarios.

The High Temperature Engineering Test Reactor

The High Temperature Engineering Test Reactor (HTTR) project was initiated in 1987 according to the Long-term Program for Development and Utilization of Nuclear Energy issued by the Japan Atomic Energy Commission [20]. The reactor's construction began in 1991. The designed thermal power is 30 MW and the maximum outlet gas temperature can reach 950 $^{\circ}C$ (see Table. 1.3) which can be used at a later stage to conduct the research on process heat utilization with HTGR.

Thermal power	30 MW
Helium inlet temperature	395 $^{\circ}C$
Helium outlet temperature	850/950 $^{\circ}C$
Helium mass flow rate	12.4/10.2 kg/s
Pressure	4 MPa
Average power density	2.5 MW/m^3
Fuel element	Hexagonal fuel block (31 pins and 33 pins)
Fuel	Low enriched UO_2 $(3-10\%)$

Table 1.3: The main design data of HTTR [15]

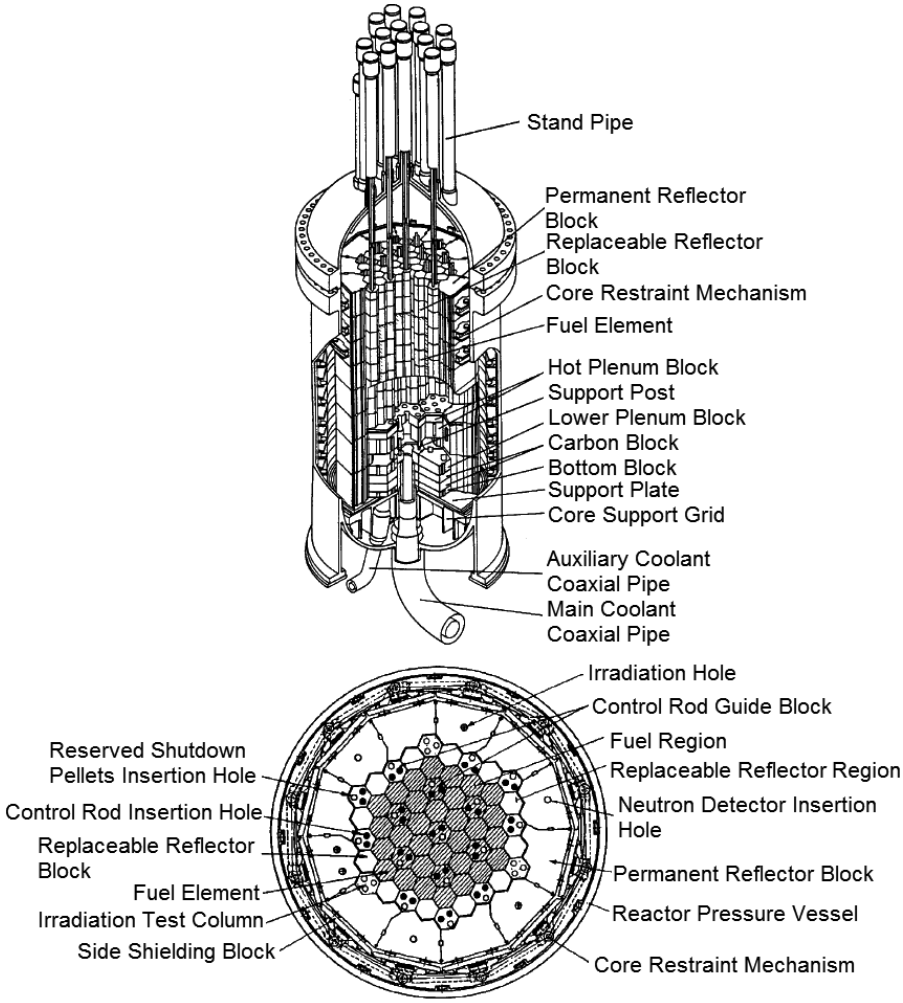

Figure 1.3: Schematic of the HTTR reactor [21]

The HTTR utilizes the pin-in-block type hexagonal fuel element. There are two types of fuel blocks, one with 33 fuel pins and another with 31 fuel pins. The coolant flows through the annular space between the fuel rod and the graphite block. The TRISO coated particles embedded in the graphite matrix of the fuel rod are fueled with low enriched uranium dioxide. The fuel blocks and the control rod guide blocks are mixed-distributed in the reactor core. Each control rod guide block has two control rod guide holes and one reserved shutdown hole. The steel RPV contains the reactor core, the replaceable reflector blocks, the permanent reflector, the restrain device and the support structure.

The reactor cooling system consists of a main cooling system (MCS), an auxiliary cooling system (ACS) and two independent vessel cooling systems (VCS). During normal operation, the reactor core is cooled by the MCS: the helium enters the reactor and rises up from the empty space of the side restrain system; then it flows through the reactor core from top to bottom and exits at the outlet. The ACS is activated automatically in response to the reactor scram signal. The residual heat of the reactor core is removed by the cooling circuit of the ACS and released into the environment. The VCS protects the reactor core and RPV against thermal damage by the residual heat after the scram. It can remove the residual heat upto a the power of 0.6 MW.

1.3 The Outline of this Thesis

While designing nuclear power reactors, the pressurized loss of forced coolant (LOFC) and de-pressurized loss of forced coolant (DLOFC) are two of the severe accident scenarios that engineers should evaluate. The deterministic simulation of the reactor under these accident conditions requires coupled neutronics and fluid mechanics calculations. MGT-3D is a three-dimensional, time dependent simulation code for pebble bed HTGR. In this thesis, the code is benchmarked, optimized and modified for block type HTGRs and applied to simulate the LOFC and DLOFC scenarios for prismatic block HTGRs. The structure is as follows:

- The calculation theory of MGT-3D will be introduced. The calculation of MGT-3D includes the neutron flux solution, the power production, gas flow calculation as well as gas and solid temperature calculation. MGT-3D is also an important part of the developing HTR code package (HCP) to study the dynamical behavior of HTR [22]. The neutron flux is calculated by solving a neutron diffusion equation which is driven by the transport equation. The powers generated by fission and decay are distinguished by local and non-local nuclear heat according to their deposited place. By solving the mass, momentum and energy conservation equations, the gas flow, and gas and solid temperatures are calculated, and coupled together. The heat source of fluid mechanics calculation is provided by the nuclear heat production. The cross sections, which are used to calculate the power production, are determined by the moderator and fuel temperatures. The numerical method and the coupling approach are explained in Chapter 2.
- There are major differences between the MGT-2D and MGT-3D codes, especially with regard to the fluid mechanics calculation. In order to validate and verify the new code model, SANA experiments are chosen to benchmark MGT-3D. SANA experiments with only a central heating element for the steady state and transient case are simulated with both MGT-3D and MGT-2D, and compared with the measured data. Then, MGT-3D is applied to SANA experiments with a central

heating element and radial heating elements, which represents a true 3D geometry and can not be calculated by MGT-2D.

- The fuel temperature has a strong influence on the resonance absorption cross sections. A simplified overheating model was chosen in MGT-3D to calculate the temperature increase in the surrounding graphite matrix [24]. The coated particle is considered as an independent point heat source with specific heat and is shielded by a heat resistant layer. The effective heat flux resistance of coated particles is hard to determine. In order to obtain a precise fuel temperature, a new kernel model has been developed to derive the temperature profile inside the coated particle. In the new kernel model, the heat conduction equation of the coated particle is solved numerically in both steady state and transient calculations.

- Due to the reason that R&D activities in German mainly focused on pebble bed reactors, MGT-3D was developed to simulate pebble bed HTGRs and their related experiments. As a part of this thesis, this code has been extended to prismatic HTGR with block type fuel elements. The extension implemented into MGT-3D includes two desirable aspects. The first refers to the unit cell which represents the structure of hexagonal fuel block and which is obtained by analyzing the fuel and coolant geometry. The heat is transferred from the fuel rod to the coolant by conduction in the fuel rod and graphite moderator, thermal radiation across the gap, and convection in the solid-gas boundary. The temperature profile of the unit cell is determined in detail and coupled with the temperature calculation of the homogeneous meshes. The 2D model to conduct the heterogeneous fuel temperature for block type reactors including GT-MHR and HTTR is developed and verified with CFX simulation. In the mean time, a method with 1D approximation of the unit cell calculation is introduced as well. The second aspect refers to the effective thermal conductivity of the homogeneous meshes, which is derived by applying an analytical method. Due to the anisotropic structure of the fuel blocks and replaceable reflector blocks, the effective thermal conductivities in axial and transverse directions are calculated by different equations.

- The extended MGT-3D is applied to simulate the NACOK-II experiment, the LOFC and DLOFC accident scenarios of the GT-MHR, and the LOFC accident scenario of the HTTR. The NACOK-II facility has a cuboidal shape. The pseudo X/Y/Z model by choosing a large initial radius coordinate has been established to simulate the ceramic heating experiment of NACOK-II. The homogeneous thermal conductivity of the ceramic block is calculated by the equation developed in Chapter 3. A new approach is proposed to calculate the long range thermal radiation transfer as well. Finally, the calculation results of fluid mechanics with MGT-3D on the block type structure are compared with the measured data. In the second part of Chapter 4, the LOFC and DLOFC accident scenarios of GT-MHR are simulated as well. It is a fluid mechanics simulation with given heat source. The fuel blocks are placed in a hexagonal annular ring. It is equivalent to a circular annular ring in the 2D simulation model. The transient calculation starts from the steady state and the accidents are simulated for 100 hours. The simulation result of MGT-3D is compared with the calculation result from the code GTAS. Parameter variations including decay heat, thermal radiation, and thermal conductivity are studied.

- For the last part of the thesis, the three runs of LOFC/HTTR experiments are simulated with the extended MGT-3D. The reactor is calculated from the first loading to the recent status of the core with the burnup of 373 equivalent full

power days, which is done with the Monte Carlo code Serpent. A new interface code between Serpent and MGT-3D is developed, which provides MGT-3D with the nuclide inventories and the operation history. All the accident simulations start from the steady state of the reactor. In the Run 1 experiment, the reactor is operated at 9 MW which LOFC is initiated in, and the RCCS is activated during the experiment. The calculation results of steady state, short-term transient, and long-term transient are presented. The reactor fission power, especially the reactor peak power and the elapsed time at the occurrence of re-criticality, is compared with the measured data, which is the main task of the project. Furthermore, variations of different parameters are studied, which include the decay heat, thermal conductivity, flow resistance, boundary temperature, and pressure of the primary circuit. In the predictive calculation of Run 2 experiment, the LOFC transient starts from the initial thermal power of 30 MW. The MGT-3D simulation supplies the possible peak power and elapsed time of the reactor re-criticality and their ranges. In the predictive calculation of Run 3 experiment, the re-criticality is forecasted by changing the boundary temperature of the RPV.

Chapter 2

Simulation Tools and Methods

In this chapter, the basic features of MGT-3D, which is a static and dynamic HTR simulation tool, are introduced. The reactor simulation has two main parts-neutronics and fluid mechanics, which include neutron flux calculation, nuclear power production, heat transfer between solid and gas, fuel temperature calculation, gas mixing, and corrosion. MGT-3D couples these two parts internally, which means that the neutronic and fluid mechanics are iterated. The algorithm which solves the multi-connected system in MGT-3D is presented.

In the second part, the SANA experiment is applied to validate the fluid mechanics part of MGT-3D. The SANA experiment had 2-dimension sets with only a central heating element and 3-dimension sets with both center and side heating elements. The 2D SANA experiment can be simulated very well with the 2D version of MGT (MGT-2D). But the 3D experiment set can only be simulated properly with the recent code MGT-3D. In order to investigate whether MGT-3D shows the same result with MGT-2D, MGT-3D simulation result is compared with MGT-2D simulation result on the 2D SANA experiment. Then a full 3D model of SANA experiment which has side heating elements is developed to validate MGT-3D against both steady state and transient cases.

2.1 The Reactor Dynamics Code MGT-3D

2.1.1 Calculation Scheme

While AVR was being constructed, the code systems which include VSOP, and TINTE that simulate the safety aspects of pebble bed reactor were developed as well. These codes played an important role in researching and licensing pebble bed HTR until today. MGT-3D was developed from TINTE, and validated by many experiments, e.g. SANA, NACOK, AVR. All these applications show that MGT-3D is a very good tool to simulate pebble bed HTR and related experiments.

Most reactor simulation methods have a specific function: some execute nuclear calculations and some execute fluid mechanics calculations. If the simulation uses the method to calculate a reactor with both nuclear and fluid mechanics and the data is exchanged between the codes, it is an externally coupled simulation. In MGT-3D, the partial problems of a reactor calculation, which include nuclear, fluid mechanics and chemistry calculation, are solved separately, but are explicitly coupled. These partial problems are also iterated during the calculation. Compared to fluid mechanics calculations, nuclear calculations need shorter time periods. Therefore, several nuclear time intervals are

used in one temperature/chemistry calculation. The calculation flow is showed in Figure 2.1.

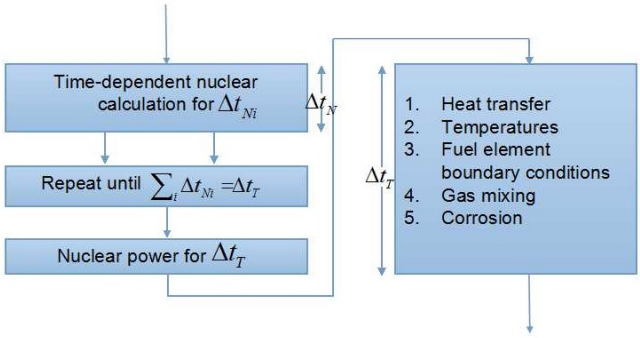

Figure 2.1: Calculation structure of MGT-3D [2]

MGT-3D can conduct both equilibrium and transient calculations. These calculations include neutron flux, nuclear power production, solid temperature, gas temperature, gas mixing and corrosion.

2.1.2 Calculation Modules

Diffusion Code for Neutron Flux Calculation

As the primary important knowledge in modeling the operation of the nuclear reactor, the neutron flux is calculated with a diffusion approximation which is derived from the neutron transport equation in MGT-3D [25]. The theory is introduced in Appendix A. The neutron energy is divided into multi-groups with the number of G. And for the g-th group, the integral equation over the g-th group is as follows:

$$\frac{\partial}{\partial t}\int_{E_g}^{E_{g-1}} \frac{1}{\nu}\phi(\boldsymbol{r},E,t)dE - \nabla\cdot\int_{E_g}^{E_{g-1}}[D(\boldsymbol{r},E,t)\nabla\phi(\boldsymbol{r},E,t)]dE + \int_{E_g}^{E_{g-1}}\Sigma_t(\boldsymbol{r},E,t)\phi(\boldsymbol{r},E,t)dE$$
$$= \int_{E_g}^{E_{g-1}}[\sum_{g'=1}^{G}\int_{E_{g'}}^{E_{g'-1}}\Sigma_S(\boldsymbol{r},E'\to E,t)\phi(\boldsymbol{r},E',t)dE']dE + \int_{E_g}^{E_{g-1}} S(\boldsymbol{r},E,t)dE \tag{2.1}$$

The neutron source term $S(\boldsymbol{r},E,t)$ includes the fission neutron source and all other neutron sources such as $(n,2n),(3,3n),(\gamma,n)$ reactions and the external neutron source. The leakage iterative method is applied to solve the three-dimensional neutron diffusion equations in MGT-3D [24, 26].

Nuclear Power Production

The total heat production in the reactor can be divided into two main components, which are prompt heat E_p and decay heat E_d [24].

$$E_f = E_p + E_d \tag{2.2}$$

If the different contributions are considered in details, these two components can be specified as:

$$E_p = E_r + E_n + E_{\gamma p} \tag{2.3}$$

$$E_d = E_{\gamma d} + E_\beta \tag{2.4}$$

These contributions are:

E_r	rebound energy of the fission fragments after fission
E_n	kinetic energy of the prompt neutrons produced by fission
$E_{\gamma p}$	prompt γ energy
$E_{\gamma d}$	delayed γ energy
E_β	β decay energy

The prompt power density in the reactor is the product of the fission rate and prompt energy of each fission:

$$\dot{Q}_p''' = \sum_{i=1}^{G} \Sigma_f^i \phi_i E_p \tag{2.5}$$

The decay heat is calculated following the DIN 25485 standard [27], which is applicable to all kinds of thermal reactors, both HTR and LWR. The calculation of decay heat is based on the power histogram of the fuel elements. The operational history is divided into a series of time intervals T_j. The contributions from all the past time intervals to the current time are accumulated to calculate the decay heat. Figure 2.2 shows the basic concept of this method. With this method, the decay heat calculation is specified as the contributions of fission products, fertile materials, minor actinides, and heavy metals. In each time interval, the average number of total fissions and details of fission types are input data and should be supplied by some other burn-up codes, e.g. VSOP or Serpent. For the time offset t_k,

$$t_k = \sum_{j=k+1}^{m} T_j$$

the decay heat can be written as:

$$\dot{Q}_d = \sum_{l=1}^{30} \alpha_l' \sum_{k=1}^{m} F_k (1 - e^{-\lambda_l T_k}) e^{-\lambda_l t_k} \tag{2.6}$$

where l denotes the 24 decay groups of fission products and 6 additional contributions from the actinides ^{239}U, ^{239}Np, ^{233}Th and ^{233}Pa. F_k are the fission rates in time interval T_k, and α_l' are values chosen to fit the DIN standard.

Consider different branches of decay heat:

$$\dot{Q}_{d,l} = \alpha_l' \sum_{k=1}^{m} F_k (1 - e^{-\lambda_l T_k}) e^{-\lambda_l t_k}$$

If the decay heat production at the end of the given life histogram is extended by a time interval Δ and a constant power is assumed during this time interval, it will obtain:

$$\dot{Q}_{d,l}(t_0 + \Delta) = \dot{Q}_{d,l}(t_0) e^{-\lambda_l \Delta} + \alpha_l' F (1 - e^{-\lambda_l \Delta}) \tag{2.7}$$

This equation is the solution to the following differential time-dependent decay heat

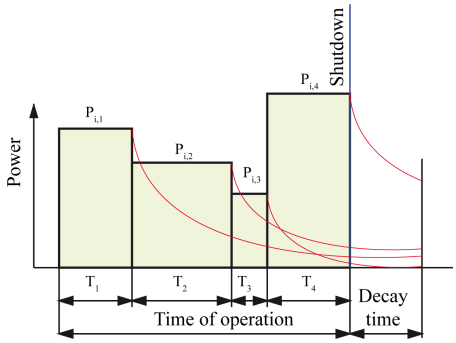

Figure 2.2: Power histogram and decay power [28]

production equation:

$$\frac{d\dot{Q}_{d,l}}{dt} = \alpha_l' \lambda_l F - \lambda_l \dot{Q}_{d,l} \tag{2.8}$$

For the steady state calculation of a reactor, decay heat should be constant ($T \to \infty$). The total fission heat is:

$$E_f = E_p + (\frac{\dot{Q}_d}{F})_{T\to\infty, t\to 0} = \frac{\dot{Q}_d}{F} \tag{2.9}$$

In this case, the decay heat is included into the effective energy per fission.

The fission events release energy in different forms: kinetic energy of the fission fragments, β-radiation, high energy neutrons, and γ-radiation. Kinetic energy of fission fragments, which is the largest fraction of the fission energy, deposits at the site where the fission happens by collision with surrounding atoms. β-radiations, which are high energy electrons, can be shielded by several millimeters of metal. The scale of HTR's fuel kernels is in millimeters as well, so energy of β-radiation can also be assumed to deposit in the local place. High energy neutrons and γ-radiation do not have charge. They can travel a long distance in the reactor core. Their energy deposits in both the fuel zone and the moderator zone. Therefore, the heat source can be divided into two parts due to the site of energy deposition:

- Local heat source, which is from fission fragments kinetic energy and β-radiation, can be defined as:
$$\dot{Q}_l = \chi_p \dot{Q}_p + \chi_d (\dot{Q}_d - \dot{Q}_B)$$
χ_P and χ_d are the ratios of local to total heat production for the prompt and decay heat respectively. $\dot{Q}_B$ is the breeding term of decay heat, which is considered as non-local.
- Non-local heat source, which includes neutron scattering interaction during moderation, neutron-γ reaction, and γ reaction.

Fluid Mechanics Calculation

Fluid mechanics calculations of reactors are governed by three conservation laws, namely conservation of mass, momentum, and energy. For the gas phase, the conservation equations are:

- Mass conservation equation:

$$\frac{\partial \rho_g}{\partial t} + \rho_g \nabla \boldsymbol{u} = S \tag{2.10}$$

Where, ρ_g is gas density, $\boldsymbol{u}$ is velocity, S is the gas source term that exists typically in the coolant inlet/outlet of the reactor.

- Momentum conservation equation:

$$\frac{\partial \rho_g \boldsymbol{u}}{\partial t} + \nabla \cdot \rho_g \boldsymbol{u}\boldsymbol{u} - \nabla \cdot \bar{\bar{\tau}} = -\nabla P + \rho_g \boldsymbol{g} \tag{2.11}$$

Where, $\boldsymbol{u}\boldsymbol{u}$ is the dyadic product of two vectors, $\bar{\bar{\tau}}$ is the viscous stress tensor, P is the pressure, $\boldsymbol{g}$ is the gravitational acceleration vector.

- Energy conservation equation:

$$\rho c_p \frac{\partial T_g}{\partial t} + \rho_g c_p \nabla \cdot (\boldsymbol{u} T_g) = \nabla \cdot (k \nabla T_g) + q_g''' \tag{2.12}$$

Where, T_g is the gas temperature, c_p is the heat capacity at constant pressure, q_g''' is the heat source. The heat source can be the heat transferred from the solid to the gas by convection and external heat injecting by means of a mass source/sink:

$$q_g''' = hA \cdot (T_s - T_g) + c_p \dot{m} T_g' \tag{2.13}$$

T_s is the solid temperature, h is the heat transfer coefficient, A is the contact area with solid, $\dot{m}$ is the mass flow rate and T_g' is the inlet/outlet gas temperature.

For the solid phase, there are neither mass transfer nor momentum transfer. The heat transfer equation in solid is:

$$\rho_s c_p \frac{\partial T_s}{\partial t} = \nabla \cdot (k \nabla T_s) + q_s''' \tag{2.14}$$

Where k is thermal conductivity, q_s''' is the heat source including the nuclear heat source q_n''', external heat source q_e''' and heat exchanging with gas:

$$q_s''' = q_n''' + q_e''' + h \cdot A \cdot (T_g - T_s) \tag{2.15}$$

In MGT-3D, the fluid mechanics calculations contains two parts, namely homogeneous calculation and heterogeneous calculation. The homogeneous calculation is based on the homogeneous meshes including solid meshes and the meshes with porous media. It can be divided into the steps including gas flow calculation, heat transfer, gas and solid temperature calculation, gas mixing, and corrosion. The gas flow calculation involves the simultaneous solution of mass and momentum conservation of the coolant gas in order to determine the pressure and mass flow rate at all of the meshes with porous media. Two regimes of heat transfer that are considered in the homogeneous calculation are: heat transfer of solid material through the homogeneous meshes and gas heat transfer. They are coupled with the heat transfer of heterogeneous calculation. The conservation of energy is solved to obtain the gas and solid temperature, and the control volume discretization and leakage iteration methods are used to solve Equation 2.14.

The heterogeneous calculation includes the temperature calculation of the representative unit of each of the homogeneous meshes and the temperature rising in the coated particles. The homogeneous calculation experiences the surface temperature of the fuel

element. The average moderator temperature of the fuel element and the temperature of the fuel kernel coated by ceramic materials are important to the nuclear reaction. Therefore it is necessary to calculate the temperature distribution within the fuel elements. Due to its solid construction of fuel element, there is only heat conduction in the fuel element. If the gap is considered in the coated particles, the heat is also transferred by thermal radiation across the gap. The governing equation is similar to Equation 2.14.

2.2 3D Simulation of the SANA Experiment

2.2.1 Experimental Setup

According to the criteria of designing a safe HTGR, it should be guaranteed that there is only a moderate release of fission products in the design-basic-accident. The safety feature of pebble bed HTGR ensures that the reactor can be shut down by negative temperature feedback, but it still must be proven that the residual heat can be removed after the accident. In the depressurized loss of forced coolant accident, which is the extreme accident of HTGR, the primary circuit pressure of reactor decrease to atmospheric pressure and forced coolant are stopped. In this kind of situation, the residual heat is partly restored in graphite and partly removed in the mechanisms of conduction, radiation, and natural convection. There is large amount of graphite, which is chosen as the moderator and reflector in the reactor, and graphite has high specific heat and heat conductivity. Therefore, the temperature of the reactor core does not increase very quickly and heat can transfer out from the core quickly. Tightness limitation of coating particle maintains that the temperature of the reactor core should not exceed 1600 $^{\circ}C$ [29], or else coating layers lose their function to maintain the fission products, which then may be released.

In order to prove that the maximum temperature is not beyond the confines of 1600 $^{\circ}C$, a series of SANA experiments are conducted to research the heat transfer in the pebble bed in both steady state and transient cases [30]. The experiments are also used to correct the Zehner-Schlünder model which is developed to calculate the effective conductivity of pebble bed [31], to study the predicted natural convection phenomena in the pebble bed, and to validate the fluid mechanics codes (THERMIX, TINTE, MGT-3D). The schematic plan of the SANA experiment is shown in Figure 2.3. The pebble bed is heated at atmospheric pressure without forced flow to simulate the DLOFC accident. The pebble bed with diameter of 1.5 m and height of 1 m has the same sphere packing as the core of pebble bed HTR. There are approximately 9500 graphite pebbles used in the experiment. To make sure that most of the heat is transferred out in the radial direction and to flatten temperature distribution in the axial direction, thermal insulation materials are constructed to model an adiabatic boundary on the top and bottom of pebble bed. Therefore, the pebble bed of the experiment can represent part of the reactor core. All of them are contained in a cylinder steel vessel. Including these insulation layers and supporting structures, the total height of the facility is about 3.2 m. There are four electrical resistance heating elements to provide the heating power. One is installed in the center of the cylinder container and the other three are symmetrically installed in the distance between the center and the boundary. The total installed power of the experiment is 50 kW, the maximum power of central heating element is about 35 kW, and the maximum of each radial heating element is 10 kW. The volume of the pebble bed is about 1.77 m^3. At full power, the average power density of pebble

bed is 28.2 kW/m^3. Taking HTR-Modul as an example, the power density is limit to 3 MW/m^3 [32]. According to Way-Wigner formula:

$$\frac{P_d}{P_{th}} = 6.22 \cdot 10^{-2} s^{-1} \cdot [t^{-0.2} - (t_0 + t)^{-0.2}] \tag{2.16}$$

the power level of SANA is comparable to the decay heat of 3 hours to 4 hours after reactor shut down. The main data of the experiments of SANA-I is presented in the following table:

Installed electrical power	50 kW
Maximum bed temperature	1600 $°C$
Diameter of pebble bed	1.5 m
Height of pebble bed	1.0 m
Complete height	3.2 m
Diameter of graphite pebble	6 cm

Table 2.1: SANA main data [30]

To avoid corrosion of graphite in high temperature, an inert gas, either helium or nitrogen, is fed into the vessel to remove oxygen before heating. A tiny amount of inert gas is continuously blown into the gaps between the heating rods and their protection tubes to prevent the corrosion of heating elements. The heat produced in the connection electrodes on the top and bottom of the heating rods is removed by an installed water-cooling system, and it is monitored by measuring the inlet and outlet temperature of cooling water. In order to investigate the influence of the boundary conditions on temperature distribution of pebble bed, some of the experiments bring an insulation layer between the pebble bed and the radial vessel wall. Thermal couples are located at the vessel wall, top and bottom insulation layers, protection layers of heating element, and at different positions of pebbles.

2.2.2 SANA Experiment with Central Heating Element

Many simulations of SANA-I experiments, which have only the central heating element, have been done with TINTE [33, 34, 37] and THERMIX/DIREKT [35, 37]. All of these results fit very well with the experiment. The central heating elements, the main parts of which include the heating zone, pebble bed, top isolation, bottom isolation, and radial boundary of the vessel, are cylindrically and symmetrically distributed in these experiments. Even though some cooling equipment on the vessel surface, and the cables of thermal couples are not symmetrically distributed, they are not considered to significantly affect the temperature. The heat taken out by these equipments is neglected, so the two dimension code TINTE can be applied to simulate these experiments.

In recent decades, fluid mechanics calculation was improved significantly, an internal cross section calculation and multi-group neutron flux solver are introduced into TINTE, which developed TINTE into MGT-2D. The latest version of TINTE does not have a difference in fluid mechanics calculation with MGT-2D. Therefore, there are no significant differences on SANA experiment simulation, which only involves the fluid mechanics part of MGT-2D. Afterwards, the code is extended to 3D R/Z/Φ geometry, which is MGT-3D. The starting coordinate of the R-direction is not restricted at 0. If

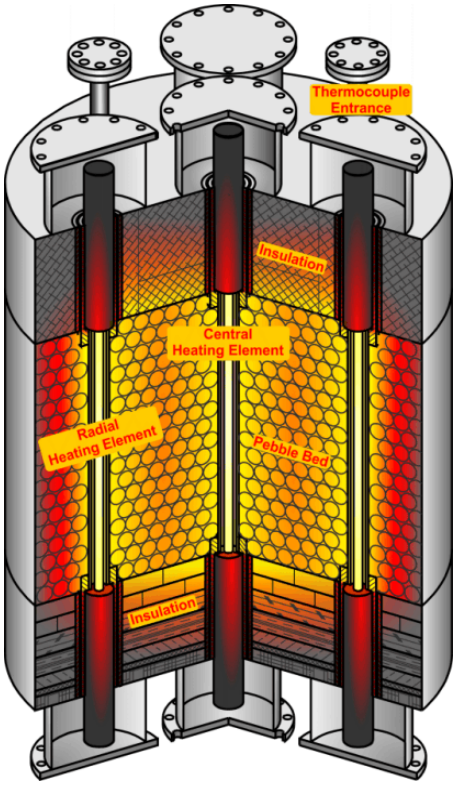

Figure 2.3: Schematic plan of SANA [30]

the R-axis starts at a considerably large value relative to the dimension of calculation zone, a pseudo X/Y/Z geometry can be simulated as well. Fluid mechanics calculation has a significant difference between MGT-2D and MGT-3D. Another dimension of the variables, which are spatial dependence, is added, and both reflective boundary and periodical boundary are introduced in azimuthal direction. In order to prove the reasonability and stability of these new features, a 3D model of SANA experiment with only one central heating element is developed based on the former MGT-2D input file. The experiment with both central and radial heating element, which can not be simulated with MGT-2D, is simulated in detail to benchmark the 3D fluid mechanics of MGT-3D. Because pebbles may penetrate into the isolation in the experiment with radial isolation, which causes uncertainty in determining the thermal conductivity of this layer, the experiments without radial isolation are chosen to validate our code.

Figure 2.4 shows the simulation model of MGT-2D of SANA experiment. Because of the cylindrical symmetry, it shows only the R/Z geometry here. The heating system, which includes the top and bottom connection electrodes, heating element, gaps, and protection tube, are simulated in detail to match the experiment. Some of the experiments use a long heating element to heat the whole pebble bed, and others use a short heating element to heat only the upper or lower part of the pebble bed. The data of experiments with long heating element is used here. The total power deposits in the cables, heating poles, and heating rods. The heat generated in the cables is lost into the environment, and does not contribute to the experiment. The power of the heating rod and connection electrodes are determined by the following equations:

$$P_{rod} + 2 \cdot P_{electrode} = P_{total} - P_{loss} \tag{2.17}$$

$$\frac{P_{rod}}{P_{electrode}} = \frac{R_{rod}}{R_{electrode}} \tag{2.18}$$

where
P_{rod}: power of heating rod
$P_{electrode}$: power of each connection electrode
P_{total} : total electric power
P_{loss}: electric power loss
R_{rod}: electric resistance of heating rod
$R_{electrode}$: electric resistance of one connection electrode
The heat transfers across the gap to the protection tube mainly by radiation, which is simulated by defining a radial radiation material with emissivity constant 0.9. The heat that is removed by cooling water is simulated by setting a fixed temperature on the boundary of the cap of the electrode room. The pebble bed, the main part of the experiment, is regarded as hexagonal close-packed with a filling factor of 0.61. It is simulated with a homogeneous porous media model. The effective thermal conductivity is calculated by Zehner-Schlünder model. Heat exchange between solid phase and gas phase is calculated by Nusselt's Law. The gas flow of the porous media is in all directions, and natural convection is considered in the model. In the transitional zone from the pebble bed to the central protection tube, the radial thickness is specified as 3 cm, which is about half of the pebble diameter, and the filling factor is 0.22. In the contacting zone between the pebble bed and the radial vessel, the radial thickness is also considered to be 3 cm, but with a filling factor of 0.52. The effective thermal conductivities of these two special pebble zones are also determined by Zehner-Schlünder model, but with correction factors. For the surrounding boundary of vessel, different layers with fixed temperature, emission constant, and heat transfer coefficients are introduced in different parts of the vessel, which can simulate the radiation and convection heat transport to

the surrounding environment.

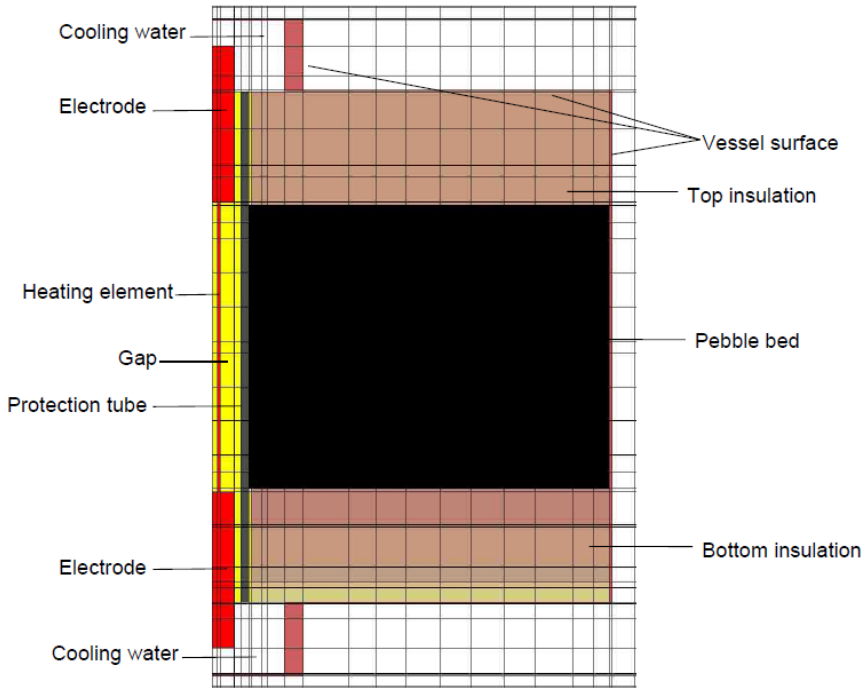

Figure 2.4: Simulation geometry of MGT-2D of SANA experiment

As mentioned above, a series of SANA experiments were performed from 1993 to 1995. In these experiment, the pebble bed is heated for about 40 hours with increasing power in the beginning and constant power subsequently, to get unchanged temperature distribution. Considering the difficulty to get the right heat transfer coefficient of the boundary with radial isolation, only the experiments without radial isolation are taken into account. The main data of these experiments are presented in Table 2.2.

No	P_{total}	P_{rod}	$P_{electrode}$	coolant	pebble type
1	10 kW	8.91 kW	0.62 kW	helium	6 cm, graphite
2	10 kW	8.91 kW	0.62 kW	nitrogen	6 cm, graphite
3	35 kW	32.02 kW	1.94 kW	helium	6 cm, graphite
4	35 kW	32.02 kW	1.94 kW	nitrogen	6 cm, graphite

Table 2.2: Data of simulated experiments [35]

The input of MGT-2D can be run directly by MGT-3D without any changes, which simulates the model with only one azimuthal mesh. In order to test the stability of MGT-3D with multiple angle meshes, the 3D model with 10 equal azimuthal meshes is simulated. Because of the symmetry, only one azimuthal mesh is chosen to display. The simulated solid temperature distributions of experiments 1, 2, 3, and 4 are sequentially

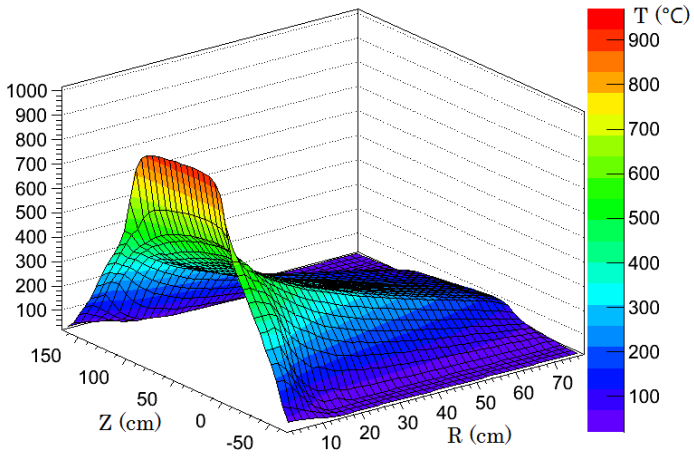

Figure 2.5: Simulated solid temperature distribution with MGT-3D, helium, 10 kW

shown in Figures 2.5, 2.6, 2.7 and 2.8. The maximum temperature appears in the center of the experiment where the heating element is. The maximum temperatures from Experiment 1 to 4 are 969.49 $°C$, 983.82 $°C$, 1560.4 $°C$, 1592.65 $°C$ respectively. This shows that the temperature with nitrogen is higher than that with helium. This is because the thermal conductivity of helium is much higher than nitrogen. Therefore, a pebble bed with helium results in a better heat conduction than one with nitrogen. Consequently, it has a steeper temperature gradient with nitrogen, which causes higher gas velocity in radial direction and better heat convection. This effect can be observed by comparing the radial gas velocity. In general, the total effect of conduction and convection shows that heat conduction dominates the heat transfer in SANA experiments.

In order to validate the new code MGT-3D, the comparison of the experiments with helium and the simulations are displayed in Figures 2.9, 2.10, 2.11 and 2.12, and a comparison of the experiments with nitrogen and the simulations are displayed in Figures 2.13, 2.14, 2.15 and 2.16. In the simulation model, the axial coordinate increases from top to bottom of the experimental installation, and the pebble bed zone is from $Z = 0$ cm to $Z = 100$ cm. The simulation result fits very well with experiment except in the point $(R = 10\ cm, Z = 50\ cm)$. The given measured data shows that temperature in the points $(R = 6.5\ cm, Z = 50\ cm)$, $(R = 10\ cm, Z = 50\ cm)$, $(R = 22\ cm, Z = 50\ cm)$ are 552 $°C$, 450 $°C$, 337 $°C$ respectively. The temperature gradient from the first point to the second point is three times as steep as the gradient from the second point to the third point, which is impossible considering that the conductivity does not change considerably in the pebble bed zone. Therefore, the measured temperature in the point $(R = 10\ cm, Z = 50\ cm)$ may have some inaccuracies [36]. The temperature differences of other points are in the range of $20°C$, which are generally small relative to the measurement deviation and sensitivity of some simulation parameters. Although the heat source is symmetry with respect to the middle plane of the pebble, the results show that top temperature is higher than the bottom temperature, which is due to the natural convection in the pebble bed. The comparisons between the simulation and the experiment show that the results with nitrogen agree better than the ones with helium

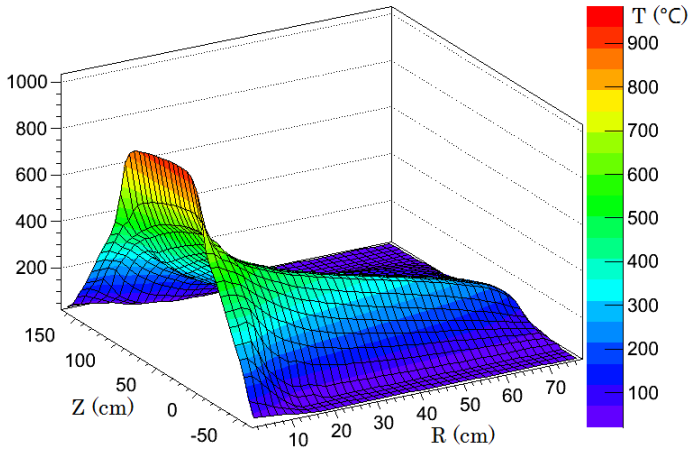

Figure 2.6: Simulated solid temperature distribution with MGT-3D, nitrogen, 10 kW

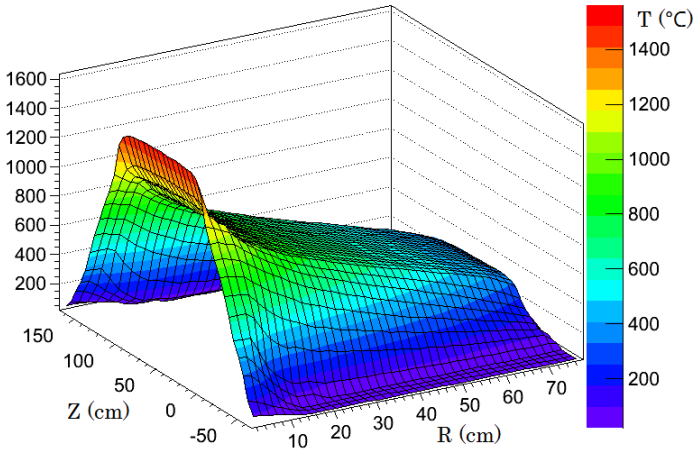

Figure 2.7: Simulated solid temperature distribution with MGT-3D, helium, 35 kW

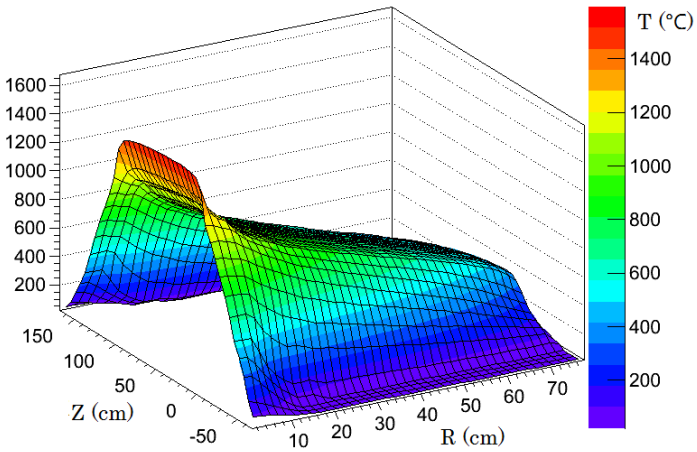

Figure 2.8: Simulated solid temperature distribution with MGT-3D, nitrogen, 35 kW

and the results with power 35 kW agree better than those with 10 kW.

Figures 2.10 and 2.14 show that measured and simulated values differ significantly in the outer boundary part in the experiments with 10 kW. The calculated value is lower than the experimental result. This is because the same heat transfer coefficient is applied in all of the simulations. The heat transfer coefficient is taken from the reference data of the experiment with 20 kW [35]. The value of the heat transfer coefficient is determined by the convection transport on vessel surface and the radiation from vessel surface to environment. Higher vessel surface temperature have stronger heat convection and radiation. By means of using the heat transfer coefficient which is suitable for 20 kW, the heat transfer coefficient is overestimated for the experiment with 10 kW, which results in a lower simulated temperature.

Additionally, a code to code benchmark has also been done. Figures 2.17 and 2.18 present solid temperature differences and gas temperature differences between MGT-2D and MGT-3D for the experiment with helium and 35 kW. The solid temperature differences are in the range of -0.005 to 0.21 $°C$, and the gas temperature differences are in the range of -0.59 to 1.03 $°C$, which is neglectable. The maximum gas temperature difference can be explained. It exists in the mesh of gas source. This gas inlet is distributed in a circle in MGT-2D, but it is restricted to one azimuthal mesh in MGT-3D. Therefore, gas flow is quite different in this mesh, and it has maximum difference. Nevertheless, the MGT-3D model is closer to real experiment situation. In summary, MGT-3D can share the same input file with MGT-2D. MGT-3D shows almost no difference with MGT-2D after adding a new dimension and the required boundary condition in azimuthal direction. It can substitute MGT-2D in steady state simulation and gives better physics model.

Basically, a reactor remains in steady state during normal operation, or it achieves thermal equilibrium after a long period of the accident. But in the accident scenario such as LOFC, air ingress, the reactor power and temperature distribution vary with time. From an experimental view, it is necessary to investigate the temperature evolu-

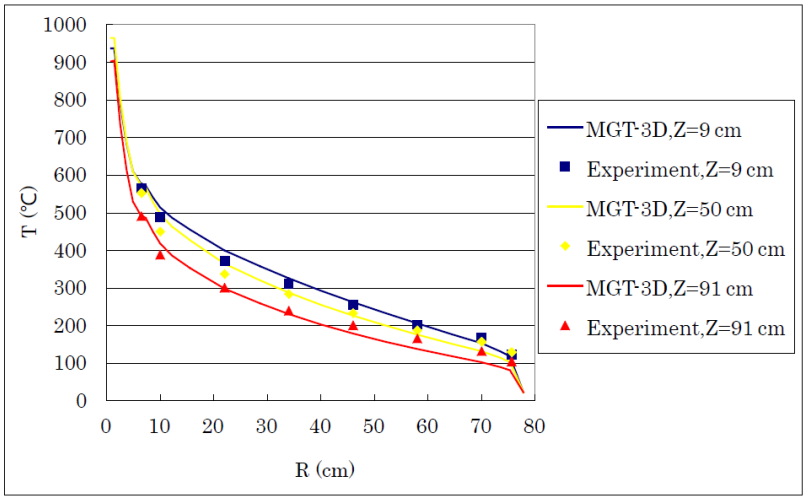

Figure 2.9: Measured and simulated solid temperature, helium, 10 kW, axial cut

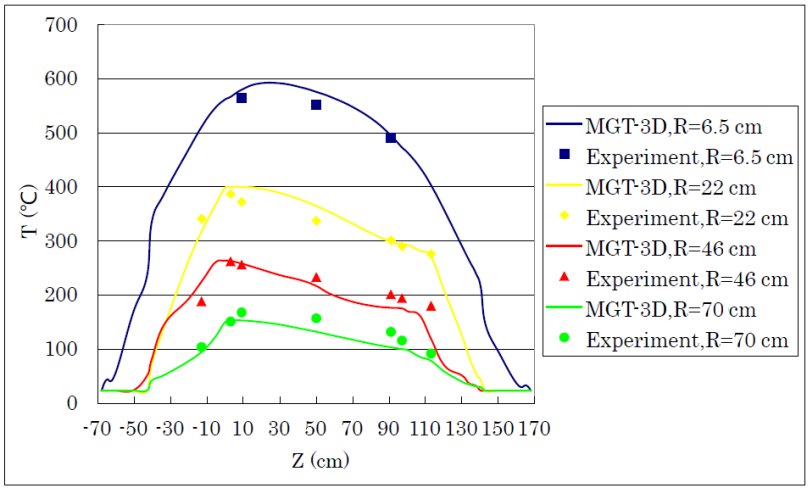

Figure 2.10: Measured and simulated solid temperature, helium, 10 kW, radial cut

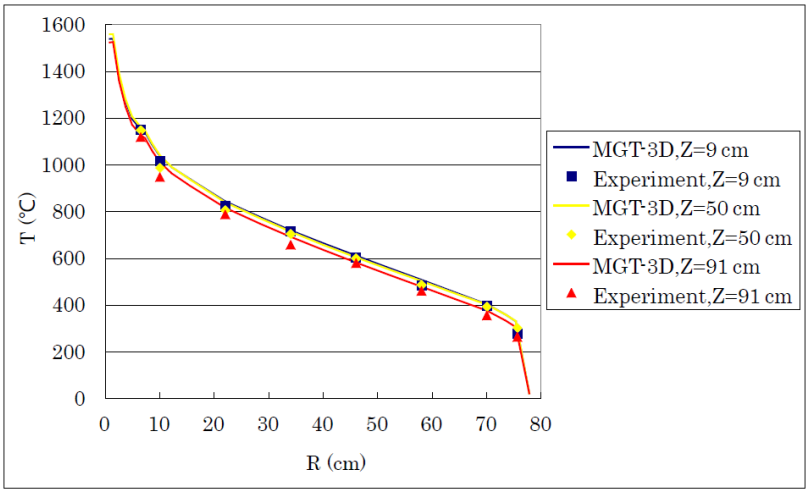

Figure 2.11: Measured and simulated solid temperature, helium, 35 kW, axial cut

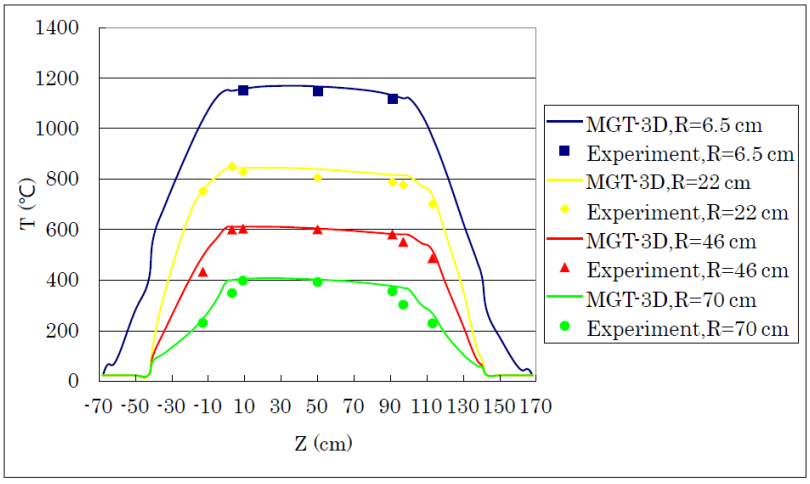

Figure 2.12: Measured and simulated solid temperature, helium, 35 kW, radial cut

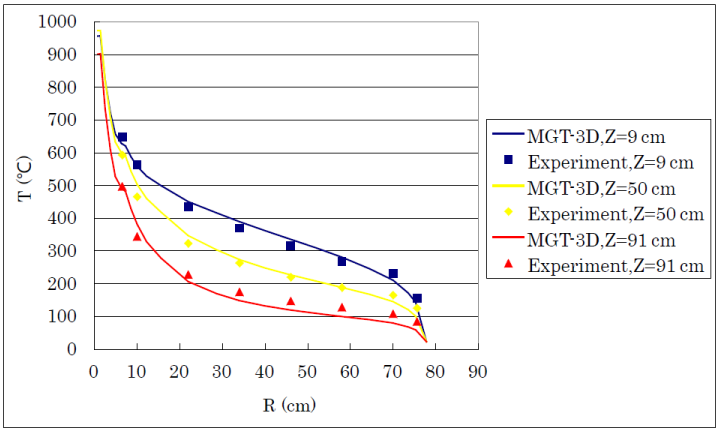

Figure 2.13: Measured and simulated solid temperature, nitrogen, 10 kW, axial cut

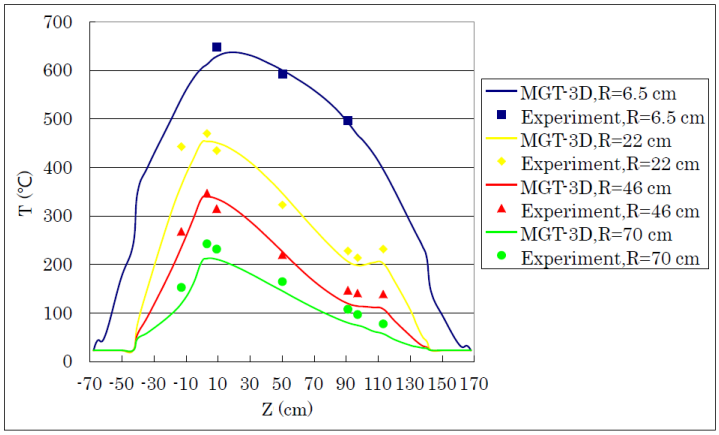

Figure 2.14: Measured and simulated solid temperature, nitrogen, 10 kW, radial cut

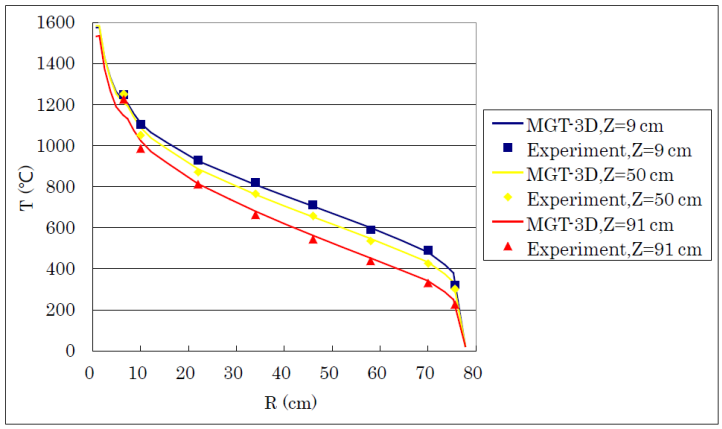

Figure 2.15: Measured and simulated solid temperature, nitrogen, 35 kW, axial cut

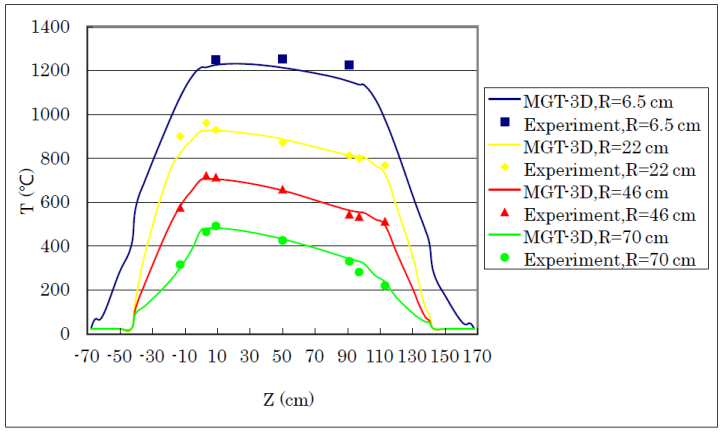

Figure 2.16: Measured and simulated solid temperature, nitrogen, 35 kW, radial cut

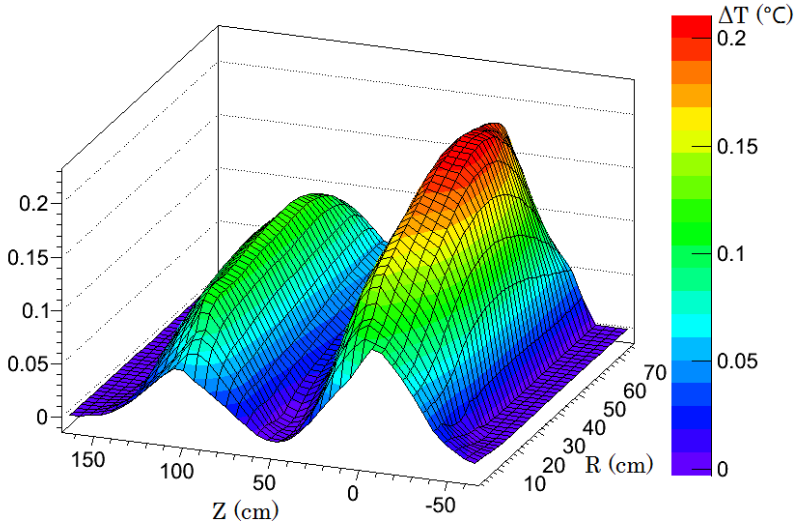

Figure 2.17: Solid temperature difference between MGT-3D and MGT-2D, helium, 35 kW

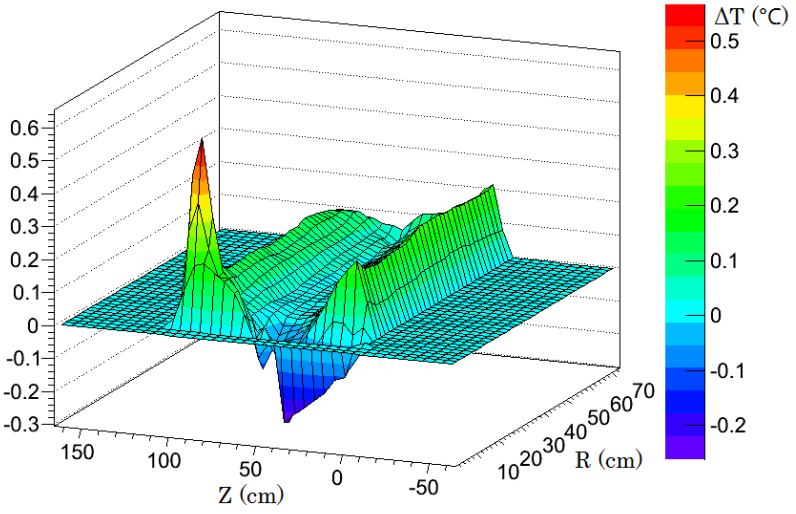

Figure 2.18: Gas temperature difference between MGT-3D and MGT-2D, helium, 35 kW

tion with power changing. From the simulation's view, MGT-3D should be validated in transient case to prove its ability to perform reactor accident simulation. Three different transient cases are investigated in SANA experiments, which are power increasing, power decreasing, and gas exchanging. These three kinds of experiments match the positive reactivity insertion, air ingress and negative reactivity insertion respectively. Here, power increasing experiment is chosen to validate MGT-3D.

In the power increasing experiment, the system starts from a defined steady state with a heating power of 10 kW, and then the power is increased to 25 kW in a short time interval. It uses a long heating element. The composition of the filling gas does not change and the gas stays at atmospheric pressure during the experiment. The pebble bed is constituted with graphite pebbles whose diameters are 6 cm. Due to a large amount of graphite with a high heat capacity, it takes more than 40 h for the experiment to achieve a new steady state.

In the simulation model, it is assumed that power increases from 10 kW to 25 kW linearly in 1 minute and that the heat transfer coefficient of vessel surface is fixed. Figures 2.19 and 2.20 display the simulation and experiment results with helium and nitrogen in the middle plane of the pebble bed. The simulation result shows that it requires about 40 hours for the system to reach a new steady state, which proves that graphite pebbles can maintain significant amounts of heat. Considering that SANA only simulates a small part of pebble bed of HTGR, the temperature responds even more inertly with the changing of reactor power. It can be deduced that the temperature peak of pebble bed appears several days after the accident happened. During this time period, significant amounts of heat can be transferred out of the reactor by conduction, radiation, and natural convection, and special measure can be taken if necessary. Also, the peak temperature does not reach extremely high.

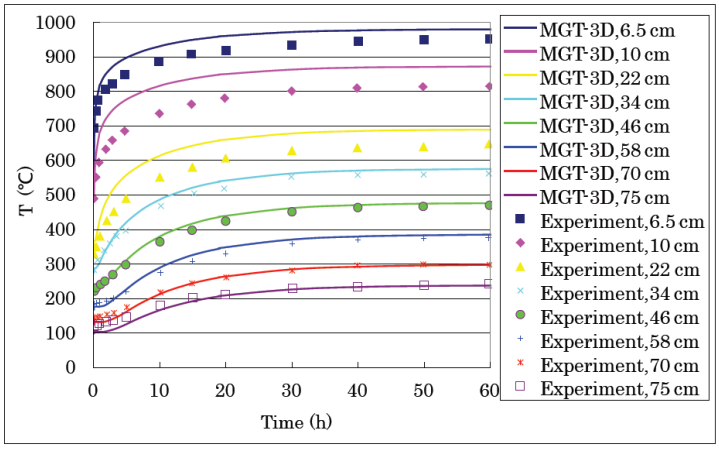

Figure 2.19: Measured and simulated solid temperature in power increasing transient, helium, power from 10 kW to 25 kW, $Z = 50$ cm

Figures 2.19 and 2.20 also show that the maximum difference is about 60 $°C$. It appears in the point $R = 10$ cm whose measured temperature is not credible, which has been explained in the steady state case. For other measured points, the simulation results are in good accordance with experiment record in the transient case, and the differences

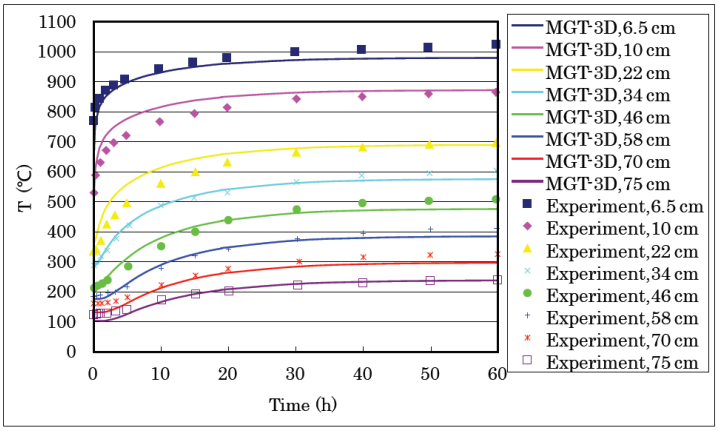

Figure 2.20: Measured and simulated solid temperature in power increasing transient, nitrogen, power from 10 kW to 25 kW, $Z = 50$ cm

are about 30 $°C$ on the average. By investigating the results in detail, the following characteristics can be observed. First, the simulation values are generally higher than the measured values with filling gas helium. Second, the simulated temperatures are generally smaller than measured temperatures with nitrogen, and fit better than the experiment with helium. Third, the difference is smaller in the end of transient than in the beginning. One of the possibilities that causes these differences is the use of an unproven method to calculate natural convection [34]: the heat transfer coefficient is calculated by the Nusselt number Nu which is extrapolated from the rule to calculate Nu of high velocity gas flow of HTGR, but the gas velocity of SANA experiment is very slow. The lack of experimental data to correct the extrapolated Nu causes uncertainties in solid temperature calculation. If the temperature is very high, thermal radiation which is proportional to T^4, becomes very strong. Then, the effect of natural convection becomes weaker, which decreases the uncertainty of the natural convection effect on temperature calculations. In the end of transient, the temperature is much higher than initial temperature, so the simulation values fit better with measured values. Another factor that causes uncertainties in the simulation model is the flattening coefficient of the effective conductivity of pebble bed in the Zehner-Schlünder model. Because it is hard to know the contacting areas between the pebbles and the contacting areas may be different in different zones of the pebble bed, the flattening coefficient is hard to correct.

The figures also show that simulation results are smaller than the measured results in the point $R = 75$ cm, but they agree very well in the end of transient. The reason is as follows: the effective heat transfer coefficient of vessel boundary with 20 kW is chosen as reference value during the transient, and this value is overestimated in the experiment with 10 kW as mentioned. After about 20 hours, the boundary temperature is comparable to that of the case with 20 kW. Then, the simulated temperature fits very well with the measured temperature.

In summary, the simulation results fit very well with the experimental results in the transient case. Both the simulation and experiment reveal that it takes several days for the system to reach equilibrium after increasing the power. Natural convection in the pebble bed affects the temperature significantly at low temperatures, and the thermal

radiation and conduction dominate at high temperature. The boundary condition of the vessel also has influence on pebble bed temperature, which proves that core temperature of reactor can be decreased by increasing the convection effect on the surface of the reactor pressure vessel.

2.2.3 SANA Experiment with Central Heating Element and Radial Heating Elements

The installed power of SANA is 50 kW. With this power level, the average power density of 3 MW/m^3 of the pebble bed in SANA experiment is closer to the decay heat of HTGR in 3 to 4 hours of the accident. In addition, it is an important topic to research the influence of a discrete heat source with high heat fluxes on temperature distribution in the pebble bed. It is also interesting to look into the natural convection in azimuthal direction, for example the helical flow. It can be achieved by adding radial heating elements in the pebble bed.

In the experiment with additional radial heating elements, three heating elements are arranged at a distance of 0.5 m far away from the center of the equipment (see Fig. 2.3). They are distributed in rotational symmetry with respect to an angle of 120°. The cylindrical symmetry of the system does not exist any more. The designed power of each radial heating element is 10 kW, and the power of central heating element is 20 kW, for a total of 50 kW. Because of mechanical problems, each of the radial heating element is limited to 9 kW during the experiment. All of the electrodes of the heating rod are cooled by water in the chamber. The graphite pebble as well as the top and bottom isolations are constructed like the experiment with only central heating element, but with some adaption around radial heating element. Because these three radial heating elements have the same geometry as the central heating element, this adaption can be made in the same way as the installation of the central heating element.

MGT-2D lacks one coordinate to describe the discrete structure in azimuthal direction. It can not be used here to simulate the experiment with radial heating elements. A special treatment with the 2D code THERMIX/DIREKT is introduced by M. Lange [35]. First, the experimental structure in R/Φ is simulated. It can illustrate the additional heating elements in detail. The temperature rise can be determined in the environment relative to the undisturbed bulk material. However, it can only calculate the solid temperature and can not calculate the gas flow. Second, an approximated model is built in R/Z plane. The power of radial heating elements are averagely distributed in a circle in this model and gas flow in axial direction can be determined. This method is an approximate treatment, and can not describe the 3D structure in detail. With MGT-3D, however, a detailed 3D description of the experiment can be performed.

The power of all radial heating elements is kept the same in the experiments, so the calculation model is also rotational symmetry with respect to 120° (see Fig. 2.21). It is not necessary to simulate the experiment in 360°. By judging geometry and physical parameters of the experiment, only the zone from 0° to 60° is included in the simulation model. The reflective boundary condition is used in azimuthal direction. The gas inlet and outlet mesh should be unique. They can only be defined in one azimuthal mesh, which breaks the symmetry. The amount of gas flow rate is below 200 L/h. It is very low and can be neglected.

The power density is very high in the zone where the radial heating element is located. Therefore the temperature gradient is large as well. In order to get a more precise

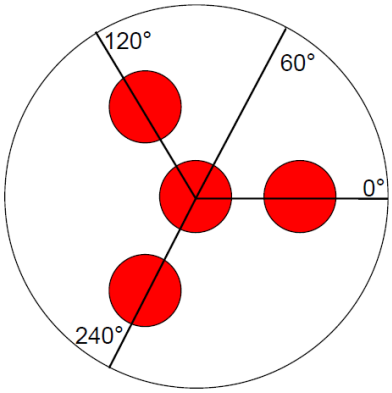

Figure 2.21: Top view sketch of SANA experiment with radial heating elements in axial cross section

temperature profile, the radial heating element and its surrounding materials should be modeled in details. The simulation model of the radial heating rod is shown in Figure 2.22. The radial heating element is represented by three meshes in R/Φ coordinate. The gap, protection tube, pebble bed around the heating element, and so on are also well considered in this 3D simulation model. The power profile of heating element is presented in Table 2.3. The boundary temperature is set at the environment temperature of 26.1 $°C$. The experiments without radial isolation in the vessel boundary are simulated and the equivalent heat transfer coefficient of the vessel boundary is taken from the reference value of the experiment with 20 kW [35].

P_{total}	P_{rod}	$P_{electrode}$
20 kW	18.12 kW	0.585 kW
9 kW	8.019 kW	0.279 kW

Table 2.3: Power set of SANA experiment with radial heating element [35]

Figure 2.23 shows the simulated temperature distribution of the model with central heating power 20 kW, each radial power 9 kW, and with filling gas helium in the cross section of $Z = 50$ cm. There are four temperature peaks where the heating elements are located. The maximum temperature which is about 1330 $°C$ is located in the center of the central heating element. The temperature peak at the radial heating elements is about 880 $°C$.

Figures 2.24, 2.25 and 2.26 display the differences between simulated temperatures and measured temperatures with helium in radial, axial, and azimuthal cut respectively. Figures 2.27, 2.28 and 2.29 display the comparison between simulated and measured results with nitrogen. The simulated results fit very well with the measured values except at some controversial points that were already discussed in SANA experiment with only one heating element. The simulated results with helium are generally higher than the measured values. They may be caused by using a lower heat transfer coefficient than the expected values in the vessel boundary. In the point ($R = 47$ cm, $Z = 50$ cm, $\Phi = 0°$), the simulated value is 100 $°C$ higher than the measured value. This is because the measured

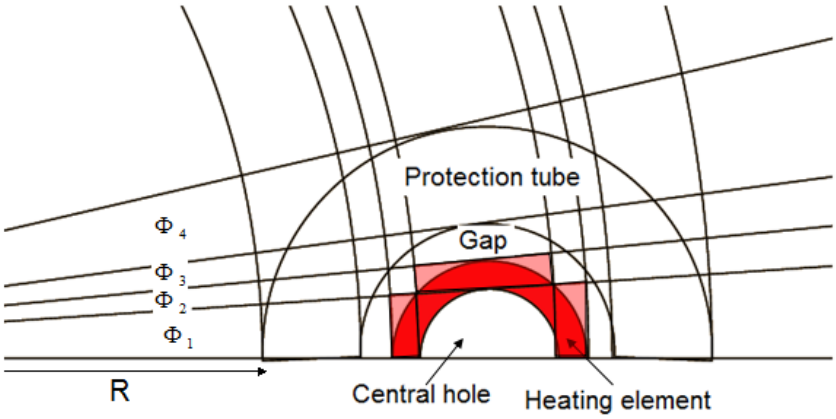

Figure 2.22: Detailed calculation model for radial heating rod

point is in the protection tube, and there is a gap where inert gas flow is continuously injected in to prevent the corrosion of heating element. Therefore, natural convection exits in this area. In the simulation model, however, only conduction and thermal radiation are taken into account, which can influence the accuracy of the simulation. Additionally, the measured value is also questioned. The measured temperature differences between point ($R = 47\ cm, Z = 50\ cm, \Phi = 0°$) and point ($R = 50\ cm, Z = 50\ cm, \Phi = 0°$) is 140 $°C$ within the distance 3 cm, and there is a gas gap whose equivalent conductivity of thermal radiation effect is comparable to the conductivity of graphite between these two points. Therefore, a solid temperature gradient, which is according to measured temperature between these two points, is unreasonable. In other points, the differences between simulated and measured solid temperature are within $30°C$, which are acceptable values.

The result also shows that the temperatures do not change significantly in the inner part (e.g. ($R = 23\ cm, Z = 50\ cm$)) of pebble bed in the azimuthal direction, but a deep temperature gradient can be observed in the outer part (e.g. ($R = 59\ cm, Z = 50\ cm$)). As mentioned, the equivalent heat transfer coefficient in the vessel wall is temperature dependent and the reference value, which is related to 20 kW is used in the simulation model. Therefore, the solid temperature of vessel wall fits better in angle mesh $\Phi = 0°$ than in angle mesh $\Phi = 60°$. The simulated results and measured values fit better with nitrogen than with helium as filling gas, which is the same as the result of 2D experiment.

In summary, MGT-3D works very well in 3D fluid mechanics calculation of SANA experiments. It can reproduce the result of the experiment with central and radial heating elements very well in all 3 dimensions (R,Z,Φ). With a detailed description of the radial heating element, the temperature rising around it can be obtained, especially the temperature rising in the heating element. The influence of the discrete heat source on temperature distribution in azimuthal direction can be observed as well. At full power, it represents the decay power of 3 hours after the accident of a modular HTGR. The simulation shows that the maximum temperature of pebble bed is below 1300 $°C$, which proves that the heat can be removed by the mechanism conduction, radiation, and convection in the pebble bed.

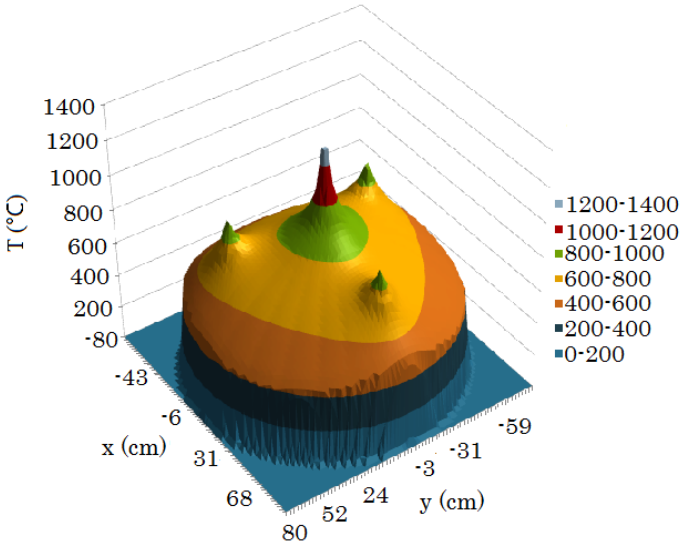

Figure 2.23: Simulated solid temperature, $Z = 50\ cm$, $20\ kW + 3 \times 9\ kW$, helium, without radial insulation

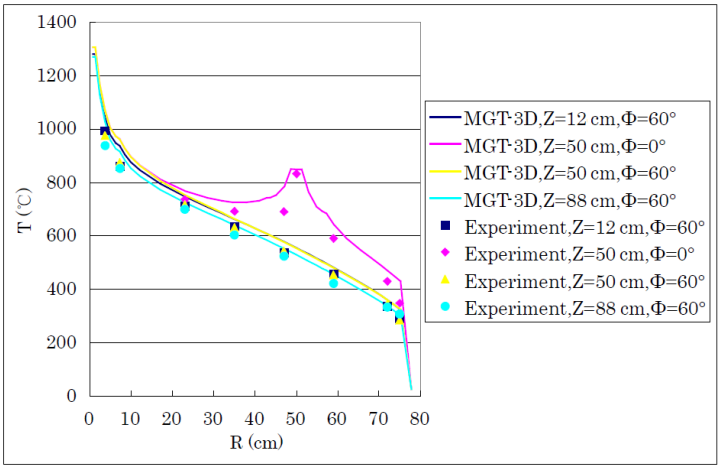

Figure 2.24: Simulated and measured solid temperature, radial cut, $20\ kW + 3 \times 9\ kW$, helium, without radial insulation

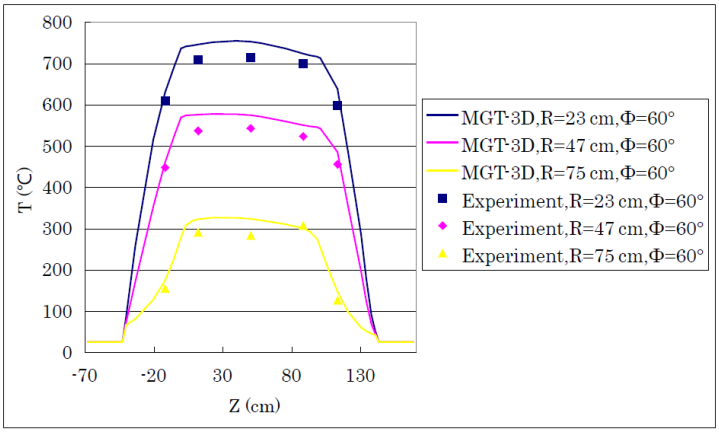

Figure 2.25: Simulated and measured solid temperature, axial cut, 20 $kW + 3 \times 9$ kW, helium, without radial insulation

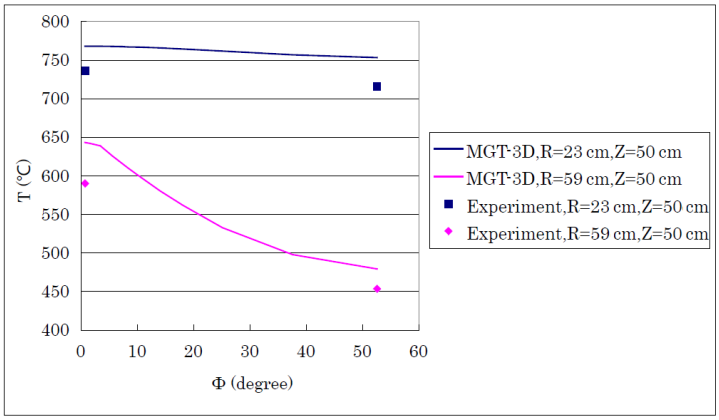

Figure 2.26: Simulated and measured solid temperature, azimuthal cut, 20 $kW + 3 \times 9$ kW, helium, without radial insulation

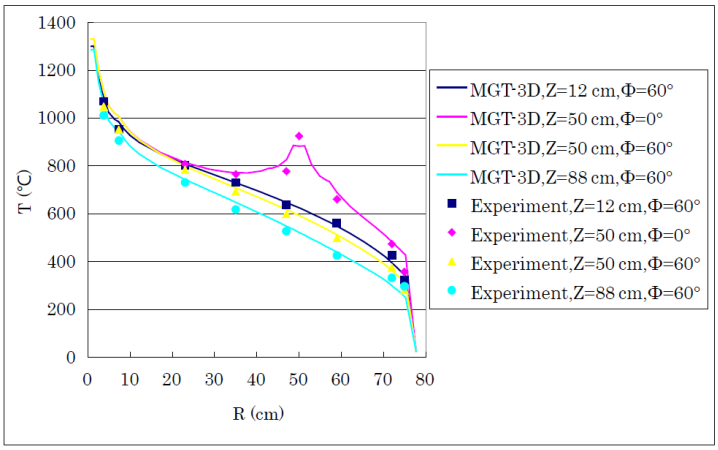

Figure 2.27: Simulated and measured solid temperature, radial cut, 20 $kW + 3 \times 9$ kW, nitrogen, without radial insulation

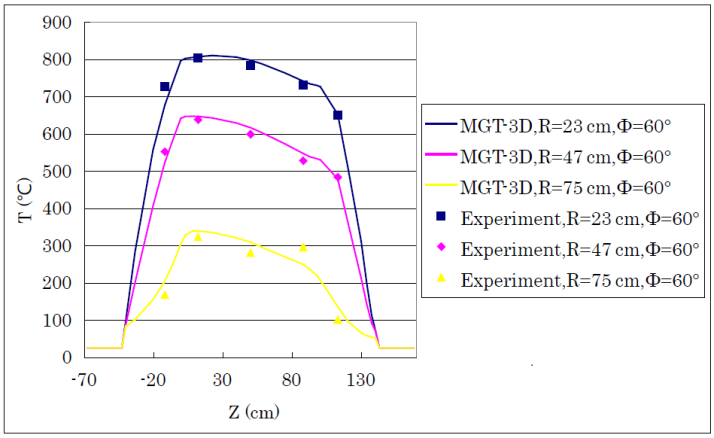

Figure 2.28: Simulated and measured solid temperature, axial cut, 20 $kW + 3 \times 9$ kW, nitrogen, without radial insulation

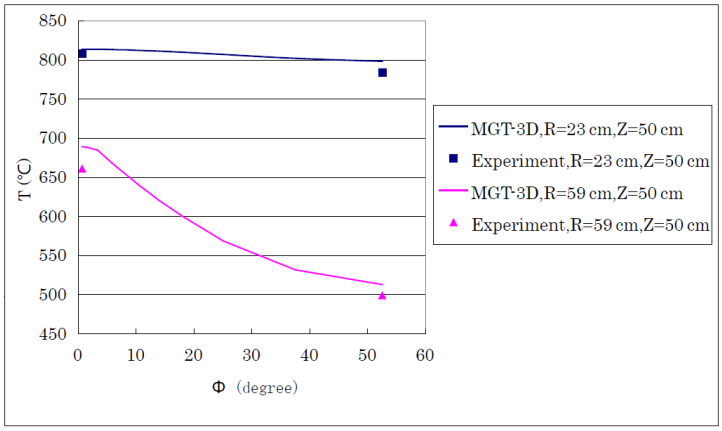

Figure 2.29: Simulated and measured solid temperature, azimuthal cut, 20 kW + 3×9 kW, nitrogen, without radial insulation

Chapter 3

Model Extension of MGT-3D

This chapter includes mainly three parts. In the first part, a new method is introduced to calculate the kernel temperature of the coated particles, which are embedded within the fuel graphite matrix. The nuclear cross sections are determined by the fuel temperature and moderator temperature. Due to the high power density of the fuel kernels, the fuel kernel temperature is significantly higher than the surrounding graphite. This temperature difference should be taken into account for the fuel temperature feedback. The new model solves the 1-D heat transfer equations in the coated particles, and it is implemented into MGT-3D. After this, two transient cases of the PBMR-400 are studied with both models. The simulation results with the new kernel model and with the old model are compared.

In the second and third parts, MGT-3D is extended to block-type HTGRs, which include the American's and the Japaneses' design. MGT-3D is developed for pebble bed HTGRs. Up to now, it calculates the temperature profile of the representative spherical fuel element to determine the nuclear cross section. As a first step towards block-type HTGRs, the unit cell, which can represent the symmetrical structure of the fuel block, is chosen to analyze the heterogeneous temperature distribution of the moderator and fuel rod. A 2-D model is advanced and verified by the CFX simulation. Afterwards, a 1-D simplification of the unit cell is discussed. Within the third part, the homogeneous anisotropic thermal conductivity of the reflector and reactor core of block-type HTGRs is calculated with the help of the rule to calculate the thermal conductivity of the multi-material medium.

3.1 The Fuel Kernel Model

Due to the Doppler effect, the fuel temperature and moderator temperature are two important factors in determining the nuclear cross section. An increase in fuel temperature leads to an increase of resonance absorption cross section of some isotopes, mainly ^{238}U and ^{232}Th. This feedback ensures HTR's passive safety during normal operation or in an accident. Therefore, it is important to calculate the UO_2 fuel temperature.

HTR's fuel elements contain a significant number of Tri-structural-Isotropic (TRISO) coated particles. The UO_2 kernel is located in the center of coated particle. It is coated with a porous carbon buffer, inner pyrolytic carbon, silicon carbide, and outer pyrolytic carbon sequentially from the center to the outside. The homogeneous temperature calculation and the pebble temperature calculation do not account for the fuel temperature which is the center temperature of the coated particles. In MGT-3D, an overheating model is applied to calculate the temperature difference between the fuel kernel and the

graphite matrix. This model homogenizes the coated materials and assumes a temperature difference between the UO_2 kernel and the graphite matrix. It defines an effective heat flux resistance α_f in the heat conduction equation. A simple heat transfer equation is solved to predict the average fuel temperature.

The original overheating model relies heavily on an unknown parameter α_f. It also assumes a small temperature difference between the fuel and moderator, and it does not consider the different thermal responses of different coated materials in the transient case. In order to get a more accurate fuel temperature feedback, an explicit model is developed to solve the heat conduction equation with mixed boundary conditions. It takes the details of energy deposition and different thermal properties of coating layers into account. This explicit model can treat both the equilibrium case and all kinds of transient cases. It is also helpful to determine the effective heat flux resistance for the original overheating model. The new model is implemented into MGT-3D, and some studies are conducted regarding the original and new models.

3.1.1 Overheating Model

The cross sections, which are polynomial expansions of fuel and moderator temperatures, gas concentrations, ^{135}Xe concentration, should be prepared at the beginning of nuclear calculations. The temperatures and gas concentrations are determined after the fluid mechanics calculations. In case of an equilibrium calculation, they are iterated. In case of a transient calculation, the fluid mechanics calculation is performed after several nuclear calculations. The iterated method can also be applied to the transient calculation in principle. However, it would consume too much computational time. If the temperature and boundary condition of the representative pebble are assumed to vary linearly with time, an extrapolated value can be obtained for nuclear feedback. The extrapolated parameters include local and non-local heat sources, fuel layer temperatures, solid material temperatures, and fuel surface boundary conditions during the nuclear intervals.

By the former assumption, the layer temperatures of the representative fuel pebble are obtained for each nuclear time interval. However, The temperatures of the UO_2 kernels are the required value to determine the resonance absorption cross section instead of the temperatures of each layers in the fuel pebbles.

The kernels are well coated by four layers' materials and then embedded in the graphite matrix. With respect to the temperature calculation, the coated particles have the following features:

- The diameter of the coated particle is about 0.92 mm. It is generally small, so the temperature difference between the fuel kernel and its surrounding graphite matrix is assumed to be small as well.
- The conductivity of the fuel kernel is much higher than that of the coating layers. This results in a distinct temperature difference across the coating layers, but the temperature becomes smooth in the kernel zone. The density and heat capacity of the coating material are much smaller than those of the uranium dioxide kernel. The coating layers respond quicker then the kernel in the transient case. Therefore, the coating layers can be considered as a gap.

- The thermal properties of the coating layers are not clear. The irradiation by neutrons and the high temperature environment affect the structure of these layers as well. The thermal conductivity, density, and even the shape of the coated particles can change after a long irradiation term. Currently, the knowledge about these mechanisms is not sufficient.

According to these features, it is not necessary to develop a detailed heterogeneous model to calculate the temperature distribution in the fuel kernels. Each particle can be considered as a hot point which has heat resistance and certain specific heat in the graphite matrix. The heat conduction, which describes heat transfer from the hot point to the surroundings, is governed by:

$$\rho_f c_f \frac{dT_f}{dt} = -\frac{1}{\alpha_f}(T_f - T_m) + \dot{Q}_f''' \tag{3.1}$$

where ρ_f is the density of fuel kernel, T_f is the fuel kernel temperature, T_m is the moderator temperature, α_f is the effective heat flux resistance, and $\dot{Q}_f'''$ is the power density of the fuel kernel. In this equation, the heat flux resistance is mostly contributed by the coating layers, but all of the heat is considered to be saved in the fuel kernel. The power density of the fuel kernel is calculated from the homogeneous local nuclear power density $\dot{Q}_l'''$. The local power which deposits in the fuel kernels, and the non-local heat which deposits in moderators, are already separated in the heat production calculation. The ratio of $\dot{Q}_l'''$ to $\dot{Q}_f'''$ is equal to the volume fraction of fuel kernels in fuel elements. Basically, it is a fixed value for all homogeneous meshes. Introducing the power ratio into Equation 3.1, it can be rewritten into:

$$\frac{dT_f}{dt} = -\frac{1}{\alpha_f \rho_f c_f}(T_f - T_m) + \frac{1}{\rho_f c_f}\frac{\dot{Q}_f'''}{\dot{Q}_l'''}\dot{Q}_l''' \tag{3.2}$$

By defining a new heat flux resistance which includes modification of the power ratio:

$$\alpha_f' \equiv \frac{\dot{Q}_f'''}{\dot{Q}_l'''}\alpha_f \tag{3.3}$$

and the time-response factor:

$$\lambda_f \equiv \frac{1}{\alpha_f \rho_f c_f} \tag{3.4}$$

The Equation 3.2 can be simplified as:

$$\frac{dT_f}{dt} = -\lambda_f(T_f - T_m) + \alpha_f' \lambda_f \dot{Q}_l''' \tag{3.5}$$

For the equilibrium case, the temperature is not time dependent and the left-hand side of Equation 3.5 is equal to zero. The kernel temperature can be obtained by the following equation:

$$T_f = T_m + \alpha_f' \dot{Q}_l''' \tag{3.6}$$

For a transient case, if the local nuclear heat and moderator temperature are assumed to vary linearly with time, their values can be linearly extrapolated during the nuclear intervals:

$$\dot{Q}_l'''(t) = \dot{Q}_{l0}''' + \frac{t - t_0}{\Delta}(\dot{Q}_{l1}''' - \dot{Q}_{l0}''') \tag{3.7}$$

$$T_m(t) = T_{m0} + \frac{t - t_0}{\Delta}(T_{m1} - T_{m0}) \tag{3.8}$$

Substituting equations 3.7 and 3.8 into the Equation 3.5:

$$\frac{dT_f}{dt} + \lambda_f T_f = \lambda_f \{(\alpha'_f \dot{Q}'''_{l0} + T_{m0}) + \frac{t - t_0}{\Delta}[(\alpha'_f \dot{Q}'''_{l1} + T_{m1}) - (\alpha'_f \dot{Q}'''_{l0} + T_{m0})]\} \quad (3.9)$$

With the initial condition $T_f(t)|_{t=t_0} = T_f(t_0)$ and the definition:

$$A_1 \equiv \alpha'_f \dot{Q}'''_{l1} + T_{m1} \quad (3.10)$$

$$A_0 \equiv \alpha'_f \dot{Q}'''_{l0} + T_{m0} \quad (3.11)$$

the solution of the differential Equation 3.9 can be obtained:

$$T_f(t) = T_f(t_0)e^{-\lambda_f(t-t_0)} + A_0[1 - \frac{t-t_0}{\Delta} - e^{-\lambda_f(t-t_0)} + \frac{1 - e^{-\lambda_f(t-t_0)}}{\lambda_f \Delta}] + A1[\frac{t-t_0}{\Delta} - \frac{1 - e^{-\lambda_f(t-t_0)}}{\lambda_f \Delta}] \quad (3.12)$$

This is the kernel temperature evolution equation during nuclear time intervals with overheating model. At the end of one nuclear time interval, fuel kernel temperature is equal to:

$$T_f(t_0 + \Delta) = A_1 + (T_f(t_0) - A_0)e^{-\lambda_f \Delta} + (A_0 - A_1)\frac{1 - e^{-\lambda_f \Delta}}{\lambda_f \Delta} \quad (3.13)$$

The values of α'_f and λ_f are dependent on layers' conductivity, specific heat, packing fraction, and geometry of the coated particles. However, there is not a fixed equation to calculate them, especially the modified effective heat flux resistance α'_f. According to Equation 3.6, the value of α'_f can be deduced if the fuel temperature of steady state is available:

$$\alpha'_f = \frac{T_f - T_m}{\dot{Q}'''_l} \quad (3.14)$$

However, it is a difficult task to measure reactor core temperature. It is almost impossible to measure the temperature of the fuel which is located at the center of a tiny coated particle. According to Equations 3.3 and 3.4, α'_f and λ_f are related. The value of α'_f can be estimated by the thermal response of reactor during a transient scenario, e.g. the movement of the control rods. Former studies suggest the region of α'_f is from 0.5 $K \cdot cm^3/W$ to 0.9 $K \cdot cm^3/W$. Recent studies also show that α'_f is close to 3.0 $K \cdot cm^3/W$ for the PBMR reactor [40].

3.1.2 Development of a New Kernel Model

An analytical result of fuel kernel temperature (see Eq. 3.13) is derived from the overheating model. It depends on the effective heat flux resistance, whose value cannot be fixed analytically. This model assumes that the temperature varies slightly from the graphite matrix to the fuel kernel. The temperature distributes smoothly in the kernel zone. Heat is saved in the fuel kernel and insulated by coating layers. It also uses temperature independent specific heat and heat resistance. This model works very well for steady-state and slow transient calculation of the reactor if proper effective heat flux resistance is given.

Nevertheless, the overheating model is not precise enough and does not include the following features of coated particles:

- The fission products only travel several micrometers, and the diameter of the fuel kernel is 0.5 mm, which means that local nuclear power remains in the fuel kernel zone. The volume fraction of the fuel kernel is less than 0.01 (1/150 for HTR-Modul). The power density of the fuel kernel is more than 100 times $\dot{Q}_l'''$. Although the size of the coated particle is very small compared with the size of fuel element, the temperature increases significantly in the coated particles according to the high power density, especially in the high power density zone of the reactor.
- In a coated particle, the fuel kernel that produces the nuclear power has high conductivity and high specific heat. A buffer layer made of porous carbon shields the IPyC from recoil damage and controls the particle pressure. This layer has very low conductivity and specific heat. The other layers, which protect the fuel kernel, maintain the fission products, and provide structure support, have high conductivity and low specific heat. Different thermal properties of these layers determine that they will have different thermal responses in the transient case.
- The conductivity and specific heat of the layers are dependent on temperature and neutron fluence. Therefore, conductivities of the layers vary in different zones of the reactor and with irradiation history. Considering that a gap is generated according to the contraction of the kernel and porous carbon after long terms of neutron irradiation, the temperature will rise a lot across the gap. In the gap zone, thermal radiation dominates the heat transfer. This effect is proportional to T^4, and causes huge variation of the effective conductivity.
- With the development of experimental technology, the thermal conductivity and specific heat of the coating layers can be measured precisely, which makes it possible to simulate the heat transfer in the coated particles with detailed numerical models [38].

Many models which can overcome the limitations of the overheating model and determine heat transfer in coated particles have been developed [39, 40]. Heat is transferred out of the coated particle by conduction. The general heat conduction equation is:

$$\rho C_p \frac{\partial T(r,\theta,\phi,t)}{\partial t} = \nabla k \nabla T(r,\theta,\phi,t) + \dot{Q}'''(r,\theta,\phi,t) \tag{3.15}$$

The coated particle is comprised of five symmetrical spherical structures (see Fig. 3.1). It is reasonable to assume that the temperature distribution of the coated particle has spherical symmetry. If the center of the particle is chosen as the origin of coordinate, the heat transfer Equation 3.15 can be simplified to:

$$\rho C_p \frac{\partial T(r,t)}{\partial t} = \frac{1}{r^2}\frac{\partial}{\partial r}(kr^2\frac{\partial T(r,t)}{\partial r}) + \dot{Q}'''(r,t) \tag{3.16}$$

To solve this differential equation, it also requires two boundary conditions and one initial condition. In the center of the particle, the temperature gradient is zero, which gives the Neumann boundary condition:

$$\frac{\partial T(r,t)}{\partial r}|_{r=0} = 0 \tag{3.17}$$

Graphite has a relatively high conductivity, so the temperature of the moderator does not vary significantly in the scale of the coated particle. The outer PyC layer merges with the graphite moderator. The moderator temperature is chosen as the boundary

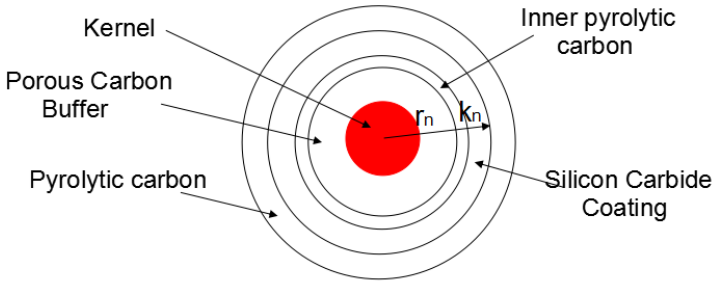

Figure 3.1: TRISO model constituents

temperature, which gives the Dirichlet boundary condition at the outer surface:

$$T(r,t)|_{r=R} = T_m(t) \tag{3.18}$$

where R is the outer radius of the coated particle. The initial condition is the temperature distribution of the coated particle when the reactor is in steady state:

$$T(r,t)|_{t=0} = T(r,0) \tag{3.19}$$

For steady state, the right hand side of Equation 3.16 is equal to zero:

$$\frac{1}{r^2}\frac{\partial}{\partial r}(kr^2\frac{\partial T(r)}{\partial r}) + \dot{Q}'''(r) = 0 \tag{3.20}$$

Although the thermal conductivity is temperature dependent for a certain layer, it does not change significantly in the temperature's variation range [39]. Therefore, the thermal conductivity of the layers is considered to be constant. The homogeneous local power density is 10 times higher than the homogeneous non-local power density. The kernel power density is 100 times higher than the homogeneous local power density. It can be concluded that the kernel power density is 1000 times higher than the non-local power densities. The power deposited at the coating layers is neglected. Then for steady state, an analytical result can be derived:

$$\begin{cases} T(r) = -\frac{\dot{Q}'''_f}{6k_1}(r^2 - R_1^2) + T(R_1) & 0 < r < R_1 \\ T(r) = \frac{\dot{Q}'''_f R_1^3}{3k_i}(\frac{1}{r} - \frac{1}{R_i}) + T(R_i) & \text{for } i = 2,3,...5 \text{ and } R_{i-1} < r < R_i \end{cases} \tag{3.21}$$

The volume-averaged kernel temperature is chosen as the representative fuel temperature that is used to calculate nuclear feedback:

$$\begin{aligned} T_f &= T_m + \sum_{i=2}^{4} \frac{\dot{Q}'''_f R_1^3}{3k_i}(\frac{1}{R_i} - \frac{1}{R_{i+1}}) + \frac{\int_0^{R_1} 4\pi r^2[-\frac{\dot{Q}'''_f}{6k_1}(r^2 - R_1^2)]dr}{\frac{4\pi}{3}R_1^3} \\ &= T_m + \sum_{i=2}^{4} \frac{\dot{Q}'''_f R_1^3}{3k_i}(\frac{1}{R_i} - \frac{1}{R_{i+1}}) + \frac{\dot{Q}'''_f R_1^2}{15k_1} \end{aligned} \tag{3.22}$$

For the transient case, a finite difference method is applied to solve the heat transfer Equation 3.16. Details are presented in Appendix C. For the test purpose, the code is

applied to calculate the following transient model:

- Fixed boundary temperature:

$$T(R_c, t) = T_m \tag{3.23}$$

  where R_c is the radius of the coated particle and T_m is a constant temperature.

- Constant power density in the kernel zone, and power densities of other zones are 0:

$$\begin{cases} \dot{Q}'''(r,t) = \dot{Q}'''_f & \text{for } 0 < r \leqslant R_f \\ \dot{Q}'''(r,t) = 0 & \text{for } R_f < r \end{cases} \tag{3.24}$$

- All layers have the same initial temperature, which is equal to the boundary temperature:

$$T(r, 0) = T_m \tag{3.25}$$

The kernel and coating layers are divided into fine meshes and their parameters are displayed in following table:

Layer	Fine meshes	Thermal conductivity $(W/(cm * k))$	ρC_p $(J/(cm^3 * k))$	Power density (W/cm^3)
UO_2 Kernel	5	0.0316	3.526	1958.46
Porous Carbon	2	0.005	1.936	0
IPyC	1	0.04	3.673	0
SiC	1	0.16	5.243	0
OPyC	1	0.04	3.673	0

Table 3.1: The parameters of the coated particle in free transient

Both the initial temperature and the boundary temperature T_m are 1048.05 $°C$. According to the limitation of the time step (see Eq. C.7), an interval of 0.0002 s is chosen as the time step. Additionally, a CFX model with the same initial and boundary condition is performed to verify the kernel model [41]. The radial temperature profile of the coated particle in steady state case calculated with both CFX and the new kernel model are shown in Figure 3.2. The maximum difference of the two model is about 1.5 $°C$.

Figure 3.3 shows the temperature transient of different coating layers in 0.5 s. The figure shows that the temperature will not increase after 0.3 s, which means the system is in equilibrium. Therefore, the relaxation time of this system is about 0.3 s. It can be seen that the temperature of the kernel increases faster than that of the other layers. As mentioned, different layers actually have different thermal responses. Figure 3.4 shows the comparison of the calculated result between the CFX model and the new kernel model. It shows a good agreement in the different time point.

The power density of the kernel, which is presented in Table 3.1, corresponds to the reactor power density 10 MW/m^3. The temperature difference between the kernel and moderator is about 30 $°C$. The temperature difference is proportional to the power density, so the average power density of 4.6 MW/m^3 of the PBMR is related to a temperature difference of 13.8 $°C$, which is not in the order of 3 to 6 $°C$. If a more precise calculation is required, the new kernel model is necessary. The fuel kernel's temperature increases very fast and the coated particle can rebuild new heat balance in

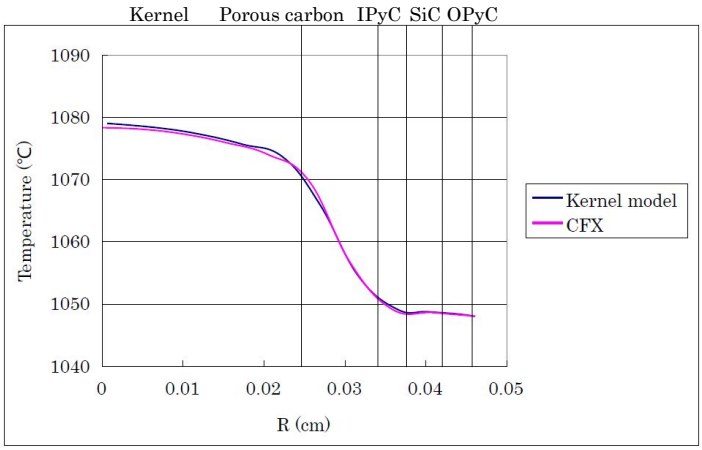

Figure 3.2: Temperature profile of the coated particle in steady state case

less than 0.3 s after inserting positive reactivity. According to the temperature feedback, the increasing reactivities can be controlled immediately. This feedback process is even more effective to control the reactor than the delayed neutrons in HTGRs.

The code is implemented into MGT-3D to calculate the representative fuel temperature of pebbles in each spatial mesh. The homogeneous temperature calculation of MGT-3D results in an averaged pebble surface temperature of the representative pebble.In the next step, the heterogeneous calculation analyzes the temperature distribution in the representative pebble. It divides the symmetrical spherical pebble into several shells in its radial direction. An one-dimension heat diffusion equation is used to calculate temperature distribution from pebble surface to pebble center. Since the boundary temperature, which is the moderator temperature in kernel model, is fixed, it is only needed to calculate temperature differences among kernel layers. If it is assumed that temperature differences between the moderator and the kernel of all pebble shells are equal, the fuel temperature can be obtained by adding this temperature difference to the moderator temperature. For a transient calculation of the reactor core, the initial condition of the kernel temperature calculation is the steady state temperature distribution of coated particles, which can be obtained from Equation 3.21. Homogeneous power densities are extrapolated by Equation 3.7, and the power density of coated particles is determined by:

$$\begin{cases} \dot{Q}'''(r) = \dot{Q}'''_f = \kappa \dot{Q}'''_l & \text{for } 0 < r < R_1 \\ \dot{Q}'''(r) = \dot{Q}'''_{nonl} & \text{for } r > R_1 \end{cases} \tag{3.26}$$

where κ is the inverse of kernel volume packing fraction in the pebble, and $\dot{Q}'''_{nonl}$ is the non-local power density. All of the required parameters are extracted from MGT-3D to conduct the kernel temperature calculation, and the representative fuel temperatures,

which are used as temperature feedback on nuclear calculations, can be achieved.

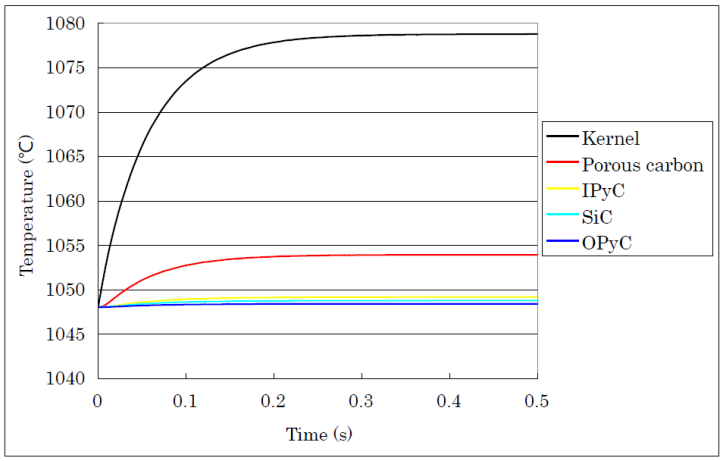

Figure 3.3: Temperature transient of different coating layers in 0.5 s

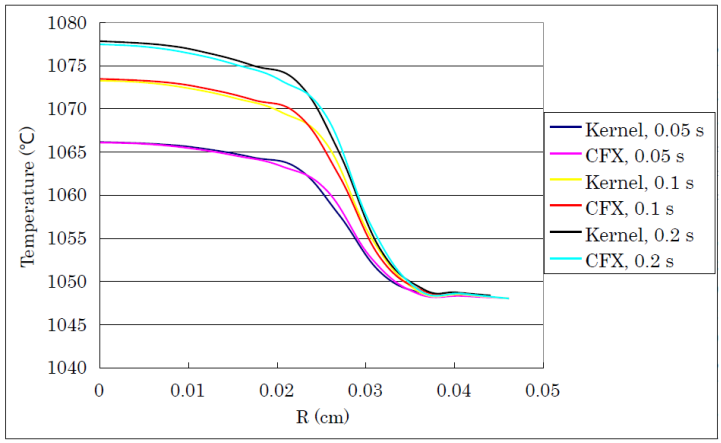

Figure 3.4: Comparison of the temperature distribution between the calculation of the CFX model and the new kernel model in different time point

3.1.3 Application of Kernel Model for PBMR

The PBMR was a helium cooling pebble bed module reactor concept. It was designed by PBMR Ltd. In order to verify existing HTR code system and develop better simulation tools to analyze the neutronics and fluid mechanics behavior for designed accidents, the Nuclear Energy Agency (NEA) organized several benchmark exercises [42]. In this section, the following PBMR operation phases, which include both steady

state and transient cases, are chosen to study the physics of the feedback of the kernel temperature on neutronics and fluid mechanics:

- Steady state: The reactor is operated at full power of 400 MW. It uses helium as the primary coolant. The primary coolant pressure is 9 MPa, and the inlet and outlet gas temperatures are 500 $°C$ and 900 $°C$, respectively. In the benchmark definition, the reactor runs from initial core to equilibrium core, where the equilibrium core is defined as the reactor operational state in which no significant changes can be observed in the properties of the core, e.g. the k_{eff}, power and temperature profile, gas flow and gas inlet/outlet temperature. During the transitional period, the reactor operates at full power and with control rods inserted 2.0 m below the bottom of top reflector and therefore 1.5 m alongside the pebble bed [42].
- Control rod withdrawal accident (CRWA): Equilibrium steady state with full-load operation is completed in the beginning (0 s), which is also defined as initial condition. The simulation runs at free transient for 300 s. Then all of the control rods are concurrently removed with a velocity of 1 cm/s and totally withdrawn in 230 s. After that, the reactor operates at free transient.
- Control rod ejection accident (CREA): In the beginning of 300 s, the reactor operates at the same condition as with control rod withdraw accident. The accident starts from 300 s and all the control rods are ejected in 0.1 s. The reactor loses forced coolant and is depressurized at the same time. Then, the reactor runs at free transient.

The system code VSOP is used to simulate the so-called running in phase of the reactor until the equilibrium core is achieved. Whereafter, the interface code which connects MGT-3D and VSOP provides MGT-3D with required nuclear data to perform the steady-state and transient analysis. Since the reactor is symmetrical, a 2D cylinder model is used to simulate it. The calculation model of the reactor is shown in Figure 3.5. Both the new kernel model and the overheating model are applied to calculate fuel temperature and the calculation results on local power density, solid temperature, kernel temperature are compared.

In the overheating model, the fuel temperature can be obtained by Equation 3.6 in the steady state case. The equation shows that greater heat flux resistance of the coated particles which have the same power density and moderator temperature will result in higher fuel temperature. Due to the Doppler effect, the resonance absorption cross section is higher. Therefore, the reactivity of the reactor will decrease with the increasing of α'_f (see Fig. 3.6). With linear extrapolation of moderator temperature and local power density during the nuclear time intervals, the fuel temperature can be obtained by Equation 3.13 in the transient case. This equation shows that the thermal response of the fuel kernel is quite dependent on the heat flux resistance α'_f. According to the temperature feedback on the reactivity of the reactor, different values of α'_f will result in different inverse reactor periods ω in transient case. The inverse reactor period is the variance ratio of the global reactor power density, which is defined by:

$$\omega = \frac{1}{\dot{Q}'''} \frac{\partial \dot{Q}'''}{\partial t} \tag{3.27}$$

A higher value of α'_f means that the coated particle is more inert to thermal conduction, and it takes longer for the nuclear heat to be transferred out of the kernel. The global reactor power changes more smoothly because of negative temperature feedback. For the

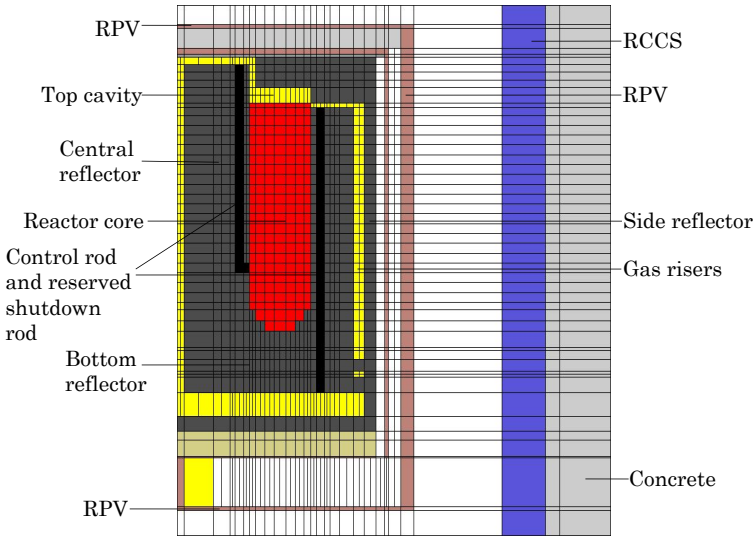

Figure 3.5: Calculation model of the PBMR

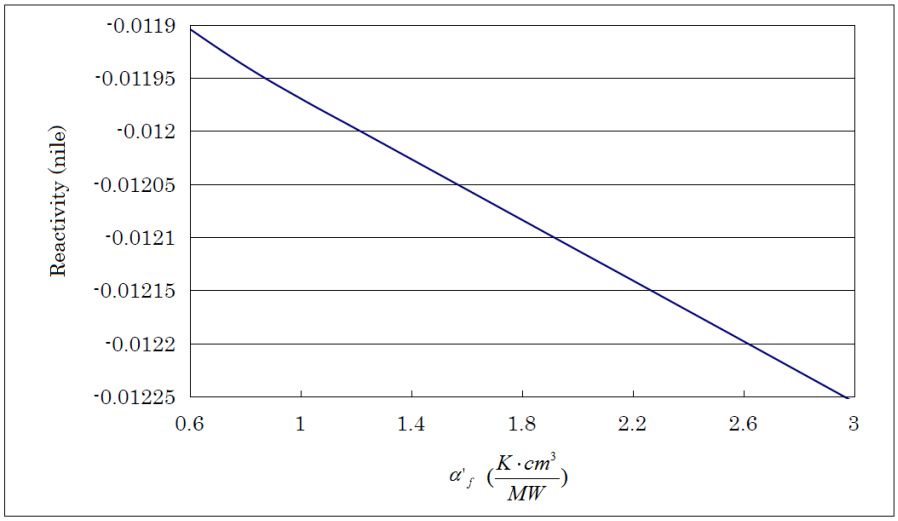

Figure 3.6: Reactivity dependence on α'_f in steady state

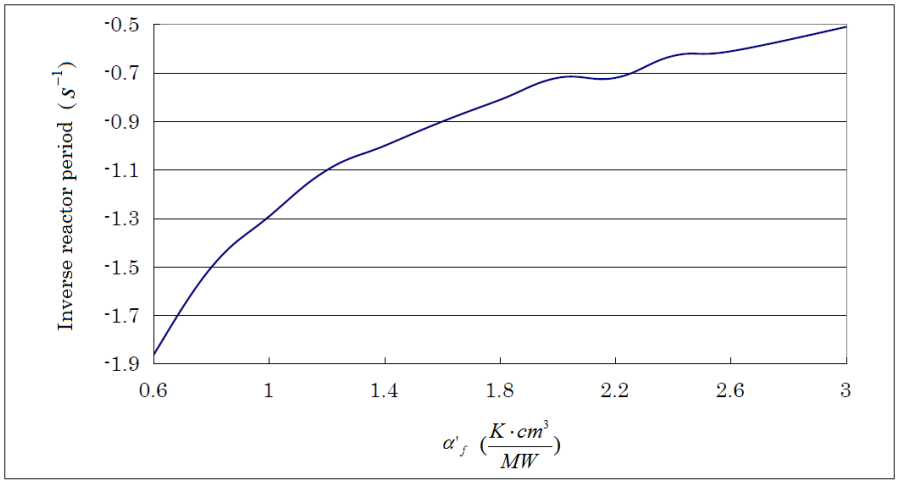

Figure 3.7: Dependence of the inverse reactor period on α'_f at 1 s after control rod ejection accident

case in which the reactor power decreases during the transient process, ω will increase with the increasing kernel heat flux resistance at the same time point. The value of ω at 1 s after a control rod ejection accident was chosen as an example to show the dependence (see Fig. 3.7).

With $\alpha'_f = 1.0\ K \cdot m^3/MW$, which is suggested by the overheating model in the former simulation, the local nuclear power distribution and solid temperature of equilibrium core of the PBMR are shown in Figures 3.8 and 3.9. Because fresh fuel pebbles are always loaded into the reactor from the top, and because neutron flux will decrease in the top cavity zone, the maximum power density is in the top-center of the core. In the radial direction, the center and side reflectors are used to reflect thermal neutrons back into the reactor, so there are power peaks in the radial boundary of the reactor core. The primary coolant is forced to rise up along gas risers to the top cavity. Then the coolant flows downward from the top through the pebble bed. Gas temperature is raised throughout the flow path. The solid temperature increases along the gas flow in the pebble bed. In the central reflector of the PBMR, there is a reactor shutdown system. In order to keep the function of this system, it is cooled by a bypass flow. There is only a small amount of heat is deposited here by γ transport. As a result, the solid temperature in the reflector is much lower than the reactor core temperature.

Considering that the properties of coating materials and even the shape of coated particles will change with neutron irradiation and high temperature, it is not necessary to adopt temperature-dependent conductivity rules in the new kernel model. The discretization meshes' number, heat conductivity, and heat capacity, which are presented in Table 3.1, are still adopted. The power density and moderator temperature in the next nuclear time interval are linearly extrapolated with Equations 3.7 and 3.8 in the transient calculation. The initial condition is interpolated from the temperature distribution of the steady state (see Eq. 3.21). MGT-3D with the kernel model simulation shows that the reactivity is -1.22 *nile* in steady state, which is close to the result with

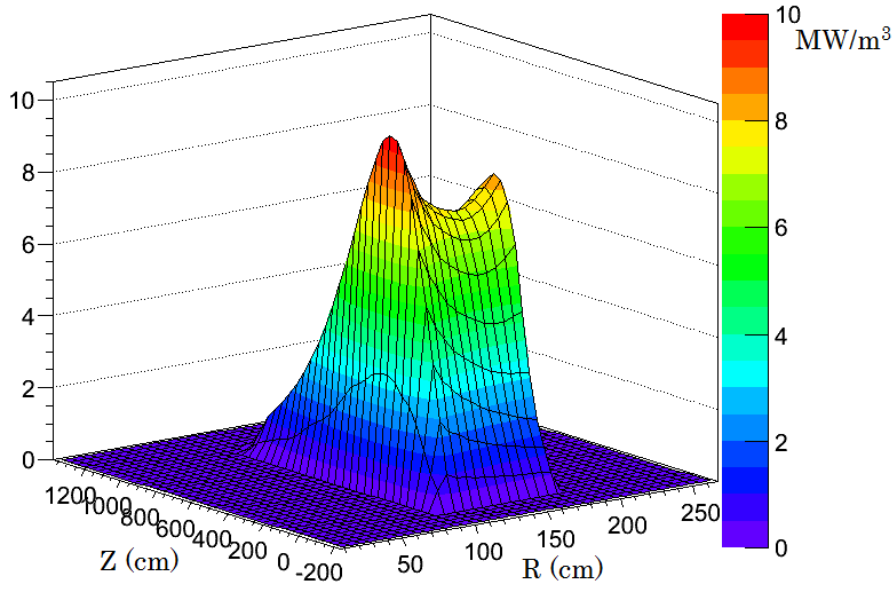

Figure 3.8: Local nuclear power density of PBMR-400

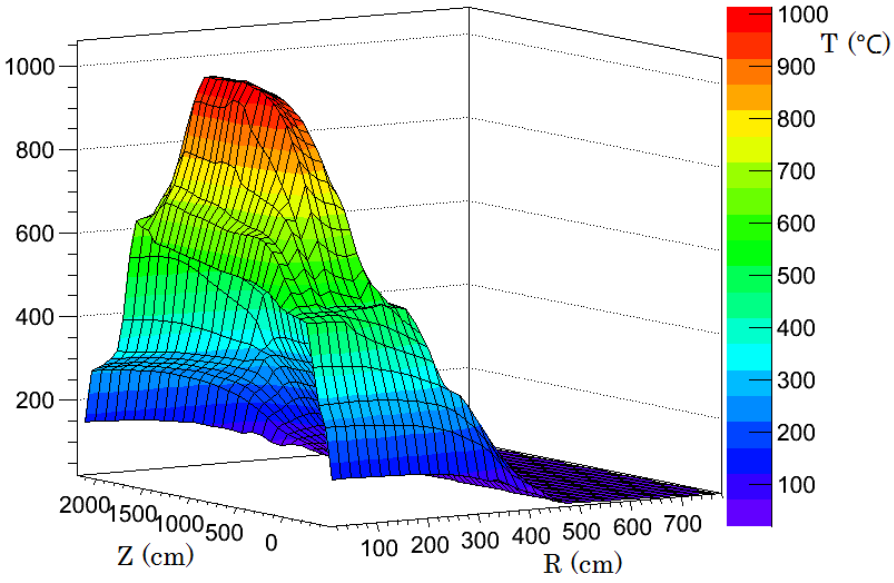

Figure 3.9: Solid temperature distribution of PBMR-400

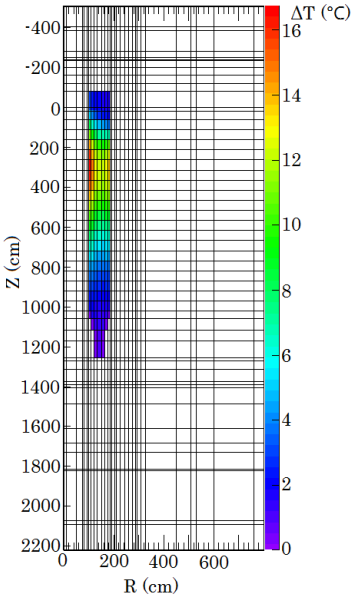

Figure 3.10: Kernel temperature difference in steady state

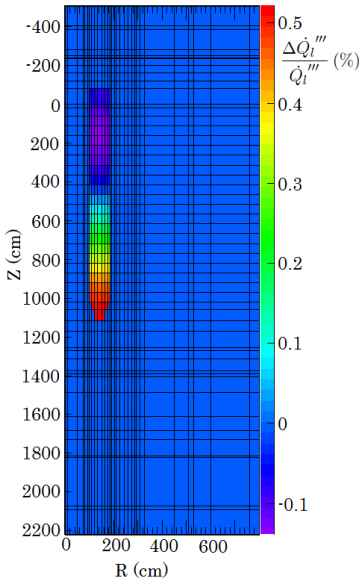

Figure 3.11: Local nuclear power density difference in steady state

$\alpha'_f = 2.6\ K{\cdot}m^3/MW$. However, the formerly suggested α'_f is $1.0\ K{\cdot}m^3/MW$. Obviously, the suggested α'_f underestimates the heat flux resistance of coating layers.

Simulation results with $\alpha'_f = 1.0\ K{\cdot}m^3/MW$ are chosen as reference data to compare with the kernel model's results. In each homogeneous mesh of MGT-3D model, a 1D heat conduction equation is solved to obtain temperature distribution in the divided shells of representative pebble. A raised temperature is added to the shell temperature to gain kernel temperature. Here, the temperatures of kernel in the center shell of the representative pebble are compared (see Fig. 3.10). Equation 3.6 denotes that kernel temperature is proportionate to local nuclear power density. The temperature difference ΔT should be proportional to $\dot{Q}_l'''$ as well. Consequently, the significant temperature difference appears where the high power density is generated. That is the reason that maximum temperature differences appear in the top-center areas, which are close to the inside and outside reflectors. All of the temperature differences are positive values, which also reveals that $\alpha'_f = 1.0\ K{\cdot}m^3/MW$ is too low to represent the equivalent heat flux resistance of coated particles.

It is also interesting to check the kernel temperature difference's impact on local nuclear power density, which is presented in Figure 3.11. The power is less than the reference data in the zone with a high temperature difference. Oppositely, it is higher in the zone with low temperature difference. The reasons are as follows: first, the simulation uses fixed total power to normalize neutron flux, which means the total neutron number is fixed; second, the local nuclear power density is proportional to thermal neutron flux, and former analysis demonstrates that temperature difference is proportional to local nuclear power density; third, higher temperature leads to stronger feedback on resonance absorption. Therefore, the neutron flux is redistributed. Additionally, the neutron flux in the zone that has high temperature difference will decrease and the neutron flux in

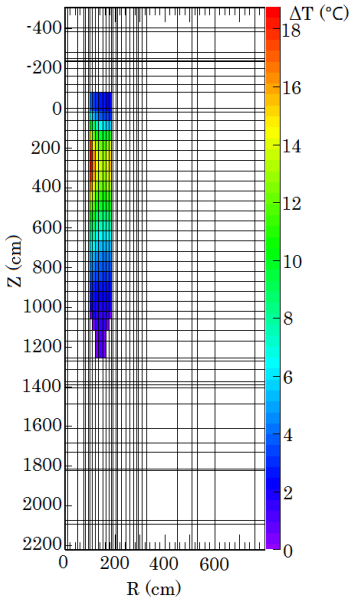

Figure 3.12: Kernel temperature difference in the center of pebbles at 30 s after CRWA

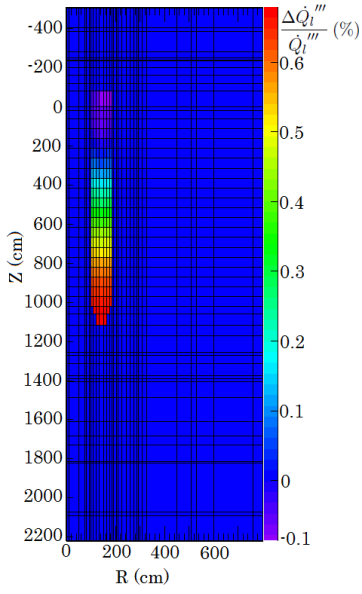

Figure 3.13: Local nuclear power density difference at 30 s after CRWA

the zone which has low temperature difference will increase. This feedback mechanism provides us with the hint that the power profile of the reactor can be flattened a little bit by using low conductivity material to coat the kernels.

Kernel temperature, which is directly dependent on heat flux resistance, has a distinct difference between these two models. Generally, the nuclear cross section makes a switch when the temperature varies in the magnitude of a hundred degrees Celsius. Therefore, the nuclear power density does not change significantly when different models are adopted. The homogeneous temperature differences between these two models are compared as well. The minimum difference is about $-0.4\ ^{\circ}C$ and the maximum difference is about $0.06\ ^{\circ}C$. These differences are quite small compared to the core temperature, which is almost a thousand degrees Celsius. Some other macroscopic parameters, e.g. gas temperature, gas pressure, non-local heat, and so on are also not very sensitive to the kernel temperature.

For the transient case, the study of the inverse reactor period's dependence on heat flux resistance proves that the reactor has different thermal and nuclear responses to different thermal parameters of coated particles. MGT-3D transient simulation includes two main parts (see Fig. 2.1), which are nuclear calculation and fluid mechanics calculation. Each temperature (fluid mechanics) time step includes one or several nuclear time steps. For the simulation of the control rod withdrawal accident, which belongs to slow transient, the temperature time step of MGT-3D is about 10 s or greater, and it contains several nuclear time steps. The nuclear time step is of several seconds. It is still much larger than 0.3 s, which is the relaxation time of the coated particles. Therefore, the kernel temperature evolution during each nuclear time interval is equivalent to a quasi-static state. Figures 3.12 and 3.13 show the kernel temperature difference and local nuclear

power density difference relative to local nuclear power density respectively at 30 s after control rod withdrawal accident. These differences look similar to the results of steady state. For the steady state and the CRWA simulation, the maximum and minimum differences with the overheating model and the new kernel model are sub-equal and appear in the same zones because each time step can be considered as a quasi-static state. It follows that using the overheating model or the new kernel model will not make a significant difference if the right heat flux resistance is applied in slow transient case.

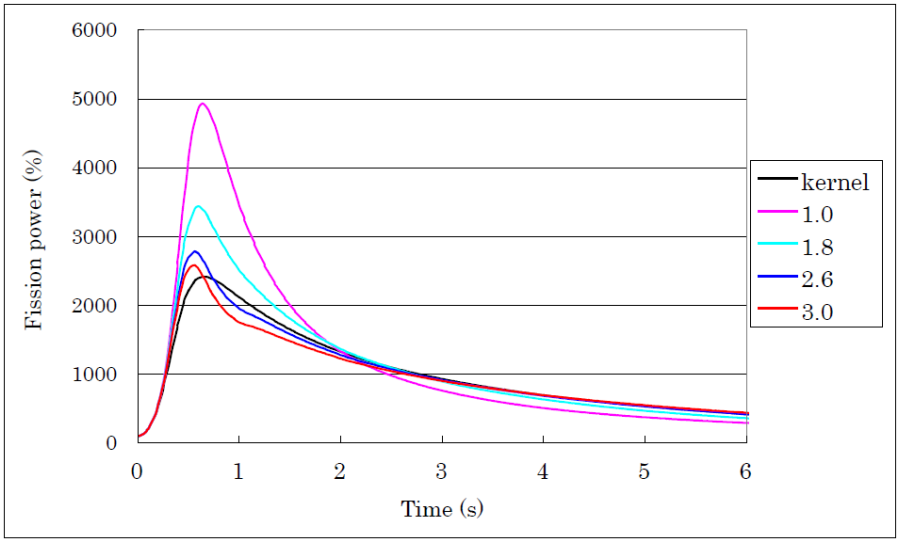

Figure 3.14: Power transient in CREA

There are some extreme cases where power varies significantly in a short period. For example, in the control rod ejection accident, the reactor power rises to more than 20 times that of the initial power within 1 s (see Fig. 3.14). The accident happens at 300s. All of the control rods are ejected in 0.1 s, and the reactor becomes depressurized at the same time. At 300.6 s, the reactor achieves the maximum power. The increasing rate of nuclear and thermal parameters are very high. According to the convergence criteria of MGT-3D, a small time step should be chosen, which is comparable to the relaxation time of coated particles. In this kind of accident, the overheating model and the new kernel model may give different results. The kernel temperature has differences as presented in steady state and slow transient. Large differences are expected in homogeneous solid temperature and local nuclear power density. Figure 3.15 displays the solid temperature at 30 s after the accident. The minimum difference is $-24.2\ ^{\circ}C$. The new kernel model generally gives a lower solid temperature than the overheating model with $\alpha'_f = 1.0\ K \cdot m^3/MW$. In Figure 3.16, however, the comparison shows that the new kernel model has bigger local power density at 330 s. Reactor power increases at the beginning of the accident and then decreases according to temperature feedback. The kernel model has higher heat flux resistance and slower nuclear and thermal responses. Therefore, the power density increases and decreases more slowly. It can be found that power density with the overheating model is higher than that with the kernel model if one compares the power densities between 300.01 s and 300.6 s.

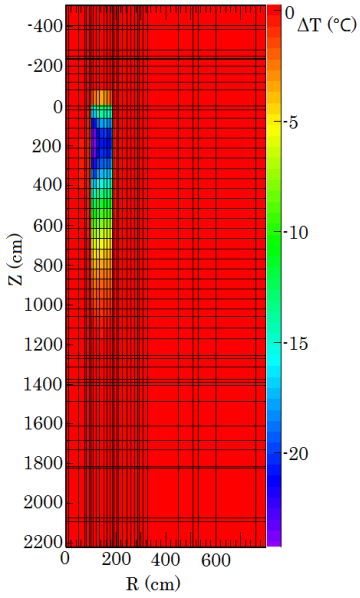

Figure 3.15: Homogeneous solid temperature difference at 30 s after CREA

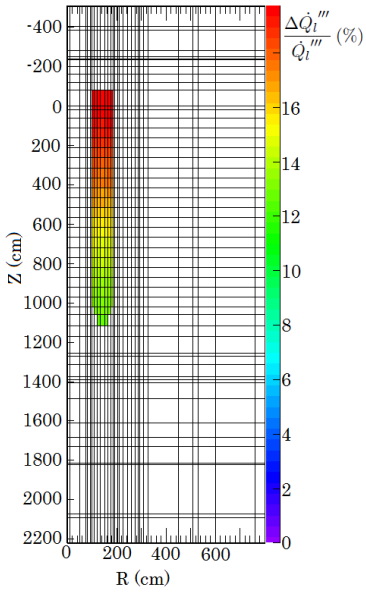

Figure 3.16: Local nuclear power density difference at 30 s after CREA

In summary, the overheating model is proper for steady state and slow transient simulation, and agrees with the new kernel model if the right α_f' is given. But for fast transient, the significant differences in macroscopic parameters such as homogeneous solid temperature, and power density can be observed. The new kernel model can be used to determine the reference value of α_f' or to replace the kernel temperature calculation subroutine of MGT-3D. Additionally, the heat conductivities of coating layers and the kernel are temperature and neutron dose dependent. The equivalent heat flux resistance is not a fixed value in different zones of the reactor, which means that the method of using a global parameter α_f' should be reevaluated. Moreover, the kernel temperature difference of these two models is proportional to power density. In extending MGT-3D to the reactor with high power density (Molten salt cooled pebble bed reactor), the new kernel is expected to behave better than the overheating model. The new kernel model also has its own limitations. It takes more calculation time than the overheating model because it calculates the detailed temperature profiles of representative coated particle. Furthermore, the more layers the coated particles are divided into, the more calculation time is required. However, the 10 layers that are given in Table 3.1 can already gain enough precision. It increases the total calculation time to about 20%, which is acceptable.

3.2 Heterogeneous Temperature Analysis of Block Type Prismatic Reactor

In MGT-3D, the fuel and moderator temperatures are calculated in each nuclear time interval by solving the heat conduction equation [43], which is the heterogeneous temperature analysis of the fuel element. The average fuel and moderator temperatures of the fuel element are required to determine the nuclear cross sections. The heat flow that is transferred from the surface of the fuel element to the surrounding coolant is important to calculate the gas and homogeneous solid temperature. The old version of MGT-3D has only the subroutines to calculate the heat transfer in the pebble fuel element. The temperature distribution of the cylindrical fuel element is not solved. Therefore, it is an important issue to write new subroutines for the fuel element temperature analysis when extending the recent MGT-3D code for block type prismatic reactor [44, 45].

3.2.1 Unit Cell Analysis of GT-MHR Fuel Block

The test reactor Dragon, that was built in the UK and operated from 1965 to 1975, used the design of TRISO fuel particles embedded in a carbonaceous matrix with the shape of hollow cylinder [46]. The fuel matrix is located in the hexagonal graphite block (see Fig. 3.17). There are six hollow cylindrical fuel matrices which are cooled by the gas flowing through their center. The central position is reserved for the various testing fuels. Later, the U.S. built a gas cooled high temperature reactor: the Peach Bottom Unit 1 [47]. It is a power reactor loaded with hollow fuel rods. The BISO coated particles are embedded in the fuel rods [48]. Based on the operation experience of these graphite moderated and gas cooled, GA built the HTGR: Fort St. Vrain reactor (FSVR). In the FSVR design, the fuel rods are inserted in the hexagonal graphite block, which is cooled by helium [49]. The pin-in-block design makes it easy to shuffle and load the fuel elements. It also behaves very well in mechanic and thermal hydraulics [50]. The reactor achieved criticality in 1975 and was operated from 1976 to 1983. The success of FSVR leads to some other design with very large thermal power and with module design.

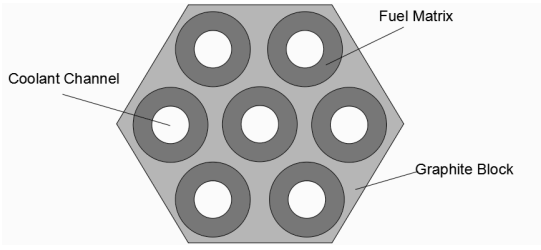

Figure 3.17: The cross section of Dragon fuel element [46]

The following Module Helium Reactors (MHR) of U.S. all use the pin-in block design. The Gas Turbine Module Helium Reactor (GT-MHR) that is designed by General Atomic is based on the FSVR. The arrangement of its fuel rod and coolant hole in the hexagonal fuel block is similar to the fuel block design with FSVR. The dimensions of fuel rod and coolant hole have some differences. Figure 3.18 presents one type of GT-MHR fuel block which does not have control rods or reserved shutdown guide holes. It

can be seen that the fuel rods and coolant holes are separated. They are arranged in the block based on a series of regular hexagon. The center of the fuel rod is the vertice, and the coolant hole is in the center of the hexagon. The heat is generated in the fuel rod and transferred out by conduction to the graphite matrix, which is cooled by helium.

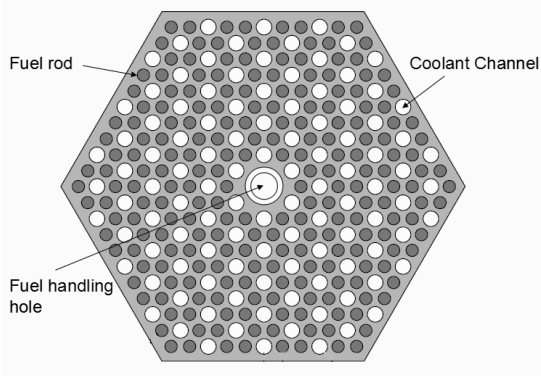

Figure 3.18: The cross section of GT-MHR fuel element [50]

In the MGT-3D simulation, the temperature distribution of fuel pebble is obtained by solving the heat conduction equation. The proposal to extend it to block type reactor was already mentioned in the reference [43]. It is coupled with the neutronics simulation, and the macroscopic scale temperature solving, which is the homogeneous temperature solving, and the microscopic scale temperature solving. With regards to block type reactor, the meso-scale temperature solving involves calculating the temperature distribution of the pitch of the channels within a block.

Normally, one MGT-3D mesh, which is built on R/Z/Φ coordinates, includes several fuel rods and coolant holes. To solve the detailed temperature distributions of these fuel rods, a great amount of calculation is required, especially considering the coupling with the homogeneous calculation of the whole core. According to the symmetry of the arrangement of fuel rod and coolant holes, the smallest symmetry unit of the fuel block is a triangular element, which is shown in Figure 3.19. It is used to represent a block or part of a block for each homogeneous mesh. The unit cell consists of 1/12 of a coolant channel and 1/6 of an adjacent fuel channel. They are separated by a graphite moderator. After the irradiation of fast neutrons, the graphite will shrink. Therefore, a gap is assumed between the moderator and the fuel rod. The unit cell is a right triangle with one angle of 30°, and all of the straight edges of the triangle are symmetric planes.

The local nuclear heat deposits in the fuel rod zone, and part of the non-local nuclear heat deposits in the moderator zone. The heat transfer mechanism in the unit cell is as follows: conduction in the fuel rod, conduction and thermal radiation across the gap, conduction in the moderator, and convection over the gas-solid boundary. The thermal radiation across the gap is equivalent to conduction by using the effective thermal conductivity. It is a two dimension system. The basic heat transport equation to be solved for the unit cell in the polar coordinate system is:

$$\rho C_p \frac{\partial T(r,\phi,t)}{\partial t} = \nabla k \nabla T(r,\phi,t) + \dot{Q}''(r,\phi,t) \tag{3.28}$$

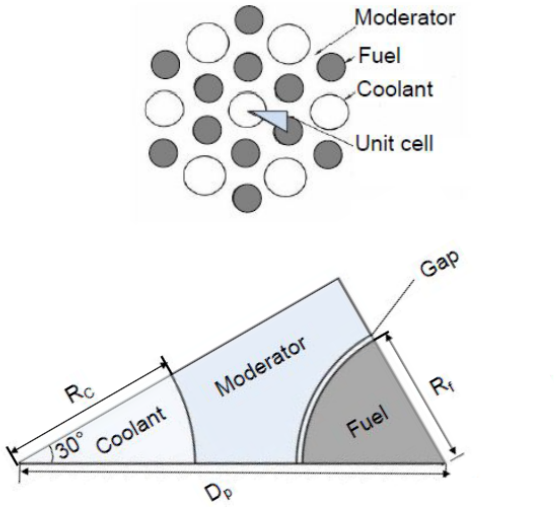

Figure 3.19: Unit cell of GT-MHR fuel block

For the boundary condition, the edges of the triangle are assumed to be adiabatic, and the curved edge that represents the coolant channel wall is specialized as forced convection boundary condition. The radial temperature gradient of the reactor is about $2-3\ K/cm$ in the macroscopic scale's point of view. The heat that is removed by conduction in the reactor core can be neglected. Therefore, the assumption of the adiabatic boundary in the symmetric plane is reasonable. The heat transfer coefficient on the surface of the coolant hole is characterized by the Nusselt number and the Reynolds number. The coolant temperature is considered to be the same value in the whole gas bulk.

Integrating both sides of Equation 3.28 with respect to the area and apply divergence theorem, yields:

$$\iint_s \rho C_p \frac{\partial T(r,\phi,t)}{\partial t} ds = \oint_l k \nabla T(r,\phi,t) d\vec{l} + \iint_s \dot{Q}''(r,\phi,t) ds \tag{3.29}$$

The control volume method is used to the equation [51]. The meshes surrounding the target mesh are sketched in Figure 3.20. The finite difference equation expressing the temperature change in the target mesh in time period Δt due to heat transfer in the target mesh is defined as:

$$\frac{\rho C_p (T'-T)\Delta S}{\Delta t} = \frac{k_N A_N}{\Delta X_N}(T_N - T) + \frac{k_S A_S}{\Delta X_S}(T_S - T) + \frac{k_E A_E}{\Delta X_E}(T_E - T) + \frac{k_W A_W}{\Delta X_W}(T_W - T) + \dot{Q}''\Delta S \tag{3.30}$$

where

Δt is the time interval,
ΔS is the area of the target mesh,
T and T' are the central temperatures of the target mesh at certain time point and after a period of time Δt respectively,

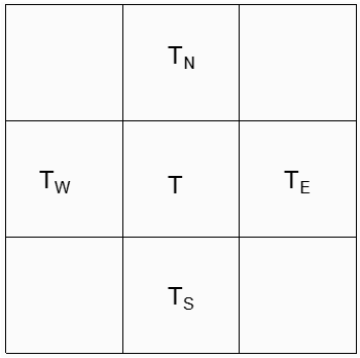

Figure 3.20: The control mesh of the numerical equation

T_N, T_S, T_E, T_W are the central temperatures of its surrounding meshes,
A_N, A_S, A_E, A_W are the average mesh surface areas between the target mesh and its surrounding meshes,
X_N, X_S, X_E, X_W are the distances between the center of the target mesh and the center of its surrounding meshes,
k_N, k_S, k_E, k_W are the composite thermal conductivities between the center of the target mesh and the center of its surrounding meshes.

The domain contains four zones: fuel compact, gap filled with stagnant gas, graphite moderator, and coolant. The radius of fuel rod and coolant hole are 6.2223 cm and 0.79375 cm respectively. The radius of the fuel rod hole is 0.635 cm. Thus, the thickness of the gap is about 0.0127 cm. The distance from the center of the fuel rod to the center of the coolant hole is 1.8796 cm. The coolant temperature is chosen as 926 $°C$. The thermal power of GT-MHR is 600 MW, and it is generated by 2.92 million fuel compacts. The average power density of fuel rod is about 33.41 W/cm^3. The power density of the fuel rod is set as 28 W/cm^3 in this simulation model, which is in the power range of GT-MHR.

Normally, the thermal conductivity and specific heat of fuel compact, gap, and graphite moderator are dependent on the temperature. To simplify the model, however, thermal conductivity and specific heat are fixed values during the calculation. With the coolant temperature of 926 $°C$, the solid temperature will be around 1000 $°C$. Therefore, the values of these parameters at 1000 $°C$ are chosen as the reference data [73]. They are shown in Table 3.2. The heat transfer coefficient is randomly taken as 0.93 $W/(cm^2K)$.

	Thermal conductivity $(W/(cm*K))$	$\rho C_p(J/(cm^3K))$	Emissivity
Fuel rod	0.0692	2.3614	0.8
Gap	0.0035	0.015	0
Graphite moderator	0.346	3.542	0.8

Table 3.2: Material properties of the simulation model

A CFX model with the same thermal parameters is built to verify the numerical model from above. In the CFX model, more than 10000 meshes are used, which provides

enough precision for the temperature calculation. Figure 3.21 shows the temperature distribution of the unit cell in the steady state case. The boundary temperature is 941 $^{\circ}C$. The heat generated in the fuel rod should be equal to the heat transferred out of the unit cell by convection. With a simple calculation, the calculated boundary temperature meets this requirement. The center temperature is about 1025 $^{\circ}C$. The temperature rises about 100 $^{\circ}C$ from the coolant to the center of the fuel rod. The temperature distribution in the fuel rod does not have exactly cylindrical symmetry due to the asymmetric boundary condition, but the temperatures do not have a large difference in the azimuthal direction.

Figure 3.22 shows the comparison of the calculation result between CFX and the unit cell analysis code along the bottom edge of the unit cell in the steady state case. The two calculation results fit very well. The unit cell analysis code uses $33(R) \times 16(\phi)$ meshes, which is much fewer meshes than the CFX model. Thus, the calculation speed of unit cell analysis code is much faster than CFX. The center temperature of the mesh adjacent to the coolant is about 945.8 $^{\circ}C$. It is 4.8 $^{\circ}C$ degree higher than the solid boundary temperature. There is small error in the first mesh. It can be improved by using more meshes. The center temperature of fuel rod by unit cell analysis code is about 1027.8 $^{\circ}C$. The temperature rises about 14 $^{\circ}C$ in the moderator zone, 29 $^{\circ}C$ across the gap, and 40 $^{\circ}C$ in the fuel element zone. The temperature does not change significantly in the moderator zone because the thermal conductivity of the graphite is very high. Because of the small thermal conductivity of the gap, the temperature jumps across the gap. The heat transfers across the gap by conduction and thermal radiation. The heat flux of thermal radiation is proportional to the fourth power of the surface temperature. The heat transported by thermal radiation is comparable to conduction when the surface temperature is more than 1200 $^{\circ}C$.

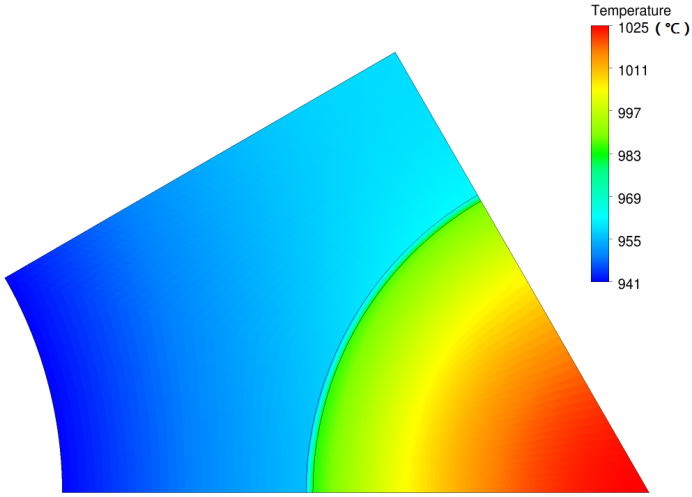

Figure 3.21: Steady state temperature profile of the GT-MHR unit cell with CFX simulation [52]

For the steady state case, the 2D unit cell analysis code is verified by the CFX model. However, it is still necessary to check whether they also fit in the transient case. A

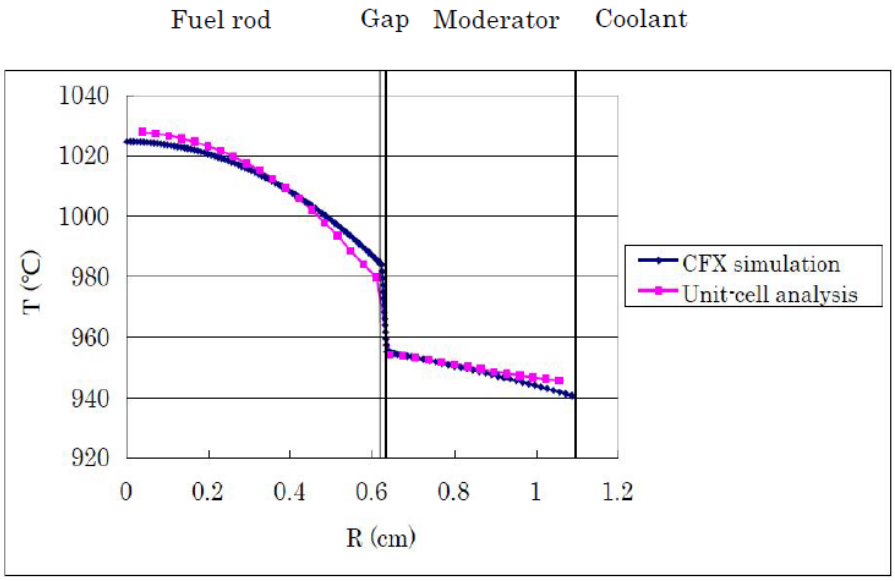

Figure 3.22: The comparison of fuel rod's central temperature of GT-MHR unit cell between unit cell analysis code and CFX in steady state case

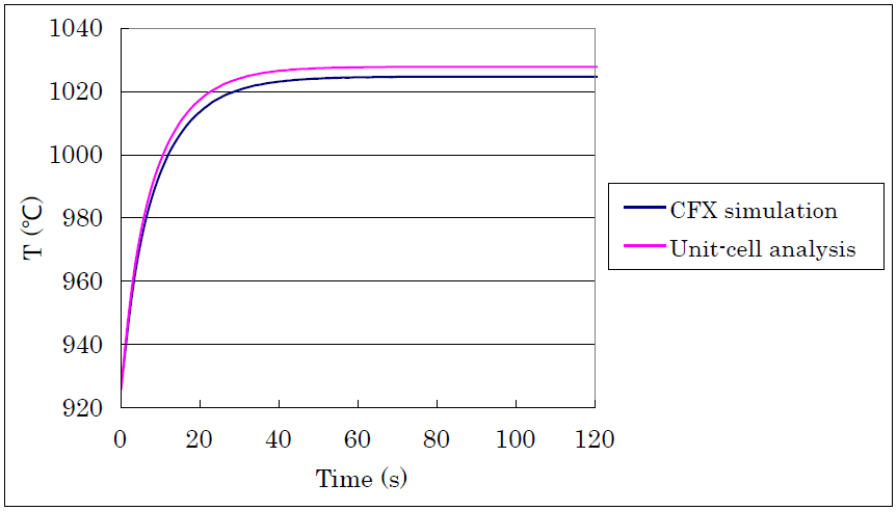

Figure 3.23: The comparison of fuel rod's central temperature of GT-MHR unit cell between unit cell analysis code and CFX in transient case

transient model is constructed to study the model. It is as follows:
All of the meshes have the same temperature in the beginning,

$$T(r,\phi,t)|_{t=0} = T_0 \tag{3.31}$$

the coolant temperature does not change during the transient process,

$$T(R_c,\phi,t) = T_0 \tag{3.32}$$

the heat is only generated in the fuel compact and the power density is constant during the transient,

$$\begin{cases} \dot{Q}'''(r,\phi,t) = \dot{Q}'''_f & \text{fuel element zone} \\ \dot{Q}'''(r,\phi,t) = 0 & \text{out of fuel element zone} \end{cases} \tag{3.33}$$

where T_0 is set as 926 $^\circ C$ as well. The power density, thermal conductivity, and specific heat are identical to the data of the steady state model.

Figure 3.23 displays the temperature evolution of the center of the fuel rod with both CFX and the 2D unit cell analysis code in 120 s. The center temperature of the fuel rod increases very quickly in the beginning and reaches the maximum value at about 90 s. This also means that the system achieves equilibrium in 90 s. The rates of temperature increase with two codes also fit very well.

In summary, the calculation results with CFX verify the 2D unit cell analysis code in the steady state as well as in the transient cases. The 2D unit cell analysis code uses much fewer meshes than the CFX model, but it can still achieve the precision. The temperature difference using these two codes is within 5 $^\circ C$ for steady state case. Furthermore, the relaxation times with these two codes for the transient case are equal.

3.2.2 Unit Cell Analysis of HTTR Fuel Block

The HTTR fuel block also has a pin-in-block design, but the arrangement of fuel rod and coolant hole is different from the design of GT-MHR's fuel block. In the HTTR fuel block, the fuel rod is inserted into the center of coolant hole. The gas flow goes through the annular channel between the fuel rod and the graphite block to cool down the structure. Figure 3.24 presents the typical structure of the fuel block with 33 fuel pins. It can be seen that the coolant hole, as well as the fuel rod are distributed symmetrically in the graphite block. The triangular unit cell marked in the figure is the smallest unit of symmetry to construct the main part of fuel block. For the block with 31 fuel pins, there are two coolant holes fewer than the 33 fuel pins block in the edge of hexagonal block (see Fig. 4.25). It does not break the symmetry of the fuel block. The triangular unit cell can still represent the construction of this kind of fuel block.

The unit cell of the HTTR fuel block consists of stagnant helium, a fuel compact, gap, graphite sleeve, coolant channel, and the graphite matrix of the hexagonal block from the center to the boundary. The center of the fuel rod is filled with stagnant helium to reduce the temperature peak in the fuel rod and to retain the gaseous fission products. This stagnant helium and the fuel compacts are sealed in the graphite sleeve. The nuclear energy is generated in the annular fuel compacts, transferred across the gap by conduction and thermal radiation, then transported in the graphite sleeve by conduction, and finally transferred by convection into the coolant. There is also a small part of heat transferred across the coolant channel by thermal radiation to the opposite graphite matrix.

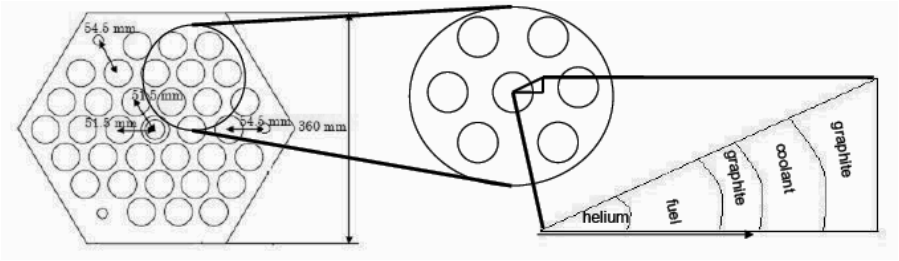

Figure 3.24: Unit cell of HTTR fuel block

The unit cell is a right triangle. The angle of the fuel rod part is 30°. It includes 1/12 of the fuel rod and coolant channel. The three edges of the triangle are the symmetric planes of the structure, like the unit cell of GT-MHR fuel block. The heat going into the unit cell across the triangle edges is equal to the heat going out of the unit cell across the edges. Thus, the boundary can be considered adiabatic. The main part of the nuclear energy is converted to heat locally in the fuel compacts. The rest of the nuclear energy is converted to heat in the graphite sleeve and moderator, which is the non-local heat.

To obtain the temperature distribution in the unit cell, the heat conduction Equation 3.28 is solved with the given boundary conditions. As mentioned, the edge of the unit cell is adiabatic. The heat is taken away by the coolant. Although a temperature gradient exists in a thin layer of coolant that is close to the solid surface, it can be neglected in the calculation model. The coolant temperature is assumed to be constant in the radial direction. There are two coolant boundaries in the unit cell. One is the outer surface of the graphite sleeve, and the other one is the inner surface of the graphite block. Heat exchanges between the solid and coolant in both surfaces.

In the unit cell, the radius of the central hole is 0.5 cm. The outer radius of fuel compact is 1.3 cm. The inner radius of the graphite sleeve is 1.3124 cm, consequently, the thickness of the gap is 0.0124 cm. The outer radius of the graphite sleeve is 1.7 cm, which is also the inner radius of the coolant channel. The outer radius of the coolant channel is 2.05 cm. The hypotenuse's length of the unit cell is about 2.97 cm.

The same numerical method is used to solve the temperature profile of the HTTR unit cell. At the same time, a CFX model is constructed to benchmark the unit cell analysis code's application on the unit cell of HTTR fuel block. In the calculation model, the power density of the fuel compact is 28 W/cm^3. The thermal properties of stagnant helium, the fuel compact, and the graphite block also use the data of Table 3.2. The graphite sleeve is fabricated from the same type of graphite as the graphite block. Therefore, the thermal conductivity and specific heat of these two parts are identical. The coolant temperature is assumed to be 926 $°C$ and the heat transfer coefficient is 0.93 $W/(cm^2K)$.

Because there is no heat source in the zone of the graphite block, the temperature of the graphite block will be equal to the coolant temperature in the steady state case. It is not necessary to calculate the temperature in the graphite block zone. Figure 3.25 displays the temperature distribution of the HTTR unit cell from the central stagnant helium to the graphite sleeve in the steady state case. The maximum temperature that is located in the center of the model is about 1098 $°C$. The solid temperature on the

surface of graphite sleeve is 939 $°C$. The temperature difference between the center of the model and the coolant is 172 $°C$. The coolant temperature is the same in the whole coolant channel, and the power density of fuel rod is homogenized. Thus, the temperature distribution from the center of the model to the boundary of graphite sleeve has cylindrical symmetry.

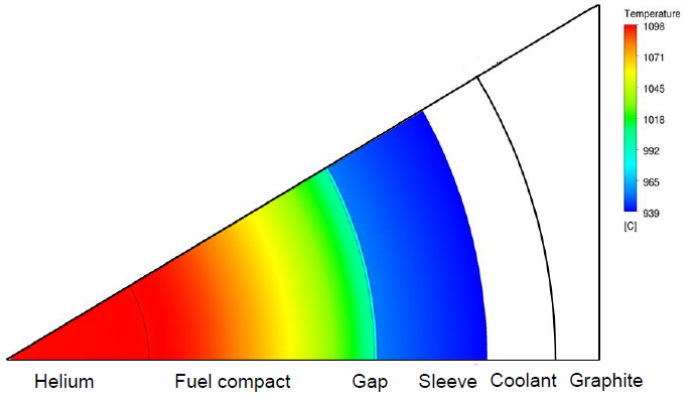

Figure 3.25: Steady state temperature profile of HTTR unit cell with CFX simulation [52]

The temperature distribution from central helium to the graphite sleeve in the radial direction is shown in Figure 3.26. The calculation results of both CFX and unit cell analysis code are presented. The temperature profiles from the central helium to the graphite sleeve, which are calculated with these two codes, fit very well. In order to obtain the precision, the CFX model uses much more meshes than the unit cell analysis code. The maximum temperature appears in the inner boundary of the annular fuel compacts. The difference in the maximum temperatures is about 1 $°C$. The temperature in the central stagnant helium is almost constant due to the lack of a heat source in this zone. The temperature does not rise significantly in the graphite sleeve because there is no heat source in the model, and its thermal conductivity is high. The variation of temperature across the gap is about 56 $°C$, which is almost 1/3 of the temperature difference between the maximum temperature and the coolant temperature. The temperature is proportional to r^2 in the fuel compact zone due to the heat source. The temperature difference between the outer surface and inner surface of fuel compact is about 91 $°C$.

For the transient case, the graphite block part of the triangle unit cell should be considered. To verify the unit cell analysis code in the transient case, a transient model, which is similar to the transient model of the GT-MHR unit cell, is created. The initial condition can also be expressed by Equation 3.31. There are two coolant boundaries in the unit cell of HTTR fuel block. The boundary conditions of the boundary close to the coolant are:

$$\begin{cases} T(R_s, \phi, t) = T_0 \\ T(R_c, \phi, t) = T_0 \end{cases} \tag{3.34}$$

where R_s is the outer radius of graphite sleeve, and R_c is the outer radius of coolant channel.

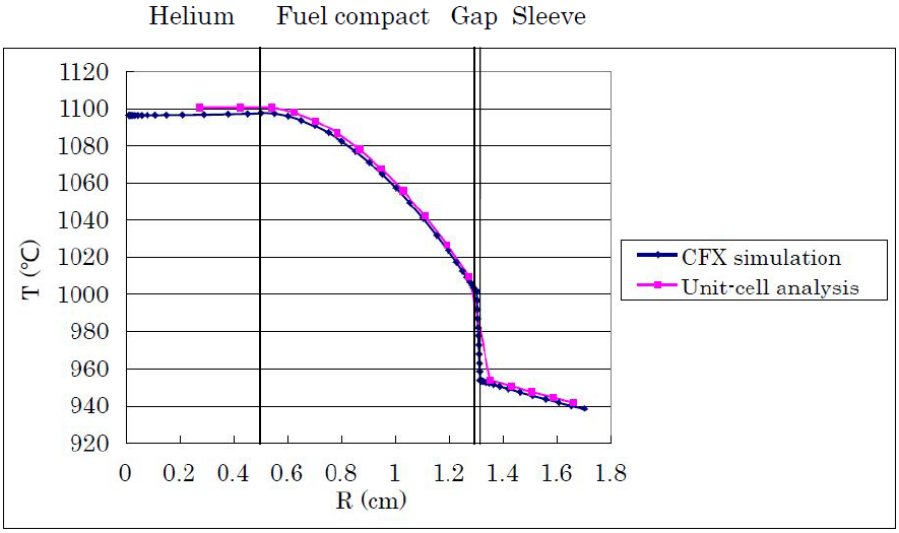

Figure 3.26: The comparison of fuel rod's central temperature of HTTR unit cell between unit cell analysis code and CFX in steady state case

Figure 3.27 shows the evolution of the temperature of the inner surface of the fuel compacts. The temperature variation curves with 2D unit cell analysis code and CFX almost coincide. The final temperature with CFX and 2D unit cell analysis code are 1099.4 $°C$ and 1100.8 $°C$ respectively. In the CFX model, the temperature difference achieves 99% of the final temperature difference between the initial temperature and equilibrium temperature at about 56 s. In the 2D unit cell analysis code, this also occurs at around 56 s. At about 60 s, system equilibrium is obtained.

It can be concluded that the calculation results for the HTTR unit cell with 2D unit cell analysis code are in agreement with the calculation result with CFX in the steady state as well as in the transient cases. The difference between these two codes is in 2 $°C$ in steady state case. For the transient case, these two calculation results obtain the same relaxation process. The unit cell analysis code can be implemented into MGT-3D to complete its simulation capability on block-type HTGRs.

3.2.3 1-D Unit Cell Models

In the MGT-3D code, the three figures, namely the maximum fuel temperature, which is used to evaluate the failure of coating layers, the average fuel temperature, and the moderator temperature, which are used to determine the nuclear cross section, are needed. For the pebble bed reactor, a 1-D calculation is applied due to the spherical symmetry of the fuel element. The basic idea for a cylindrical fuel element has already been discussed in the reference as well [43]. Figure 3.21 shows that the temperature does not have a significant difference in the same radius in the fuel rod zone of the GT-MHR unit cell. Figure 3.25 shows that the temperature profile of the HTTR unit cell has cylindrical symmetry. Thus, the 1D models will be a good approximation to calculate the modera-

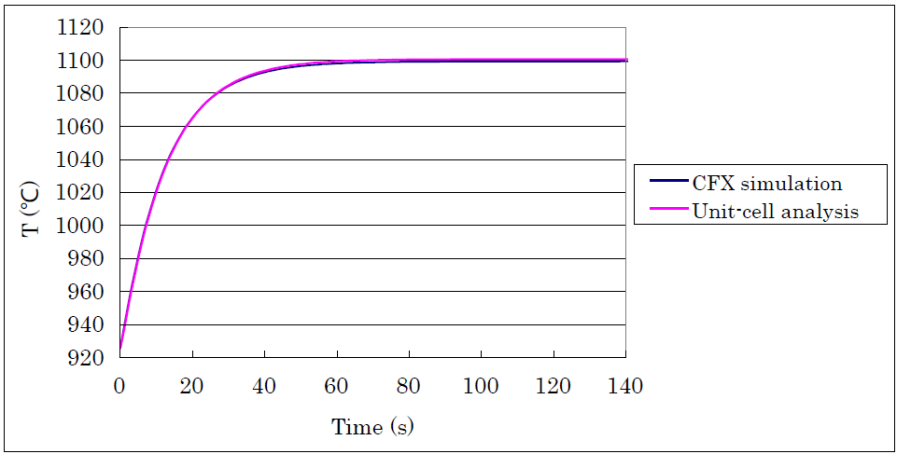

Figure 3.27: The comparison of central temperature of HTTR unit cell between unit cell analysis code and CFX in transient case

tor temperature and fuel temperature. The temperature profiles can be determined with some simple formulas [74].

The 1D heat transfer equation of the cylindrical fuel element is:

$$\rho c_p \frac{\partial T}{\partial t} = \frac{1}{r}\frac{\partial}{\partial r} r k \frac{\partial}{\partial r} T + q''' \tag{3.35}$$

For the steady state, the left hand side of the equation is zero. The general solution of the equation in steady state is:

$$T(r) = a + b ln(r) - \frac{q''' r^2}{4k} \tag{3.36}$$

where the constants a and b are determined by the boundary conditions. For the transient case, a finite difference method with centered temperature, which is interpreted as the average temperature over the mesh of fuel element, is applied to solve the transient temperature evolution of the represented fuel element.

The fuel and coolant holes are arranged in the fuel block of the HTTR and the GT-MHR in different ways. In the fuel block of the GT-MHR, the coolant hole and fuel rod are separated. The model with two cylinders is developed (see Fig. 3.28). One is with fuel in center, and the other one is with coolant in center. The heat transfer equation is solved in both cylindrical zones with proper connection in the surface meshes of two cylinders. Figure 3.24 shows that there are 1/12 of the coolant hole and 1/6 of the fuel rod in the unit cell, which means that there are two fuel rod and one coolant hole in the basic unit of the fuel block structure. Therefore, the connection of the surface meshes are as follows: first, the surface temperature of these two cylinders should be equal; second, the heat flow current that comes into the coolant cylinder is twice of the heat flow current that leaves the fuel rod cylinder; third, the total amount of the graphite in the two cylinders should be equal to the amount of the graphite of the basic unit.

In the fuel block of the HTTR, the fuel rod is located in the center of the coolant

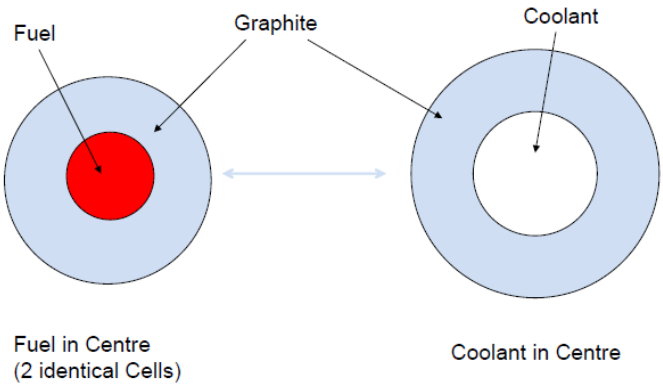

Figure 3.28: The 1D unit cell model of the GT-MHR

hole. The 1D cylinder model with multi materials can be applied to calculate the fuel and moderator of the fuel block (see Fig. 3.29). The outer boundary of the model is considered as adiabatic. The outer radius of the 1D model is chosen to guarantee that the model has the same amount of graphite with the basic unit of the geometry.

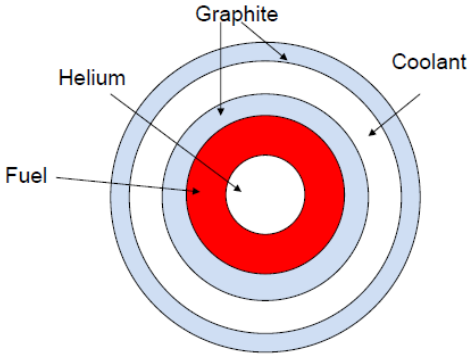

Figure 3.29: The 1D unit cell model of the HTTR

3.3 Homogeneous Conductivity of the Reactor Core

In the previous section, the temperature profile of the fuel rod and graphite moderator in the meso-scale were discussed. The smallest symmetrical unit cell which can represent the structure of the fuel block is used to predict the heat transfer between

the fuel rod and its surrounding graphite and coolant channels. The structure of the fuel rod, gap, moderator, and coolant are resolved in details. In the macroscopic scale, the heat is exchanged by convection in one homogeneous mesh or between different porous homogeneous meshes, conduction between adjacent homogeneous meshes, and thermal radiation on the surface of solid materials. The convection is determined by the properties of forced flow and the geometry of flow channel. The thermal radiation is characterized by the emissivity and the surface temperature of solid materials. The heat conduction of the fuel block is contributed to by several parts that include the fuel element, graphite, and stagnant gas. The smearing of individual conductivities must be performed in the homogeneous meshes of MGT-3D. For the pebble bed reactor, the method developed by Zehner-Schlüder [31] or Robold [53] are used to calculate the effective conductivity of porous media. For the block type reactor, the effective conductivity will be anisotropic, with the geometry in the axial direction being different from the geometry in the transverse directions. In this section, the methods used to calculate the effective conductivity of GT-MHR fuel block and HTTR fuel block are discussed.

There are several theoretical approaches to calculate the effective thermal conductivity of porous media [54, 55]. The numerical approaches with finite element models are also developed to determine the effective thermal conductivity of the GT-MHR fuel block [45] and HTTR fuel block [56]. The simplest model used to calculate the effective thermal conductivity of a porous medium is to assume the medium consisting of a fluid and a solid layer either in parallel or in series with respect to the heat flow direction. The equations to calculate the effective thermal conductivity of the medium composed of two discrete materials are presented in reference [57]. For the parallel case, the effective thermal conductivity can be calculated with a simple volume weighted average. The calculation method can be extended to the axial effective thermal conductivity of GT-MHR and HTTR fuel blocks, which are composed of multi-layer materials:

$$k_e = \upsilon_f k_f + \upsilon_g k_g + \upsilon_{He} k_{He} \tag{3.37}$$

where k_e, k_f, k_g, k_{He} are the effective thermal conductivity in the axial direction, thermal conductivity of fuel compacts, thermal conductivity of graphite, and thermal conductivity of stagnant helium respectively. υ_f, υ_g, υ_{He} are the volume fractions of the fuel compacts, graphite, and helium respectively. The sum of these three volume fractions is equal to 1. For the GT-MHR fuel block, υ_{He} is also the volume fraction of coolant channels. For the HTTR fuel block, however, υ_{He} is the sum of the volume fraction of the stagnant helium, which is sealed in the graphite sleeve of fuel rod and the volume fraction of the annular coolant channels. The transverse effective thermal conductivity of GT-MHR is already discussed in reference [45]. The method based on Maxwell's analysis is extended to calculate the homogenized thermal conductivity of the structure with the coolant holes and fuel rods located in discrete positions [60].

The Selengut's relation [58], developed for neutron diffusion, can be extended to the effective thermal conductivity calculation of the media consisting of two discrete materials [59]. If the medium is constructed with helium and graphite, the effective thermal conductivity can be obtained by following equation:

$$k_e' = \frac{(1+n\upsilon)k_0 + n(1-\upsilon)k_g}{(1-\upsilon)k_0 + (n+\upsilon)k_g} k_g \tag{3.38}$$

where
$n = 0, 1, 2$ for one-, two-, and three-dimensional medias, respectively;
k_0 is the thermal conductivity of the hole region (here, stagnant helium including an

allowance for thermal radiation).

Equation 3.38 can be applied on both axial direction and transverse plane of the reflector block and fuel block. For the axial direction, it is the one-dimension case. With $n = 0$, it can be seen that Equation 3.37 with two discrete materials is the degenerate form of Equation 3.38. In the transverse plane, the effective thermal conductivity in radial direction is equal to its value in azimuthal direction. The two-dimension version ($n = 1$) of Equation 3.38 should be used.

As mentioned, the conductivity of the coolant channel part includes the stagnant helium conductivity and the equivalent conductivity of thermal radiation. If the temperature of the solid surface of the coolant channel is very high (1000 $^{\circ}C$), the heat transferred across the channel by thermal radiation will be significant. It can be accounted into the conduction part by adding an equivalent conductivity onto the conductivity of stagnant helium. Therefore, the thermal conductivity of region with gas hole is [59]:

$$k_0 = k_{He} + k_r = k_{He} + \frac{4\sigma \bar{T}^3 \delta}{2(\frac{1}{\varepsilon} - 1) + \frac{\pi}{2}} \tag{3.39}$$

where
σ is the Stefan-Boltzmann constant;
$\bar{T}$ is the average temperature of solid surface of coolant channel;
δ is the diameter of the circular coolant channel;
ε is the emissivity of graphite.

The top and bottom reflector blocks of the HTTR are constructed with graphite block and circular coolant tubes (see Fig. 4.26 and 4.27). There are two different materials. The thermal radiation is mainly in the transverse directions. Therefore, the effective conductivity of the reflector blocks can be written as:

$$\begin{cases} k_e = \upsilon_g k_g + \upsilon_{He} k_{He} & \text{axial direction} \\ k'_e = \frac{(1+\upsilon_{He})k_0 + (1-\upsilon_{He})k_g}{(1-\upsilon_{He})k_0 + (1+\upsilon_{He})k_g} k_g & \text{transverse directions} \end{cases} \tag{3.40}$$

where k_0 is determined by Equation 3.39. There are also two different materials in the reserved shutdown block, control rod block, and the replaceable reflector block of GT-MHR. They are different in the radius and the volume fraction of coolant holes. Thus, the effective thermal conductivities of the reserved shutdown block, control rod block, and the top and bottom reflector block aligned with the fuel block can also be calculated by Equation 3.40 with adjusted k_0 and void fraction.

The fuel block of HTTR block consists of fuel compacts, helium, the graphite sleeve, and graphite block. The structure is much more complicated than the reflector block. The calculation method with three levels of homogenization is developed to calculate the transverse thermal conductivity of the HTTR fuel block. First, the coated particles smearing in the graphite matrix forms the fuel compact. The thermal conductivities of coated particles and their surrounding graphite matrix are homogenized to obtain the thermal conductivity of fuel compact. Second, the coolant channel, graphite sleeve, fuel compacts, and stagnant helium are coaxially located in the reserved cylindrical hole. The thermal conductivities of these materials are homogenized. The effective thermal conductivity of the coolant hole including fuel rods is derived. Finally, the fuel block is considered to be constructed by the graphite block and homogenized coolant hole. The Equation 3.38 can be applied to calculate the effective thermal conductivity of fuel block, namely the thermal conductivity of MGT-3D meshes.

The homogenized thermal conductivities of the fuel compact are not calculated specifically. Its value without irradiation and at the maximum irradiation dose of $6.4 \times 10^{18}\ n/cm^2$ are taken directly from the reference data [103]. To calculate the homogenized conductivity of the coolant hole, a simplified model is constructed: the coaxial cylinders with infinite length and with thermal conductivity k_0, k_f, k_s, and k_0' from the center to outer radius are embedded in the domain with thermal conductivity k_g. A heat flow perpendicular to the axial direction of the cylinder is imposed across the domain. The material along the diameter of the circular is arranged in series with respect to the temperature gradient. It is assumed that the radius of the coaxial cylinder are R_{He}, R_f, R_s, R_c from the inside to the outside. The effective thermal conductivity along the diameter can be calculated by following formula:

$$\frac{1}{k_d} = \frac{1}{k_0}\frac{R_{He}}{R_c} + \frac{1}{k_f}\frac{R_f - R_{He}}{R_c} + \frac{1}{k_g}\frac{R_s - R_f}{R_c} + \frac{1}{k_0'}\frac{R_c - R_s}{R_c} \tag{3.41}$$

where k_0 is the thermal conductivity of the central helium including thermal radiation, k_0' is the thermal conductivity of stagnant helium including thermal radiation in the annular coolant channel.

The effective thermal conductivity along the chord of the circular can be taken as the projection of the thermal conductivity along the diameter. Assuming that the angle between the chord and its related diameter is ϕ, the effective thermal conductivity along the chord can be written as:

$$k_\phi = k_d cos\phi \tag{3.42}$$

Taking an average k_ϕ in half circle, the effective thermal conductivity of the coaxial cylinders can be obtained:

$$k_h = \frac{1}{\pi}\int_{-\frac{\pi}{2}}^{\frac{\pi}{2}} k_d cos\phi d\phi = \frac{2}{\pi}k_d \tag{3.43}$$

where k_d is determined by Equation 3.41.

In the transverse plane of the fuel block, it can be considered to be constructed with two materials with thermal conductivities of k_h and k_g after homogenizing the thermal conductivity of coolant holes. Equation 3.38 with the case of $n = 1$ can be applied to calculate the effective thermal conductivity of the HTTR fuel block. It can be obtained by substituting Equation 3.43, the volume fraction of coolant hole, and the thermal conductivity of graphite into Equation 3.38. The effective thermal conductivity of axial direction can be calculated by the simple volume average, as in Equation 3.37. They are as follows:

$$\begin{cases} k_e = \upsilon_{He}k_{He} + \upsilon_f k_f + \upsilon_s k_s + \upsilon_c k_H e + \upsilon_g k_g & \text{axial direction} \\ k_e' = \frac{(1+\upsilon_h)k_h + (1-\upsilon_h)k_g}{(1-\upsilon_h)k_h + (1+\upsilon_h)k_g} k_g & \text{transverse directions} \end{cases} \tag{3.44}$$

The core components, which include the fuel compacts, graphite sleeve, fuel block, and replaceable fuel block, are fabricated from very fine grain graphite IG-110 [61, 62]. Its thermal conductivity is dependent on the irradiation history, which includes the temperature and radiation dose (see Fig. 3.30). The thermal conductivity of IG-110 without irradiation is:

$$k_g = 0.3398(\frac{T}{1000})^2 - 0.9786\frac{T}{1000} + 1.1246 \quad (W/cm\cdot^\circ C) \qquad 400^\circ C < T < 1400^\circ C \tag{3.45}$$

The thermal conductivity of IG-110 with irradiation at 600 $^{\circ}C$ for 660 EFPD is:

$$k_g = 0.0415(\frac{T}{1000})^2 - 0.1307\frac{T}{1000} + 0.3081 \quad (W/cm \cdot^{\circ} C) \qquad 400^{\circ}C < T < 1400^{\circ}C \tag{3.46}$$

Normally, the solid temperature of core components is within a temperature range of $[400^{\circ}, 1400^{\circ}C]$. If the temperature is out of this range, the thermal conductivity is extrapolated from the same equation. The thermal conductivity of stagnant helium is temperature and pressure dependent [63]:

$$k_{He} = 0.144 \times 10^{-2}(1 + 2.7 \times 10^{-4}P)(\frac{T + 273.15}{273.15})^{0.71(1-2\times10^{-4})} \quad (W/cm \cdot^{\circ} C) \tag{3.47}$$

where P is the pressure in bar.

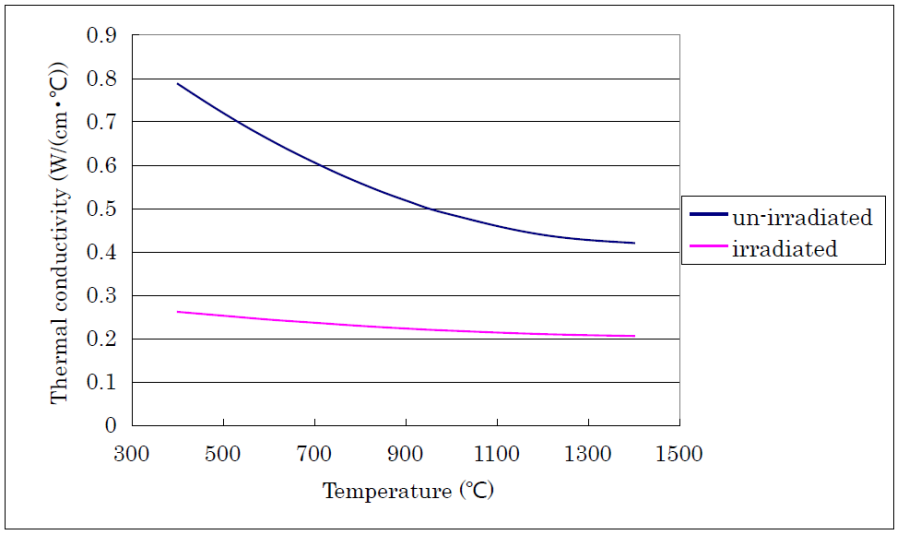

Figure 3.30: The thermal conductivity of the graphtie IG-110

The emissivity of the fuel compact and graphite is 0.8. For the equivalent thermal conductivity of central hole of fuel rod k_0, the value of δ is the diameter of the central hole of fuel rod. To calculate the equivalent thermal conductivity of the annular coolant channel k_0', the value of δ is taken as the square root of the hole's cross-sectional area.

The effective thermal conductivities of the fuel block, replaceable reflector block, control rod guide block, and reserved shut down block are discussed in this section. They are anisotropic values. An analytical model is developed to derive the equations used to calculate the effective thermal conductivities of axial direction and transverse directions of both HTTR and GT-MHR's core components. The equations can be used in MGT-3D to determine the thermal conductivity of related homogenized meshes.

Chapter 4

Validation and Application

This chapter will introduce the application of MGT-3D to the simulation of the NACOK-II experiment, LOFC and DLOFC accidents of the GT-MHR, and the LOFC experiments of the HTTR. In the first section, the NACOK-II experiment that heats the ceramic cuboid block is presented. The experiment is calculated with MGT-3D, and the simulation result is compared to the measured data to validate the code.

In the second section, the design features of the GT-MHR is introduced, and the code-to-code benchmark of the LOFC and DLOFC accidents is described. The LOFC and DLOFC accidents are simulated with MGT-3D. The homogeneous temperature solution with given heat source is applied. After this, the simulated results are compared to the benchmark of the Co-ordinate Research Project (CRP-3) organized by International Atomic Energy Agency (IAEA) to verify the homogeneous calculation part of MGT-3D [79].

In the third section, the reactor core and the cooling system of the HTTR are presented in detail. The burnup calculation is conducted by the Monte Carlo code Serpent. The calculation results are coupled with MGT-3D by an interface code, which provides the nuclide inventories and operational histogram for the nuclear calculation of MGT-3D. The LOFC experiments of the HTTR are simulated by MGT-3D. The simulated result of the elapsed time and peak power level at the occurrence of re-criticality is compared to the measured data.

4.1 NACOK-II Experiment with Cuboid Block

The air ingress accident due to the break of the pressure boundary is considered to be one of the severe hypothetical accidents of HTGRs [64]. After a break of the pressure boundary of HTGRs, the reactor will lose the forced coolant of the primary circuit. Then the reactor becomes depressurized, and the air may enter into the reactor core by diffusion when the pressure of the reactor core is equal to the atmospheric pressure on the outside. It will cause corrosion damage to the core and reflector graphite if the air continuously streams into the reactor and the reaction gas is continuously removed by means of natural convection.

The NACOK-I (Naturzug im Core mit Korrosion) was built at Forschungszentrum Jülich (FZJ) in Germany to research the natural convection driven by the chimney effect, the temperature evolution, and graphite corrosion in the event of the air ingress of HTGRs [65]. The experiment provides useful data to benchmark the codes such as TINTE, DIREKT and SPECTRA (Sophisticated Plant Evaluation Code fro Thermal-hydraulic Response Assessment) [66, 67, 68]. In the NACOK-I experiment, the tested block or

pebble bed could not be heated to a very high temperature due to its constructional limits. The achieved temperature was less than 700 $°C$, which is below the reactor core temperature in the DLOFC accident. The Boudouard reaction is not significant in this temperature scale [69]. The NACOK-I experiment did not monitor the gas flow very well.

Recently, the NACOK-II experiment, which is based on the NACOK-I experiment, has been proposed to understand the coupled fluid mechanics and chemical reaction kinetics [70, 71]. In the test experiment of NACOK-II, the channel temperature can reach 1300 $°C$. The Boudouard reaction will be significant at the temperature level of 1000 $°C$. Therefore, both the graphite oxidation with the product of carbon dioxide and the Boudouard reaction can be investigated in the NACOK-II experiment. New instrumentation systems like Particle Image Velocimetry (PIV) are applied in the experiment to monitor the gas flow of natural convection. The fluid mechanics and chemical reactions in the experiments with the cuboid block as well as the pebble bed are planed to be examined in the NACOK-II equipment. Pre-testing of the power system and measurement system have been done with the ceramic block and pebble bed heating experiment. In this section, the pre-test experiment with the ceramic block is simulated with MGT-3D, and the simulation ability of MGT-3D on a prismatic block system is examined.

4.1.1 Experimental Facility

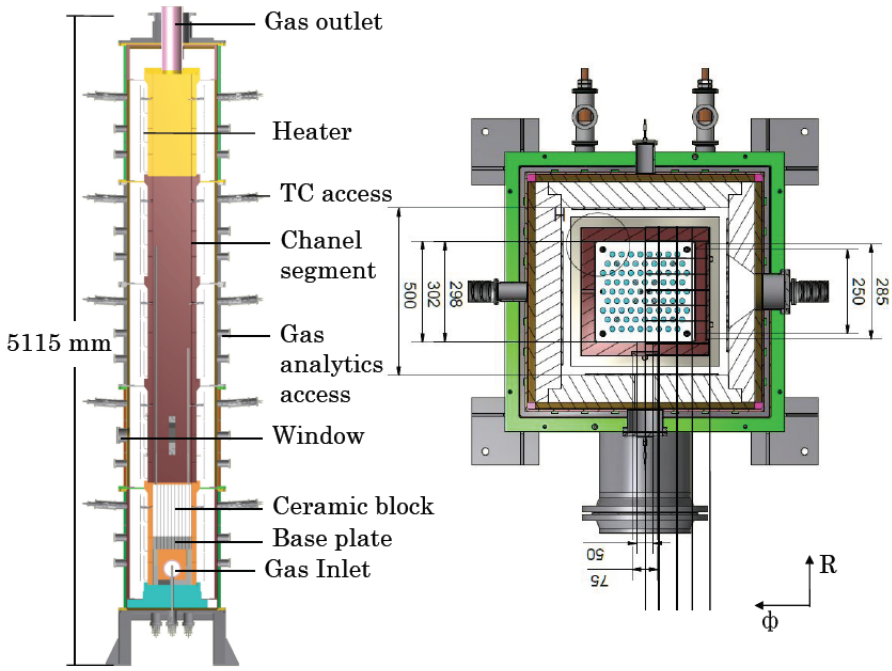

Figure 4.1: Schematic of NACOK-II [70]

The total height of the NACOK-II facility is about 5.1 m (see Fig. 4.1). It includes the support structure, five main segments with cuboidal shape, the top gas exhaust,

the electrical heating system, the water cooling system, and the monitor system which includes thermocouples (TC), gas analytical system, and PIV. Each of the main segments has a height of 80 cm. The horizontal cross section of the segment is shown in Figure 4.1. It consists-from inside to outside-of the ceramic flow channel, which allows flexible handling of samples like spherical fuel elements, as well as cuboid blocks, the gap, heating elements, thermal insulation, water cooling pipes, and the metallic furnace shell. The furnace shell is cooled with water to maintain a defined boundary temperature. The inner cross section of the channel is 30 $cm \times 30$ cm. The segments are identified by the index 1 to 5 from bottom to top. The heating system of each segment is independently installed. The 1st and 2nd segments have a heating capacity of 40 kW each, and the others have a heating capacity of 25 kW each. Therefore, the maximum heat capacity of the furnace is 155 kW in total. All of the ceramic channels can withstand temperatures up to 1600 $°C$, and a heating rate of 30 $°C/h$.

The PIV flow field measurement is located in the window of the second segment. A laser beam is injected into the channel from the chink on the surface which is perpendicular to the window surface. The laser is reflected into the PIV receiver outside the window by the particles which are added into the gas flow. The gas inlet connected to the environment, a helium, or a nitrogen gas tank is controlled by pneumatic valves. The exiting gas is cooled by the installed gas cooler to protect the pneumatic valve from temperatures higher than 200 $°C$ in the exhaust line. The gas concentration and gas pressure inside the flow channel and in the gap between the ceramic flow channel and furnace heating rods are monitored by the gas analytics system.

In the cuboid ceramic block heating experiment, the temperature of the outer wall of the ceramic channel is chosen as the control parameter due to the difficulty of fixing the electrical power. The ceramic block is located on top of the cuboid base plate, and its coolant channels are aligned with the coolant channel of the base plate. The facility is heated up to 1320 $°C$. The system achieves steady state with continuous heating for 52 hours, and the experiment is kept in steady state for several hours. The outer wall temperatures of the five ceramic channel segments are 1315 $°C$, 1295 $°C$, 1285 $°C$, 1265 $°C$, 1265 $°C$ from the bottom segment to the top segment. The air flows into the channel with a volume flow rate of 50 m^3/h and with a temperature of 20 $°C$.

The ceramic block is fabricated of the same material as the channel and the base plate. It is shaped as a cuboid with a length of 29.5 cm, width of 29.3 cm, and height of 40.5 cm. The diameter of the coolant channel is 1.59 cm. The coolant channel arrangement is shown in Figure 4.1.

4.1.2 Simulation Model and Result

The cross section of the facility has a square shape. The 2D simulation model is not suitable to simulate the structure in detail, so a 3D pseudo X/Y/Z coordinate is applied to simulate the NACOK-II experiment. In MGT-3D, the radial coordinate is not needed to start at $R = 0$, which enables the user to describe approximately X/Y/Z problems by choosing very large radial coordinates compared to the scale of the model.

In the ceramic block heating experiment, the outer wall temperature of the ceramic channel is fixed in the steady state case. It is not necessary to simulate the heating system, the water cooling system because they are out of the boundary. The window in the second segment does not significantly affect the gas flow in the cuboid block, so the asymmetry caused by the PIV window is neglected in the simulation model. The

radial coordinate is started at $R = 500\ m$. Considering that the width of the facility is about 50 cm, the model makes a maximum deviation of 0.5 mm with the pseudo X/Y/Z coordinate. The sketch of the R/Φ mesh of the MGT-3D model is presented on the right-hand side of Figure 4.1. On the left side of the azimuthal direction, a reflective boundary is applied. With the radial coordinate starting at $R = 500\ m$, the angular coordinate is in the range of [0, 0.02188°]. There are $15(R) \times 8(\Phi) \times 29(Z)$ meshes in total.

The density of the air at room temperature and atmospheric pressure is 1.2 kg/m^3. So the mass flow rate of the inlet gas is 0.017 kg/s. The air is represented by the gas combination of 78% nitrogen and 22% oxygen. The heat sink is defined as infinite volume with the reference pressure of 1 bar.

The cuboid block is constructed with ceramic and the coolant hole that is filled with air. It has only two discrete materials. It has an anisotropic thermal conductivity in the radial direction and transverse directions. The equivalent thermal conductivity of the coolant hole and the homogeneous thermal conductivity of the cuboid block can be obtained from Equations 3.39 and 3.40 by substituting graphite and helium into ceramic and air at 1 bar.

In the NACOK-II experiment, the heat flux of thermal radiation from the inner wall of the channel to the top surface of the cuboid block and to the bottom surface of the base plate can not be treated by the effective thermal conductivity. The net heat deposited on the surface can be on the kilowatt level if the wall temperature is up to 1000 $°C$. MGT-3D does not include the option to calculate long-range heat transfer by thermal radiation penetrating the transparent medium (see Fig. 4.2). So an external heat source is defined on the top and bottom surface. The heat transferred between two vertical surfaces by thermal radiation can be calculated by Equation [72]:

$$\dot{Q}_{12} = \frac{\sigma \varepsilon_1 \varepsilon_2 A_1 \varphi_{12}}{1 - (1 - \varepsilon_1)(1 - \varepsilon_2)\varphi_{12}\varphi_{21}} (T_1^4 - T_2^4) \tag{4.1}$$

where
σ is the Stefan-Boltzmann constant,
A_1, A_2 are the areas,
ε_1, ε_2 are the emissivity constants,
φ_{12}, φ_{21} are the view factors of the two surfaces. To determine the heat flux from the segment wall to the surface of the cuboid block, the surface temperatures are required. To obtain the correct surface temperature, the heat deposited on the surface should be pre-determined. Therefore, the iteration between the heat flux of thermal radiation and surface temperature is applied in the steady state calculation. First, the guessed external heat source is added on the top meshes of the cuboid block and the bottom meshes of the base plate. With the guessed heat source, the surface temperature can be obtained, and the external heat source can be checked and adjusted by substituting the surface temperature into Equation 4.1. After several iterations, the final heat deposited on the top surface is about 1.78 kW, and the heat deposited on the bottom surface is about 3.73 kW. Hence, the thermal radiation is significant in the NACOK-II simulation.

The calculated solid temperature distribution on the symmetrical plane and the measured points are shown in Figures 4.3 and 4.4. The solid temperature profile on the top and bottom surface shows higher values than the surrounding temperatures because of the heating by thermal radiation, which can also be observed in the CFX simulation [36]. In the bottom-center of the cuboid block, the temperature is lower than in the surrounding meshes due to the cooling of the gas flow. The gas flows to the center meshes

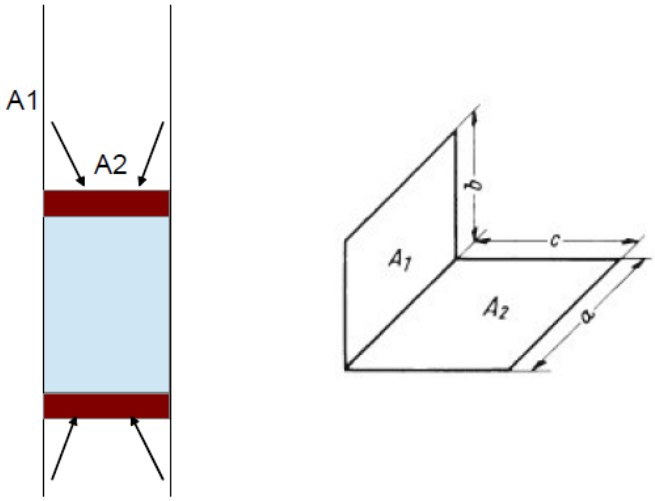

Figure 4.2: Thermal radiation of NACOK-II experiment

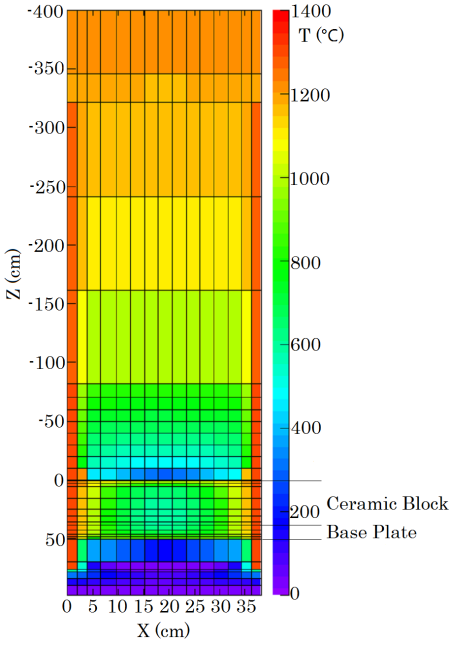

Figure 4.3: Solid temperature in the central plane

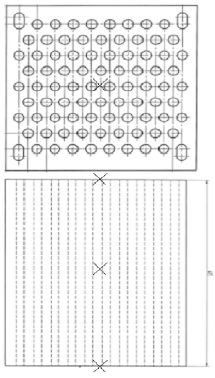

Figure 4.4: Measurement points in the cuboid block

on top of the cuboid block because its gas pressure is lower than in the surrounding meshes. Table 4.1 displays the comparison between the MGT-3D simulation results and the experimental data. The maximum deviation is about 30 $°C$. At the middle-top and the middle-middle points, the measured values are higher than the simulation results. The reason is that probably the calculated heat transfer coefficient is too small.

	Experiment ($°C$)	MGT-3D ($°C$)	ΔT ($°C$)
middle-top	1167	1136.9	-30.1
middle-middle	625	594.9	-30.1
middle-bottom	614.3	619.9	5.6

Table 4.1: Comparison between the simulation results and the measured temperatures

In this section, the NACOK-II experiment was introduced. To test the heating system and the measurement system of the experimental facility, the ceramic block heating experiment was conducted. The homogeneous model is applied to calculate the solid temperature profile, and the calculation results show generally good agreement with the measured values, which validates the application of MGT-3D to ceramic blocks. The simulation results also prove that thermal radiation plays an important role in the experiment. The heat exchange by thermal radiation across a long distance cannot be solved by MGT-3D properly, but it can be solved by the equivalent external heat source.

4.2 LOFC and DLOFC Simulation of GT-MHR

In the 1960s, the U.S. had already begun to design gas-cooled nuclear reactors. The first example was the 3.4 MW (thermal power) nitrogen-cooled Army's Mobile Low Power Reactor (ML-1) with gas turbine power conversion system [75]. Later, the Peach Bottom reactor was built [47]. It was the first high-temperature, helium-cooled reactor in the U.S. using cylindrical fuel elements which were composed of BISO particles. The Peach Bottom Unite 1 provides the thermal power of 115 MW and electrical power of 40 MW. This reactor was successfully operated, which proved the technology of a HTGR with cylinder fuel elements and coated particles. All of these concepts were used to design the commercial Fort St. Vrain Reactor (FSVR) whose thermal power and electrical power were 842 MW and 330 MW, respectively. In the late 1970s, the HTGR concepts with thermal power levels up to 3800 MW were developed [73]. They used a Prestressed Concrete Reactor Vessel (PCRV) to contain certain high pressure levels in the primary circuit like 4.9 MPa in the FSVR. Many researches were conducted on these large-size reactors, but they never materialized.

There are also disadvantages of the reactor with high installed power. For normal operation, the reactor is operating at a high temperature level, which increases the possibility of fission product release. In an accident situation, the temperature of the reactor center can be very high due to the large scale of the reactor, which can cause the failure of coating particles. In order to build a "simpler, safer" HTGR, the "module" concept was developed. The first proposed design is the MHTGR with a thermal power of 350 MW. It uses the traditional Rakine cycle. This module reactor can also be coupled to gas turbine power conversion systems to achieve a high energy conversion efficiency, which is the Gas Turbine Modular Helium Reactor (GT-MHR). It uses the

direct Brayton cycle. In order to improve economic efficiency, the designed thermal power is increased to 450 MW and subsequently to 600 MW, all of which still retain the safety features of the MHR designs [76].

4.2.1 Description of the GT-MHR

The GT-MHR, which is fueled with weapon grade plutonium, is developed by a group of the Russian Federation Ministry for Atomic Energy (MINATOM), General Atomics (GA) in the United States, the French Framatome, and the Japanese Fuji Electric. The reactor is designed to burn the surplus weapon grade plutonium with the burnup of 90% of the initially loaded plutonium-239. The average core fuel residence time is about 840 days. It can make full use of the high enrichment plutonium which is provided by the dismissed nuclear weapons. The installed thermal power per unit is 600 MW. It achieves a power conversion efficiency of 47% with the direct Brayton cycle, which corresponds to an electrical power of 286 MW. It can supply the electrical power 1144 MW with 4 units. The power conversion system integrates the turbine, generator, recuperator, compressor, intercooler, and precooler together in a steel vessel. The reactor core is contained in a steel reactor pressure vessel, which is connected to the integrated power conversion system with a cross vessel. The reactor pressure vessel and the power conversion system are placed in parallel in two separated rooms. The reactor pressure vessel is cooled by the reactor cavity cooling system to protect the integrity of reactor pressure vessel and to remove the residual heat. The heat is transferred from the RPV to the water cooling pipes by thermal radiation and natural convection. The module is located in a containment that is 39 m below the ground. The containment can withstand high pressures and retain the fission products in accident situations. The module and direct power conversion design make the system simpler and safer.

The primary circuit is constituted with central reflector, fuel blocks, outer reflector, reactor control system, reactor support system, core barrier, and RPV. The hexagonal graphite blocks are placed in the center of reactor core as the central reflector. 102 columns of fuel block are annularly arranged around the central reflector. There are 10 layers of fuel blocks and consequently 1020 hexagonal fuel blocks in the core. Both the central reflector and fuel block are replaceable. 36 operating control rods, 12 start-up control rods, and 18 reserve shutdown channels are distributed in the inner and outer boundary of annular cores. The replaceable outer reflector and permanent reflector blocks are laid in the outside of the fuel rings. There are also two layers of reflector blocks on the top and bottom of fuel blocks. The gas risers are distributed in the permanent reflectors. A 10 cm thick region, which contains B_4C between the graphite reflector blocks and the core barrel, is used as a neutron shielding layer to prevent irradiation damage to the RPV. The core restraint elements, which are used to provide adequate dimensional stability during the operation of the reactor, are assembled between the core barrel and RPV. They can also absorb the vibrations resulting from an earthquake.

Helium is used as the primary coolant in the reactor. The reactor runs at 7 MPa during normal operation. The helium flow rate is 320 kg/s. The inlet and outlet pressure are 7.07 MPa and 7.01 MPa, respectively. The inlet and outlet helium temperatures are 490 $^{\circ}C$ and 850 $^{\circ}C$. The high temperature helium flows through the cross vessel from the hot duct of the primary circuit to the power conversion system [76]. It expands in the turbine and drives the generator directly, and then exits the turbine at a temperature of about 510 $^{\circ}C$ and 2.64 MPa. The helium, still at high temperature, flows through the recuperator and returns part of residual thermal energy to the system. Then it enters

into the precooler, which is used as the main heat sink for the cycle. The cool and low-pressure helium at 26 $°C$ is compressed in the intercooler and then directed into the high pressure side of recuperator, where it is heated up with the residual thermal energy of the turbine [79]. Then, the helium at high pressure exits the power conversion system and reenters into the cold duct of the reactor core through the outer shell of the annular cross vessel. In the reactor core, the helium enters into the cold plenum from the cold duct and flows upwards through the gas risers in the permanent side reflector to the upper plenum, which can reduce the vessel temperature during normal operation and accidents and reduce the upper plenum metallic temperature in accidents. Then, the helium streams into the coolant holes of the fuel blocks or the gap among the blocks from top plenum to the bottom flow distribution blocks. Furthermore, the gas flow exits as jets around the support posts into the lower plenum (outlet plenum). The helium is heated when it passes through the fuel blocks. During the loss of forced coolant accident, the natural convection between the top and lower plenum can cool down the reactor core effectively, but the direction of the gas flow is inversed, which is from the lower plenum to the upper plenum.

The three types of flow of the reactor core can be distinguished by their paths: the main flow, bypass flow, and cross flow. The main flow is the flow that passes through the coolant holes. It occupies about 90% of the total gas flow. From the diameter and length of the coolant channels of about 1.6 cm and 8 m, respectively, a turbulent flow is expected in such long tubes. These flow channels provide most of the primary circuit flow resistance accounting for the main part of the pressure drop. The heat transfer coefficient in the channels is characterized by the Nusselt number which is determined by the Reynolds number, $Re \cong 50,000$. The bypass flow is defined as any flow that does not pass through the coolant holes. It includes the flow through the vertical gaps between blocks, the flow through the control rod holes and reserved shutdown system channels, and the flow passing through the gap between fuel rod and graphite block. These flows comprise the remaining 10% of the total gas flow. Generally, the bypass flow should be minimized because it reduces the flow which passes the main coolant holes. However, some part of the bypass flow is necessary to cool the control rods. The fuel rods, which are located in the boundaries of the fuel block, also benefit from the cooling effect of the bypass flow. Therefore, bypass flows should be optimized rather than minimized. The cross flow is defined as the horizontal flow through gaps at block axial boundaries. It is driven by the pressure gradients among the blocks and crosses from block to block. Some hot blocks with a high power density may be cooled more efficiently because of the short circuit of cross flow. Thus, it should be optimized as well. In general, the bypass flow in the gaps between adjacent blocks can be avoided by adding some sealing devices between the blocks.

In the annular fuel zone of the core, there are two types of hexagonal fuel blocks: a standard fuel block, and a fuel block with control rod holes or reserved shutdown holes. The fuel blocks use the same hexagonal shape and dimensions as in the FSVR. The pitch of the fuel block is 36 cm, and the height of the fuel block is 80 cm. The fuel holes and coolant holes are located in parallel in the graphite through the length of fuel block. The fuel compacts, which are inserted in the fuel holes, are distributed in a regular hexagonal array, and a coolant hole is located in the center of each fuel hexagonal array. In the block-to-block contact face in the axial direction, there are four dowel/socket connections to fix the position of fuel block and align the coolant holes. In the center of the fuel block, there is a fuel handling hole with the depth of 26.4 cm. It has a ledge where the fuel handling machine with a grapple can run in to install or take out the fuel block. Generally, a standard fuel block contains 210 fuel holes with the

diameter of 1.27 *cm*, 120 coolant holes with the diameter of 1.6 *cm*, and 6 small coolant holes with the diameter of 1.27 *cm*. The other type of fuel blocks with control rod holes or reserved shut down holes has 186 fuel holes, 86 large coolant holes, 7 small coolant holes, and one big hole with the diameter of 13 *cm* for the control rod or reserved shut down channel. The fuel block also includes 6 lumped burnable poison compacts with the diameter of 1.25 *cm* and with the height of 72.14 *cm* in the six corners of the hexagonal block. They are used to control the reactivity of the reactor and the burnout rate of fuel compacts. The control rod is composed of boron carbide, and the total active length is 930 *cm*. The reflector blocks, which are on the top and the bottom of fuel blocks, have the same coolant hole structure as the fuel blocks in the same column.

The GT-MHR fuel compact consists of TRISO-coated particles based on the same principle as the coated particles of pebble fuel element. The TRISO-coated particles fueled with plutonium dioxide and are bonded together with graphite shim particles in a carbonaceous matrix forming a cylinder rod-shaped compact with the diameter of 1.245 *cm* and with the length of 4.93 *cm*. The packaging fraction of coated particles is 0.12978 in the graphite matrix [77]. These fuel compacts are filled into the fuel holes in the hexagonal fuel block. The top and the bottom of the fuel holes are sealed with graphite plugs to enclose the stacked compacts. The TRISO-coated particle is comprised of a fuel kernel ($PuO_{1.7}$), a porous carbon layer, an inner pyrolitic carbon, SiC, and outer pyrolitic carbon layers.

There are four barriers to retain the fission products. The first barrier is the coated particles. The fuel compact is the second barrier and it can prevent the metallic fission product release. The primary circuit is the following barrier. The small amount of fission products released from coated particles by diffusion will get into the coolant, and is enclosed in the RPV. The radiation of coolant is monitored during the operation, and the coolant is purified if necessary. All of the fission products can be retained in the primary circuit during normal operation. If an accident happens, the containment, which is the final barrier, can make sure that fission products will not be released into the environment under any kind of accident scenario.

In order to protect the concrete of containment and the RPV, a water-cooled Reactor Cavity Cooling System (RCCS) is introduced between the RPV and the wall of containment [78, 79]. It consists of a surface cooler, which includes two independent cooler arrays, a RCCS header, a water-water heat exchanger, a quench tank, the connecting piping, and a measurement system. The heat exchange between the RPV surface and the air in the cavity by natural convection can remove part of the heat in the RPV and decrease the surface temperature. Then the heat is transferred into the surface cooler by natural convection as well. Another part of the heat is transported by thermal radiation from the RPV surface to the surface coolers. Thus, the heat is transferred from the PRV to the surface cooler only by natural circulation. The surface cooler is located on the side, top and bottom of the cavity. It is cooled by water pipes, and pumps are used to supply the water. Then the heat is taken out by an exchanger between this circuit and another circuit, which connects with a huge heat sink.

The functions and basic requirements of RCCS include:

- The RCCS provides the shield of direct thermal radiation to the concrete wall. It can prevent the directly heating of concrete wall.
- The RCCS must remove all wasted heat during normal operation to ensure that the RPV and concrete temperature do not exceed the limits. The designed tem-

perature of the RPV and the concrete wall of containment are 490 $^{\circ}C$ and 80 $^{\circ}C$ respectively in normal operation.

- The RCCS must remove all of the residual heat during all of the designed accidents (e.g LOFC, DLOFC). The designed temperature of the RPV and the concrete wall of the containment are 540 $^{\circ}C$ and 100 $^{\circ}C$ respectively in accident scenarios.
- The RCCS uses water as coolant in both the first circuit and the circuit which connects with the heat sink outside, and they work at atmospheric pressure. Basically, the water temperature should not exceed 100 $^{\circ}C$, or the water will evaporate and reduce its cooling ability.
- If the water in first circuit of RCCS evaporates, it will supply the heat sink for the cooling system. It should be guaranteed that emergency cooling function is maintainable without intervention for at least 48 hours in accidents.

The GT-MHR design simplifies the system into four main parts: primary circuit, power conversion unit, RCCS, and containment. The high integration design reduces the complexities of conventional reactor systems and makes the reactor simpler, smaller, safer, and more efficient. It keeps the inherent safety characteristics of HTGR that the reactor can be shut down by itself when temperature rises. The reactor has very slow transient responses by using lots of graphite in the core and reflector. Several barriers can retain the fission production effectively. The annular fuel assembly design of the core can reduce the center temperature's peaking. The fuel blocks are surrounded by a graphite reflector, which can make full use of the neutrons, flatten the thermal neutron flux, and therefore reduce the power's peaking. The high conductivity of graphite guarantees that the heat can be transported out of the core rapidly in accident scenarios. The reactor has a height of more than 25 m. It enhances the natural convection in the cavity of RCCS. So that the reactor pressure vessel can be cooled down efficiently in normal operation and accident scenarios.

The CRP-3 benchmark, which was organized by IAEA, is chosen to verify MGT-3D. There are three phases in the benchmark problems:

- Steady state: The reactor is at normal operation with inlet helium temperature 490 $^{\circ}C$ and outlet helium temperature 850 $^{\circ}C$. Heat balance is achieved in the reactor core. The surface cooler panels with water cooling are operational to guarantee that the vessel temperature limitations are not exceeded.
- LOFC accident: The accident starts from the steady state. The blowers of the reactor are stuck, and the coolant stops flowing in a short time interval. At the same time, the reactor is shut down with the reserved shutdown system. The pressure of the primary circuit remains in the initial pressure. Heat transfers out by natural convection, conduction, and radiation. The RCCS works to cool the RPV and containment concrete wall as designed. The object is to predict the maximum temperature, fuel temperature distribution, vessel temperature, heat transfer mechanism.
- DLOFC accident: As the LOFC accident, it starts from steady state. The reactor loses the coolant and is depressurized rapidly. The pressure is equivalent to atmospheric pressure. It is accompanied by a scram as well. The RCCS works, and the concrete wall temperature remains at 65 $^{\circ}C$. The object is to research whether the residual heat can be removed, and whether the designed fuel temperatures are exceeded in the extreme accident.

4.2.2 Simulation Model

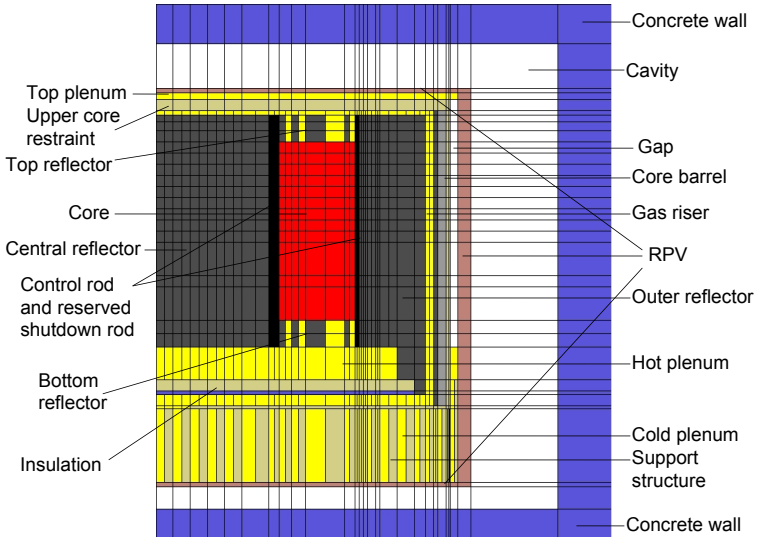

Figure 4.5: Simulation geometry of GT-MHR

The GT-MHR benchmark problems treated in the IAEA CRP-3 project were a code to code comparison [79]. The participating countries used different approaches and different codes to do the fluid mechanics simulation, and the comparisons between the simulation results were presented in reference [81]. The suggested 2D model [78] is used in the MGT-3D simulation as well. Then the calculation results of MGT-3D and the Russian's code GTAS are compared.

The simulation geometry with material sharing which is identified by different color is shown in Figure 4.5. It is a two dimensional, cylindrically symmetric model with $28(R) \times 32(Z)$ meshes. The model includes the primary circuit and the RCCS. It simulates the fluid mechanics of the primary circuit with a homogeneous model, and uses a given heat source. The hexagonal annular core can not be simulated with a two-dimension model, but it can be approximated by an equivalent circular annular core with an inner radius of 1.485 m and an outer radius of 2.455 m. The thermal conductivity of the fuel block is homogenized, and it is anisotropic in the radial direction and the axial direction [2]. The flow path is homogenized in R/Z direction in a cylinder coordinate system, and defined as bundles of one-dimensional flow tubes with a diameter of 1.6 cm and a homogenized void factor of 0.216. The heat exchange between solid and gas by convection is considered by defining a convective heat source. The heat source of the reactor core is homogenized in the solid phase of the block instead of specified in the fuel compacts. The reflector blocks above and below the fuel blocks share the same thermal parameters.

The thermal properties of other parts, which include the central reflector, outer reflector, permanent side reflector, thermal shield, core barrel, and reactor pressure vessel,

were specified and agreed upon by the CRP partners. In order to simulate the bypass flow in the central reflector and outer reflector, some one-dimension flow tubes with a small diameter are assumed in these blocks. The shape of the gap can not be determined in detail, but this approximation method can be used by adjusting the diameter of these small flow tubes, the flow resistance, and the void factor of reflector blocks. The fraction of bypass flow which passes through the reflector block can be used as the criterion to adjust these parameters. Nevertheless, this method can only simulate the vertical bypass flow, while the cross bypass flow is neglected. The impact of the gap on homogeneous conductivity is not considered as well. However, the specific heats of these blocks are multiplied by the solid factor.

The holes for reserved shutdown rods and control rods are dispersed in the inner and outer circuit of fuel columns. In the simulation model, these holes are concentrated in two circular annular meshes, which are defined as flow meshes. The void factor is calculated according to the ratio of total holes' area to the circular annular meshes' area. The gas risers are treated with the same method.

The restrain system between core barrel and RPV is simulated by a gap mesh. The gas does not flow in this mesh. It can be considered as a solid mesh with the conductivity and specific heat of the gas, and it is transparent for thermal radiation. The gas inlet and outlet are arranged in meshes of the cold plenum and hot plenum, respectively. The top cap and bottom catcher are designed in a semi-spherical shape, which can not be described in a two dimension model. They are represented by two cylinder cavities.

For the reactor cavity cooling system, the structure of the cooling pipes is not simulated in detail. The concrete wall is set as the boundary, and the boundary temperature is fixed at 65 $^{\circ}C$. The convective heat transfer in the cavity is simulated by an effective thermal conductivity. The radiative heat transfer from the RPV to the concrete wall is simulated, and their emissivities are equal to 0.8.

For the steady state, the power density, which was given as input to the CRP partners, is shown in Figure 4.6. The gas streams into the inlet with 490 $^{\circ}C$ and 318 kg/s, and the outlet temperature is 850 $^{\circ}C$. The simulation starts from arbitrary initial condition and the thermal equilibrium is achieved after several iterations.

The LOFC accident starts from the thermal equilibrium in normal operation. The coolant rate decreases from 318 kg/s to 0 linearly in 10 seconds, which is quite a short time interval. The pressure of coolant stays at 70 bar. The accident is accompanied by a scram of the reactor. The reactor is assumed to be shut down immediately, and the power decreases exponentially. It is also assumed that the power decreases in the same ratio everywhere. The power histogram relative to the initial power is presented in Figure 4.7.

The initial condition of the DLOFC accident is the equilibrium core in normal operation. The coolant flow is cut down in 0.1 s, and the reactor is depressurized in the same time, which means that the pressure of the primary circuit is 1 bar. In the simulation, the special command "NKNV" is used. With this option, all calculations involving gas, e.g gas flow, gas diffusion, gas temperature, and convective heat transfer, are omitted. The reactor is shut down with beginning of the LOFC accident scenario, and the same heat source which is shown in Figure 4.7 is used during the simulation.

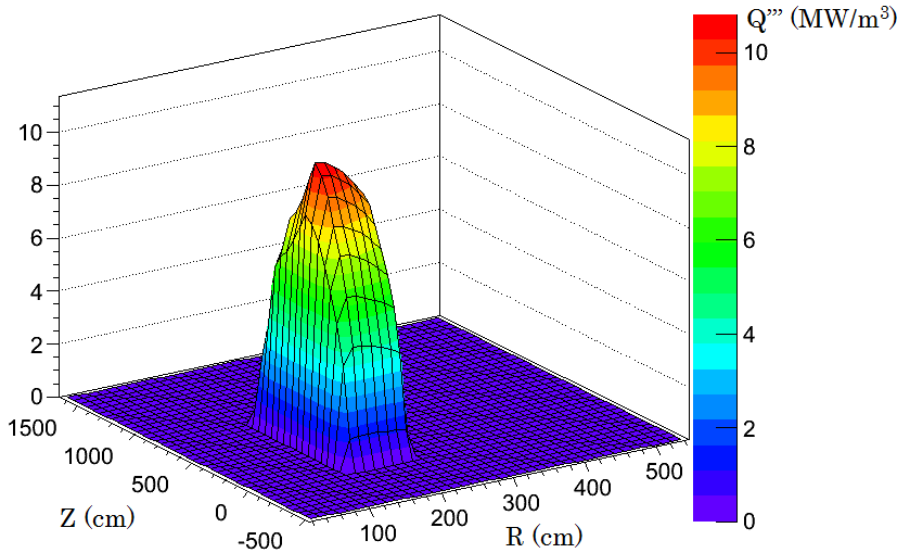

Figure 4.6: Given power density of GT-MHR as specified in the CRP-3 benchmark

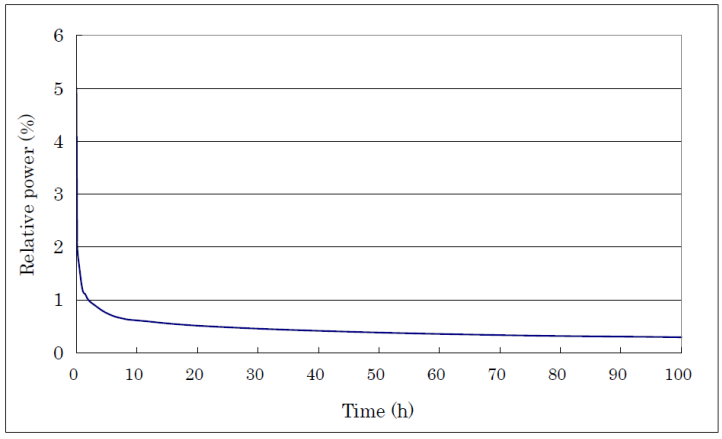

Figure 4.7: Relative power histogram of LOFC and DLOFC accidents

4.2.3 Simulation Result

LOFC

The solid temperature distributions calculated with MGT-3D at 0 h, 20 h, 50 h, and 100 h of the LOFC accident are displayed in Figures 4.8 and 4.9. During normal operation, the coolant goes from the top to the bottom of the reactor core, where the forced convection dominates. The top of the reactor is cooled down effectively by convection, and the coolant is heated along the flow path. Consequently, the bottom of core is hotter than the top, although power density on the top is higher than that at the bottom. With the bypass flow in the reflector blocks, the central and side reflectors are also cooled. There is no heat source in these zones. Therefore, there is a temperature jump at the inside and outside edges of the active core. The temperature is much lower in the reflector zones. It proves the importance of a bypass flow in cooling the control rods located in the reflector blocks.

After the accident, the gas flow is terminated. Without cooling, the heat is mainly transferred out by conduction and radiation, even though there is natural convection. The flow direction of natural convection is from bottom to top, which is inverse to the initial forced flow direction. Additionally, the zone with highest power density is in the center of the reactor. Therefore, the hot center of reactor shifts from the bottom to the top center of the reactor. Figures 4.8 and 4.9 also show that the hot zone spreads from one part of the core to the whole core and the reflector zone. This process takes 100 hours at least, which proves that the large amount of graphite in the core and reflector can store a large amount of heat and prevents fast temperature rising. The maximum temperature over time is presented in Figure 4.10. It can be seen that the temperature increases in the beginning because of the reduced flow, and decreases later because of the reduction of the heat source. The peak value of 1376 $°C$ appears at about 60 hours. It is sufficiently low for the coated particles not to lose their containment function for fission products.

The transient vessel temperature of the middle plane is displayed in Figure 4.11. The vessel temperature decreases at first because the reactor power decreases, and the reactor core has not been heated up. Then, the temperature increases due to the heating up of the reactor core. The maximum vessel temperature is about 420 $°C$, far below the design limit.

The comparison between MGT-3D and Russian code GTAS is presented in Figures 4.12 and 4.13. Both of the presented zones are located in the reactor fuel zone. These two simulation results fit very well during normal operation and at the beginning of the accident. Large differences appear after 50 hours. Differences are small in the RPV, core barrel, and side reflector part. The radial solid temperature distribution (see Fig. 4.12) shows that simulated solid temperature of GTAS is higher than the results of MGT-3D in the fuel zone and in the central reflector. The axial solid temperature distribution (see Fig. 4.13) shows that the result of GTAS is lower on the top and higher on the bottom than the result of MGT-3D. One reason that causes these differences is the different simulation approach to natural convection. These two codes use different equations to calculate the flow resistance friction factor. For GTAS, the correlation for friction is calculated by the following Equations [79]:

$$\begin{cases} \xi = \frac{64}{Re} & \text{laminar flow} \\ \xi = \frac{0.316}{Re^{0.25}} & \text{turbulent region} \end{cases} \tag{4.2}$$

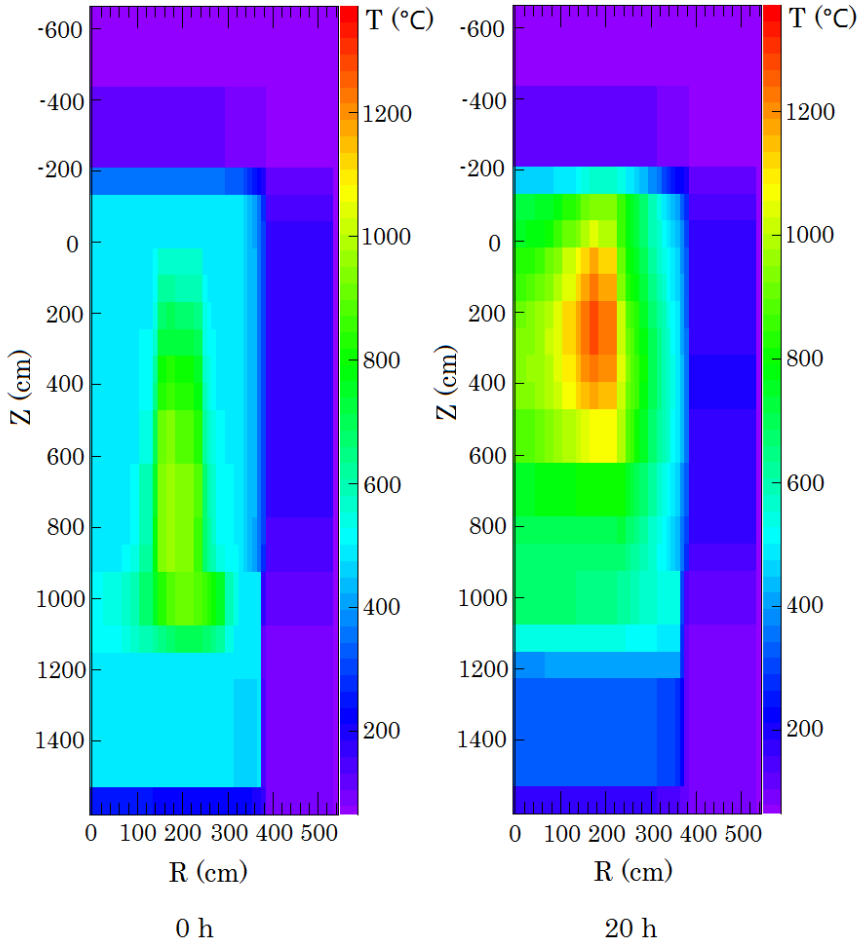

Figure 4.8: Simulated solid temperature distributions of the LOFC accident at 0 h and 20 h

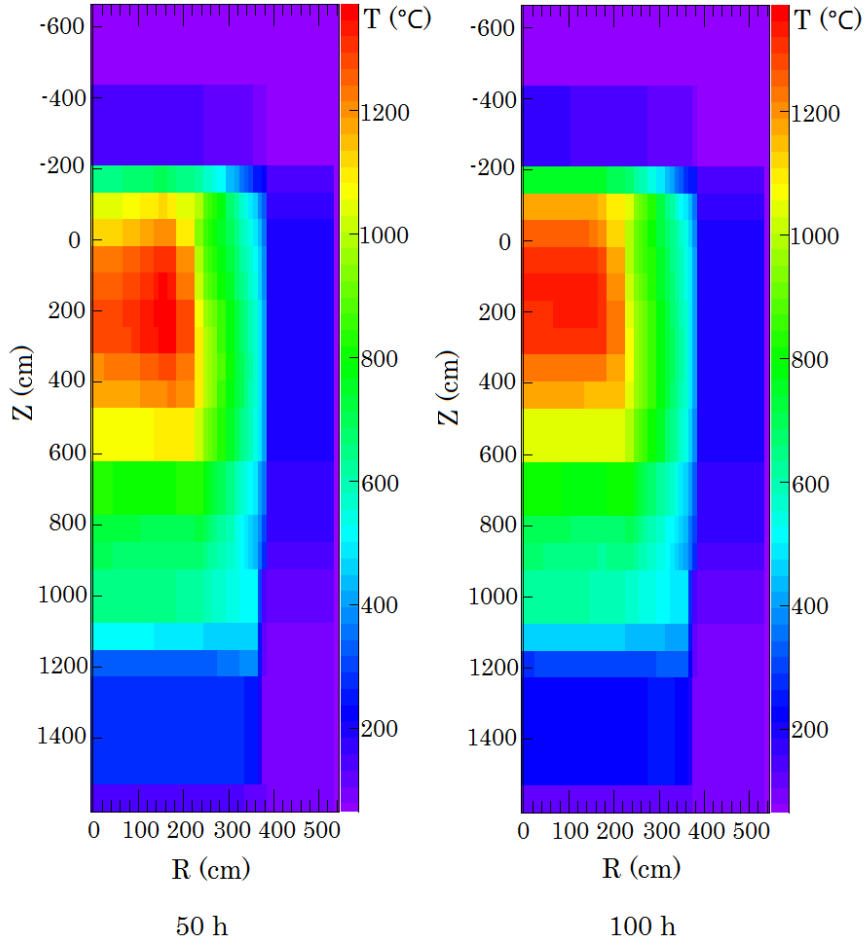

Figure 4.9: Simulated solid temperature distributions of the LOFC accident at 50 h and 100 h

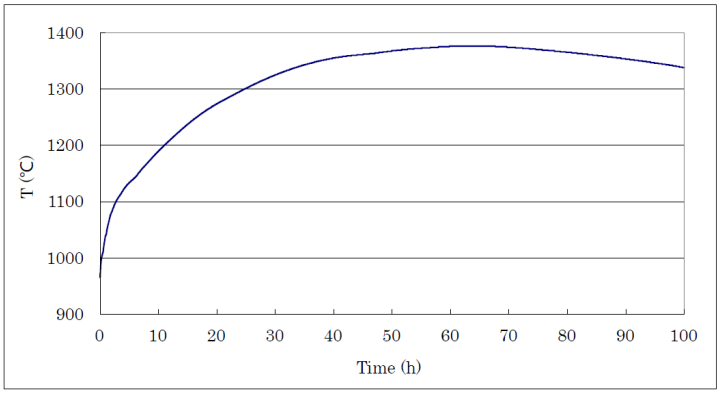

Figure 4.10: Transient maximum solid temperature of the LOFC accident

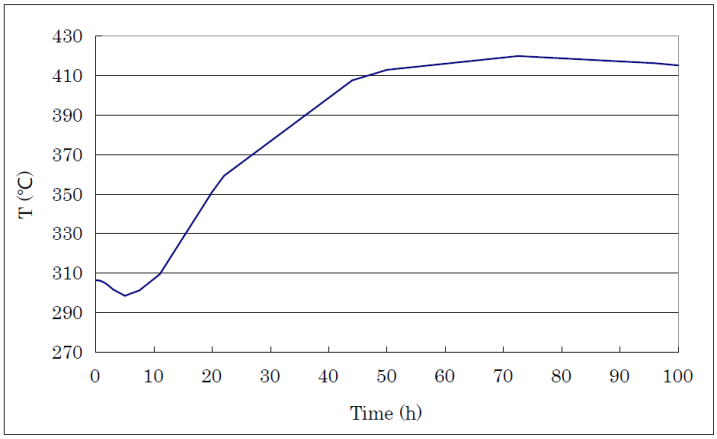

Figure 4.11: Transient vessel temperature of the LOFC accident in the middle plane

In MGT-3D, the resistance friction factor is determined by the following equations:

$$\begin{cases} \xi = \frac{64}{Re} & \text{for } Re \leq 2320 \\ \xi = \frac{64}{Re} + \frac{0.3164}{Re^{0.25}} \frac{(Re-2320)}{8000-2320} & \text{for } 2320 \leq Re \leq 8000 \\ \xi = \frac{64}{Re} + \frac{0.3164}{Re^{0.25}} & \text{for } 8000 \leq Re \leq 10^5 \\ \xi = \frac{64}{Re} + 0.0054 + \frac{0.3964}{Re^{0.3}} & \text{for } Re > 10^5 \end{cases} \tag{4.3}$$

Another reason is the different pressure condition used in these two simulations. In the MGT-3D simulation for LOFC, the pressure is assumed to be unchanged during the process. In fact, if the blower is tripped and the pressure is not released during the accident, the pressure will rise because of the increasing temperature. A pressure of 50 *bar* is used in other simulation [81]. The temperature difference of LOFC accident with different pressure of primary circuit at 100 hours is presented in Figure 4.14. The simulation results in a pressure of 70 *bar* as the reference in this comparison. It can be seen that with 50 *bar* the solid temperature is about 80 $^{\circ}C$ higher than with 70 *bar*, which is equal to the difference between GTAS simulation and MGT-3D simulation. If this difference is added to the MGT-3D simulation with 70 *bar*, the results fit very well. In the plane $R = 172$ *cm*, the solid temperature of the top part with 50 *bar* is about 50 $^{\circ}C$ lower than that with 70 *bar*. Therefore, the difference in Figure 4.13 in long transient can also be partly explained.

Furthermore, Figure 4.12 shows that the calculation results of the two codes on RPV temperatures fit very well during the accident. Thus, the method to use an effective conductivity to represent the convection in the gap zone works very well.

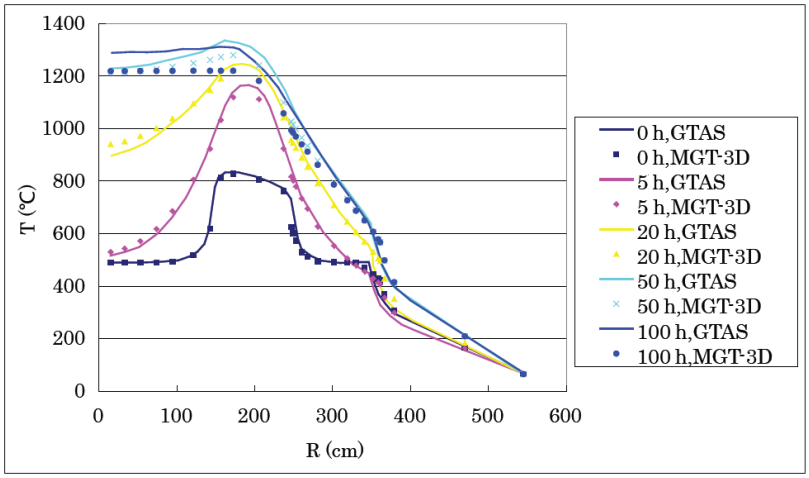

Figure 4.12: Comparison between MGT-3D and GTAS in the middle plane of the reactor core in the LOFC accident

DLOFC

The solid temperatures of DLOFC accident at 0 *h*, 20 *h*, 50 *h* and 100 *h* are displayed in Figures 4.15 and 4.16. The temperature increases in the same manner as the LOFC accident. There are also some differences. For example, the hottest part is not in the top

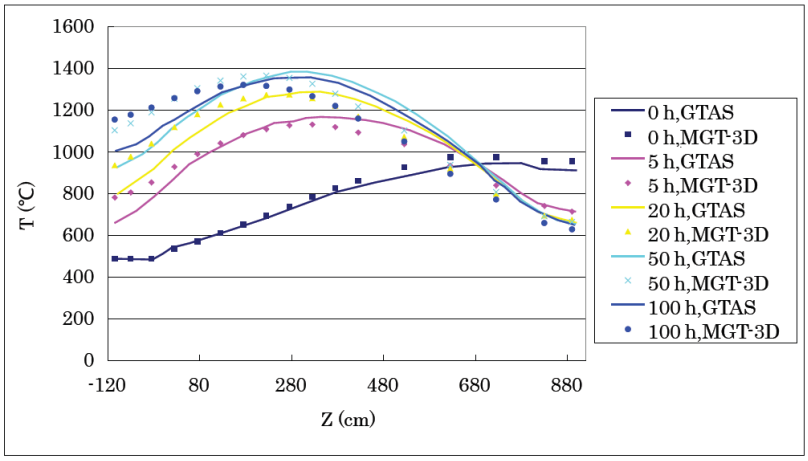

Figure 4.13: Comparison between MGT-3D and GTAS on radius of 1.72 m in the LOFC accident

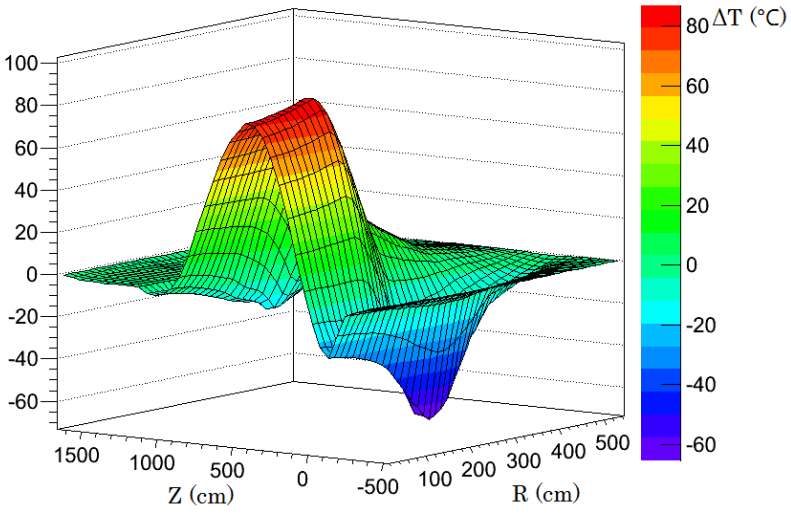

Figure 4.14: Comparison of MGT-3D simulation between 50 *bar* and 70 *bar* of the LOFC accident at 100h

center of the core, but in the center of the core. The reason is that the flow direction of natural convection is from bottom to top. The hot gas causes the top part of the core to be hot as well. But in the DLOFC accident, as mentioned above, the calculations were conducted with all the gas flow calculation disregarded. The heat is removed by thermal radiation and conduction. The hottest zone arises at the position with highest power density, which is in the central plane of the reactor core.

The maximum temperature evolution is presented in Figure 4.17. The peak value is 1535 $°C$ after 70 hours, which is about 159 $°C$ higher than the maximum temperature of the LOFC accident. It is still below the limitation of the HTR design. It also confirms that the reactor core can not be cooled effectively without natural convection.

The transient vessel temperature of the middle plane of the reactor is displayed in Figure 4.17. It decreases first and then increases, similar to the LOFC accident. However, the maximum value, which is about 448 $°C$, is higher than the value in the LOFC accident.

Figures 4.18 and 4.19 show that MGT-3D and GTAS simulation results on DLOFC accident fit very well both in short term transient and long term transient. In general, the differences are in the range of 50$°C$. The simulation results of MGT-3D are generally higher than the simulation results of GTAS. The reason is that all of the gas calculations are neglected in MGT-3D simulation. In fact, the natural convection also exists although it does not dominate in the reactor core. The simulations of both LOFC and DLOFC accidents show that the temperature does not change significantly after 70 hours.

Parameter Variations

Several parameter variations of the DLOFC accident were studied as well to investigate the parameters sensitivity of the model. They include decreasing the effective radiation emission constant of the gap between core barrel and RPV, increasing the decay power, and decreasing the thermal conductivity of reactor core and reflector. These variations have an impact on the maximum solid temperature and vessel temperature. The results are presented in Figures 4.20 and 4.21.

With a decrease of the thermal conductivity of the reactor core and reflector by 20%, the peak value of maximum temperature increases to 1637 $°C$, about 100 $°C$ higher than the reference value. Because the heat is transported mainly out of the core by conduction, the temperature rises significantly with decreasing conductivity. Also, the peak appears several hours later than with default thermal conductivity. This is because the decreasing conductivity makes the thermal relaxation time increasing. With the decrease of the thermal conductivity of the reactor core and reflector, the vessel temperature does not change significantly.

With an increase of power density by 10%, the peak value is about 1662 $°C$, which is 127 $°C$ higher than the reference value. The maximum temperature is very sensitive to the power density. In the scram scenario, the decay heat is the only heat source. According to Equation 2.16, the decay power is proportional to the initial reactor power. Thus, the power density can not be too high for HTGR. Otherwise, the temperature will exceed the temperature limitation. Additionally, the maximum vessel temperature increases to 466 $°C$.

There are many gaps and air cavities in the reactor, e.g. gaps between the blocks, the gap between the core barrel and RPV, the top plenum, the bottom plenum, the cavity between the RPV and RCCS. The thermal conductivity is very low in these areas, and

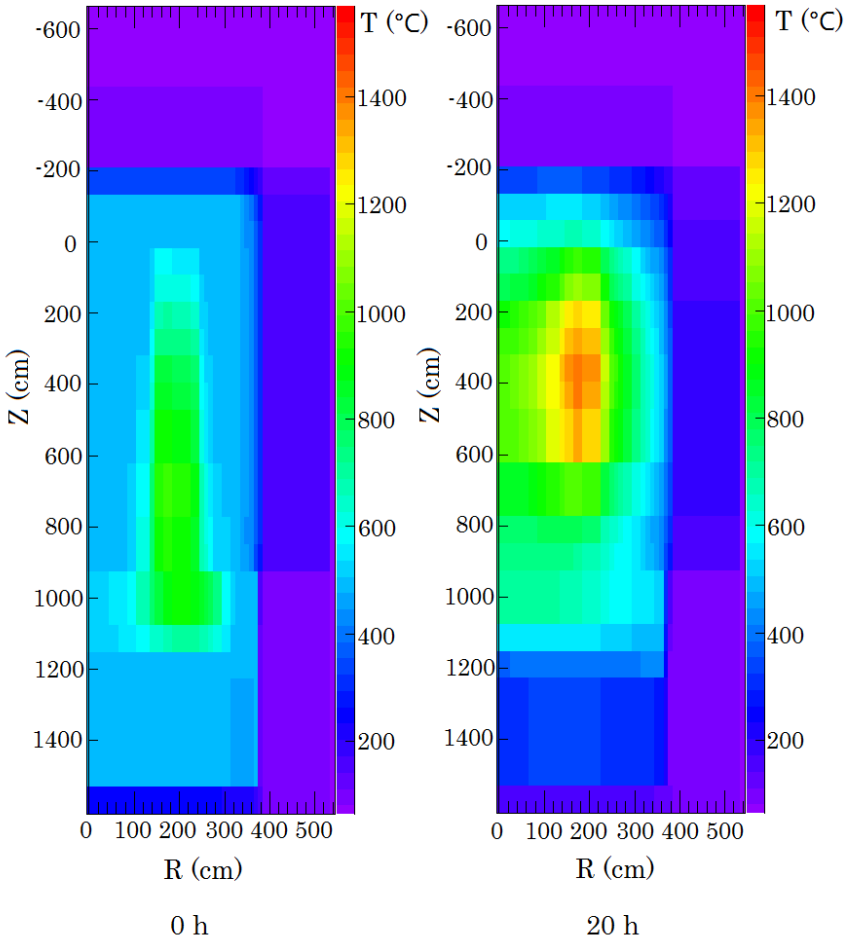

Figure 4.15: Simulated solid temperature distributions of the DLOFC accident at 0 h and 20 h

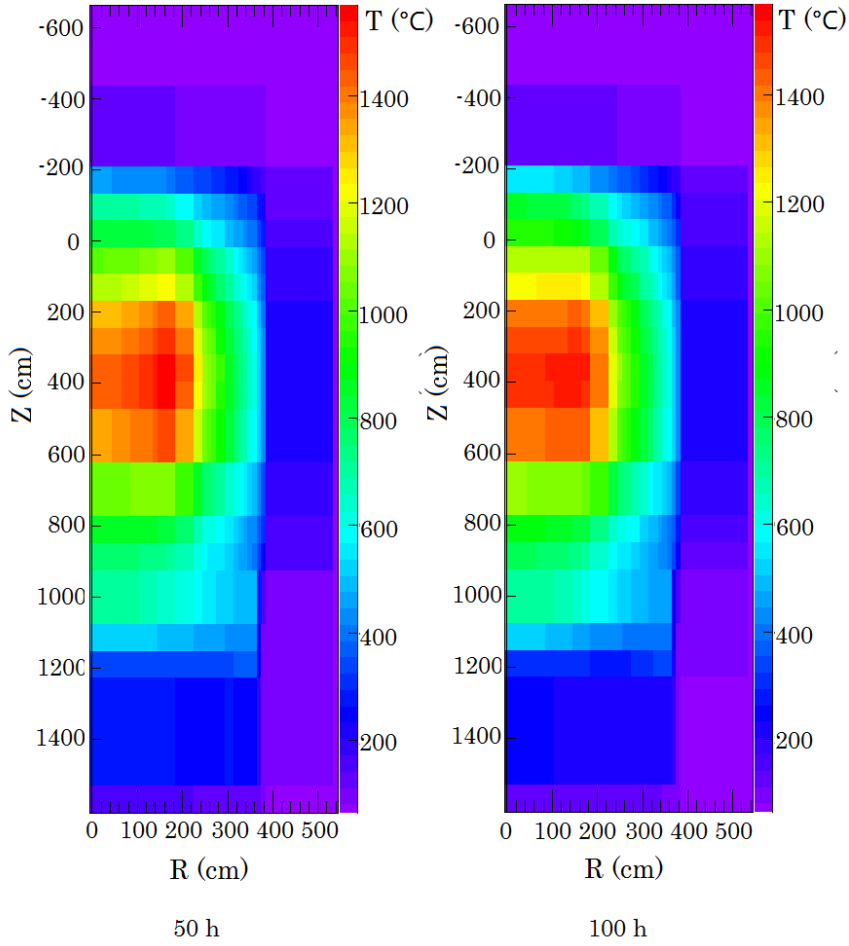

Figure 4.16: Simulated solid temperature distributions of the DLOFC accident at 50 h and 100 h

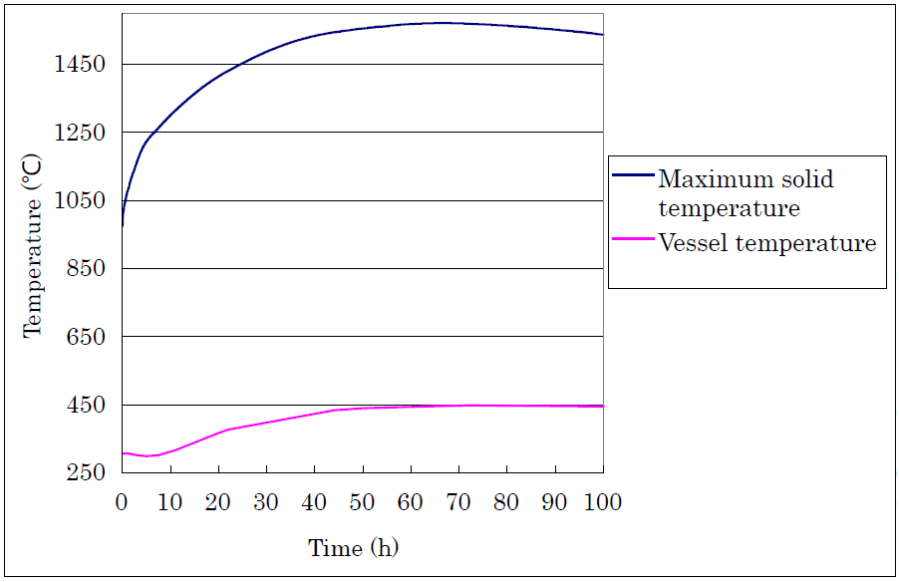

Figure 4.17: Transient maximum solid temperature and vessel temperature of the DLOFC accident

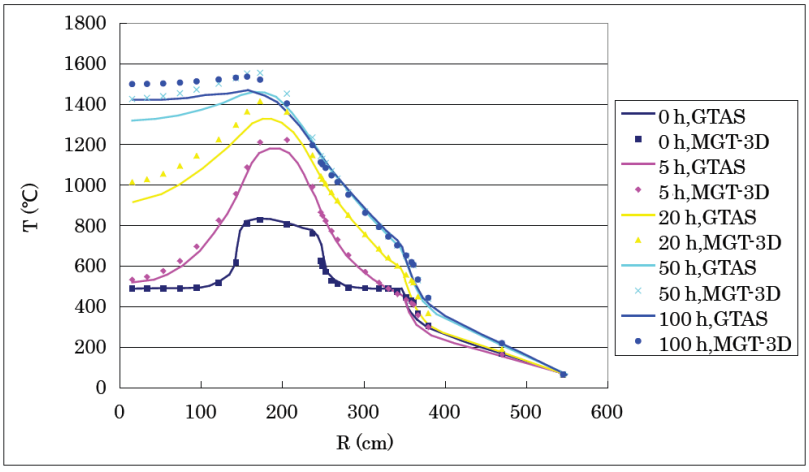

Figure 4.18: Comparison between MGT-3D and GTAS in the middle plane of the reactor core in the DLOFC accident

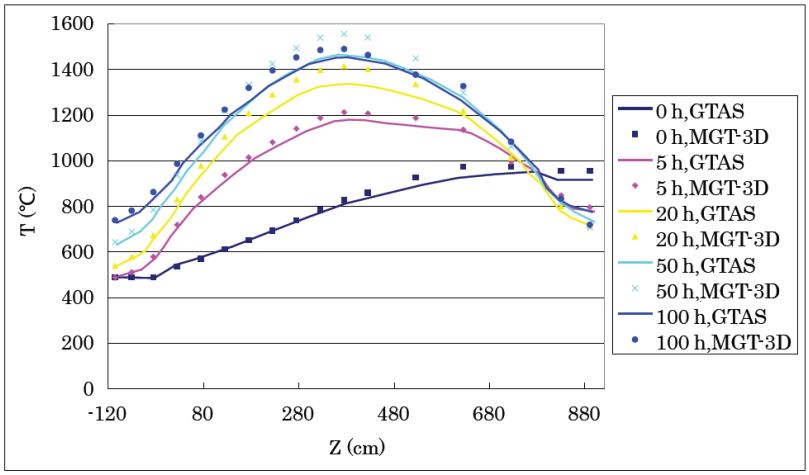

Figure 4.19: Comparison between MGT-3D and GTAS at a radius of 1.72 m in DLOFC accident

the heat is transferred mainly by thermal radiation and natural convection in accident scenarios. The heat flux of radiation is calculated by the Stefan-Boltzmann law:

$$j = \varepsilon \sigma T^4 \tag{4.4}$$

where j is the heat flux per area, ε is emissivity, and σ is Stefan-Boltzmann constant. It can be concluded that the thermal radiation heat flux is proportional to T^4, which means that it will dominate in the cavity with a high temperature zone ($T > 800\ ^\circ C$). The gap between the core barrel and RPV is chosen to investigate the affect of thermal radiation on core temperature. In MGT-3D, the effective radiation emission constant of the cylindrical annular gap is determined by Equation [2]:

$$REPS = \frac{1}{\frac{1}{\varepsilon_1} + \frac{F_1}{F_2}(\frac{1}{\varepsilon_2} - 1)} \tag{4.5}$$

where ε_1, ε_2 and F_1, F_2 are the emissivities and areas of the two surfaces. By decreasing the emissivity from 0.8 to 0.46, the effective radiation emission constant is reduced from 0.67 to 0.3. The peak value of the time-dependent maximum temperature is about 1591 $^\circ C$, which is 54 $^\circ C$ higher than the reference value. The vessel temperature decreases with the decrease of emissivity because less heat transfers from the barrel to the RPV by radiation.

4.3 LOFC Simulation of the HTTR

The Committee on the Safety of Nuclear Installations (CSNI) of OECD/NEA established a Task Group on Advanced Reactor Experimental Facilities (TAREF) to provide an overview of facilities suitable for carrying out safety research on gas-cooled and sodium fast reactors in 2007. This group compiles questionnaires regarding facilities that can

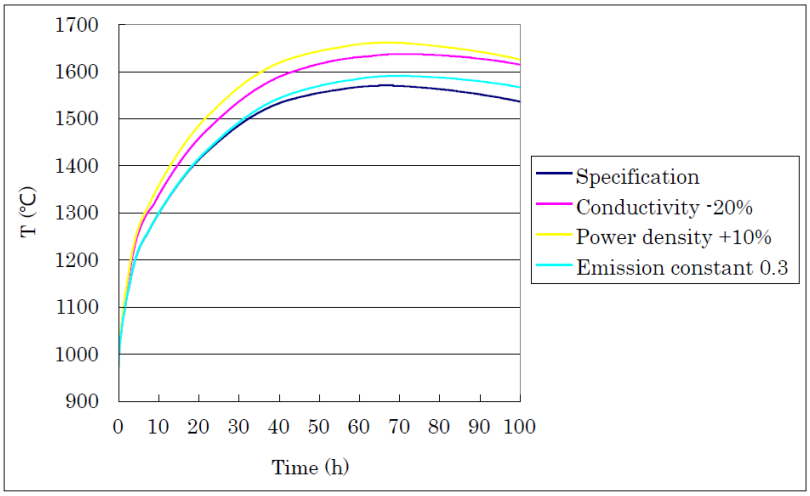

Figure 4.20: Sensitivity studies of maximum solid temperature

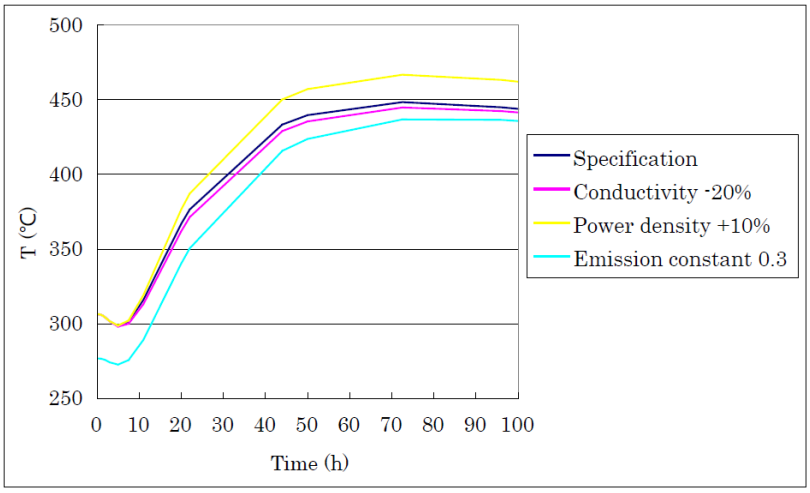

Figure 4.21: Sensitivity studies of vessel temperature

be used to do experimental studies, develops and inspects the phenomenon identification and ranking tables (PIRT) as well as questionnaire responses, and makes suggestions to the CSNI for the facility operation which is related to reactor safety aspects. The High-Temperature Engineering Test Reactor (HTTR), which was built by Japan Atomic Energy Agency (JAEA), is the only running HTGR facility in OECD countries. Therefore, it is a very good tool to investigate the safety aspects identified in TAREF. The group proposed a project to study the technical capabilities of HTTR on the safety issues and to help the member countries in maintaining and further developing the scientific and technical knowledge of HTGRs and in validating corresponding analysis tools. HTGR is chosen as one of the candidates of generation IV reactors because of its particular safety character. The proposed studying topic is the loss of forced coolant accident in a pressurized primary circuit and without scram. It is important to examine whether the power level decreases and the maximum fuel temperature exceeds the limitation. A first experiment was conducted by JAEA in 2010, and the results were distributed to the participating countries that are the Czech Republic, France, Germany, Hungary, the Republic of Korea, Japan, and the USA. Another two experiments are still planned and expected to be finished as soon as possible.

4.3.1 Introduction of HTTR and LOFC Benchmark Description of the HTTR

The HTTR had been built from 1991 to 1996 and achieved the first criticality in November 1998, with full power operation starting in 2001. It was licensed as a research reactor on March 6th, 2002. HTTR is a helium cooled and graphite moderated high temperature reactor with designed thermal power of 30 MW. The core diameter is 290 cm, and the power density is about 2.5 MW/m^3. The primary coolant pressure is 4 MPa, and the inlet gas temperature is 395 $°C$. The outlet helium temperature is 850 $°C$ in nominal running phase and achieves 950 $°C$ in high temperature running phase. It uses the prismatic fuel block which is fueled with low enriched uranium dioxide with enrichment levels from 3% to 10%.

The HTTR applies a double containment concept, which consists of reactor containment vessel (C/V) and reactor pressure vessel. The containment vessel, with 18.5 m in diameter and 30 m in height, is made of steel and is located in the center of the reactor building. The RPV, Secondary Pressurized Water Cooler (SPWC), helium circulators, Intermediate Heat Exchanger (IHX), and Primary Pressurized Water Cooler (PPWC) are integrated in the containment vessel. With this design, the containment vessel behaves as one of the multiple barriers against fission product release in normal operation and accident scenarios. It can also prevent air ingress from the environment if the pipes or the vessel of primary circuit is ruptured.

Reactor Pressure Vessel

The reactor pressure vessel, which is made of Cr-Mo steel, is fabricated as a shape of vertical cylinder with hemispherical top and bottom head closures. The stand pipes are located in the top heat closures (see Fig. 4.22). They include control rods, reserved shutdown rods, and irradiation stand pipes. There is a thermal shield layer inside the top RPV to protect the closures and RPV from overheating by rising gas in LOFC or DLOFC accident. The height of cylinder part of RPV is 7.67 m. The diameters of top and bottom hemispherical plenum are all 5.5 m, which is also equal to the diameter of the cylinder part. The total height of the RPV is 13.22 m.

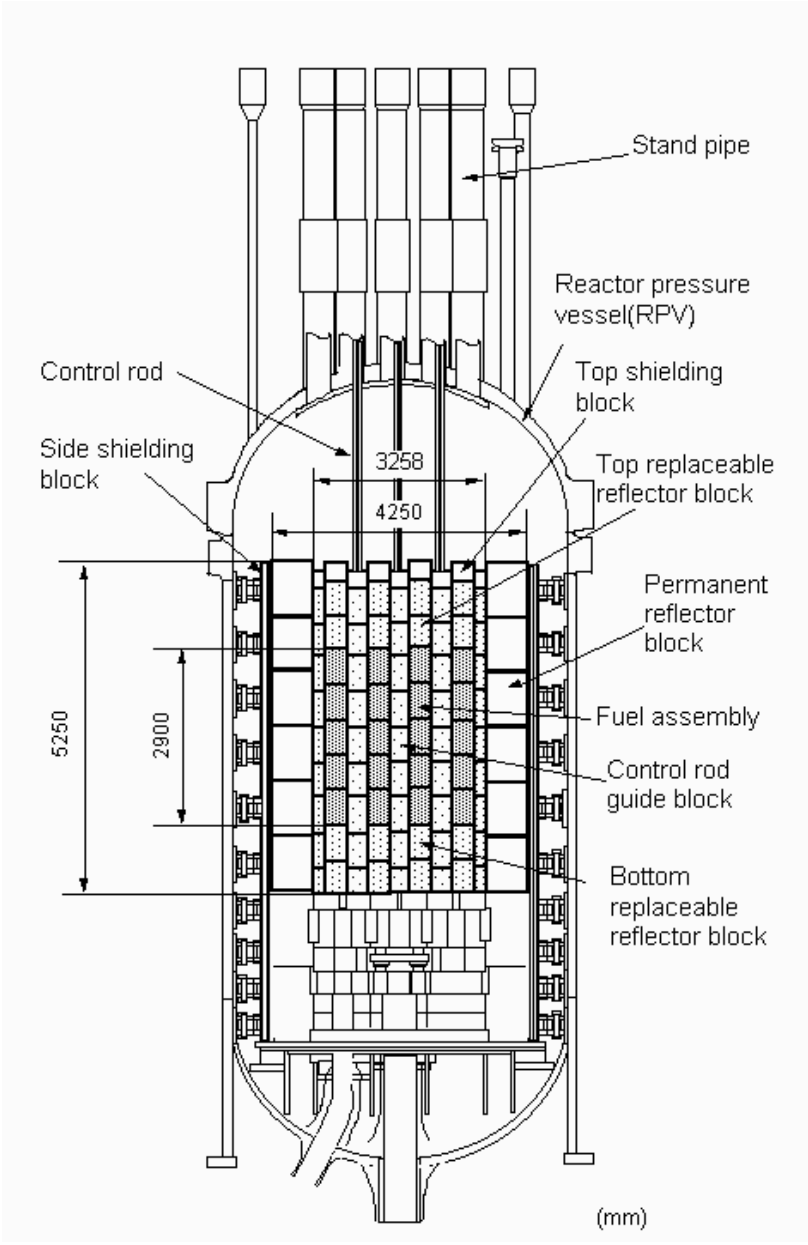

Figure 4.22: Vertical view of the HTTR [82]

Core Configuration

Considering the advantage of flattening the neutron flux, decreasing the center temperature of the reactor core, inherent safety characteristics for loss of forced coolant accidents, and so on, the reactor core uses the typical annular assemble design as well [83, 84, 85]. The position of the core is identified by naming of column in horizontal direction and by naming of layer in vertical direction. The reactor core consists of fuel columns, control rod guide columns, irradiation columns, and replaceable reflector columns (see Fig. 4.23). They are made of hexagonal graphite blocks like GT-MHR. Two types of fuel blocks, which have 12 columns of 33 fuel rods and 18 columns of 31 fuel rods, are placed in the core in an hexagonal annular shape. The fuel blocks with 33 fuel rods are arranged in the central and middle annular ring and the fuel blocks with 31 fuel rods are arranged in the outer annular ring. There are 5 layers of fuel blocks. As a result, 150 fuel blocks are loaded in the reactor. The active core, which is 290 *cm* in height and 230 *cm* in effective diameter, consists of 30 fuel columns that are grouped concentrically into 4 fuel zones and 7 control rod guide columns. One control rod guide column is located in the center of the core, and another six columns are placed in the middle annular ring with an arrangement of separated by fuel columns. It is occupied by 12 replaceable reflector columns, 9 control rod columns, and 3 irradiation columns in the outermost ring.

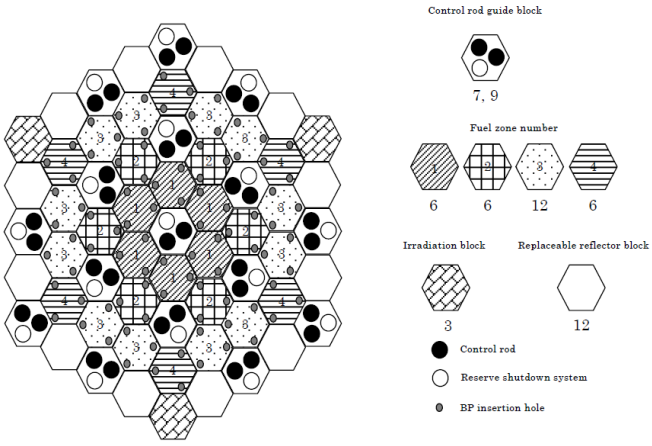

Figure 4.23: Horizontal cross sections of the HTTR [82]

The fuel blocks with 33 and 31 fuel pin holes are presented in Figures 4.24 and 4.25. The fuel block is a prismatic hexagonal block that is made of IG-110 graphite. The height of the block is 58 *cm*, and the across flat in width is 36 *cm*. The diameter of the coolant hole is 4.1 *cm*. The hole is reserved for inserting the fuel pins. The center-to-center distance of adjacent holes is 5.15 *cm*. In the top-center of the block, there is a fuel handling hole. The fuel handling hole is shaped as an inverted truncated cone on the top to guiding the fuel-handling machine. It forms a ledge for the grapple head to stand against in the bottom cavity to lift the fuel block during shuffling. It has three dowel pins on the top and three dowel sockets on the bottom. Under each of the unscrewable dowel pins, there is a hole with diameter of 1.5 *cm* and 50 *cm* in height for burnable poison rod.

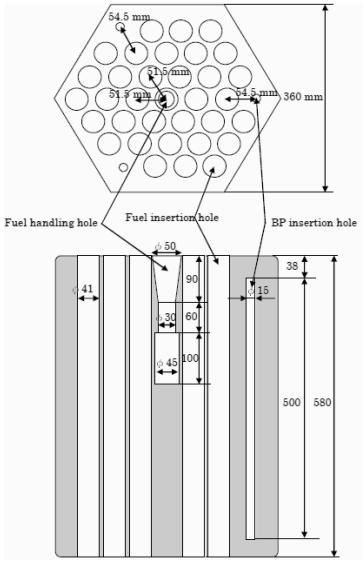

Figure 4.24: Fuel block with 33 pin holes [82]

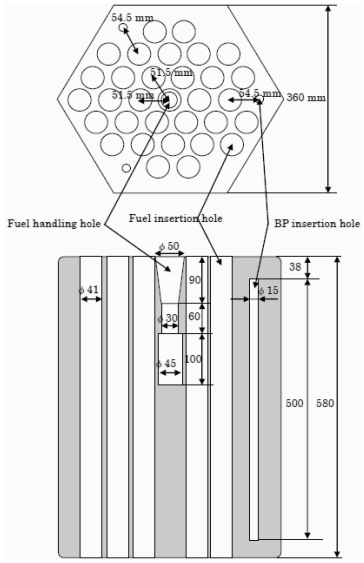

Figure 4.25: Fuel block with 31 pin holes [82]

The dowel pins are inserted in the down sockets of the top block to fix the position of the fuel block, seal the burnable poison holes, and align the cooling holes. The burnable poison rod is fabricated from graphite and boron carbon (B_4C) and its diameter is about 1.4 cm. Normally, two burnable poison rods are used in reactor operation.

There are replaceable graphite blocks with coolant holes located on the top and the bottom of fuel blocks. They are used to reflect the neutrons back to the reactor core to make full use of the neutron flux, to avoid the high power peak and to protect the RPV systems from neutron irradiation. The replaceable reflector block of 1st, 2nd, and 8th layers in the 33 pin column and the 31 pin column are presented in Figures 4.26 and 4.27 respectively. They have the same hexagonal shape and dimension as the regular fuel blocks. The coolant holes of reflector block are aligned with the contacted fuel blocks. The diameter of the coolant hole of replaceable reflector block is chosen as 2.3 cm with which its cross sectional area is equal to the cross sectional area of annular flow path of fuel block. Therefore, the flow velocities and gas densities are the same in the aligned flow path.

The envelope dimensions of the control rod guide blocks are the same as the graphite blocks, and they are made of graphite of the same type. They also have the same handling structure and dowel/socket structure. Each control rod guide block has three holes with diameter of 12.3 cm: two for control rod insertion and another one for the emergency reserved shutdown rod [86]. There are in total 16 pairs of control rods and 16 reserved shutdown rods. The control rods are made of B_4C/C pellets and metal spine. Each control rod has a length of 309.4 cm. The control rods can penetrate until the 7th layer, which is one block below the bottom fuel block. The blocks of 9th layer do not have control rod guide holes. The control rods are installed to control the reactivity during normal operation and to shut down the reactor reliably and safely in all of the designed accidents. They are designed to be fail-in-safe. They are driven by AC motors in normal

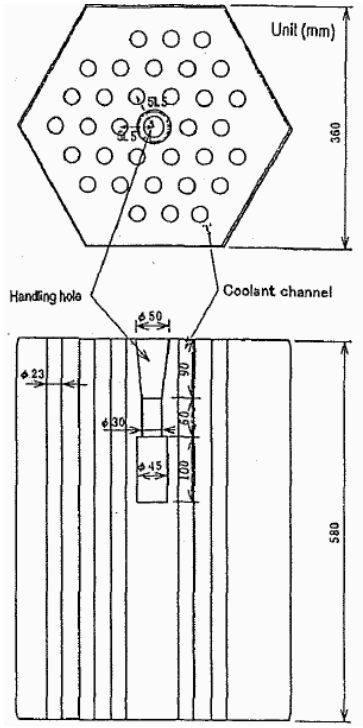

Figure 4.26: 1th, 2nd and 8th layers reflector block in 33 pin column

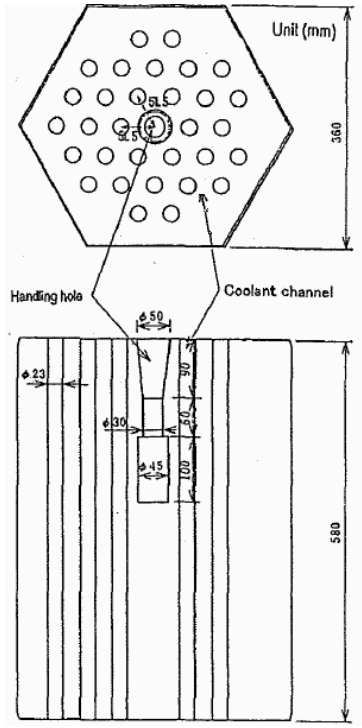

Figure 4.27: 1th, 2nd and 8th layers reflector block in 31 pin column

case and can drop down by gravity if the driven system does not work. The reserved shutdown system is composed of cylindrical B_4C/C pellets, hoppers that surround the pellets, driving mechanisms, an electric plug, and a guide tube. If the control rods can not be inserted into the reactor in the accident, the electric plug will be pulled out, and the pellets will fall down through the guide tube by gravity. They are designed to hold the reactor below the criticality in emergency cases. The guide holes for reserved shutdown rod are sealed in the bottom of the 7th layer.

Fuel Rod and Coated Particle

The HTTR fuel block uses pin-in-block design [88]. It is shown in Figure 4.28. The fuel rod consists of fuel compacts graphite sleeves, plugs and spacers. Each fuel rod is filled with 14 fuel compacts. They are stacked together and sealed in the graphite sleeve with graphite plugs. The fuel rod is inserted in the coolant holes. It has several spacers out of the graphite sleeves to support the fuel rod. The spacers are designed to make sure that the fuel rod is located in the center of the coolant hole. With the support of the spacers, it forms an annular gap between the fuel rod and the graphite block. The helium flows in the annular gap to transport the fission heat out. In the fuel compact, coated particles are homogeneously mixed with graphite. The fuel compact is shaped as a hollow cylinder with a 1 *cm* inner diameter, a 2.6 *cm* in outer diameter, and a 3.9 *cm* height. The center hole is filled with helium, which is sealed in the graphite sleeve to be stagnant. Each fuel compact contains about 13000 TRISO-coated particles, which have the same structure as the coated particles of pebble bed HTGR. The center of the coated particle is a dioxide uranium fuel kernel with as average enrichment of 6%. The fuel kernel is coated with porous carbon, inner PyC, SiC, outer PyC from inside to outside. The coated particle, fuel compact, and graphite sleeve can retain both metallic and gaseous fission products in a large temperature range.

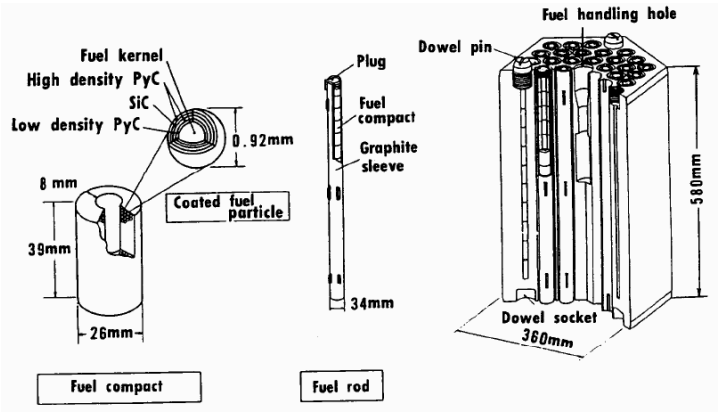

Figure 4.28: The fuel rod structure of HTTR [82]

Permanent Reflector and Neutron Shielding Block

The core components are surrounded by a permanent reflector that is fabricated from grade PGX graphite in radial direction. The permanent reflector consists of 12 circumferential segments in 8 axial layers [87]. The shape of the permanent reflector block is a large polygonal graphite block. The width across the horizontal cross section of the core, including the permanent reflector blocks, is 425 *cm* as shown in Figure 4.22. There

are some holes in the permanent reflector blocks for irradiation tests, temperature measurements, and neutron flux detectors. The permanent reflector blocks are surrounded by side shielding blocks that consist of B_4C/C and casing of SUS316.

Restraint System

The core restraint mechanism is installed outside the side shielding blocks to stress the reactor core, to supply a stable support during normal operation and seismic events, and to provide enough space for the coolant flow between RPV and permanent reflector. The stress from the restraint mechanism is transferred from the side shielding block and permanent reflector blocks to the reactor core. Thus, it can stress the reactor core to reduce the bypass gaps among the blocks. The restraint mechanism consists of restraint bands, bands support, restraint rings, and radial keys. The restraint bands can reduce approximately 60% of the restraint force by the relaxation of the material at the end of the plant life [87]. The restraint mechanism is connected with the RPV by the keys on it. The RPV is made of $2.25Cr - 1Mo$ steel. The inner diameter is 550 cm and the thickness of the RPV wall is 12.2 cm.

Two layers of graphite reflector blocks are placed on the top and bottom of the fuel and replaceable reflector columns. In total, there are 9 layers except the top shielding blocks. They are identified by 1st to 9th layer from top to bottom. In the fuel columns, the blocks with a height of 58 cm are stacked together. The fuel blocks are arranged from the 3rd to 7th layers. The total height of the active core is 290 cm. The 1st, 2nd, 8th, and 9th layers are reflector blocks with the same height of 58 cm. There is a shielding block with a height of 30 cm on the top of the 1st reflector block. Therefore, the height of a fuel column is 552 cm. In the control rod guide columns and replaceable reflector columns, the highest block is also the shielding block with a height of 30 cm. The lowest (9th) block is 48 cm high. Therefore, the total height of a control rod guide column or a replaceable reflector column is 542 cm.

Top Plenum and Bottom Support Structure

There is a hemispherical cavity on the top of the shielding block, which is reserved space for the control rod, shutdown rod, and measurement devices. The top hemispherical cover of the RPV is screwed together with the cylinder body. It can also be opened to shuffle the fuels. A thermal shield, which is constructed of 10 or 4 layers of stainless steel plates, adheres to the inside surface of top RPV to prevent its overheating.

The reactor bottom internals are comprised of a hot plenum block, support post, lower plenum block, carbon block, bottom block, support plate, and core support grid. The details are shown in Figure 4.29. The support plate and core support grid are made of metallic material, and the others are fabricated from IG-110 graphite, ASR-ORB, and PGX graphite, which have excellent erosion resistance and thermal properties. The geometry of these structures is as follows:

- Hot plenum block: There are 7 hot plenum blocks, which consist of seal blocks on the top and key connection blocks on the bottom. Each seal block is 23 cm in height and 95 cm in width across flats, and has 7 flow holes. The connection blocks with a height of 67 cm have the same across flat as the seal block. Each of them has only one flow hole.
- Support post: These hot plenum blocks are supported by a post with a diameter of 15 cm and a height of 60 cm. The support structure forms a big cavity where the hot coolant meets together.

- Lower plenum block: The supports post stands on seven lower plenum blocks made of PGX graphite. The height is 35 *cm*, and the across flat is about 95 *cm*. The central one has one flow tube. The off-center coolant block has also one flow tube, but with different diameter with the former one, which is reserved for the auxiliary coolant. The other five blocks are solid without any coolant flow hole in them.
- Carbon block: There are seven columns and two layers of carbon block with a total height of 60 *cm*. The width across flats of each block is 95 *cm* as well. These blocks are made of the material ASR-ORB. They have the same structure as the lower plenum block, and their coolants holes are aligned with the coolant holes of lower plenum blocks.
- Bottom block: The bottom blocks are arranged in the same way as the carbon block. The height of bottom block is 20 *cm*. They are fabricated from PGX graphite.

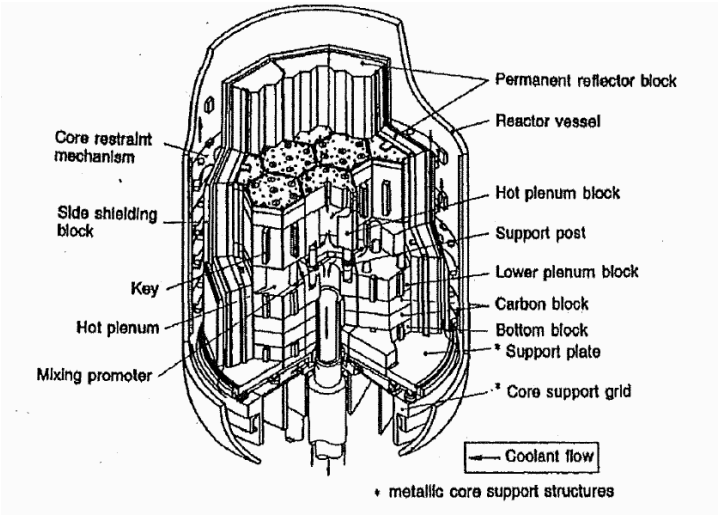

Figure 4.29: The bottom intervals of HTTR [87]

- Support plate and core support grid: They are made of metallic material. The support plate supplies the reactor core with the basic foundation surface. Its thickness is about 9 *cm*, and its radius is about 485 *cm*. The support plate is separated from the support grid by steel support posts. Therefore, there is a gap with height of 9 *cm* between the support plate and the support grid. The forced coolant is guided to flow through this gap to cool down the support plate and support grid in normal operation. The total weight of the reactor core stands on the support plate, and then it is transferred to the hemispherical bottom RPV head closure through the support ribs.

The bottom internals play a role of insulating the reactor core from the RPV, mixing the coolant flow, guiding the coolant to the outlet, and providing the stable foundation for the reactor core in both normal situations and in earthquake.

Reactor Cooling System

There are two cooling systems to remove the heat from the primary circuit [88, 82]: the main cooling system (MCS) and auxiliary cooling system (ACS). The details are shown in Figure 4.30. The MCS consists of a primary helium cooling system (PHCS), a secondary helium/pressurized water cooling system (PWCS), a secondary helium/helium cooling system (SHCS), and the pressurized water air cooler. In the PHCS, there are two primary gas circulators (PGC) to blow the coolant into the reactor, and the coolant flows through the core and exits from the hot gas duct. In the PWCS, the heat transfers from the hot gas into the cooling water in the primary pressurized water cooler (PPWC), and then the heat is transported out of the system in the pressurized water air cooler to the environment. In the SHCS, the heat exchanges between the primary helium circuit and secondary helium circuit, which is driven by a secondary gas circulator in the intermediate heat exchanger (IHX). The SHCS includes a secondary pressurized water cooler (SPWC). The water is pumped into the SPWC by a pressurized water pump. At last, the heat is taken away by the pressurized water air cooler and released into the environment. The SHCS shares the pressurized water air cooler with the PWCS. The pressure of secondary helium of SHCS is set to be always about 0.1 MPa higher than the primary circuit in normal operation [82]. It guarantees that there are no leakages of radioactive materials from the primary circuit to the secondary circuit. The pressure of the water loops is about 3.5 MPa, which is lower than that in both of the helium loops. It can prevent water ingress into the helium loops and then into the reactor core in the accident when the cooling pipes of SPWC and PPWC break.

The reactor is operated at 4.0 MPa during full power operation. The cold helium is blown into the reactor through the outer annulus of the concentric flow tube which is located in the bottom center of RPV. It passes through the empty space under the metallic core support plate, to make sure that the support plate is cooled effectively. The empty space is connected with the restraint system. Therefore, the flow rises up from the restraint system to the top cold plenum. The mixed coolant is redistributed into the coolant hole of the fuel block, where it is heated by fission energy. The hot helium, which is from a different flow path, is ejected into the mixing promoter. Then it flows down to the inner tube of the concentric flow tube, which is connected to the heat exchanger.

The MCS has two operational modes: one is the parallel loaded operation mode in which both PWCS and SHCS are operated, the other one is the single loaded operation mode in which only the PWCS works. If the reactor runs at the full power of 30 MW and in the parallel loaded operation mode, the PWCS will remove about 20 MW of the total power, and SHCS will remove about 10 MW. The reactor is cooled only by the PWCS during the single loaded operation.

The ACS is constituted of the auxiliary heat exchanger (AHX), auxiliary gas circulator (AGC), auxiliary water air cooler, and auxiliary water pump. The water is pumped into the AHX by the auxiliary water pump. The hot helium, which is from the reactor core, is cooled down by the water in the AHX. The heat of the water is dissipated to the atmosphere in the auxiliary water air cooler. The heat transfer capacity of the ACS is about 3.5 MW. The helium is blown into the reactor core with a mass flow rate of about 200 kg/h in normal operation. In the ACS, the helium passes through a primary helium purification system, in order to remove impurities contained in the reactor coolant. The auxiliary cooling system starts automatically in an accident to remove the residual heat. Although the residual heat of the core can be removed out of the RPV by the vessel cooling system, the ACS reacts quicker than the vessel cooling system.

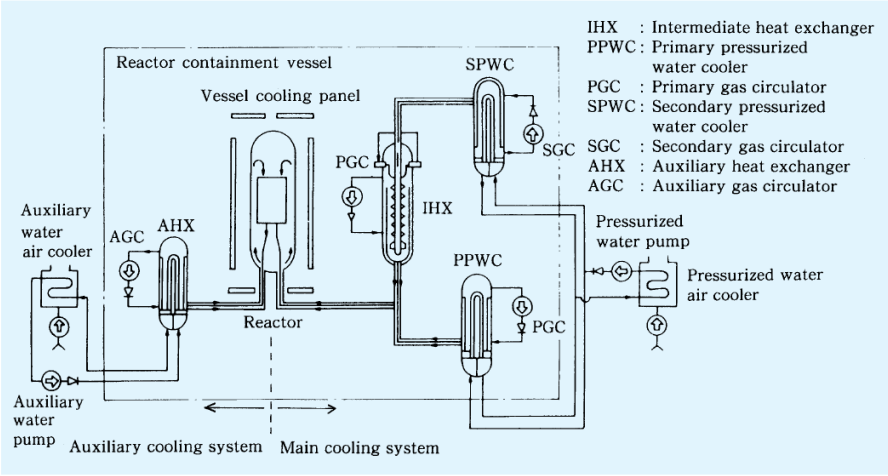

Figure 4.30: The cooling system of HTTR [88]

Vessel Cooling System

The vessel cooling system (VCS) is designed to protect the RPV and biological shielding concrete wall against thermal damage in normal operation and accident scenarios. It consists of cooling panels and cooling water circulation. There are two independent complete sets, which are an engineered safety feature with redundancy. The cooling panels with cooling tubes in them are installed on the top, bottom, and side of the RPV. The flow rates of the cooling water of the side panel, the top panel, and the bottom panel are 72 ton/h, 6.5 ton/h, and 6.5 ton/h respectively. The total flow rate of the cooling water is about 85 ton/h in each VCS set. The cooling panels are located in front of the concrete wall, which can protect the wall from directly heating by thermal radiation. The amount of the heat removal can be adjusted by controlling the water flow rate in the cooling tubes. The designed removal power of the VCS is 0.6 MW. If the outlet gas temperature of 950 $°C$ is gained, the removal power should be adjusted to be less than 0.6 MW during normal operation. The removal power of the VCS should be more than 0.3 MW to avoid that the temperature of the reactor core and RPV exceeds limitations.

LOFC Test Description

In order to investigate the safety characteristics in support of the licensing of HTGR and to validate the current code simulation ability and model precision, several experiments of loss of forced cooling accident are proposed to be done in HTTR. The project is devised to provide detailed experimental data for the reactor safety research of the participating countries and to prove the safety characteristics of HTTR. The LOFC accident is an integrated large scale test. The reactor performance under this accidental condition is investigated in the experimental test [89]. In the project, JAEA plans to conduct three runs of LOFC without scram experiments. During the LOFC transient, the reactor power is monitored to measure the re-criticality time and re-criticality power level. It involves the reactor kinetics, core physics, and fluid mechanics. Thus, it is one of the most important safety aspects of the reactor. At the same time, the temperature

evolution during the transient is recorded as well. The performance of the reactor cavity cooling system, which is an important system to protect the RPV and remove the residual heat in HTGRs, is researched as well. All of these data supply the participants with experimental data to benchmark their code and simulation models.

In the LOFC test, all of the three helium gas circulators in the main cooling system of HTTR are tripped and the auxiliary cooling system is deactivated as well [90]. The accidents are designed without shutdown. In order to avoid the scram of the reactor due to its response on accident scenarios, the control rods and reserved shutdown system are forced to deactivate during the experiment. The control rods and reserved shutdown rods stay in their position as in normal operation. The project consists of three runs of experiments as following:

- Run 1: The reactor operates at the initial thermal power of 9 MW. The coolant inlet and outlet temperatures are 180 $°C$ and 320 $°C$ respectively. The pressure of primary circuit is 2.8 MPa. The mass flow rate of the coolant is 12.4 kg/s. The front of the control rods in the center control rod guide block is 55.5 cm below the top surface of the 1st layer of the fuel block. The front of the control rods in one of the 1st ring control rod guide blocks is 56.2 cm below the top surface of the 1st layer of the fuel block, and other control rods in the 1st ring control rod guide blocks are 56.5 cm below the top surface of the 1st layer of the fuel block. The control rods in the 2nd ring control rod guide blocks are also 56.5 cm below the top surface of the 1st layer of the fuel block. The control rods in the 3rd ring control rod guide blocks are fully withdrawn out of the reactor core. All of the helium gas circulators are tripped, and the gas flow of the primary circuit decreases from 12.4 kg/s to 0 kg/s in 10 s. During the transient process, the position of the control rods are fixed. The forced cooling system is closed. The residual heat is transferred out of the reactor by conduction, thermal radiation, and natural convection. The VCS is activated to cool down the RPV and containment.
- Run 2: The initial power has a significant effect on the fluid mechanics such as solid temperature evolution, and natural convection, after the forced coolant is closed. It also impacts the decay heat, initial Xenon density and so on. Therefore, the total effects of initial power on the re-criticality time and power peak are important issues to investigate. In order to collect more information about this topic, the Run 2 experiment is proposed. In the Run 2 experiment, the reactor operates with an initial thermal power of 30 MW. The inlet and outlet coolant temperatures are 395 $°C$ and 850 $°C$ respectively. The primary circuit runs at 4 MPa, and the coolant flow rate is 12.4 kg/s. The control rods of center, 1st ring, and 2nd ring control rod guide block are located at 15 cm below the top surface of the 1st layer of the fuel block. The control rods of the 3rd ring are totally withdrawn. All of the control rods keep their position during the experiment. To simulate the LOFC accident, all of the helium gas circulators are tripped, and the forced flow rate reduces to 0 kg/s in 10 s. The VCS is fully loaded, as in the experiment of Run 1.
- Run 3: The reactor cavity cooling system is an important passive cooling system of HTGRs. It is designed to remove the decay heat, and to cool the RPV and containment wall, mainly by natural convection in the cavity between the RPV and the VCS. In order to research the fluid mechanics of reactor cavity cooling system, the Run 3 experiment is carried out with the deactivation of the VCS. The initial condition is the same as with Run 1 with a thermal power of 9 MW. The impact of VSC on RPV temperature, re-criticality time, and power level, and

fluid mechanics of reactor core are studied in Run 1 and Run 3 experiments. The Run 3 experiment tests the fluid mechanics and neutronics evolution of HTTR in the case of a loss of all the cooling systems. The experiment data can also provide suggestions to make the design range of VSC of HTGRs.

The general information of the initial condition of these three runs of experiments is summarized in the following table:

Case No.	Reactor power (MW)	Gas inlet/outlet temperature ($^{\circ}C$)	Pressure(MPa)	Flow rate (kg/s)
Run 1	9 MW	180/320	2.8	12.4
Run 2	30 MW	395/850	4.0	12.4
Run 3	9 MW	180/320	2.8	12.4

Table 4.2: Initial conditions of the test experiments

In the experiment, the wide range monitoring system and the power range monitoring system are used to measure the reactor power. The control rod position is measured with an encoder sensor, and many thermocouples are used to measure the gas temperature, permanent reflector block temperature RPV temperature, VSC temperature, and concrete temperature. The measurement results supply the participants with experimental data to prove the occurrence of reactor re-criticality in the case of the anticipated transient with LOFC and without scram to validate their codes on fluid mechanics, reactor kinetics, and core physics, to test the capability of the codes on coupled fluid mechanics and neutronics simulation, and to study the parameter dependency of their codes.

4.3.2 Serpent Model of the HTTR

Serpent is a three-dimensional continuous energy Monte Carlo reactor physics burnup calculation code. It has been developed at VTT Technical Research Center of Finland [91]. It is based on the universally constructive solid geometry model, which is similar to MCNP and Keno-VI. Serpent can be used to simulate reactor physics, neutron transportation, and burnup of both light water reactor (LWR) and HTGRs. It can be applied to the calculation of fuel pin, fuel assembly and core levels. Serpent can use the parallel calculation mode with the Message Passing Interface (MPI). It also provides some interfaces for the data exchange with other codes in the input and output files, so that it is easier to be coupled with other codes. INL has developed a Serpent model of HTTR and conducted code-to-code benchmarking with the MC code MCNP5, the deterministic transport codes INSTANT, DRAGON, and HEXPEDITE [92]. Also at FZJ, an independent model for HTTR has been developed to calculate its burnup and simulate the reactor physics such as effective and infinite multiplication factors, assembly pin-power distributions, normalized neutron flux, fission rates, etc. The data required by MGT-3D is converted to the right format from the output of Serpent by an interface program for the further MGT-3D simulation.

The geometry definition of Serpent is based on lattice and surface. The lattices of the model are connected by the surfaces. The material content is defined in the lattice. The geometry is constructed with independent levels such as the reactor core, fuel assembly, fuel pin, and coated particles, which are required for HTGRs' model. Serpent provides

some specific geometric features, such as fuel pins for American and Japanese type HTGRs, spherical pebbles for pebble bed HTGR, square and hexagonal lattices for LWR geometries, and circular cluster arrays for CANDU fuels.

In the HTTR simulation, the geometry model consists of independent levels of reactor core, hexagonal fuel, reflector and control rod guide block, fuel pins, and coated particles, which are embedded in the graphite matrix of fuel compacts. They are nested into each other. At the first level, the coated layers of fuel particles are described in detail from the central fuel kernel to the outer pyrolytic carbon, the surface of each layer is defined as sphere, and the contents of the layers are defined as the isotopes from which they are fabricated. At the fuel pin level, the definition of annular cylinder material surface is used, and the coated particles are randomly dispersed in the fuel compacts, which are encapsulated in the fuel pins. At the assembly block level, the fuel pin and B_4C/C poison sticks are located in the graphite blocks with the hexagonal shape. At the reactor core level, fuel blocks, control rod guide blocks, and reflector blocks are placed in the cylindrical reactor core as they are assembled in the core. Figure 4.31 displays the Serpent model of HTTR in the horizontal cross section showing the thermal neutron fluxes in the topmost fuel block layer as a function of the intensity of the blue color (white = high, blue = low). The red circles identify the fuel compacts.

The mean-free-path length of thermal or epithermal neutrons in graphite is about 2.4 cm. It is quite small compared to the dimension of the reflector block with 58 cm in height and 36 cm in across flat. The neutron flux is already very low after passing through 1 or 2 reflector blocks. It is not necessary to include the whole structure of the RPV in the Serpent model. In vertical direction, the topmost layer is the reflector block on the top of the fuel block. The lowest layer is the bottom reflector block. Namely, the Serpent model covers the zone from the 2nd layer to the 9th layer. In the radial direction, it reaches the outer boundary of the permanent reflector block, by means of 212.5 cm in radius. This zone is already enough to simulate the reactor physics and neutron transportation.

In the Serpent input, the geometry is constructed with lattices and surfaces. The materials that consist of nuclides associated with a cross section library are defined in the lattices. The temperature is required to determine the cross section of each nuclide. In the serpent model, the temperature distribution of the reactor core is taken from the reference [93]. The helium temperature is set at 900 $°C$. These temperatures are fixed during the burnup process. It is an important parameter to calculate the Doppler-broadening of resonance peaks and to determine the thermal scattering libraries for moderator nuclides.

The initial ^{235}U enrichment and natural boron concentration of poison sticks are taken from the published data of JAEA [94]. According to the operational histogram of HTTR, the accumulated operation time of the reactor is about 14639 h, and the accumulated thermal heat is about 11202.83 MWD. Therefore, the effective full power day (EFPD) of the reactor until the LOFC experiment is about 373.43 days. During the calculation process, the positions of the control rods are fixed as well. They are all inserted through to the bottom of the first fuel layer, which is different from the changes of control rod insertion depth with burnup [95]. The integral reaction rate estimates are more or less arbitrarily normalized in Monte Carlo simulation. In HTTR simulation, the thermal power density, which is averaged by the total initial mass of fissile isotopes, is used to normalize the neutron source rate. The irradiation history is condensed to 373 EFPD, and it is divided into 10 time intervals.

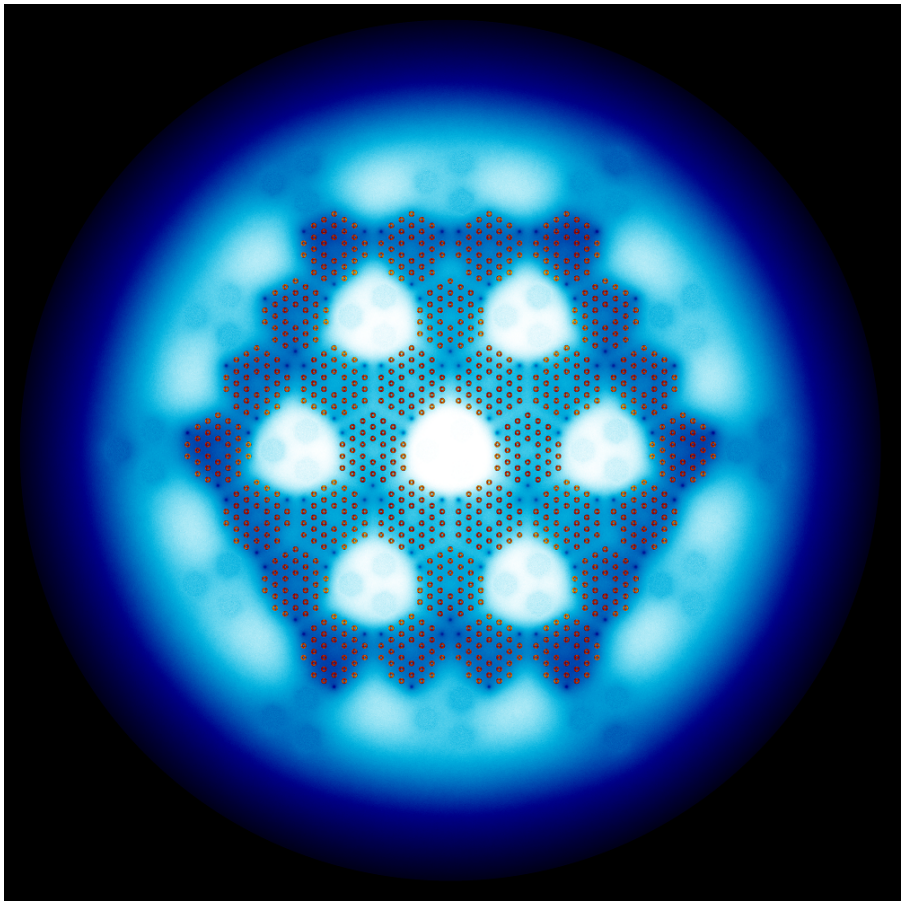

Figure 4.31: The horizontal view of HTTR Serpent model [4]

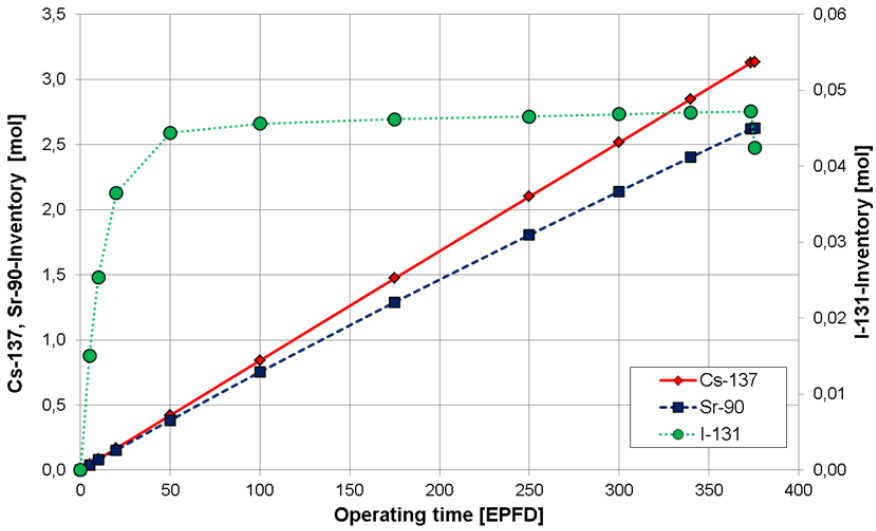

Figure 4.32: The nuclide inventory evolution of ^{137}Cs, ^{90}Sr and ^{131}I during the operation [28]

The short-lived fission products can be accumulated and decay quickly. Their nuclide densities are sensitive to the reactor power. The long-lived fission products will slowly increase during the burning process of the reactor, and it takes a long time for them to achieve equilibrium. All production rates of these nuclides are dependent on the irradiation power. Considering the productive rate of the nuclides' dependence on the irradiation power, 5 extra days with a thermal power of 9 MW are added after 373 days irradiation with 30 MW for the burnup calculation of Run 1 experiment. Figure 4.32 displays the nuclide inventory evolution of ^{137}Cs, ^{90}Sr, and ^{131}I during the operation. The half life of ^{137}Cs, ^{90}Sr, and ^{131}I are 30.17 years, 28.79 years, and 8.0197 days respectively. It can be seen that the amount of the long-lived products ^{137}Cs, and ^{90}Sr increase linearly with the operation time in the irradiation period with 30 MW, and the accumulation rate decreases in the irradiation period with 9 MW. The amount of the short-lived product ^{131}I increases quickly and reaches equilibrium after about 300 days. It also decays very quickly, and its amount decreases significantly in the irradiation process with 9 MW. The cross section of the homogeneous meshes of MGT-3D is decided by the nuclide densities. The initial nuclide density of ^{135}Xe is an important parameter to calculate the re-criticality of the reactor. Its half life is 9.2 hours. Thus, it is important to extend the burnup process with 9 MW for several days in the simulation models of Run 1 and Run 3 experiments.

The decay heat calculation of MGT-3D is based on the DIN 25485. It counts the fission product contribution of the isotopes ^{235}U, ^{238}U, ^{239}Pu, ^{241}Pu, the contribution of the actinides ^{239}U, ^{239}Np, ^{233}Th, ^{233}Pa. In order to distinguish these contributions during the burnup process, the detectors, which are defined on the blocks, are set to detect the fission numbers of different isotopes.

4.3.3 MGT-3D Model of the HTTR

The reactor protection system and engineered safety system can be simplified by taking the inherent safety of HTGRs into account. The accurate simulation of a LOFC event without scram is very important to such a design approach in a HTGR. The behavior of the reactor in a LOFC accident is determined by both the reactor's neutronics and the fluid mechanics design characteristics. From the neutronics' point of view, the cross section is dependent on the nuclide inventory, the fuel and moderator temperatures can broaden the neutron transport and absorption cross section, and the nuclide density of ^{135}Xe, which has a large neutron absorption cross section, decays very fast during the process. All of these parameters affect the reactivity performance of the reactor. The reactivity is used to predict the converging level of reactor fission power, which is an important factor in determining the fuel and moderator temperature. From fluid mechanics' point of view, part of the heat is removed from the core to the outside by conduction, thermal radiation, and natural convection, and part of the heat is stored in the graphite of the reactor core due to its high heat capacity. In the reactor core, heat is mainly transferred by conduction and thermal radiation, while on the surface of the RPV, it is mainly transferred by natural convection and thermal radiation. Therefore, the thermal conductivity of graphite is crucially important in predicting the fuel and moderator temperature, and the cooling effect of RCCS is important in decreasing the RPV temperature. As mentioned above, the temperature is the required parameter to obtain the right nuclear cross section. Consequently, the simulation of LOFC accident without scram needs coupled neutronics and fluid mechanics. MGT-3D is a coupled reactor kinetics and fluid mechanics code.

Figure 4.33 shows the structure of HTTR as horizontal cross section including fuel blocks, control rod guide blocks, irradiation blocks, replaceable blocks, and permanent blocks. It shows that the structure does not have a cylindrical symmetry. The fuel blocks of HTTR are distributed in four hexagonal annular rings. The fuel blocks of the second fuel ring are separated by control rod guide blocks. Thus, the second ring can not be replaced with the circular annular ring in MGT-3D. It is essential to build a 3D model for the HTTR simulation. If the asymmetry of the position of two control rods in each control rod block is neglected, the core can be considered as rotational symmetry of order 3. It is not necessary to establish a model in 360°. After using the reflection boundary condition in the azimuthal direction, only the core in 60° is considered in the MGT-3D model. This symmetry structure was also used by the 3D fluid mechanics simulation of HTTR with the code "STAR-CD" [96]. The calculation zone of the R/Φ plane is displayed in Figure 4.33 with the meshes in cylindrical coordinate system. In this MGT-3D model, both azimuthal boundaries are set as reflective boundaries.

The MGT-3D simulation model of HTTR is a three dimensional model based on R/Z/Φ coordinates. According to the arrangement of the blocks' type, the azimuthal zone within 60° is divided into 10 meshes so that the 5th and 6th meshes can be merged together (see Fig. 4.33). The key in defining the meshes in the R/Φ plane is that blocks of the same type are kept as much in the same simulation mesh as possible by adjusting the azimuthal and radial coordinates. In the simulation model, both the primary circuit and the RCCS are included. Figures 4.34, 4.35 and 4.36 present the details of 3rd, 5th, and 10th angle meshes. Each angle mesh is divided into $30(R) \times 41(Z)$ sub-meshes the in R/Z plane. The zone in the marked red frame is the neutronics calculation zone, which is limited by the simulation model of Serpent.

The input mainly includes two parts: neutronics data and fluid mechanics data. They

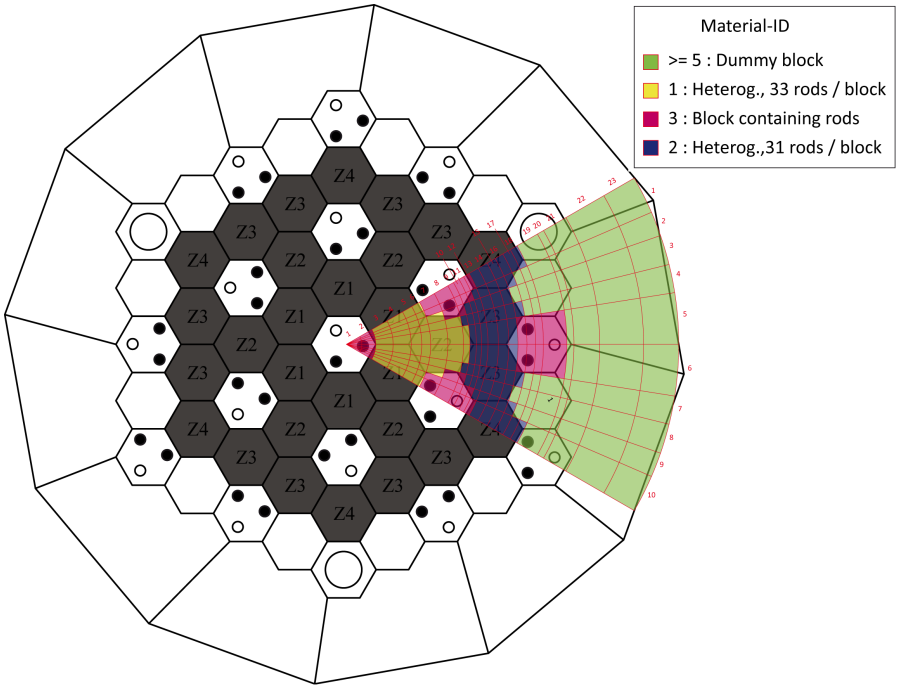

Figure 4.33: Simulation model in the horizontal cross section [28]

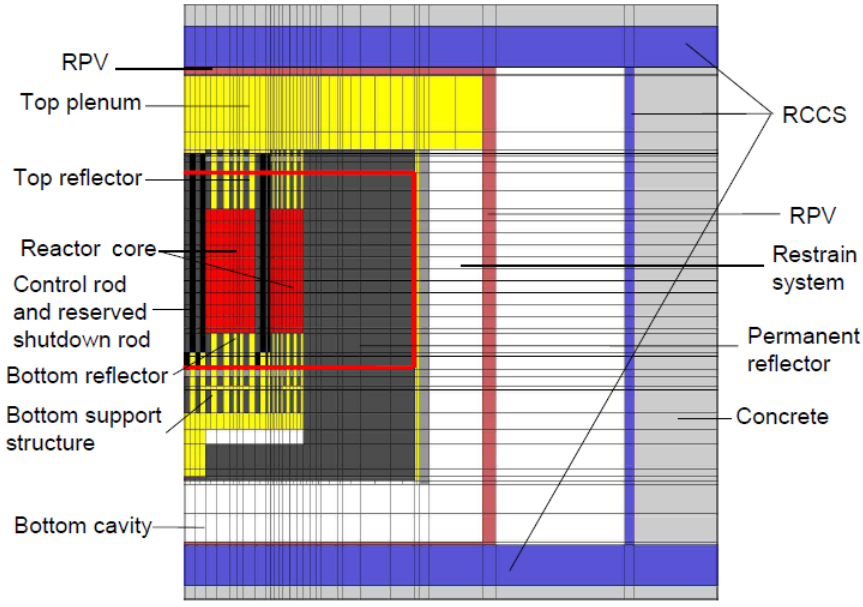

Figure 4.34: Simulation model in the 3rd angle meshes

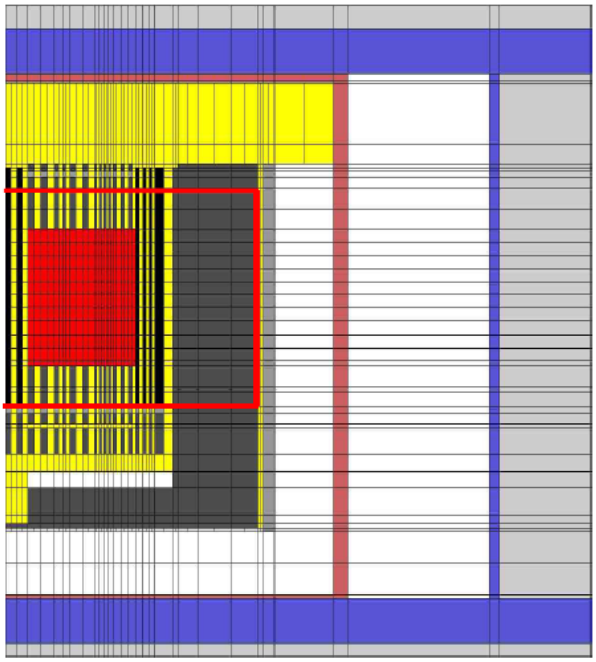

Figure 4.35: Simulation model in the 5th angle meshes

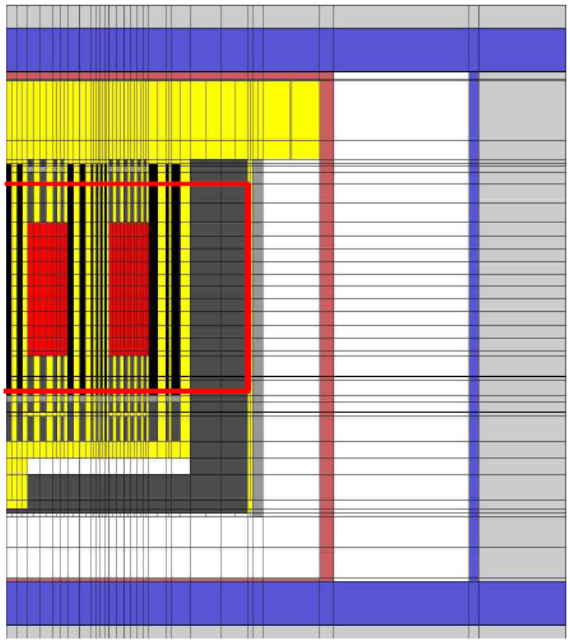

Figure 4.36: Simulation model in the 10th angle meshes

are provided in separated files. For the neutronics, the group structure of neutron energy, data library, nuclide inventory, and life histogram are given to calculate the neutron flux, fission power, decay power, gamma transport. Normally, the nuclear cross section data is provided by the interface with VSOP in the pebble bed reactor simulation [2]. However, VSOP does not have the function to calculate the burnup of HTTR. Serpent is used to calculate the burnup and nuclide inventory evolution. The nuclide inventory and life histogram are prepared by the interface between Serpent and MGT-3D. The nuclide inventories of the moderator and the control rods are taken from the documents [97, 98]. In the project, the recommended decay heat is calculated by the following equation [99]:

$$\frac{P}{P_0}(\infty, t_s) = A t_s^{-\alpha} \tag{4.6}$$

where $P_0 = 200\ MeV/fission$, and t_s is the elapsed time since the start of the test. The constants A and α are time dependent and shown in Table 4.3.

The data library of MGT-3D is based on ENDF/B-VII evaluated data files. It is able to handle up to 43 neutron energy groups [17]. In the HTTR simulation, the cross sections of 43 fine groups are condensed to 6 groups, which include 3 thermal groups and 3 fast groups. The neutron energy boundaries of these 6 groups are shown in the following table:

Regarding the fluid mechanics, both the homogeneous calculation of the reactor and the heterogeneous calculation of the fuel elements and coated particles are involved. The fission heat and decay heat deposit mostly in the fuel rod and partly in the moderator. In the heterogeneous model of the fuel rod, it is assumed that all of the heat deposits

	A	α
$0.1 \leq t \leq 1$	0.0605	0.03
$1 < t < 10$	0.0618	0.12
$10 \leq t < 10^2$	0.0689	0.17
$10^2 \leq t < 10^3$	0.082	0.21
$10^3 \leq t \leq 10^4$	0.1301	0.277
$10^4 < t \leq 10^9$	0.1301	0.283

Table 4.3: The constants to calculate the decay heat of HTTR

Group number	Neutron energy range (ev)	Spectrum
1	$2.5 \times 10^{-3} - 1.2 \times 10^{-1}$	thermal
2	$1.2 \times 10^{-1} - 4.5 \times 10^{-1}$	thermal
3	$4.5 \times 10^{-1} - 3.06$	thermal
4	$3.06 - 1.3 \times 10^{2}$	fast
5	$1.3 \times 10^{2} - 6.39 \times 10^{5}$	fast
6	$6.39 \times 10^{5} - 1.0 \times 10^{7}$	fast

Table 4.4: The neutron energy group structure of HTTR simulation

in the annular cylindrical fuel compacts. There is stagnant helium in the center of the fuel rod, and the gas pressure is taken as 4 MPa. The heat conductivity and specific heat of helium are related to 4 MPa. The neutron irradiation will cause damage to the structure and properties of graphite. The graphite will pass through volume shrinkage after a large dose of neutron irradiation [100]. Therefore, an annular gap filled with helium is assumed between the fuel compacts and the graphite sleeve. The emissivity of the graphite is set as 0.8. The heat conductivity and specific heat of the graphite sleeve and fuel compacts are taken from the distributed data [101]. Heat is transferred by conduction and thermal radiation from the fuel compacts to the graphite sleeve. After this, the heat is transferred to the coolant and graphite block by convection and thermal radiation.

The homogeneous model of fluid mechanics calculation is comprised of the reactor core, top plenum, bottom support structure, side restrain system RPV, and VCS, as former description. There are five zones in the reactor core: the 33 fuel pins zone, 31 fuel pins zone, control rod guide block zone, reflector block zone with coolant holes (top and bottom replaceable reflector block), and reflector block zone without coolant holes (permanent reflector block). The 33 fuel pins zone and 31 fuel pins zone are homogenized in the 1D flow tubes meshes. Their void fractions are 0.121 and 0.114 respectively, which do not include the sealed helium in the center of the fuel pins. The contribution of the stagnant helium and fuel handling hole should be considered when calculating the specific heat. Therefore, the homogeneous specific heat of these meshes is the product of graphite's specific heat and the solid fraction, which is 0.85 and 0.86 for 33 fuel pins zone and 31 fuel pins zone, respectively. The thermal radiation is considered as the equivalent thermal conductivity. The top replaceable reflector blocks are defined in the 1D flow tubes meshes. They are aligned with their related fuel blocks. The void fractions are 0.121 and 0.114 as well. For the bottom replaceable reflector blocks, the homogeneous thermal properties are adjusted due to their design feature as well. The graphite blocks of the 9th layer of the control rod guide column have only a small gas flow tunnel for the vertical bypass flow of control rod guide block. This bypass flow is used to cool down the

control rods, and it is about 5%-8% of the total flow [93]. In order to simulate this bypass flow without losing the precision for the heat conduction calculation, the void fraction is set as 0.012, and the specific heat and heat conductivity correction factor are set as 0.2. The cross bypass flow is considered as zero in the simulation model. The permanent reflectors, which are constructed with 12 integral graphite blocks, are considered as solid material since the cross bypass flow from the permanent reflectors to the core blocks or the hot plenum is neglected. The boundary of the permanent reflector is a regular dodecagon. It is represented by a circle with a radius of 212.5 cm. The hot plenum blocks, which use key-connection design, are defined as 1D flow tubes as well. All of the vertical flows meet together in the hot cavity, which is supported by the support post [87]. A cavity with gas flow in all directions and with height of 40 cm is employed to simulate it. It is connected with the mesh of gas outlet directly.

The permanent reflector block, hot plenum, lower plenum, and bottom support graphite block are fabricated from PGX graphite. The core components, which include the fuel compacts, fuel block, control rod guide block, and replaceable reflector block, are made of IG-110 graphite. The thermal conductivity is dependent on the fast neutron flux irradiation and temperature [102, 103]. The thermal conductivity changes significantly after long-term neutron irradiation. However, there are few differences between the irradiation with 330 EFPD and the irradiation with 660 EFPD. Therefore, the thermal conductivity of IG-110 under irradiation of 660 EFPD is used to calculate the homogenized thermal conductivity of fuel blocks, control rod guide blocks, and replaceable reflector blocks.

The top and bottom hemispherical structures are equivalent to cylindrical cavities. The height of the cylinder is chosen to make sure that they have the same volume. For the top cavity, it is filled with the gas flow coming from the gas risers. The inlet gas is mixed in the top cavity and distributed into the 1D flow tubes of the fuel blocks and control rod guide blocks. For the bottom cavity, it is separated from the reactor core by the core support plate. The core support grid is in the bottom hemispherical cavity. There is no gas flow entering this cavity. Therefore, these meshes are defined as "solid" with corrected heat conductivity and specific heat.

The core restraint system is also designed for the path of rising gas flow. There are two paths for the rising gas flow: one path is the empty space between the permanent reflector and the neutron shielding blocks, which are composed of sintered B_4C/C and SUS316 casing, and the other path is the empty space around the restraint bands. In order to make the model easy to converge, the simulation model restricts the gas flow in the first path. The restrain system is considered as no gas flow zone. The conductivity rule of stainless steel with corrective multiplication factor is used to calculate the thermal conductivity of the restrain system. The corrective multiplication factor is related to the solid fraction in this zone. The emissivities of the neutron shielding blocks and the RPV are equal to 0.8, which are used to calculate the radial thermal radiation across the empty space of the restrain system.

The gas inlet mesh, which is connected with the source, is set in the rising flow path. The helium inlet temperature is 180 $^{\circ}C$, and the forced flow rate is 12.4 kg/s. The helium rises from the restrain system to the top plenum. Then it streams down through the 1D coolant holes in the fuel blocks and control rod guide blocks. The gas flows from different paths mix in the bottom hot plenum. Finally, the hot helium exits the outlet mesh, which is set in the hot plenum. This mesh is connected to an opened heat sink with reference pressure 2.8 MPa and 4.0 MPa for initial thermal power 9 MW and 30 MW respectively.

Considering the limitation of MGT-3D on the simulation of large cavities, the RCCS is simulated in the same way as GT-MHR's MGT-3D model. The natural convection in the cavity is simulated by an effective thermal conductivity. The thermal radiation from the RPV to the containment wall is also considered. The emissivity of the material is set as 0.8. The temperature of the containment wall is fixed at $30°C$ during the transient. Another simplified method is also used to simulate the Run 1 experiment. In the Run 1 experiment, the RPV temperature is measured. This transient temperature is set as the boundary temperature of RPV.

MGT-3D provides the option of the external one-dimensional flow network, which consists of "components" and "nodes" for the simulation of heat exchanger, steam generators, over-pressure valves, gas blowers, and so on. The simple heat transfer, pressure loss, or gas flow are calculated in these components. They are coupled with the 3D meshes of the reactor model. Considering that the gas inlet and outlet temperatures, and pressure of primary circuit are given values, it is not necessary to build the complete model for the secondary cooling system. An infinite heat sink is used. The gas inlet and outlet meshes should be defined in the same angle mesh in MGT-3D.

In the simulation of the Run 1 experiment, the calculation achieves steady state on fluid mechanics and neutronics after several iterations at first. The power to normalize the neutron flux is 9 MW. In the beginning of the accident, the flow rate of forced coolant decreases from 12.4 kg/s to 0 in 10 s. Then, the reactor runs at free transient. The pressure of the primary circuit is kept at 2.8 MPa during the transient. The boundary temperature of the RPV is set with the value taken from Reference [105].

In the simulation of the Run 2 experiment, the calculation achieves steady state in the beginning as well. The power to normalize the neutron flux is 30 MW. The gas inlet and outlet temperatures are chosen as $395°C$ / $850°C$ as shown in Table 4.2. For the LOFC accident, the flow rate is assumed to decrease from 12.4 kg/s to 0 in 10 s as well. The following calculation is done with free transient. The pressure and the RPV temperature are assumed to remain unchanged during the transient.

4.3.4 Interface between MGT-3D and Serpent

MGT-3D allows simulation of the reactor in both steady state and transient case with coupled neutronics and fluid mechanics solver, but it can not perform the burnup calculation. In the pebble bed reactor simulation, the reactor core status of MGT-3D is determined with the help of VSOP. In case of the prismatic block type HTTR, the nuclide densities and life histogram are provided by Serpent. Therefore, it needs an interface approach to transfer the data from the output of Serpent to MGT-3D. Figure 4.37 shows the details of the interface program.

In the Serpent simulation, the initial nuclear inventory, time steps, and reactor power are given as input data. The detectors that collect the data for decay heat calculation are defined on the fuel block as well. After the required 330 EFPD, the depletion file and the detector file are obtained. The depletion file includes the nuclide densities of fuel pellets of each individual fuel block, burnable poison sticks, and control rod guide blocks. All of the data is based on the geometry of block/pin-wise. The data arrangement of MGT-3D is based on the Cartesian mesh grids (R/Z/Φ). The superimposed MGT-3D grid on the prismatic blocks is presented in Figure 4.33. Considering that the blocks are the same in the same level of axial direction, the transformation matrix is determined in the 2D plane. The transformation matrix is used to calculate the contribution of each hexagonal

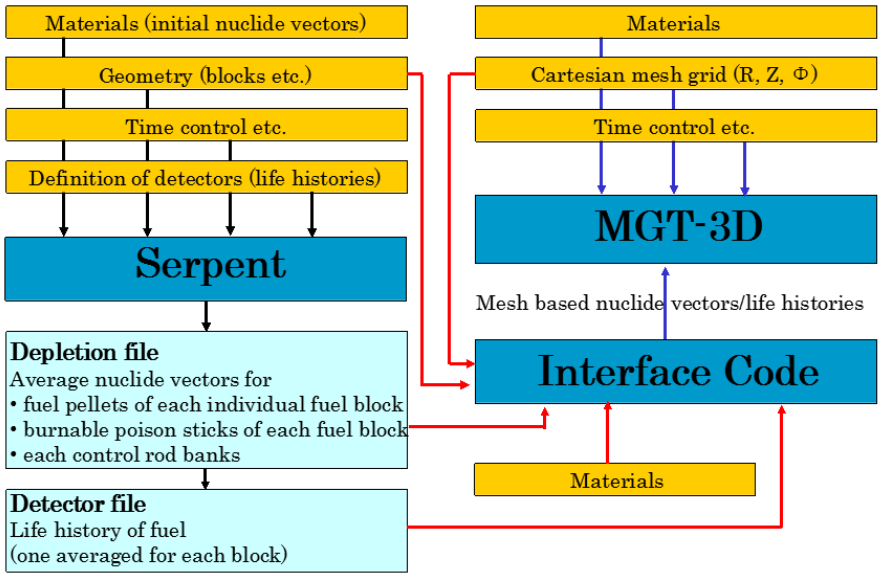

Figure 4.37: Interface process between Serpent and MGT-3D [28]

block on the MGT-3D mesh. The matrix is calculated by the following approach: first, the prismatic block is equally divided into a certain number of triangles; second, the MGT-3D mesh in which the center of the triangle is located is determined by the code, and the number of the triangles is counted; and finally, the ratio of the triangles that are located in a certain MGT-3D mesh to the total triangles of the Serpent block is the element of the matrix. The precision of the transformation matrix can be improved by increasing the number of triangles.

The transformation matrix is composed of the weighting factor of each hexagonal block's contribution on MGT-3D mesh. The product of the transformation matrix and the physics value vector of hexagonal block is the physics value vector of each MGT-3D mesh. For example, the nuclide density of each block multiplied by the transformation matrix is the nuclide density of each MGT-3D mesh. The life history of each mesh is calculated in the same way. The mesh based nuclide inventory and life history are written in a file with fixed formate, which is used by MGT-3D to calculate the nuclear cross section and decay heat.

4.3.5 Post-Calculation of Run 1 Experiment

Steady State of Run 1 Experiment

In the Run 1 experiment simulation, the total power of the reactor is 9 MW. To simplify the calculation, the top and side RPV temperature are set as 170 $°C$, and the bottom RPV temperature is set as 150 $°C$ [105]. After the iteration between fluid mechanics and neutronics, the calculation converges in solid temperature, gas temperature, and effective multiplication factor. The steady state of the reactor is obtained. The effective neutron multiplication factor of the normal operation is 0.99746. The maximum

fuel temperature is $471°C$. In the normal operation, 99% of the heat produced in the fuel compacts is transferred into the coolant by forced convection.

The spectrum calculation subroutine of MGT-3D is based on the MUPO program [107]. It uses an algorithm that directly solves the 0-dimensional diffusion equation with arbitrary leakages for 43-energy groups and replaces an explicit resonance calculation with a look-up table [2]. The heterogeneity effects of fuel element and coated particle are accounted for by the input of energy dependent disadvantage factors. The disadvantage factors are benchmarked by MCNP for the pebble bed reactor. For the HTTR simulation, the same disadvantage factors are used. The normalized neutron spectrum of HTTR with 9 MW is presented in Figure 4.38. With the result of the neutron spectrum, the spectrum weighted average absorption cross section of ^{135}Xe is 2.15×10^6 barn.

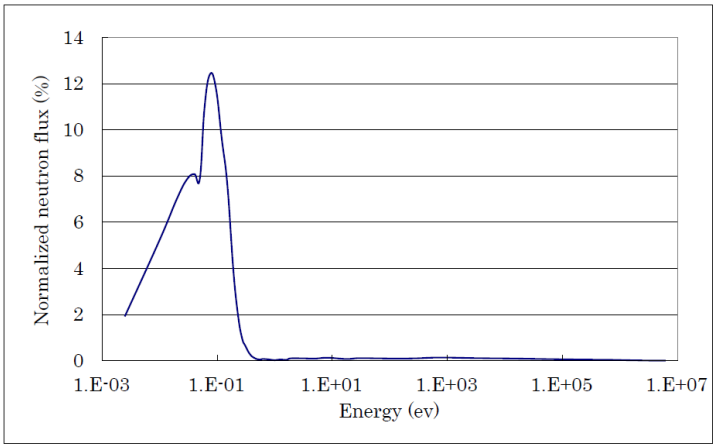

Figure 4.38: Normalized neutron spectrum of the HTTR, 9 MW

The neutron flux densities of the first energy group and the last energy group in the R/Z plane are presented in Figures 4.41 and 4.39. According to Table 4.4, the neutrons of the first energy group are thermal neutrons, and the ones of the last group are fast neutrons. The top one and the bottom one in the figures are the neutron flux density in the third angular mesh and in the fifth angular mesh respectively. Corresponding to Figure 4.34, the fuel zone is discrete in the third angular mesh and continuous in the fifth angular mesh. Therefore, these two typical fuel distribution zones are chosen to plot.

Figures 4.41 and 4.42 show that the fast neutron flux reaches the peak value in the fuel zone. The reason is that the fission process occurs in the fuel zone and produces high energy neutrons. The mean free path of neutron transportation is several centimeters. The generated fast neutrons can arrive in the surrounding moderator block, and they are moderated to thermal neutrons in the graphite. Thus, the fast neutron flux density decreases in the moderator zone.

It can be seen in Figures 4.39 and 4.40 that the thermal neutron flux is lower in the moderator block than in the fuel block, which is opposite to the distribution of fast neutron flux. As mentioned, the fast neutrons are turned into thermal neutrons by the scattering in the nucleus. The thermal neutrons are mainly absorbed by uranium

or plutonium to sustain the nuclear chain reaction. Therefore, the thermal neutrons are much less in the fuel zone than in the moderator zone. On the top fuel blocks of the third azimuthal mesh, there are two zones where thermal neutron flux decreases significantly. They are the control rod guide blocks and the control rods are inserted into the top fuel block. Therefore, a large amount of thermal neutrons are absorbed there.

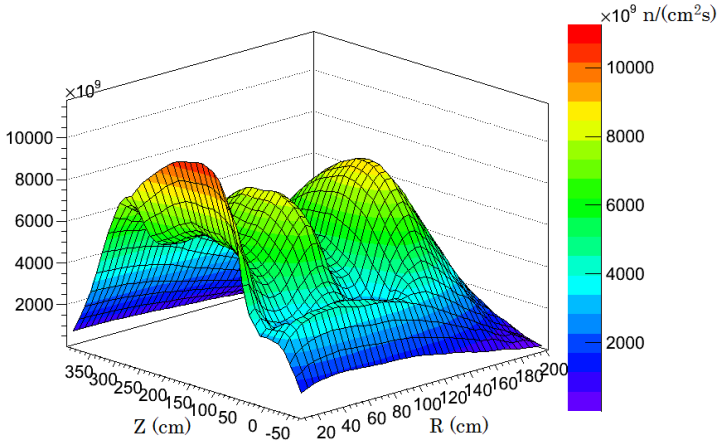

Figure 4.39: Flux density of first group neutron, 3rd angle mesh, 9 MW, steady state

Nuclear power is generated in the fuel rod. Part of the energy deposits in the fuel rod and part of the energy deposits in the moderator by γ transport [106]. The local nuclear power density in the azimuthal meshes is displayed in Figures 4.43 and 4.44. It shows that the local nuclear heat is discrete in the third azimuthal mesh and continuous in the fifth azimuthal mesh due to the location of fuel blocks. The ^{235}U enrichment decreases from the top to the bottom fuel block [94]. Also, the control rods are located in the top fuel blocks. Therefore, the zone with high power density is close to the center of the reactor. The maximum value is about 1.3 MW/m^3.

Figure 4.45 shows the local nuclear power density in the transverse cross section with $Z = 159.5\ cm$, which is the bottom part of the third fuel layers. It is plotted with X/Y coordinates. The reactor center is located at the point ($x = 0\ cm, y = 0\ cm$). The power density is zero in the center of the reactor because the control rod guide block is placed there. There are six other control rod guide blocks in the middle annular ring where the local nuclear power densities are also zero (see Fig. 4.23).

The solid temperature of the homogenized mesh is equivalent to the surface temperature of the fuel elements in MGT-3D. Both the solid temperature of the homogenized mesh and the temperature of fuel kernels are displayed in the output file. The temperature difference between the homogenized solid temperature and the fuel kernel temperature is determined by the power density in the steady state case (see Eq. 3.28, 3.20). From the fluid mechanics' point of view, the homogenized solid temperature is the important parameter in calculating the heat transfer between the solid and the gas flow. The solid temperatures of the third and fifth azimuthal meshes are presented in Figures 4.46 and 4.47. It shows that the solid temperature increases along the coolant hole of

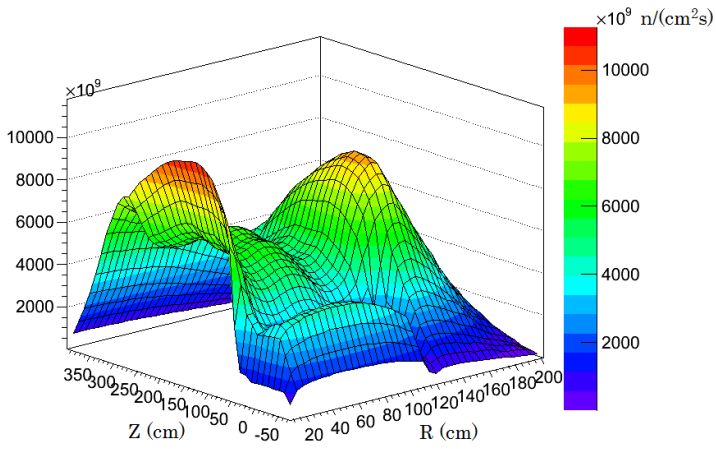

Figure 4.40: Flux density of first group neutron, 5th angle mesh, 9 MW, steady state

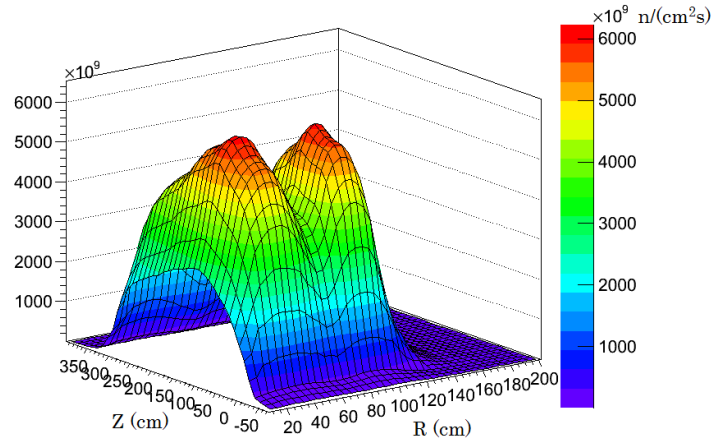

Figure 4.41: Flux density of sixth group neutron, 3rd angle mesh, 9 MW, steady state

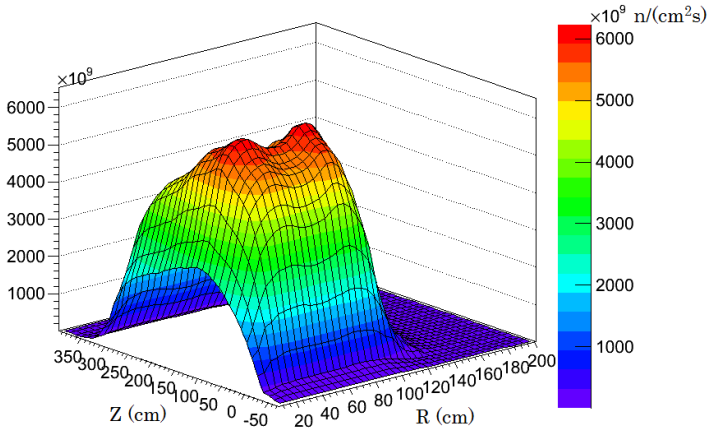

Figure 4.42: Flux density of sixth group neutron, 5th angle mesh, 9 MW, steady state

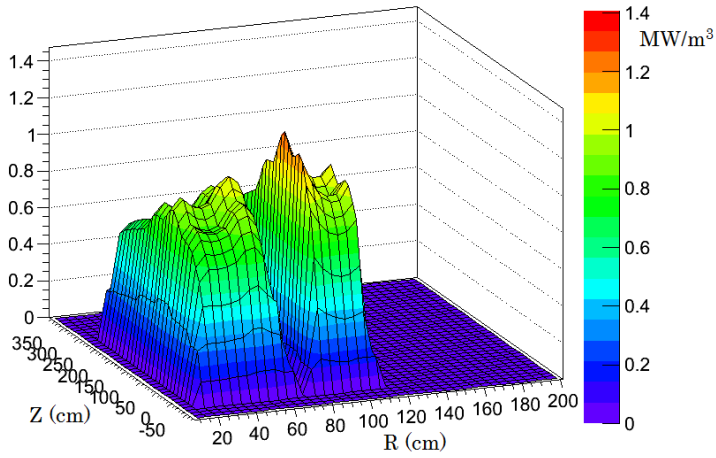

Figure 4.43: Local nuclear power density in the 3rd azimuthal mesh, 9 MW, steady state

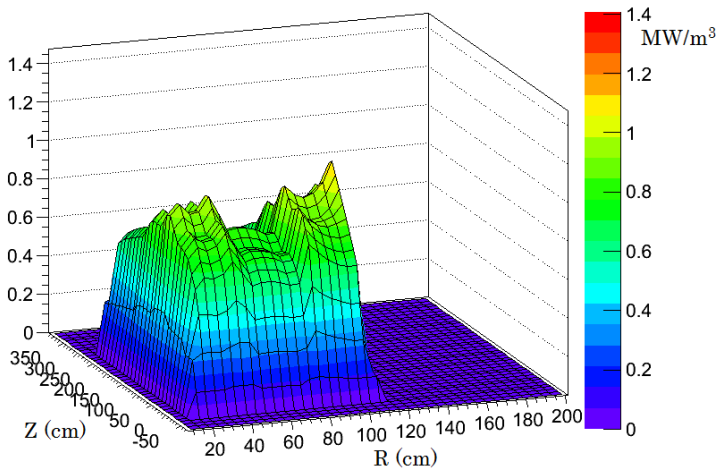

Figure 4.44: Local nuclear power density in the 5th azimuthal mesh, 9 MW, steady state

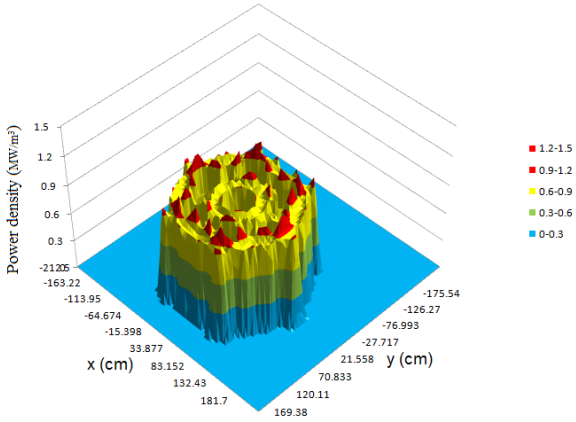

Figure 4.45: Local nuclear power density in the transverse cross section, 9 MW, steady state

fuel block due to the heated process of the coolant along the flow path. The maximum solid temperature is in the bottom of the last fuel layers. It is about 425 $°C$.

The solid temperature in the transverse cross section with $Z = 159.5\ cm$ is presented in Figure 4.48. The temperature reaches the peak in the fuel block of first ring. The central temperatures of the central control rod guide block and other control guide blocks are lower than their surrounding fuel blocks, because they are cooled by the bypass flow. Although the flow fraction is very small, it is already enough to cool down the control rod. If there were no bypass flows in these blocks, their temperatures would be comparable with those of the surrounding fuel block, which may destroy the casing of the control rods in the high temperature running phase.

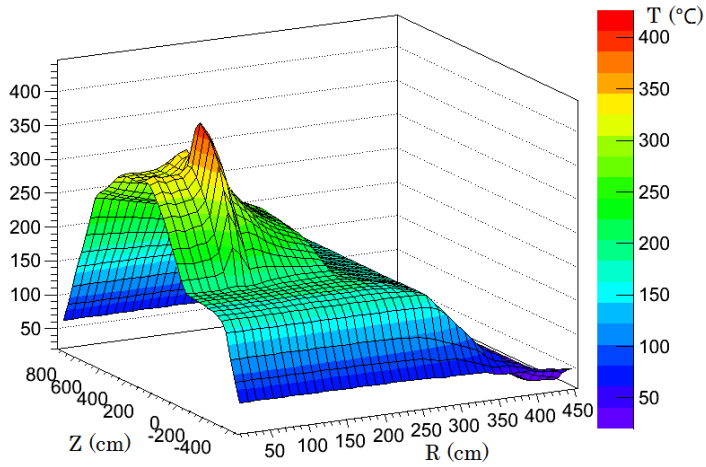

Figure 4.46: Solid temperature in the 3rd azimuthal mesh, 9 MW, steady state

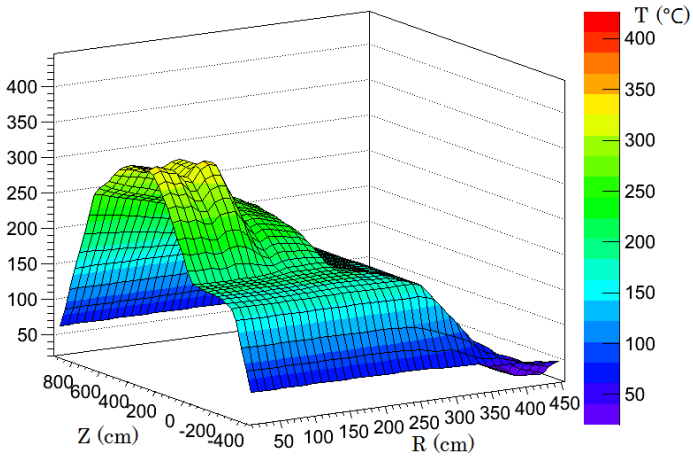

Figure 4.47: Solid temperature in the 5th azimuthal mesh, 9 MW, steady state

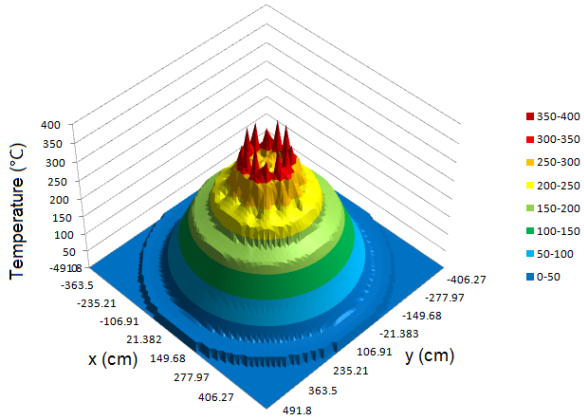

Figure 4.48: Solid temperature in the transverse cross section, 9 MW, steady state

LOFC Transient of Run 1 Experiment

The HTTR was operated at 30 MW from the beginning of January 2010 to the end of March 2010 [108]. The total operation time was about 2010 hours. Then the reactor was shut down for about 9 months. The Run 1 experiment was started on December 13th, 2010. It was operated at 9 MW at steady state for about 8 days, and the LOFC experiment was performed on December 21st, 2010.

As mentioned, the operation history is condensed to 373 EFPD in the burnup calculation of Serpent and is divided into 10 continuous time intervals. In the decay heat calculation of MGT-3D, it accumulates the contribution of the decay heat from the detailed operation process. Due to lack of details of the operation history in the Serpent model, special treatment is needed for the operation history part of the MGT-3D input file. In order to describe the operation process of the reactor, the MGT-3D input file is as follows: at first, the HTTR runs at full power for 373 days; then, it is shut down for 300 days; at last, it starts to run at 9 MW for 8 days.

In the experiment, the reactor power is monitored with the wide range monitoring system (WRM), that is located in the irradiation blocks, and the power range monitoring system (PRM), that is located in the concrete shielding. The temperatures of the permanent reflector block, RPV, VCS, concrete are measured during the transient process.

The forced gas flow of the HTTR is tripped in 10 seconds. Afterwards, the reactor runs in a free transient. The data of the reactor was measured for 12 hours after the LOFC test started. Therefore, the free transient process is sustained for 15 hours in the simulation. The maximum fuel temperature evolution is shown in Figure 4.49. It can be seen that the maximum fuel temperature decreases in the beginning of the accident due to the reactor power decreasing exponentially. Afterwards, it increases slowly because the heat is removed from the reactor mainly by thermal conduction and thermal radiation, which are less efficient compared to forced convection. Towards the end of the calculation, the maximum fuel temperature is still increasing because the reactor has not reached equilibrium in fluid mechanics. If the free transient process is prolonged, it will be observed that the reactor achieves equilibrium in fluid mechanics after about 80 hours.

The average fuel temperature and moderator temperature have a difference of about 44 $°C$ in the beginning of the accident due to the heat transfer mechanism from the fuel rod to the coolant, which has been discussed in the section of heterogeneous temperature calculation of the unit cell of the HTTR fuel. The reactor is shut down automatically after several minutes of the LOFC accident. Then the local nuclear power density is negligible. The thermal relaxation time of the unit cell is about one minute. Therefore, the average fuel temperature and average moderator temperature are almost equal at 10 minutes after the LOFC accident.

In the LOFC accident, the reactor power decreases due to the broadened resonance absorption cross section of ^{238}U. The reactor is shut down automatically. The amount of ^{135}Xe will stop accumulating. ^{135}Xe is an unstable isotope with a half-life of about 9.2 hours. It will decay in hours, and the reactivity of the reactor will increase. The reactor can achieve re-criticality after a time period. Therefore, the re-criticality process of the reactor is a comprehensive effect of neutronics and fluid mechanics. The re-criticality time and power level of the reactor are important parameters in benchmarking the simulation model.

Figure 4.50 shows the comparison of fission power between the MGT-3D simulation and the experimental values measured by WRM. The reactor power is normalized by the total thermal power 9 MW. The simulation result with MGT-3D fits very well with the measured data. The reactor power will decrease to 1% of the initial power in 500 s. The HTTR achieves re-criticality at 8.02 hours after the accident, and the re-criticality power is 3.2% of the initial power. The simulation result shows that the re-criticality happens at 7.9 hours after the LOFC, and the re-criticality power is 4.12% of the initial power. The full width at half maximum (FWHM) of the re-criticality power peak is about 0.215 h during the experiment. The simulated FWHM of the re-criticality power is about 0.24 h. The specific heat of the reactor core is very large due to the large amount of graphite. Thus, there is a delay of the rise or fall of the fuel and moderator temperature when the power is increasing or decreasing. The reactor power vibrates for several periods after the first re-criticality occurs. After that, the reactor power increases gradually without vibration. The final measured power level is about 2.3% of the initial power. The final simulated power level is also about 2.3% of the initial power.

The fuel temperature, moderator temperature, and ^{135}Xe concentration are the main parameters in determining the reactor reactivity. The fuel temperature has a negative feedback effect on the reactivity due to the broadened resonance absorption cross section of ^{238}U. The graphite moderator temperature has a positive feedback on the reactivity. The concentration of ^{135}Xe has a negative feedback effect on the reactivity due to its large thermal absorption cross section. The average fuel temperature and average moderator temperature are presented in Figure 4.49. Figure 4.51 displays the percent of neutrons which are absorbed by ^{135}Xe. The evolutions of these parameters fit with their reactivity feedbacks in the references that analyze the reactivity balance with point kinetics model [110, 111]. Therefore, the calculation results with deterministic coupled neutronics and fluid mechanics solution can also provide information for the method with point reactor kinetics.

The reactor power reaches the peak after around eight hours; then it oscillates several times due to the negative reactivity feedback effect (see Fig. 4.52). The power increases because of the continuous decay of ^{135}Xe and decreases because of the increase of fuel temperature, which causes the oscillation of the reactor power. Moreover, it gradually decreases to a steady state case. In the steady state case, the amount of ^{135}Xe reaches equilibrium between the decay and the production due to fission. Basically, it takes

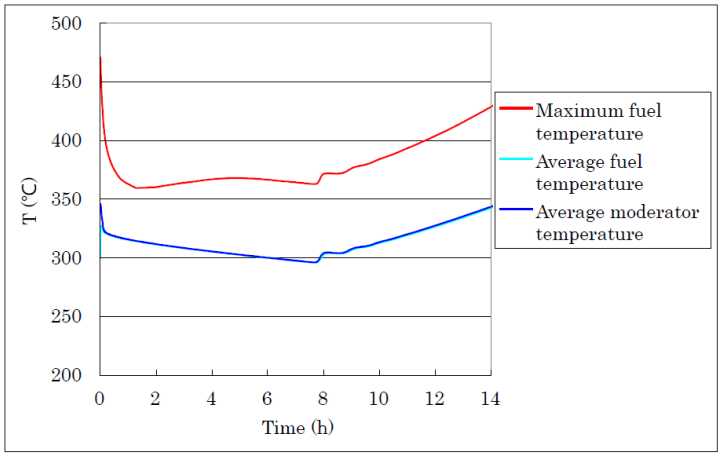

Figure 4.49: Maximum fuel temperature, average fuel temperature and average moderator temperature after the accident, 9 MW, LOFC

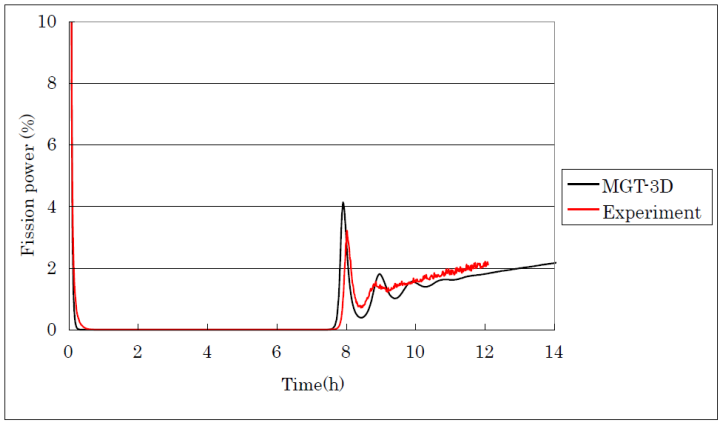

Figure 4.50: Re-criticality of the HTTR after LOFC accident, 9 MW

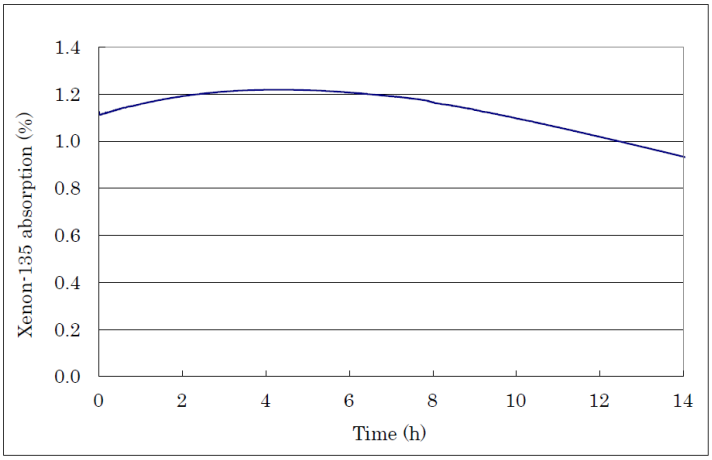

Figure 4.51: Fraction of ^{135}Xe neutron absorption, 9 MW, LOFC

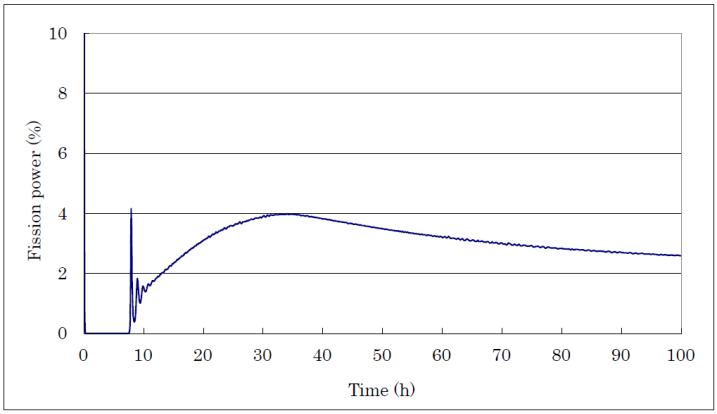

Figure 4.52: Reactor fission power for 100 hours, 9 MW, LOFC

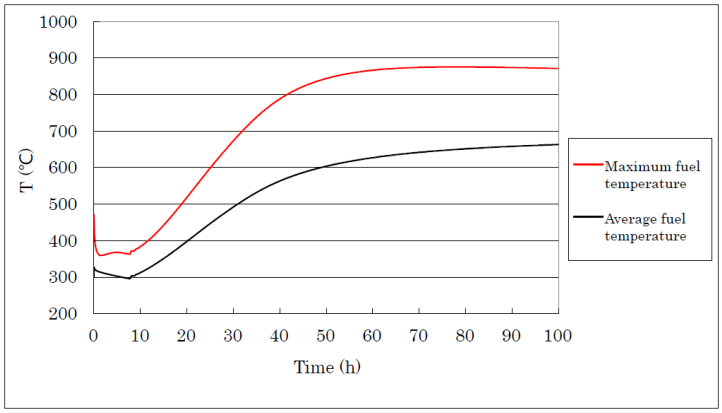

Figure 4.53: Maximum fuel temperature and average fuel temperature for 100 hours, 9 MW, LOFC

several days for the ^{135}Xe to achieve steady state. The reactor will reach equilibrium in fluid mechanics as well in 80 hours (see Fig. 4.53). The reactor power remains constant.

In summary, the post-calculation of Run 1 experiment with MGT-3D fits very well the experimental data. Although the operation history is condensed to 373 EFPD in the Serpent burnup calculation, the operation process of one year before the Run 1 experiment is considered in detail when calculating decay heat with DIN 25485 standard. The fuel temperature, moderator temperature, and ^{135}Xe neutron absorption are also presented. The trends of the evolutions of these parameters also fit with the analysis result with point reactor kinetics method in general.

Parameter Variations

The decay heat is calculated according to DIN 25485 standard in MGT-3D, which is different from the formula (see Eq. 4.6) suggested by JAEA. Decay heat is the only heat source after the reactor is shut down, so it is an important parameter in determining the re-criticality of the reactor. The study of GT-MHR shows that the solid temperature is sensitive to the decay power. In order to investigate the impact of decay power on the re-criticality time and power level, several life histories are assumed. At first, the reactor is operated at 30 MW for 373 days. Then it is shut down for 10 days, 30 days, 100 days, or 360 days. Finally, the reactor runs at 9 MW for another 2 days.

Figure 4.54 displays the elapsed time and reactor power peak level at the occurrence of the re-critical reactor power with different operation histories. It can be concluded that the elapsed time and reactor power peak level increases with the decreasing of the shutdown period. The calculated elapsed time and reactor power peak level fit with the experimental data if the shutdown period is chosen as 100 days. In order to find the reason that leads to this result, the dependence of decay power on shutdown period should be determined. The decay powers with different shutdown terms are presented in Figure 4.55. The amount of isotopes that contribute to the decay heat reduces with time. Therefore, the longer the period in which the reactor is shut down, the less decay heat will be generated during the LOFC experiment. Consequently, it takes more time for the temperature to decrease to the level of re-criticality.

If the shutdown period is set as 30 days, the decay heat calculated by MGT-3D fits with the suggested values before the re-criticality. In MGT-3D, the operational history is extended after the end of a given life histogram by a short time period. The time-dependent decay heat production is calculated by Equation 2.8. Thus, the decay heat calculated by MGT-3D is higher than the suggested values after the re-criticality.

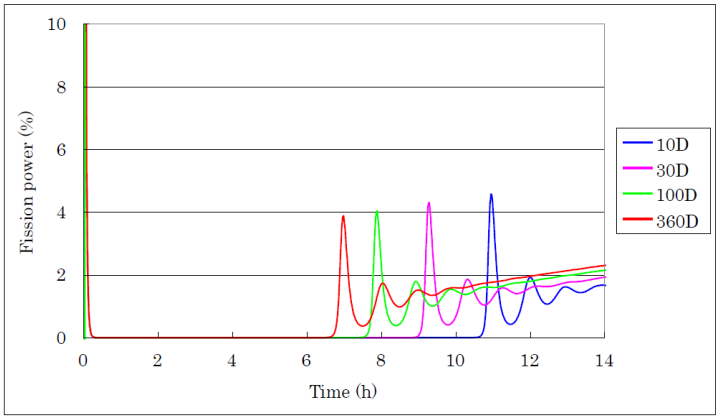

Figure 4.54: Elapsed time and power level at the occurrence of the re-criticality with different shutdown terms, 9 MW, LOFC

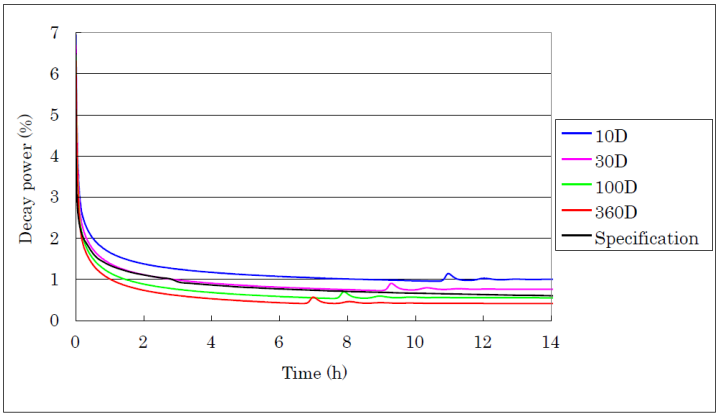

Figure 4.55: Decay heat of the HTTR with different shutdown terms, 9 MW, LOFC

After the forced gas flow is tripped, heat will be transferred out of the reactor mainly by thermal conduction and thermal radiation. Therefore, the homogenized conductivity of MGT-3D meshes is an important parameter to achieve the right elapsed time and reactor power peak level at the re-criticality. The thermal conductivity of graphite is dependent on the irradiation temperature and neutron dose. It varies significantly during the operation of the reactor, which is presented in Figure 4.56. Thus, the thermal conductivity of the graphite with different irradiation conditions will result in different

moments in time for the re-criticality of the reactor. The calculation result with the non-irradiation graphite and the graphite with 660 EFPD irradiation are presented in Figure 4.57. In order to obtain the same decay heat with the suggested decay data, both calculations use the operation history with 30 days's shutdown period. The elapsed time and reactor power peak level with unirradiated graphite are 7.5 hours and 4.16%, respectively. The values are 9.28 hours and 4.31%, respectively, when assuming 660 EFPD irradiated graphite.

The thermal conductivity of unirradiated graphite is much larger than that of graphite with long-term irradiation. The relaxation time of the reactor is smaller with the unirradiated graphite. It takes less time for the reactor to be cooled down by thermal conduction. Therefore, the re-criticality occurs earlier than it does with the irradiated graphite.

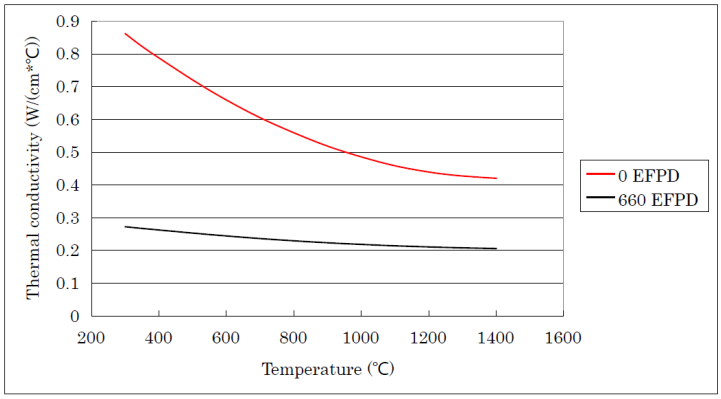

Figure 4.56: Thermal conductivity of IG-110 graphite as a function of temperature

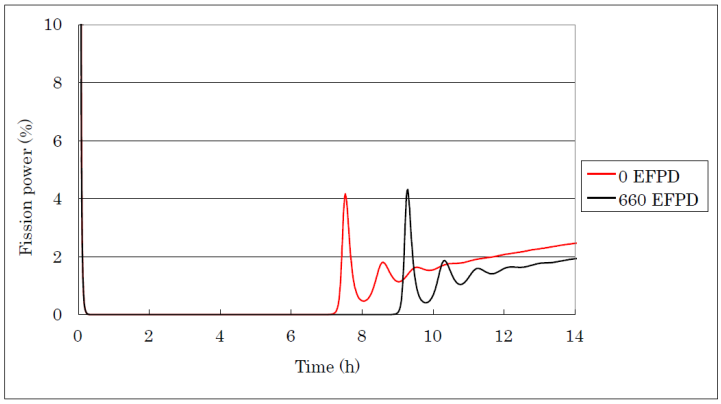

Figure 4.57: Elapsed time and power level at the occurrence of the re-criticality with different thermal conductivity, 9 MW, LOFC

Although there is no forced flow in the LOFC accident, natural convection will establish in the reactor core. The natural convection can be significant at low temperatures. If the temperature of the reactor core is about 1000 $°C$, the thermal conduction and radiation will dominate. To change the flow distribution of natural convection, an additive term, which is three times the initial flow resistance, is added to the normal flow. The calculation results with and without additive flow resistance are plotted in Figure 4.58. They do not show noteworthy differences.

According to the studies for the GT-MHR, the increasing pressure in the primary circuit may decrease the solid temperature. Therefore, the reactor operation with 9 MW and 4 MPa is studied. The re-criticality of the reactor power with different pressures is displayed in Figure 4.59. The elapsed time for re-criticality of the reactor at 4 MPa is 3 hours later than for the reactor at 2.8 MPa. The natural convection is suppressed at low pressures in an enclosure [112]. The amount of heat that is transported by natural convection is increased by enhancing pressure of the primary circuit. Thus, the temperatures will decrease faster with higher pressure. Then it will take less time for the reactor to achieve re-criticality.

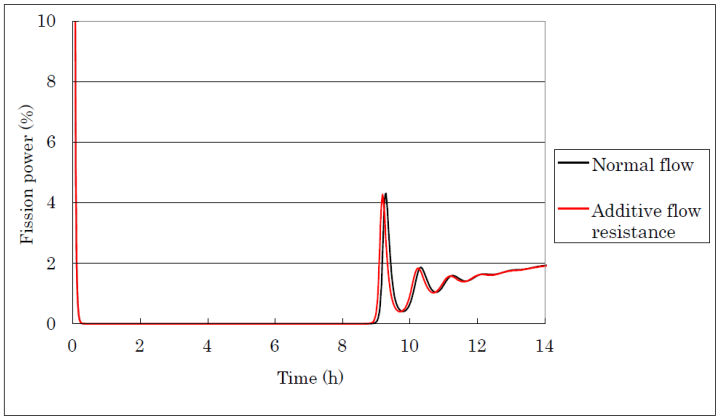

Figure 4.58: Elapsed time and power level at the occurrence of re-criticality with different flow resistance, 9 MW, LOFC

The experiment has shown that the side RPV temperature decreases from 170 $°C$ to 160 $°C$ in 12 hours with operating RCCS. To simplify the model, the former simulation uses a fixed RPV boundary condition. In order to investigate the impacts of the boundary temperature on elapsed time and peak power level of the re-criticality, a linear temperature ramp is applied in the simulation. The calculated results with a fixed boundary temperature and with a time-dependent boundary condition are presented in Figure 4.60. The transient processes are almost the same in these two situations. The maximum temperatures have some difference, but they are not significant. Therefore, the fixed boundary temperature is a good approximation.

The studies of parameter variations indicate that decay heat, thermal conductivity of the reactor graphite, and primary pressure have a strong impact on the elapsed time and power peak level of the re-criticality of the reactor. The different flow resistances will result in different re-criticality of the reactor as well, but the difference is not obvious. If the reactor shutdown period is chosen as 30 days, the calculated decay heat fits with the

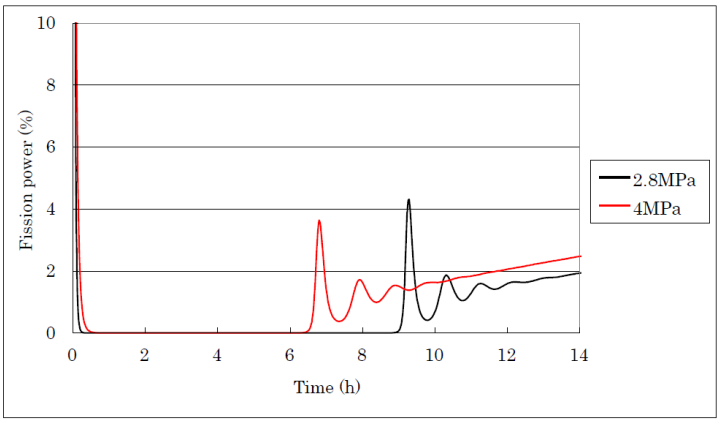

Figure 4.59: Elapsed time and power level at the occurrence of re-criticality with different pressures of primary circuit, 9 MW, LOFC

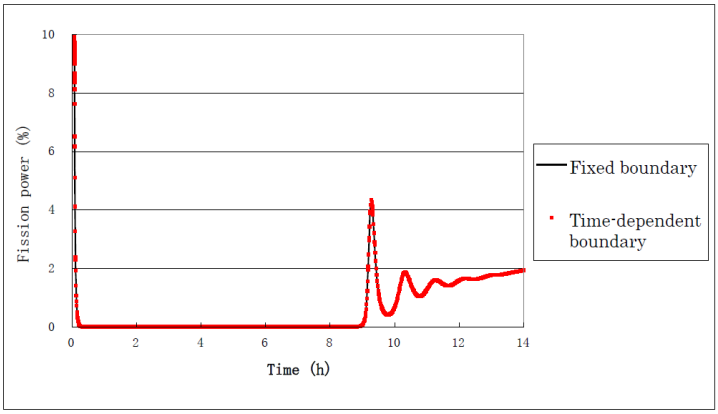

Figure 4.60: Elapsed time and power level at the occurrence of re-criticality with the fixed RPV temperature and with time-dependent boundary condition, 9 MW, LOFC

data suggested by JAEA. However, the elapsed time and power peak level do not fit very well with the measured values. The result can be optimized by considering the operation history in as much detail as possible. The thermal conductivity with irradiation of 330 EFPD does not differ significantly from the thermal conductivity with irradiation of 660 EFPD, but it does differ from the un-irradiated graphite. A good simulation result can be obtained by using the thermal conductivity of graphite with irradiation of 660 EFPD.

4.3.6 Pre-Calculation of Run 2 and Run 3 Experiments

Steady State of Run 2 Experiment

The Run 2 experiment will start from steady state running phase with a thermal power of 30 MW. The reactor operates in the low temperature phase with the inlet gas temperature of 395 $°C$ and outlet gas temperature of 850 $°C$. The radial RPV temperature is set at 360 $°C$, and the top and bottom RPV temperatures are set at 300 $°C$ [105]. The calculated outlet gas temperature is 854 $°C$. The effective neutron multiplication factor is 0.9669 in the steady state case. The calculated maximum fuel temperature is 1334 $°C$.

The normalized neutron spectrum of HTTR with 30 MW is presented in Figure 4.61. When the reactor runs at a different power level, the positions of control rods are inserted at different positions and the nuclide inventory is also different. Therefore, the neutron spectrum has some difference when the reactor is operated at different power level. The average absorption cross section of ^{135}Xe weighted by the neutron spectrum is 1.52×10^6 barn when the reactor operates at 30 MW.

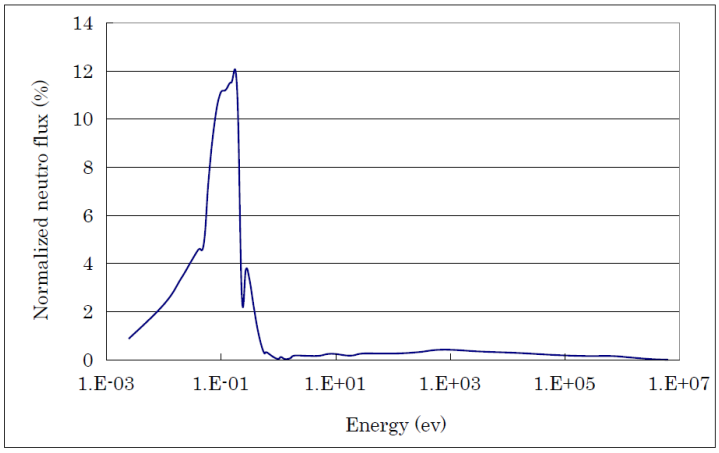

Figure 4.61: Normalized neutron spectrum of the HTTR, 30 MW

The local nuclear power densities of the third and fifth azimuthal meshes are presented in Figures 4.62 and 4.63. Because the top layer fuel block has the highest enrichment and the control rod is only inserted into the first fuel layer with about 29 cm, the maximum power density is in the bottom part of the first layer of fuel blocks, and its value is about

4.9 MW/m^3. Figure 4.64 displays the local nuclear power density in the transverse cross section of the reactor with $Z = 159.5\ cm$. The power density is comparable to the average nuclear power density of the reactor. The power peak factor of the main part in this part of the reactor is approximately 1, which means that the reactor power profile is flat in the transverse directions avoiding too large temperature gradients of the reactor core.

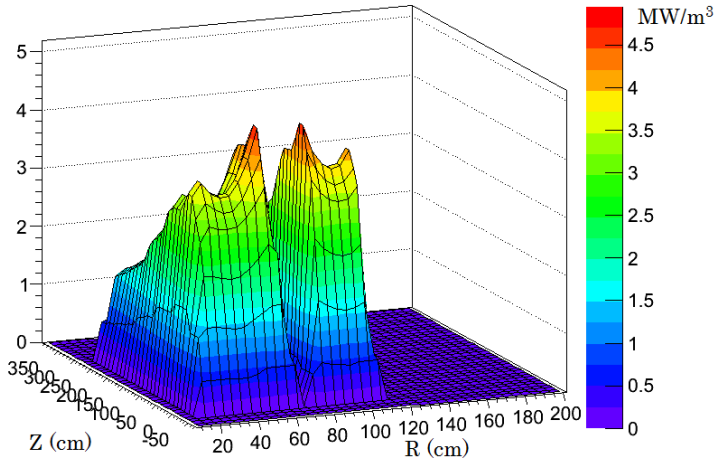

Figure 4.62: Local nuclear power density in the 3rd azimuthal mesh, 30 MW, steady state

Figures 4.65 and 4.66 display the homogenized solid temperature in the R/Z plane with respect to the third and fifth azimuthal meshes. The maximum temperature is achieved in the fuel blocks located in the third fuel ring and the fifth fuel layer. The figure also shows that the solid temperature of the control rod guide block, in which the control rods are inserted, is around 500 $°C$ due to the cooling effect of the bypass flow. Therefore, the control rods are protected against melting down. The solid temperature in the R/ϕ plane with $Z = 159.5\ cm$ is shown in Figure 4.67. The solid temperature of the reactor core is in the range between 600 $°C$ and 1200 $°C$. Considering the temperature difference between the moderator and the fuel rod, the fuel temperature is still far below a temperature of 1600 $°C$ when the reactor is operated at full power.

LOFC Transient of Run 2

In the Run 2 experiment, the reactor is initially operated at 30 MW. The neutron flux is normalized by the thermal power of the reactor. The coolant flow is assumed to be tripped in 10 s. Due to the operation of the RCCS, the boundary temperatures on the top, bottom, and side of the RPV are assumed to be constant during the transient. The studies of the flow resistance's impact on the reactor re-criticality shows that the flow resistance does affect the re-criticality of the reactor significantly. In order to make the simulation converge in the gas flow calculation, the flow resistance is multiplied by a factor of 2.

The pressure of the primary circuit is 4 MPa and is assumed to be constant during the accident. The thermal conductivity of graphite IG-110 irradiated by neutrons for 660 EFPD is taken into account in the simulation model. It is assumed that the reactor

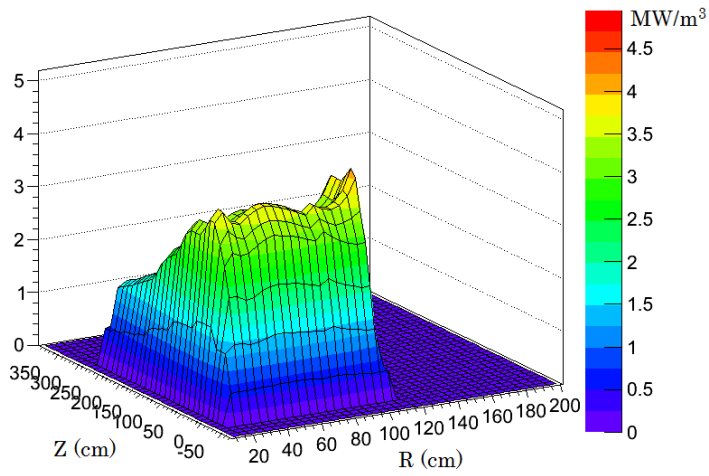

Figure 4.63: Local nuclear power density in the 5th azimuthal mesh, 30 MW, steady state

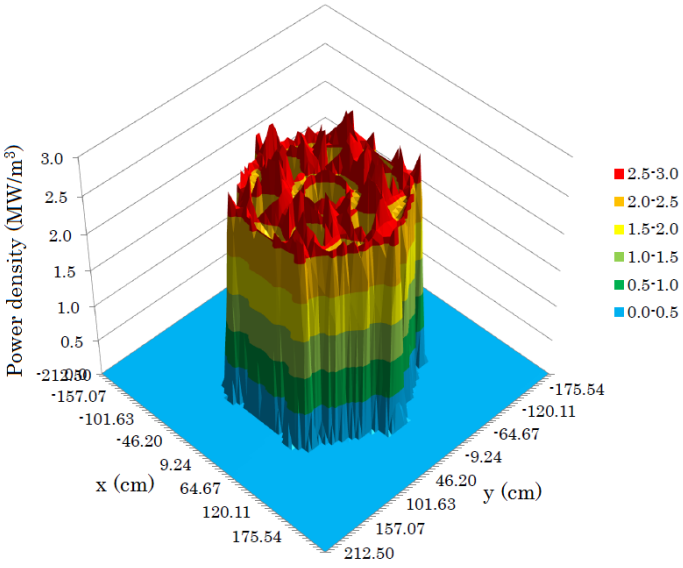

Figure 4.64: Local nuclear power density in the transverse cross section, 30 MW, steady state

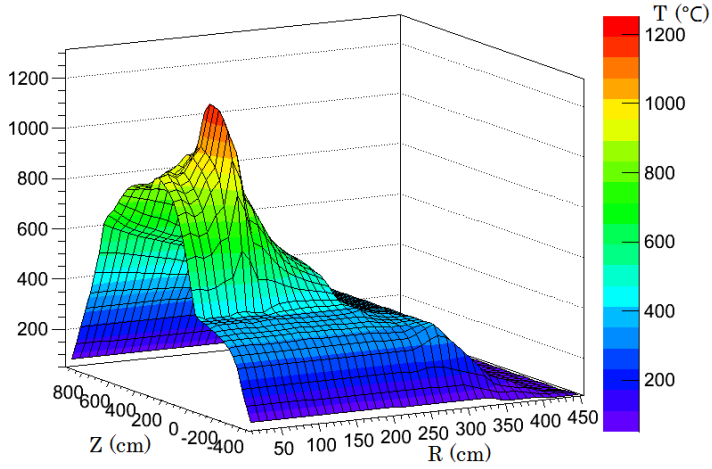

Figure 4.65: Solid temperature in the 3rd azimuthal meshes, 30 MW, steady state

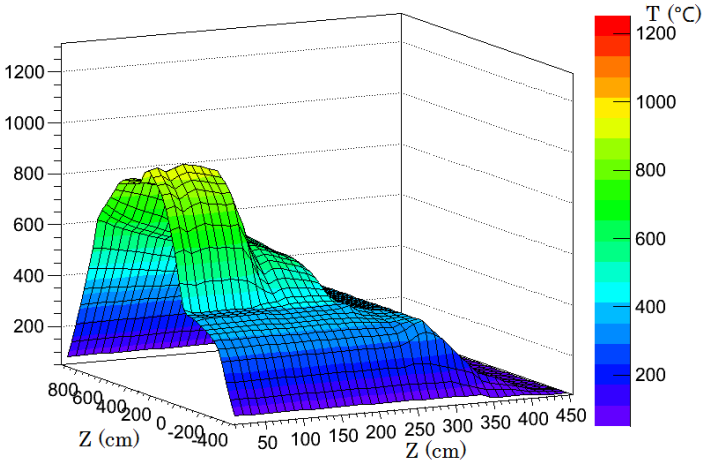

Figure 4.66: Solid temperature in the 5th azimuthal meshes, 30 MW, steady state

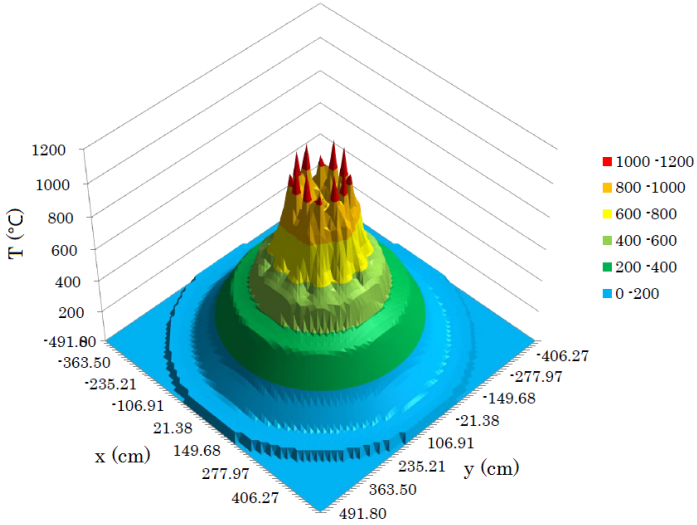

Figure 4.67: Solid temperature in the transverse cross section, 30 MW, steady state

has been operated for two days at 30 MW before the LOFC accident occurs. Figures 4.68 and 4.69 display the fission power and the decay power of the reactor for two cases: without shutdown phase, and with the shutdown period of 30 days before the Run 2 experiment. The fission power and decay power are normalized by the initial power of 30 MW. If the shutdown period was not added between the 373 EFPD operation and the Run 2 experiment, the decay heat according to DIN 25485 standard will correspond to the decay heat suggested by the project. With the 373 EFPD's operation and 2 additional full power days operation, the elapsed time of re-criticality is 13.73 h, and the peak power level is 5.44% of 30 MW. The fission power decreases to 1% of the initial power at 784 s, and the reactor is considered to be shutdown.

The evolution of the maximum fuel temperature, average fuel temperature, and average moderator temperature are presented in Figure 4.70. The initial difference between the average fuel temperature and average moderator temperature is about 100 $°C$. It is greater than the temperature difference when the reactor is operated at 9 MW due to the higher power density. Because the reactor is shut down at 784 s, and the thermal relaxation time of the fuel-moderator unit cell is about 60 s, the difference between average fuel temperature and average moderator temperature becomes less than 2 $°C$ after 20 minutes of the LOFC accident. The maximum fuel temperature of the reactor is still increasing after 20 hours, which means that the reactor has not achieved equilibrium due to the large heat capacity of the reactor core graphite.

The thermal conductivity is another important parameter in calculating the re-criticality of the reactor power. Therefore, the reactor power evolutions with different thermal conductivities are investigated (see Fig. 4.71). Considering that the re-criticality of the reactor power occurs earlier with a longer shutdown period, the reactor operation with a 30 day shutdown period is chosen as the reference to determine the range of the elapsed time and peak power level of the re-criticality. The reactor achieves re-criticality at 10.66 h, and the peak power is 4.48% of 30 MW assuming unirradiated graphite. The

elapsed time and peak power level of re-criticality are 11.56 h and 4.56% of initial power with the graphite irradiated to 660 EFPD.

In conclusion, the upper range of the elapsed time and peak power level is (13.73 h, 5.44%) and the lower range is (10.66 h, 4.48%). With the suggested decay heat, the elapsed time and peak power of re-criticality are 13.73 h and 1.632 MW, respectively. The maximum fuel temperature reaches 1260 $°C$ after 20 hours.

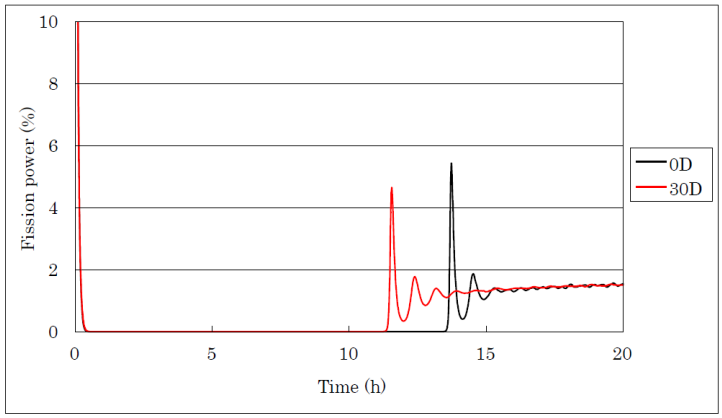

Figure 4.68: Elapsed time and power level at the occurrence of the re-criticality with different shutdown terms, 30 MW, LOFC

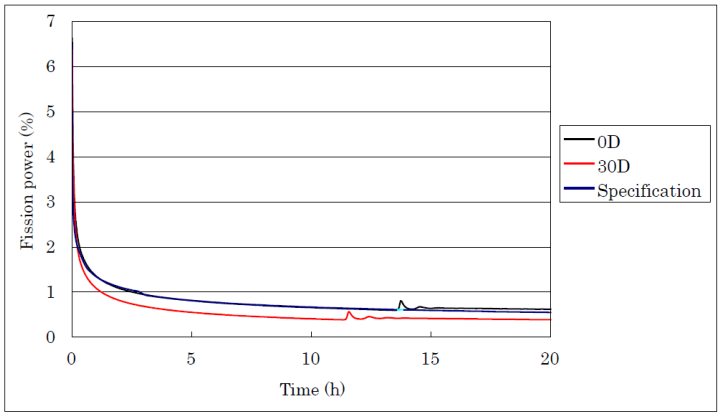

Figure 4.69: Decay heat of the HTTR with different shutdown terms, 30 MW, LOFC

LOFC Transient of Run 3

In the Run 3 experiment, the initial thermal power is again 9 MW, as in the Run 1 experiment. But different from Run 1, the Run 3 experiment is carried out with the deactivation of both active cooling trains of the VCS. As mentioned earlier, the recent MGT-3D does not calculate the heat transfer from the RPV to the VCS. In

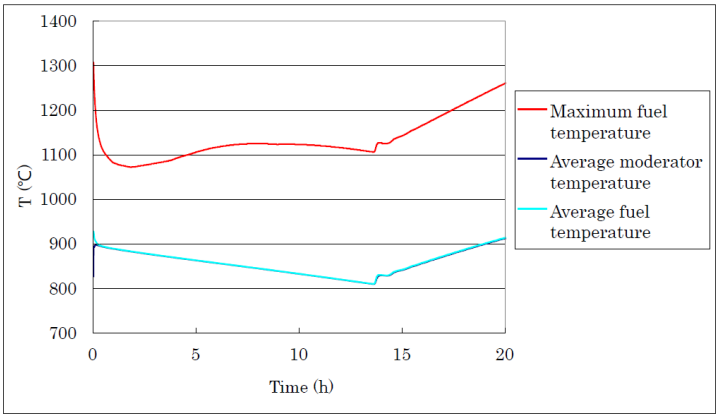

Figure 4.70: Maximum fuel temperature, average fuel temperature and average moderator temperature after during LOFC, 30 MW

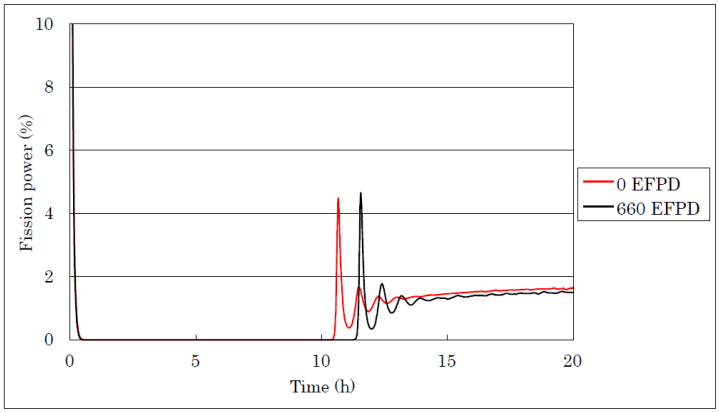

Figure 4.71: Elapsed time and power level at the occurrence of the re-criticality with different thermal conductivities, 30 MW, LOFC

the experiment of Run 1, the RPV temperature decreases from 170 $°C$ to 160 $°C$ in 12 hours. In the simulation results, the elapsed time and peak power level of the re-criticality do not have significant differences with a fixed RPV temperature and with a transient temperature (see Fig. 4.60). If the RCCS is inactive, the RPV temperature should increase during the accident.

The concrete wall temperature will be below 65 $°C$, and the RPV temperature will not exceed 190 $°C$ in the LOFC accident without the operation of the RCCS [90]. In order to investigate the impact of the RPV temperature on the elapsed time and peak power level of the re-criticality, the RPV temperature is supposed to increase from 170 $°C$ to 220 $°C$ in the MGT-3D simulation, which is far more than the suggested maximum RPV temperature in the Run 3 experiment. A shutdown period of 30 days is added to the operation history to guarantee the decay heat fitting with the suggested value. The calculated result is shown in Figure 4.72. The elapsed time and the peak power level overlap with different boundary conditions on the RPV. Fuel and moderator temperatures should be higher than those in the Run 1 experiment due to the loss of the VSC.

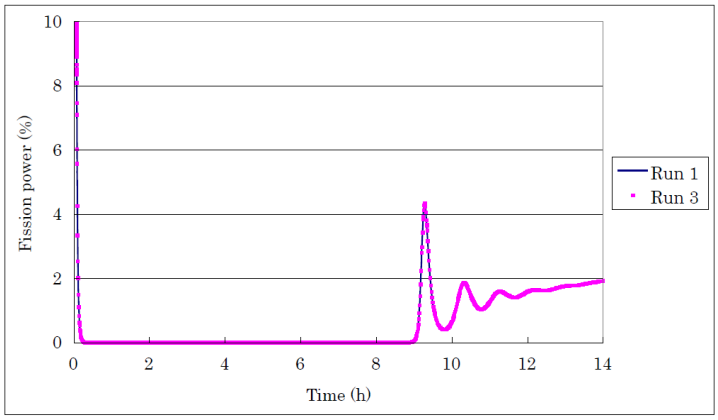

Figure 4.72: Prediction of the elapsed time and power level at the occurrence of the re-criticality in Run 3 experiment, 9 MW, LOFC

In this section, the neutronics and fluid mechanics design of the HTTR have been introduced. The LOFC accident is simulated from the initial core to the end of the experiment with the coupled neutronics and fluid mechanics method. The operation history is condensed to 373 EFPD, and the burnup is calculated with the MC code Serpent, for the purpose of obtaining the status before the LOFC accident experiment of the reactor core. For the LOFC accident with initial thermal power 9 MW, the reactor is extended to operate at a low power level over several days. It is quite necessary to do so because the atom density of short-lived nuclides, which include ^{135}Xe, is different when the reactor is operated at different power levels.

A new approach has been applied to generate the data required to calculate the nuclear cross sections, namely the interface between Serpent and MGT-3D. The nuclide density and operation history of the hexagonal block are homogenized in the block-wise geometry. Then, the calculation result of Serpent is interfaced with the input of MGT-

3D, which is based on $R/Z/\Phi$ coordinates, to determine the nuclide inventories and operation history of the MGT-3D meshes.

To simulate the HTTR in detail, a 3D deterministic model has been built. The reactor was calculated from steady state to the end of the LOFC transient. The calculations of both short-term and long-term transient were performed. The simulated results of Run 1 experiment regarding the re-criticality of reactor power fit very well with measured values. The parameter studies show that the decay heat and thermal conductivity of irradiated graphite have a great impact on the elapsed time and peak power level of the re-criticality. Based on the post-calculation of Run 1 experiment, the pre-calculations of Run 2 and Run 3 experiments were discussed as well.

Chapter 5

Conclusions and Outlook

The Very High Temperature Reactor (VHTR) has been chosen as one of the candidates of the generation IV reactors due to its excellent safety characteristics and its large potential for nuclear process heat applications. Safety features are given, for example, by the fuel to withstand temperatures much more than 1400 $°C$ in accident scenarios without significant damage, and by the huge amount of graphite and low power density in the reactor core. The pressurized LOFC and depressurized LOFC accidents without scram are two of the serious design basis accident scenarios in the Phenomena Identification and Ranking Table (PIRT) of VHTRs that include both pebble bed HTGRs and block type HTGRs. It is of utmost importance to conduct research on the evolution of neutronics and fluid mechanics of those HTGRs during LOFC and DLOFC accidents.

In this thesis, the coupled neutronics and fluid mechanics code MGT-3D is further developed for pebbled bed reactor simulations and extended to simulate HTR with prismatic fuel elements. The code is validated against experiments, verified with the simulation results of other codes, and then applied to study the LOFC and DLOFC of representative reactors and related experiments.

SANA experiment with only a central heating element is calculated with both the new code MGT-3D and MGT-2D. For the steady state case, the differences between the measured solid temperatures and the calculated solid temperatures with MGT-3D are within a range of 20 K. The maximum difference of the solid temperatures which are calculated by MGT-3D and MGT-2D is about 0.2 K. Because thermal radiation will be more important than natural convection in the temperature regime above 1000 $°C$, the calculated solid temperatures fit better with the measured temperatures in the case of a heating power of 35 kW in comparison to the case of 10 kW. For the transient case, the maximum difference between the measured temperatures and the calculated temperatures is about 30 K. Both the experiment and the simulation show that it takes about 40 h for the facility to achieve a new steady state. Then, MGT-3D is applied to calculate SANA experiment with both central heating element and three additional radial heating elements. In the 3-D model, the radial heating elements are simulated in detail. It shows that the solid temperatures of the pebble bed around the radial heating element rises significantly due to the heat source. The results clearly demonstrate the good performance of the 3-D model. In the pebble bed, the difference between the calculated solid temperatures and measured temperatures is in the range of 30 $°C$. The maximum solid temperature is about 1300 $°C$. Comparing the average power density of the experiment to the decay power density of HTR-Modul, it confirms that the residual heat can be removed from the reactor by conduction, natural convection, and thermal radiation without exceeding critical temperatures when the DLOFC accident happens in pebble bed HTGR.

Up to now, the old overheating model that considers coated particles as an independent point-like heat source with heat storage and heat flux resistance was applied to calculate the temperature difference between the graphite matrix of fuel element and the fuel kernel of coated particle. The temperature difference was added to the moderator temperature to obtain the fuel temperature. This overheating model has been re-evaluated, and a new kernel model that solves the 1-D heat transfer equation in a coated particle is developed to calculate the distinct temperature profile inside the coated particles. The new kernel model solves the temperature profile of the coated particle in detail. Therefore, it will take longer computation time with the new kernel model than with the overheating model. In any case, the new kernel model provides an analytical method to determine the effective heat flux resistance for the overheating model. The heat flux resistance which was used in the overheating model is suggested to be $3.0\ K \cdot m^3/MW$ instead of $1.0\ K \cdot m^3/MW$ for PBMR. In addition, a CFX model is set up to verify the new kernel model. The difference between the temperatures calculated by the new kernel model and the temperatures calculated by CFX model is less than $1.5\ K$ in the steady state. Both the CFX model and the new kernel model show that the relaxation time of coated particles is about $0.3\ s$. The new kernel model has been implemented into MGT-3D and applied to the simulation of both steady state and different transient cases of the PBMR. The comparison of the calculation results between the old overheating model and new kernel model proves that they do not result in significant differences for the steady state and slow transient case such as a control rod withdrawal accident. However, there is some difference for fast transient cases such as the control rod ejection accident. This is because the relaxation time of the coated particle is shorter than the nuclear time step in the slow transient, and the nuclear time step of MGT-3D is comparable with the relaxation time of the coated particle.

Block-type reactors can be treated in a coarse way as homogeneous cores with 1-D vertical flow in MGT-3D. To extend the applicability of MGT-3D to coupled neutronics and fluid mechanics calculations for block-type reactors, it is necessary to implement a new approach to calculate the temperature profile of the fuel element located in the hexagonal fuel block. The smallest symmetric geometry is chosen as the unit cell to represent the structure of the fuel block. The heat conduction equation is solved in the unit cells of the fuel block concepts for both GT-MHR and HTTR. In addition, the CFX models are established to verify the calculation results of the unit cell analysis. In the steady state case for the unit cell of the HTTR, the differences in the temperatures calculated with these two models are not larger than $2\ K$. In the transient case, both models show that the temperatures do not change significantly after about $60\ s$. A simplified 1-D model of the unit cells is introduced in the thesis as well. To extend for treating MGT-3D into block-type reactors, it is also necessary to calculate the thermal conductivity of the homogeneous meshes. The effective thermal conductivity of the homogeneous meshes, which is anisotropic, i. e. different in axial direction and in transverse direction, is driven by an analytical model. The replaceable reflector blocks, control rod guide blocks, and reserved shutdown blocks consist of two discrete materials, and the fuel block consists of three discrete materials. Therefore, different equations are chosen to calculate their effective thermal conductivity, all of which have been implemented into MGT-3D.

The extended MGT-3D including the implementation of block-type reactors is then applied to simulate a heat-up experiment of NACOK-II with a ceramic cuboid block. Considering the geometry of the experimental facility, a pseudo X/Y/Z model is used to simulate the experiment. Due to the limitations of MGT-3D on the calculation of thermal radiation, a new method with an external heat source is introduced to represent the heat

transferred by thermal radiation across the transparent cavity. The maximum difference between the calculated temperatures and the measured values of solid temperature is about 30 K at the point where the temperature is higher than 600 $°C$. The experimental data provide a good validation for the analytical equation to calculate the homogeneous thermal conductivity of a cuboid block. The external heat source can be obtained by an iteration approach in the steady state. However, the iteration method can not be applied in transients. For the transient case, the following approach is suggested: first, the transient process is divided into many time intervals, in which the external power changes linearly; in a second step, the equilibrium calculation is performed to obtain the equivalent external heat at the beginning and end time point of each time interval.

The LOFC and depressurized LOFC accident scenarios are simulated with MGT-3D. The code-to-code comparison is made, and the simulation results of MGT-3D are in good agreement with the benchmark data obtained within the IAEA directed CRP-3 project. The results represent an excellent verification of the MGT-3D model. In the normal operation, the difference of the temperatures calculated by MGT-3D and the code GTAS is in the range of 10 $°C$. The maximum solid temperature was determined to be 1376 $°C$ in the LOFC scenario, and 1535 $°C$ in the depressurized LOFC scenario. The calculation results also show that the temperatures of the reactor do not change significantly after around 100 hours in the accident. Studies of parameter variations reveal that the thermal conductivity and decay heat have a significant impact on the solid temperatures. The study of the LOFC accident shows that the pressure of the primary circuit affects the solid temperature significantly due to natural convection. The changes of solid temperature can reach 80 K if the pressure of the primary circuit decreases from 70 bar to 50 bar. In the LOFC and DLOFC simulation for the GT-MHR, a 2-D model is applied. The fuel blocks and control rods are homogenized in the annular circle. The positions of the control rods cannot be specified in the 2-D model, and rather require the development of a 3-D description for the reactor. Additionally, it only involves the fluid mechanics calculation with given heat source. If the nuclide inventories and operational history are supplied separately by some burnup code, the coupled neutronics and fluid mechanics simulation can be made by MGT-3D. By developing the HTR code package (HCP), the steady state and transient operating conditions of the GT-MHR can be simulated with a full 3D model.

The full time-dependent, coupled neutronics and fluid mechanics calculation is employed to simulate the LOFC experiments conducted and planned, respectively, with the HTTR, which is the LOFC project of OECD/NEA. The post-calculation of the Run 1 experiment with the initial power of 9 MW shows that the elapsed time and peak power level at the occurrence of re-criticality are 7.9 h and 0.37 MW, respectively, which fits with the measured values of the wide range monitoring (WRM) system. The long term transient calculation concludes that the solid temperatures do not rise again after about 70 h into the LOFC scenario. The studies on decay heat, which has a significant impact on the re-criticality, show that the suggested equation of decay heat is in good agreement with the calculated results according to DIN 25 458 when the initial thermal power is 30 MW, but there are differences when the initial thermal power is 9 MW. It means that the suggested equation of decay heat should be re-evaluated. The study on thermal conductivity of graphite reveals that the elapsed time with re-criticality is lower with higher thermal conductivity. Flow resistance and boundary temperature do not have significant influence on the re-criticality. Due to the Fukushima accident, the restart of HTTR is delayed later than April, 2015. The Run 2 experiment has not yet performed. In this thesis, the calculation of the Run 2 experiment with initial power 30 MW has been performed as a prediction. The simulated elapsed time and peak pow-

er level of the re-criticality are 13.7 h and 1.63 MW, respectively. The discussion of the Run 3 experiment with an initial power of 9 MW concludes that its elapsed time and peak power level will be the same as in the Run 1 experiment. The major parameters which have a significant effect on reactor kinetics during loss of forced cooling of HTGR are the thermal conductivity of reactor core internals, the heat transferred by natural convection, and the concentration of the neutron poison nuclides. They are well considered in the MGT-3D model. However, some features are still not included, such as the location of the B_4C poison sticks in the hexagonal fuel block, the nuclides which represent the fission products of ^{233}U, ^{235}U, ^{238}U, and so on. This may be the reason for the calculated peak power at the occurrence of the reactor re-criticality being greater than the measured value.

MGT-3D can be applied to calculate steady state and transient scenarios of pebble bed HTGRs and has been extended to calculate block-type HTGRs in this thesis. However, there are still some issues that need to be optimized in MGT-3D. First, for the gas flow through porous media, the viscous sheer stresses and momentum changes as a result of flow diversions are accounted for by an equivalent flow resistance. The flow in the big cavity cannot be simulated precisely. Also the process of the gas mixing cannot be simulated. Second, the thermal radiation across the gap or cavity is simulated by a contribution to the thermal conductivity, and the average temperature of the surface of the gap is used to calculate the effective thermal conductivity. It causes a certain error when calculating the radiation heat transfer across big gaps or big cavities, especially in the cases of high temperatures. As mentioned above, the gas flows are not calculated by solving the momentum conservation equation with the finite element method in MGT-3D. However, the NACOK-II experiment with measuring the gas flow in the porous media can be used to validate the gas flow procedure implemented in MGT-3D.

Appendix A

The Nuclear Flux Diffusion Equation

The neutron diffusion equation is the derivation of the following neutron transport equation:

$$\begin{aligned}&\frac{1}{\nu}\frac{\partial}{\partial t}\varphi(\boldsymbol{r},E,\hat{\Omega},t)+\hat{\Omega}\cdot\nabla\varphi(\boldsymbol{r},E,\hat{\Omega},t)+\Sigma_t(\boldsymbol{r},E,t)\varphi(\boldsymbol{r},E,\hat{\Omega},t)\\&=\int_{4\pi}\int_0^{\infty}\Sigma_S(\boldsymbol{r},E'\to E,\hat{\Omega}'\to\hat{\Omega},t)\varphi(\boldsymbol{r},E',\hat{\Omega}',t)dE'd\hat{\Omega}'+s(\boldsymbol{r},E,\hat{\Omega},t)\end{aligned}\tag{A.1}$$

For equilibrium:

$$\begin{aligned}&\hat{\Omega}\cdot\nabla\varphi(\boldsymbol{r},E,\hat{\Omega},t)+\Sigma_t(\boldsymbol{r},E,t)\varphi(\boldsymbol{r},E,\hat{\Omega},t)\\&=\int_{4\pi}\int_0^{\infty}\Sigma_S(\boldsymbol{r},E'\to E,\hat{\Omega}'\to\hat{\Omega},t)\varphi(\boldsymbol{r},E',\hat{\Omega}',t)dE'd\hat{\Omega}'+s(\boldsymbol{r},E,\hat{\Omega},t)\end{aligned}\tag{A.2}$$

Integrate Equation $A.1$ over direction, which is specified by the variable $\hat{\Omega}$. The result is:

$$\begin{aligned}&\frac{1}{\nu}\frac{\partial}{\partial t}\phi(\boldsymbol{r},E,t)+\nabla\cdot\boldsymbol{J}(\boldsymbol{r},E,t)+\Sigma_t(\boldsymbol{r},E,t)\phi(\boldsymbol{r},E,t)\\&=\int_0^{\infty}\Sigma_S(\boldsymbol{r},E'\to E,t)\phi(\boldsymbol{r},E',t)dE'+S(\boldsymbol{r},E,t)\end{aligned}\tag{A.3}$$

Where,

ϕ is the scalar neutron flux: $\phi(\boldsymbol{r},E,t)=\int_{4\pi}\varphi(\boldsymbol{r},E,\hat{\Omega},t)d\hat{\Omega}$

$\boldsymbol{J}$ is the neutron current density: $\boldsymbol{J}(\boldsymbol{r},E,t)=\int_{4\pi}\hat{\Omega}\varphi(\boldsymbol{r},E,\hat{\Omega},t)d\hat{\Omega}$

Σ_S is the scattering cross section from the energy E' to energy E:

$$\Sigma_S(\boldsymbol{r},E'\to E,t)=\int_{4\pi}\Sigma_S(\boldsymbol{r},E'\to E,\hat{\Omega}'\to\hat{\Omega},t)d\hat{\Omega}$$

S is the neutron source: $S(\boldsymbol{r},E,t)=\int_{4\pi}s(\boldsymbol{r},E,\hat{\Omega},t)d\hat{\Omega}$

If the high-order terms of the expansion are neglected, the expressions of the angular neutron flux and the scattering cross section are as follows:

$$\varphi(\boldsymbol{r},E,\hat{\Omega},t)=\frac{1}{4\pi}\phi(\boldsymbol{r},E,t)+\frac{3}{4\pi}\hat{\Omega}\cdot\boldsymbol{J}(\boldsymbol{r},E,t)\tag{A.4}$$

$$\Sigma_S(\boldsymbol{r},E'\to E,\hat{\Omega}'\to\hat{\Omega},t)=\frac{1}{4\pi}\Sigma_{S0}(\boldsymbol{r},E'\to E,t)+\frac{3}{4\pi}\mu_0\Sigma_{S1}(\boldsymbol{r},E'\to E,t)\tag{A.5}$$

Where $\mu_0 = \hat{\Omega} \cdot \hat{\Omega}'$.

Substituting Equations $A.4$ and $A.5$ into the equilibrium transport Equation $A.2$ and separating the zero-order and first-order, it obtains:

$$\nabla \boldsymbol{J}(\boldsymbol{r}, E) + (\Sigma_t - \Sigma_{S0})\phi(\boldsymbol{r}, E) = S(\boldsymbol{r}, E) \tag{A.6}$$

$$\frac{1}{3}\nabla\phi(\boldsymbol{r}, E) + \boldsymbol{J}(\boldsymbol{r}, E)(\Sigma_t - \Sigma_{S1}) = 0 \tag{A.7}$$

Extending Equation $A.7$ to the time dependent case, it obtains:

$$\boldsymbol{J}(\boldsymbol{r}, E, t) = -D(\boldsymbol{r}, E, t)\nabla\phi(\boldsymbol{r}, E, t) \tag{A.8}$$

with

$$D(\boldsymbol{r}, E, t) = \frac{1}{3[\Sigma_t(\boldsymbol{r}, E, t) - \bar{\mu}_0(\boldsymbol{r}, E, t)\Sigma_S(\boldsymbol{r}, E, t)]} \tag{A.9}$$

and

$$\begin{aligned} \bar{\mu}_0(\boldsymbol{r}, E, t) &= \frac{\Sigma_{S1}}{\Sigma_{S0}} \\ &= \frac{2\pi \int_{-1}^{+1} \mu_0 \Sigma_S(\boldsymbol{r}, E, \mu_0, t) d\mu_0}{2\pi \int_{-1}^{+1} \Sigma_S(\boldsymbol{r}, E, \mu_0, t) d\mu_0} \end{aligned} \tag{A.10}$$

With this first-order approximation, the diffusion coefficient $D(\boldsymbol{r}, E, t)$ is obtained. Substituting Equation $A.8$ into the neutron diffusion Equation $A.3$, the simplified diffusion equation can be obtained:

$$\begin{aligned} &\frac{1}{\nu}\frac{\partial}{\partial t}\phi(\boldsymbol{r}, E, t) - \nabla \cdot [D(\boldsymbol{r}, E, t)\nabla\phi(\boldsymbol{r}, E, t)] + \Sigma_t(\boldsymbol{r}, E, t)\phi(\boldsymbol{r}, E, t) \\ &= \int_0^\infty \Sigma_S(\boldsymbol{r}, E' \to E, t)\phi(\boldsymbol{r}, E', t) dE' + S(\boldsymbol{r}, E, t) \end{aligned} \tag{A.11}$$

As for the neutron source part, $S(\boldsymbol{r}, E, t)$ includes the fission neutron source and other neutron sources, e.g. $(n, 2n), (n, 3n), (\gamma, n)$ reactions and external source. Divide the energy interval $[0, \infty)$ into following G groups:

$$E_G(=0) < E_{G-1} < ..... < E_1 < E_0(=\infty)$$

The energy interval of g-th group is $[E_g, E_{g-1})$ with g=1,...G. Integrate the equation($A.11$) over the g-th group:

$$\begin{aligned} &\frac{\partial}{\partial t}\int_{E_g}^{E_{g-1}} \frac{1}{\nu}\phi(\boldsymbol{r}, E, t) dE - \nabla \cdot \int_{E_g}^{E_{g-1}} [D(\boldsymbol{r}, E, t)\nabla\phi(\boldsymbol{r}, E, t)] dE + \int_{E_g}^{E_{g-1}} \Sigma_t(\boldsymbol{r}, E, t)\phi(\boldsymbol{r}, E, t) dE \\ &= \int_{E_g}^{E_{g-1}} [\sum_{g'=1}^{G} \int_{E_{g'}}^{E_{g'-1}} \Sigma_S(\boldsymbol{r}, E' \to E, t)\phi(\boldsymbol{r}, E', t) dE'] dE + \int_{E_g}^{E_{g-1}} S(\boldsymbol{r}, E, t) dE \end{aligned} \tag{A.12}$$

Doing the integration for g=1,...G, the G group neutron diffusion equations set can be obtained, which is multi-group neutron diffusion equations. In MGT-3D, the equation is solved in the $R/Z/\Phi$ coordinate system.

Appendix B

The Fluid Mechanics Calculation

The Fuel Element Temperature

In MGT-3D, a numerical method based on the analytical result is introduced to calculate the temperature profile of the fuel element which includes the spherical fuel element and the representative unit of the block type fuel blocks [43]. Recently, a finite difference method solution with mesh centered temperature is coded for the one dimension case.

To solve the solid temperature profile of the fuel element, the energy conservation equation is employed:

$$\rho_s c_p \frac{\partial T_s}{\partial t} = \nabla \cdot (k \nabla T_s) + q''' \tag{B.1}$$

The boundary conditions are in the center and at the outer edge of fuel element are as follows:

$$\begin{cases} \frac{\partial T(r,t)}{\partial r}|_{r=0} = 0 \\ -k\frac{\partial T(r,t)}{\partial r}|_{r=R} = \alpha(T(R,t) - T_g) \end{cases} \tag{B.2}$$

where α is the effective heat transfer coefficient, $T(R,t)$ is the surface temperature of fuel element, and T_g is the surrounding temperature. Integrating Equation $B.1$ over a domain of volume, it obtains:

$$\int_V \rho C_p \frac{\partial T(r,t)}{\partial t} dV = \oint_S k \nabla T(r,t) \cdot d\boldsymbol{S} + \int_V q'''(r,t) dV \tag{B.3}$$

The fuel element is divided into several numerical mesh grids and they are identified with $i = 1, ...I$ from center to the outer layer. The discretization equation of the i-th layer of the time interval n is:

$$\frac{\rho C_p \Delta V_i}{\Delta t}(T_i^n - T_i^{n-1}) = L_{i-1}(T_{i-1}^n - T_i^n) - L_i(T_i^n - T_{i+1}^n) + q_i''' \Delta V_i \tag{B.4}$$

where L_i is the coefficient to calculate the heat flux across the surface.

For the spherical fuel element, L_i is determined by the following equation:

$$L_{i-1} = \frac{r_{i-\frac{1}{2}}^2}{\frac{r_{i-\frac{1}{2}} - r_{i-1}}{k_{i-1}} + \frac{r_i - r_{i-\frac{1}{2}}}{k_i}} \tag{B.5}$$

where r_i is the central radius of the i-th mesh, $r_{i-\frac{1}{2}}$ is the radius of the surface between the $(i-1)$-th mesh and the i-th mesh, k_i is the thermal conductivity of the i-th mesh.

For the cylindrical fuel element, L_i can be written as:

$$L_{i-1} = \frac{r_{i-\frac{1}{2}}}{\frac{r_{i-\frac{1}{2}}-r_{i-1}}{k_{i-1}} + \frac{r_i - r_{i-\frac{1}{2}}}{k_i}} \tag{B.6}$$

The Solid Temperature

The solid temperature of the homogeneous meshes is defined as the mesh centered temperature in the meshes with compact solid body and is defined as the solid surface temperature in the meshes with porous media. In the normal operation, the heat generated in the fuel rod is mainly taken away by convection. In some defined accidents such as LOFC, the heat is mainly removed by thermal conduction and thermal radiation. To calculate the heat transferred by thermal conduction and thermal radiation, the effective thermal conductivity including the effect of thermal radiation is introduced in the porous media [43].

There are not mass transfer and momentum transfer in the solid materials. Therefore, the solid temperature is obtained by solving the energy conservation equation (see Eq. 2.12). It is coupled with the heterogeneous fuel element temperature and the gas temperature calculation with the term of heat source. The energy conservation equation of the solid phase has the same form with the diffusion equation of neutron flux. The leakage iteration method is applied to calculate the solid temperature profile in the homogeneous meshes [24].

The heat transfer in the homogeneous meshes includes the thermal conduction between the solid materials, the thermal radiation and the convection between the solid and the gas. For a homogeneous target mesh, the heat which is transported from the solid surface into its surrounding gas, is:

$$J_g = \alpha A(\bar{T}_R - T_g) \tag{B.7}$$

where $\bar{T}_R$ is the average solid temperature of the porous media, A is the contact surface between gas and solid material. The heat exchange of the target mesh with its neighboring meshes by thermal conduction is:

$$J_s = \sum_{i=1}^{n} \frac{k_i A_i}{\Delta l_i}(\bar{T}_R - \bar{T}_{Ri}) \tag{B.8}$$

where $\bar{T}_{Ri}$ is the average solid temperature of the neighboring mesh, A_i and Δl_i are the contact surface area and the center distance between the target mesh and its neighboring mesh. The heat exchange across the gap and the thermal radiation between the fuel elements are calculated with different ways [2]. The total heat flux transferred out of the target mesh is:

$$J = J_g + J_s = (\alpha A + \sum_{i=1}^{n} \frac{k_i A_i}{\Delta l_i})\bar{T}_R - (\alpha A T_g + \sum_{i=1}^{n} \frac{k_i A_i}{\Delta l_i}\bar{T}_{Ri}) \tag{B.9}$$

Assuming that the total heat flux can be written as

$$J = \alpha_{eff} A(\bar{T}_R - T_{eff}) \tag{B.10}$$

the effective heat transfer coefficient and the effect surround temperature are

$$\begin{cases} \alpha_{eff} = (\alpha + \sum_{i=1}^{n} \frac{k_i A_i}{A \Delta l_i}) \\ T_{eff} = \frac{1}{\alpha_{eff}} (\alpha A T_g + \sum_{i=1}^{n} \frac{k_i A_i}{\Delta l_i} \bar{T}_{Ri}) \end{cases} \tag{B.11}$$

The Gas Flow

The gas flow calculation involves the solution of mass and momentum conservation equations (see Eq. 2.10, 2.11). The momentum conservation equation implies the momentum density balance which is determined by the pressure gradient, gravity and friction. If there is a gas sink or source in the homogeneous mesh, the source term should be added in the right hand side of Equation 2.11.

Helium is used as coolant in the HTGRs. The inertness of helium is very small. The new equilibrium can be achieved after a short time interval if the flow conditions change. Therefore, the transient case of the gas flow can be treated with "quasi-stationary", as a sequence of equilibrium states. Based on the speed of sound of helium and the size of the reactor core, it can be concluded that the small disturbance of flow condition can propagate through the reactor at the time interval of centisecond, which is smaller than the normal time step of MGT-3D. It is not clear whether it is suitable for the very fast transient. For the stationary case, the momentum conservation equation is:

$$\nabla \cdot \rho_g \boldsymbol{u}\boldsymbol{u} - \nabla \cdot \bar{\bar{\tau}} + \nabla P - \rho_g \boldsymbol{g} = 0 \tag{B.12}$$

The flow resistance is determined by an experiment under controlled conditions. The viscous sheer stresses and/or momentum changes as a result of flow diversions due to obstacles and bends in the flow path can be accounted for by introducing the right resistance:

$$\nabla \cdot \rho_g \boldsymbol{u}\boldsymbol{u} - \nabla \cdot \bar{\bar{\tau}} = W \rho_g \boldsymbol{u} \tag{B.13}$$

Submit Equation $B.13$ into Equation $B.12$, it can be obtained:

$$\nabla P - \rho_g \boldsymbol{g} + W \rho_g \boldsymbol{u} = 0 \tag{B.14}$$

From Equation $B.14$, it can be obtained:

$$\rho_g \boldsymbol{u} = \frac{\rho_g \boldsymbol{g} - \nabla P}{W} \tag{B.15}$$

Integrating the mass conservation Equation 2.10 over volume ΔV and applying the generalized divergence theorem, it gives:

$$\int_{\Delta V} \frac{\partial \rho_g}{\partial t} dv + \oint_{\boldsymbol{A}} \rho_g \boldsymbol{u} d\boldsymbol{A} = \int_{\Delta V} S dv \tag{B.16}$$

Substitute Equation $B.15$ into Equation $B.16$:

$$\int_{\Delta V} \frac{\partial \rho_g}{\partial t} dv + \oint_{\boldsymbol{A}} \frac{\rho_g \boldsymbol{g} - \nabla P}{W} d\boldsymbol{A} = \int_{\Delta V} S dv \tag{B.17}$$

which is applied to solve the pressure distribution of the gas flow.

Appendix C

New Kernel Model

Integrating Equation 3.15 over a small volume V_i on both sides and using the divergence theorem, we can obtain:

$$\int_{V_i} \rho C_p \frac{\partial T(r,\theta,\phi,t)}{\partial t} dV = \oint_S k \nabla T(r,\theta,\phi,t) \cdot d\boldsymbol{S} + \int_{V_i} \dot{Q}'''(r,\theta,\phi,t) dV \tag{C.1}$$

Finite volume method is chosen to solve this equation numerically [42]. Considering the spherical symmetry, we divide the coated particles into numerical cells. The discretized form of Equation C.1 in cell i in time interval n is:

$$\rho_i C_{pi} V_i \frac{T_i^{n+1} - T_i^n}{\Delta t} = Q_{i-\frac{1}{2}}^n - Q_{i+\frac{1}{2}}^n + \dot{Q}_i''' V_i \tag{C.2}$$

where index i is used to identify center parameters, index $i - \frac{1}{2}$ and $i + \frac{1}{2}$ are used to identify surface parameters, V_i is the control volume, T_i is the center temperature, $Q_{i-\frac{1}{2}}$ is the heat flux transferring from the $(i-1)$-th cell into the control volume, $Q_{i+\frac{1}{2}}$ is the heat flux transferring out of the control volume into the $(i+1)$-th cell. This discretized equation follows the energy conservation laws. The heat flux entering a given volume is identical to that leaving the adjacent volume. Heat transferred across the inside surface of the control volume can be expressed as:

$$Q_{i-\frac{1}{2}}^n = -k_{i-1}(A\frac{\partial T^n}{\partial r})|_{i-\frac{1}{2}} = -k_{i-1}A_{i-\frac{1}{2}} \frac{T_{i-1}^n - T_{i-\frac{1}{2}}^n}{r_{i-1} - r_{i-\frac{1}{2}}} = -k_i A_{i-\frac{1}{2}} \frac{T_{i-\frac{1}{2}}^n - T_i^n}{r_{i-\frac{1}{2}} - r_i} \tag{C.3}$$

The center radius r_i is evaluated by: $r_i = \sqrt{r_{i-\frac{1}{2}} r_{i+\frac{1}{2}}}$. Eliminate surface temperature $T_{i-\frac{1}{2}}^n$ in Equation C.3:

$$Q_{i-\frac{1}{2}}^n = A_{i-\frac{1}{2}} \frac{k_{i-1}k_i}{k_i(r_{i-\frac{1}{2}} - r_{i-1}) + k_{i-1}(r_i - r_{i-\frac{1}{2}})} (T_{i-1}^n - T_i^n) \tag{C.4}$$

In a similar way, we can get the heat transferred across the outside surface:

$$Q_{i+\frac{1}{2}}^n = A_{i+\frac{1}{2}} \frac{k_i k_{i+1}}{k_{i+1}(r_{i+\frac{1}{2}} - r_i) + k_i(r_{i+1} - r_{i+\frac{1}{2}})} (T_i^n - T_{i+1}^n) \tag{C.5}$$

Equations C.2, C.4 and C.5 use the explicit time differencing method. There is no matrix solving for this method, but time step is limited by stability consideration. The value of time step $n+1$ can be used to evaluate the RHS of Equation C.1, which is the implicit time differencing method. After introducing a time weighting factor α, the

general discrete equation is written as:

$$\rho_i C_{pi} V_i \frac{T_i^{n+1} - T_i^n}{\Delta t} = (1-\alpha)(Q^n_{i-\frac{1}{2}} - Q^n_{i+\frac{1}{2}}) + \alpha(Q^{n+1}_{i-\frac{1}{2}} - Q^{n+1}_{i+\frac{1}{2}}) + \dot{Q}_i''' V_i \tag{C.6}$$

where $0 \leqslant \alpha \leqslant 1$. If $\alpha = 0$, the equation degenerates into explicit discrete form. If $\alpha = 1$, it is the fully implicit discrete form. The critical time step of this model can be estimated by the following equation:

$$\delta t' = \frac{1}{1-2\alpha} \frac{\rho c_p}{k} (\delta r) \tag{C.7}$$

Like for steady state, the volume-averaged kernel temperature is used to represent fuel temperature:

$$T_f^n = \frac{\sum_{i=1}^{N_f} T_i^n V_i}{V_f} \tag{C.8}$$

Bibliography

[1] A Technology Roadmap for Generation IV Nuclear Energy Systems. GIF-002-00, 2002.

[2] H. Gerwin, W. Scherer, A. Lauer. TINTE-A two-dimensional code for reactor dynamics. *Berichte des Forschungszentrums Jülich*, Jül-4294, 2009.

[3] https:// www.iecd-nea.org/jointproj/lofc.html

[4] Private communication with S. Herber, 2014.

[5] R. C. Allen. The British Industrial Revolution in Global Perspective. Cambridge: Cambridge University Press, 2009.

[6] Next Generation Nuclear Plant Pre-Conceptual Design Report. INL/EXT-07-12967, 2007.

[7] R. U. Ayres, B. Warr. The Economic Growth Engine: How Energy and Work Drive Material Prosperity. Cheltenham: Edward Elgar, 2009.

[8] C. M. Cipolla. The Economic History of World Population. London: Pelican Books, 1962.

[9] Energy, Electricity and Nuclear Power Estimates for the Period up to 2050. IAEA-RDS-1/33, 2013.

[10] R. Reimert, M. Schad. Process heat from modularized HTR. *Nuclear Engineering and Design*, 251: 244-251, 2012.

[11] A. J. Goodjohn. Summary of gas-cooled reactor programs. *Energy*, 16: 79-106, 1991.

[12] R. Schulten. Pebble-bed HTRs. *Annals of Nuclear Energy*, 5: 357-374, 1978.

[13] S. Fujikawa, O. Baba et al. Present status of the HTTR and topics from operation. *Proceedings of the Seminar on HTGR Application and Development, Beijing, China, March2001*, 2001.

[14] H. Frewer, W. Keller, R. Pruschek. The modular high-temperature reactor. *Nuclear Science and Engineering*, 90: 411-426, 1985.

[15] Z. X. Wu, Z. Y. Zhang. The Advanced Nuclear Energy System and High Temperature Gas-cooled Reactor. Tsinghua University Publishing House, 2004.

[16] A. Koster, H. D. Matzner, D. R. Nicholsi. PBMR design for the future. *Nuclear Engineering and Design*, 222: 231-245, 2003.

[17] C. Druska, St. Kasselmann, A. Lauer. Investigations of space-dependent safety-related parameters of a PBMR-like HTR in transient operating conditions applying a multi-group diffusion code. *Nuclear Engineering and Design*, 239: 508-520, 2009.

[18] Current Status and Future Development of Modular High Temperature Gas Cooled Reactor Technology. IAEA-TECDOC-1198, 2001.

[19] J. W. Sterbentz, B. Phillips et al. Reactor physics parametric and depletion studies in support of TRISO particle fuel specification for the next generation nuclear plant. INEEL/EXT-04-02331, 2004.

[20] S. Saito. Present status of the HTGR development program in Japan. *Energy*, 16: 129-136, 1991.

[21] S. Saito, et al. Design of the High Temperature Engineering Test Reactor. JAERI 1332, 1994.

[22] H. J. Allelein, S. Kasselmann et al. Progress on the development of a fully integrated HTR code package. *Nuclear Engineering and Design*, 251: 400-406, 2012.

[23] S. Nakagawa, K. Takamatsu et al. Safety demonstration tests using high temperature engineering test reactor. *Nuclear Engineering and Design*, 233: 301-308, 2004.

[24] H. Gerwin, W. Scherer, A. Lauer. TINTE-Nuclear calculation theory description report. *Berichte des Forschungszentrums Jülich*, Jül-4317, 2010.

[25] P. Lourens. Verification of the mathematical models for the neutron flux of the code TINTE. Internal documents of PBMR project, 2004.

[26] Y. Naito, M. Maekawa, K. Shibuya. A leakage iterative method for solving the three-dimensional neutron diffusion equation. *Nuclear Science and Engineering*, 58: 182-192, 1975.

[27] Deutsches Institut für Normung. Berechnung der Nachzerfallsleistung der Kernbrennstoffe von Hochtemperaturreaktoren mit kugelförmigen Brennelementen. DIN 25485, 1990.

[28] Private communication with A. Xhnneux,2014.

[29] W. Schenk et al. Spaltproduktfreisetzungsverlauf von Kugelbrennelementen bei Störfalltemperaturen. *Berichte des Forschungszentrums Jülich*, Jül-2091, 1986.

[30] B. Stöcker, H.F. Nießen. Data sets of the SANA experiment: 1994-1996. *Berichte des Forschungszentrums Jülich*, Jül-3409, 1997

[31] P. Zehner, E.U. Schlünder. Wärmeleitfähigkeit von Schüttungen bei mäßigen Temperaturen. *Chemie Ingenieur Technik*, 42: 933-941, 1970.

[32] F. Li, X.Q. Jing. Comparison of fuel loading pattern in HTR-PM. *2nd International Topical Meeting on HIGH TEMPERATURE REACTOR TECHNOLOGY*, Beijing, China, 2004.

[33] Y. Sun, H. Gerwin et al. Pre-calclation of the SANA1 experiment with the TINTE programme. *Berichte des Forschungszentrums Jülich*, KFA-ISR-IB-9/92, 1992.

[34] B. Lee, H. Gerwin et al. On the validation of the reactor-dynamics code-system TINTE post-calculation of the SANA I experiments with a radial insulator. *Berichte des Forschungszentrums Jülich*, KFA-ISR-IB-2/95, 1995.

[35] M. Lange. Experimente zur selbsttätigen Abfuhr der Nachwärme bei Hochtemperatur-Reaktoren: Planung, Vorbereitung und Ergebnisse. *Berichte des Forschungszentrums Jülich*,Jül-3012, 1995.

[36] J. Baggemann. CFD-Modellierung der Strömungs- und Transportprozesse im Reaktorkern eines VHTR während eines Lufteinbruchstörfalls. PhD thesis, Technischen Universität Dresden, 2014.

[37] B. Stöcker. Untersuchungen zur selbsttätigen Nachwärmeabfuhr bei hochtemperaturreaktoren unter besonderer Berücksichtigung der Naturkonvektion. *Berichte des Forschungszentrums Jülich*,Jül-3504, 1998.

[38] TRISO Coated Particle Fuel Phenomenon Identification and Ranking Tables(PIRTs) for Fission Product Transport Due to Manufacturing, Operation, and Accidents, NUREG/CR-6844, USNRC, vol.1, 2004.

[39] J. Ortensi, A. M. Ougouag. Improved prediction of the temperature feedback in TRISO-fueled reactors. Report INL/EXT-09-16494, 2009.

[40] O. Ubbink, P. S. Toit, P. Lourens, W. R. Joubert. PBMR fuel kernel model for the prediction of accurate temperature profiles. ICONE16, Orlando, Florida, USA, May 11-15, 2008.

[41] Private communication with T. Zhang, 2014.

[42] PBMR Coupled Neutronics/Thermal-hydraulics Transient Benchmark. Volume 1. The Benchmark Definition. NEA/NSC/DOC(2013)10.

[43] H. Gerwin. Das zweidimensionale Reaktordynamikprogramm TINTE Teil 1: Grundlagen und Lösungsverfahren. *Berichte des Forschungszentrums Jülich*, Jül-2167, 1987.

[44] E. A. Harvego, L.J. Siefken. Extensions to SCDAP/RELAP5/ATHENA for analysis of HTGRs. INEEL/CON-03-01199, 2004.

[45] R. Stainsby et al. Investigation of local heat transfer phenomena in a prismatic modular reactor core. NR001/RP/001 R02, 2009.

[46] E. N. Shaw. Europe's nuclear power experiment: history of the OECD dragon project. Pergamon Press, New York, 1983.

[47] J. L. Everett, E. Kohler. Peach bottom unit no. 1: A high performance helium cooled nuclear power plant. *Ann. Nucl. Energy*, 5: 321, 1978.

[48] K. I. Kingrey. Fuel summary for Peach Bottom Unit 1 High-Temperature Gas-Cooled Reactor cores 1 and 2. INEEL/EXT-03-00103, 2003.

[49] W. R. Martin, J. C. Lee et al. Creation of a full-core HTR benchmark with the Fort St. Vrain initial core and assessment of uncertainties in the FSV fuel composition and geometry. Final Report for Project 09-771, DE-AC07-05ID14517, 2012.

[50] H. R. W. Cobb. Mechanical test of full-size Fort St. Vrain fuel blocks. GA-A13917, 1976.

[51] S. S. Clark, J. F. Petersen. TAC2D: A general purpose two-dimensional heat transfer computer code, mathematical formulations and programmer's guide. GA-9262, 1969.

[52] Private communication with Johannes Baggemann, 2013

[53] K. Robold. Wärmetransport im inneren und in der randyone von kugelschüttungen. *Berichte des Forschungszentrums Jülich*, Jül-1796, 1982.

[54] K. Vafai. Handbook of Porous Media. Taylor and Francis, New York, NY, USA, 2nd edition, 2005.

[55] P. Cheng, C. T. Hsu. The effective stagnant thermal conductivity of porous media with periodic structures. *Journal of Porous Media* 2(1): 19-38, 1999.

[56] K. Takamatsu, S. Nakagawa, T. Takeda. Core dynamics analysis for reactivity insertion and loss of coolant flow tests using the HTTR. *15th International Conference on Nuclear Engineering*, ICONE-15-10158, 2007.

[57] R. G. Deissler, J. S. Boegli. An investigation of effective thermal conductivities of powders in various gases. *ASME Trans*, 80: 1417-1425, 1958.

[58] D. S. Selengut. Diffusion coefficients for heterogeneous system. *Trans. Am. Nucl. Soc.*, 4: 398, 1961.

[59] J. C. Han, M. J. Driscol, N. E. Todreas. The effective thermal conductivity of prismatic MHTGR fuel. Massachusetts Institute of Technology Energy Lab, Sep 1989.

[60] H. S. Carslaw, J. C. Jaeger. Conduction of Heat in Solids. 2nd edition, Oxford University Press, 1959.

[61] K. Kunitomi, et al. Thermal transient analyses during a depressurization accident in the High Temperature Engineering Test Reactor (HTTR). JAERI-M 95-163, 1995.

[62] T. Burchell, R. Bratton, W. Windes. NGNP graphite selection and acquisition strategy. ORNL/TM-2007/153, 2007.

[63] H. Petersen. The properties of helium: density, specific heats, viscosity and thermal conductivity at pressures from 1 to 100 bar and from room temperature to about 1800 K. Risö, 224, 1970.

[64] S. Ball, M. Richards, S. Shepelev. Sensitivity studies of air ingress accidents in modular HTGRs. *Nuclear Engineering and Design*, 238(11): 2935-2942, 2008.

[65] H. F. Nissen, et al. NACOK experiment experimental set-up, execution of the test, experimental results. RAPHAEL, Deliverable D-ST3.3, 2008.

[66] Y. H. Zheng, M. M. Stempniewicz. Investigation of NACOK air ingress experiment using differenct system analysis codes. *Nuclear Engineering and Design*, 251: 423-432, 2012.

[67] H. Haque. Input data, assumptions and preliminary results, Technical Note, Areva. RAPHAEL ST WP3: Air Ingress Experiment NACOK, Pre-calculation, 2008.

[68] M. M. Stempniewicz. SPECTRA-Sophisticated Plant Evaluation Code for Thermal-hydraulic Response Assessment, Version 3.60, vol. 4 - verification. NRG report K5024/10.101640, 2010.

[69] B. Schlögl. Oxidationskinetik innovativer Kohlenstoffmaterialien hinsichtlich schwerer Lufteinbruchstörfälle in HTR's und Graphitentsorgung oder Aufarbeitung. ISBN 9783893366767, 2010.

[70] B. Schlögl, S. Kasselmann. Definition of combined primary corrosion and boudouard tests in NACOK II. Deliverable documents of ARCHER project, 2013.

[71] H. J. Allelein, B. Schlögl et al. Experimental investigations and analytical improvements for HTR pebble bed cores. *20th International Conference on Nuclear Engineering*, ICONE20-POWER2012-54041, 2012.

[72] VDI-Wärmeatlas. Springer, Auflage: 10, 2006.

[73] A. S. Shenoy, D. W. McEachern et al. HTGR core thermal design methods and analysis. GA-A12985, General Atomics, San Diego, CA, 1974.

[74] C. H. Lee, Z. Zhong et al. Enhancement of REBUS-3/DIF3D for whole-core neutronic analysis of prismatic Very High Temperature Reactor (VHTR). ANL-GenIV-076, 2006.

[75] Army Reactor Systems Program. *Power React. Technol*, 6: 57, 1963.

[76] C. A. Baxi, E. Perez et al. Evolution of the power conversion unit design of the GT-MHR. GA-A25381, April 2006.

[77] K. H. Lee, K. S. Kim et al. IAEA GT-MHR benchmark calculations by using the HELIOS/MASTER physics analysis procedure and the MCNP Monte Carlo code. *Nuclear Engineering and Design*, 238: 2657-2667, 2008.

[78] S. J. Ball, CRP-3 benchmark problem description for GT-MHR Pu Burner Accidents, ORNL, February, 1997

[79] Heat Transport and Afterheat Removal for Gas-cooled Reactors Under Accidents Conditions, IAEA-TECDOC-1163, 2000

[80] C. Oh, E. Kim et al. Comprehensive thermal hydraulics research of the very high temperature gas cooled reactor. *Nuclear Engineering and Design*, 240: 3361-3371, 2010.

[81] H. Haque, W. Feltes, G. Brinkmann. Thermal response of a modular high temperature reactor during passive cooldown under pressurized and depressurized conditions. *Nuclear Engineering and Design*, 236: 475-484, 2006.

[82] Evaluation of High Temperature Gas Cooled Reactor Performance: Benchmark Analysis Related to Initial Testing of the HTTR and HTR-10. IAEA-TECDOC-1382, 2003.

[83] K. Yamashita et al. A new HTR concept concerning a modular system with block-type fuel elements and its comparison with a pebble-bed-type HTR. *Berichte des Forschungszentrums Jülich*, Jül-1842, 1983.

[84] K. Kunitomi et al. Development of new type of HTGR. *Proc.* 73^{rd} *JSME Fall Annual Meeting*, JSME, Japan, 1995.

[85] A. J. Neylan, F. A. Silady, A. M. Baxter. Gas turbine module heium reactor (GT-MHR): A multipurpose passively safe next generation reactor. *Proceedings of the ASME/JASME* 3^{rd} *International Conference on Nuclear Engineering*, ASME, 1995.

[86] Y. Tachinana, H. Sawahata et al. Reactivity control system of the high temperature engineering test reactor. *Nuclear Engineering and Design*, 233: 89-101, 2004.

[87] J. Sumita, M. Ishibara et al. Reactor internals design. *Nuclear Engineering and Design*, 233: 81-88, 2004.

[88] Design of High Temperature Engineering Test Reactor (HTTR). JAEARI 1332, 1994.

[89] U.S.NRC, Next Generation Nuclear Plant Phenomena Identification and Ranking Tables (PIRTs) Volume 1: Main Report, NUREG/CR-6944.

[90] S. Nakagawa, K. Takamatsu et al. Investigation of the loss of forced cooling test by using the High Temperature engineering Test Reactor (HTTR). *JAEA-Technology*, 2007-056, 2007.

[91] J. Leppänen. Serpent-a Continuous-energy Monte carlo Reactor Physics Burnup Calculation Code, User's Manual. VTT Technical Research Center of Finland, 2009.

[92] J. Ortensi, J. J. Cogliati et al. Deterministic modeling of the High Temperature Test Reactor. INL/EXT-10-18969, 2010.

[93] S. Maruyama, N. Fujimoto et al. Evaluation of core thermal and hydraulic characteristics of HTTR. *Nuclear Engineering and Design*, 152: 183-196, 1994.

[94] N. Fujimoto, N. Nojiri et al. Nuclear Design. *Nuclear Engineering and Design*, 233: 23-36, 2004.

[95] M. Goto. M. Shinohara et al. Long-term high-temperature operation of the HTTR. *Nuclear Engineering and Design*, 251: 181-190, 2012.

[96] D. Tochio, S. Nakagawa. Numerical simulation of three-dimensional thermal-hydraulic behavior for HTTR. *Nuclear Engineering and Design*, 241: 1616-1626, 2011.

[97] N. Fujimoto,U. Ohlig et al. Analysis of the HTTR's benchmark problems and comparison between the HTTR and the FZJ code systems. JAERI-Tech, 98-060, 1998.

[98] N. Nojiri, M. Nakano et al. Benchmark problem's data for the HTTR's start-up core physics experiments. JAERI-memo, 10-005, 1998.

[99] K. Tasaka, T. Katoh et al. Recommendation on decay heat power in nuclear reactor. *Journal of Nuclear Science and Technologh*, 28: 1134-1142, 1991.

[100] Irradiation Damage in Graphite due to Fast Neutrons in Fission and Fusion Systems. IAEA-TECDOC-1154, 2000.

[101] HTTR Data for Loss-of-Forced Cooling Analyses: On the OECD/NEA HTTR/LOFC Project. Internal documents.

[102] E. Kunimoto, T, Shibata et al. Expansion of irradiation date by interpolation and extrapolation for design of graphite components in High Temperature Gas-cooled Reactor. JAEA-Research, 2009-008, 2009.

[103] T. Kikuchi, K. Iwamoto et al. Experimental determination of thermal conductivity and gap conductance of fuel rod for HTGR. JAERI-M, 84-236, 1984.

[104] K. Takamatsu, S. Nakagawa, T. Takeda. Development of the dynamics analysis of coolant flow reduction tests of HTTR. *Proceedings of 3rd International Topical Meeting on High Temperature Reactor Technology*, 2006

[105] A. Saikusa, Y. Tachibana, K. Kunitomi. Benchmark problems for rise-to-power test of High Temperature Engineering Test Reactor in IAEA coordinated research program. JAERI, Oarai, Japan, 2000.

[106] W. Scherer, H. Gerwin. Progress and problems in modelling HTR core dynamics. *International Working Group on Gas-Cooled Reactors*, 149 p, 36-42, 1991.

[107] H. J. Neef. Rechenprogramm MUPO-4-D. *Berichte des Forschungszentrums Jülich*, KFA-IRE-70-15, 1970.

[108] Operation, Test, Research and Development of the High Temperature Engineering Test Reactor (HTTR) (FY2009). JAEA-Review, 2010-055, 2010.

[109] Operation, Test, Research and Development of the High Temperature Engineering Test Reactor (HTTR) (FY2010). JAEA-Review, 2011-036, 2011.

[110] K. Takamatsu, S. Ueta, K. Sawa. Analysis of a loss of forced cooling test using the high temperature engineering test reactor (HTTR). *19th International Conference on Nuclear Engineering*, ICONE19-43224, 2011.

[111] K. Takamatsu, K. Sawa. Reactor kinetics in a loss-of-forced-cooling (LOFC) test of HTGRs. *Proceedings of the 2012 20th International Conference on Nuclear Engineering*, ICONE19-POWER2012, 2012.

[112] M. Saidi, R. H. Abardeh. Air pressure dependence of Natural-Convection. *Proceedings of the World Congress on Engineering*, Vol II, 2010.

[113] Generation IV Roadmap: Description of Candidate Gas-cooled Reactor Systems Report. GIF-016-00, 2002.

[114] R. B. Vilim, W. D. Pointer, T. Y. C. Wei. Prioritization of VHTR system modeling needs based on phenomena identification, ranking and sensitivity studies. ANL-GenIV-071, 2006.

Band / Volume 244
Effects of Cercospora leaf spot disease on sugar beet genotypes with contrasting disease susceptibility
S. Schmittgen (2015), 121 pp
ISBN: 978-3-95806-021-0

Band / Volume 245
Light scattering and trapping in thin film silicon solar cells with an n-i-p configuration
W. Böttler (2015), 132 pp
ISBN: 978-3-95806-023-4

Band / Volume 246
Nanostructured Si-alloys for silicon solar cells
K. Ding (2015), 210 pp
ISBN: 978-3-95806-024-1

Band / Volume 247
Electrochemical Texturing and Deposition of Transparent Conductive Oxide Layers for the Application in Silicon Thin-Film Solar Cells
J.-P. Becker (2015), ix, 156, XXIV pp
ISBN: 978-3-95806-027-2

Band / Volume 248
Stoffliche Charakterisierung radioaktiver Abfallprodukte durch ein Multi-Element-Analyseverfahren basierend auf der instrumentellen Neutronen-Aktivierungs-Analyse – MEDINA –
A. W. Havenith (2015), 311 pp
ISBN: 978-3-95806-033-3

Band / Volume 249
Quantitative Two-Layer Inversion and Customizable Sensor-Array Instrument for Electromagnetic Induction based Soil Conductivity Estimation
A. T. Mester (2015), viii, 119 pp
ISBN: 978-3-95806-035-7

Band / Volume 250
Partial Neutron Capture Cross Sections of Actinides using Cold Neutron Prompt Gamma Activation Analysis
C. Genreith (2015), vii, 166, XXXII pp
ISBN: 978-3-95806-036-4

Band / Volume 251
Long Term Aerosol Composition Measurements at the CESAR Tower at Cabauw, NL
P. Schlag (2015), iii, 228 pp
ISBN: 978-3-95806-037-1

Band / Volume 252
Modellbasierte Spezifikationsmethodik zur effizienten Systementwicklung von Brennstoffzellenantrieben
R. Biurrun Sotelo (2015), 255 pp
ISBN: 978-3-95806-038-8

Band / Volume 253
Three-dimensional ray-tracing simulations of convective gravity waves
S. Kalisch (2015), iii, 183 pp
ISBN: 978-3-95806-040-1

Band / Volume 254
First-Principles Study on Pyrites and Marcasites for Photovoltaic Application
T. Schena (2015), 206 pp
ISBN: 978-3-95806-041-8

Band / Volume 255
Glass-Ceramic Sealant Reinforcement for High-Temperature Applications
B. Cela Greven (2015), xi, 119 pp
ISBN: 978-3-95806-042-5

Band / Volume 256
Entwicklung planarer $Ba_{0,5}Sr_{0,5}Co_{0,8}Fe_{0,2}O_{3-\delta}$-Membranmodule zur Sauerstoffabtrennung und Analyse ihres Transportverhaltens
P. Niehoff (2015), VIII, 134 pp
ISBN: 978-3-95806-044-9

Band / Volume 257
Extension of the Reactor Dynamics Code MGT-3D for Pebblebed and Blocktype High-Temperature-Reactors
D. Shi (2015), x, 162 pp
ISBN: 978-3-95806-045-6

Weitere ***Schriften des Verlags im Forschungszentrum Jülich*** unter
http://wwwzb1.fz-juelich.de/verlagextern1/index.asp

Energie & Umwelt /
Energy & Environment
Band / Volume 257
ISBN 978-3-95806-045-6

JÜLICH
FORSCHUNGSZENTRUM